CRANFIELD UNIVERSITY

COLLEGE OF AERONAUTICS

Ph.D THESIS

Academic year 1995/96

C. LOWE[1]

CFD MODELLING OF SOLID PROPELLANT IGNITION

Supervisors J.F. Clarke & E.F. Toro

July 1996

This thesis is submitted in partial fulfillment of the requirements for the degree of Doctor of Philosophy.

[1]Sponsored by the Defence Research Agency, Fort Halstead

ABSTRACT

Solid propellant is the highly energetic fuel burnt in the combustion chamber of ballistic weapons. It is manufactured, for this purpose, in either granular or stick form. Internal ballistics describes the behavior within the combustion chamber throughout the ballistic cycle upto projectile exit from the muzzle of the gun barrel. Over the last twenty years this has been achieved by modelling the process using two-phase flow equations.

The solid granules or sticks constitute the first phase, which can be assumed to be incompressible over typical pressure ranges within the chamber. The gas-phase is composed of both the original ambient gas contained around the propellant and additional gas produced by the propellant gasifying on heating. Equations can be derived that describe the conservation of mass, momentum and energy in terms of average flow variables. The equations are a highly non-linear system of partial-differential- equations. High-speed flow features are observed in internal ballistics and ordinary finite-difference methods are unsuitable numerical methods due to inaccurate prediction of discontinuous flow features. Modern shock-capturing methods are employed, which solve the system of equations in conservation form, with the ability to capture shocks and contact discontinuities.

However, although the numerical solutions compare well with experiment over the bulk of the combustion chamber, the ignition models used in internal ballistics are unreliable. These are based on either gas or solid-surface temperature achieving some empirically measured 'ignition temperature' after which the propellant burns according to an empirical pressure dependent burning law. Observations indicate that this is not an adequate representation of ignition. Time differences between first solid gasification and ignition imply two distinct processes occurring. Further, ignition occurring in gas-only regions indicates that ignition is controlled by a gas-phase reaction.

This thesis develops simple ideas to describe possible mechanisms for these physical observations. The aim is to provide an improved model of the ignition of solid propellant. A two stage reaction process is described involving endothermic gasification of the solid, to produce a source of reactant gas, followed by a very exothermic gas-phase ignition reaction.

Firstly the gas-phase ignition is considered. A very simple reaction is suggested which is assumed to control the combustion of reactant gas, produced by solid gasification. Ignition is, by definition, the initiation of this exothermic reaction. Chemical kinetics are included in the gas-phase flow equations to

explore the evolution of the reactant gas that is subject to changes in temperature and pressure. By assuming spatial uniformity, analytical solutions of the problem are deduced. The physical interpretation of the solution is discussed, in particular, the relationship between temperature, reactant concentration and ignition is explored.

Numerical methods are required to solve the one-dimensional flow equations. Development of suitable CFD methods provides a method of solution. Finite-volume schemes, based on the original work by Godunov, are used to solve the conservation form of the equations. A simple test problem is considered whereby reactant gas is injected into a cylindrical combustion chamber. By examining the resulting flow histories, valuable information is gathered about the complicated coupling of chemistry and flow.

Chemistry is included into a system of two-phase flow equations. By using standard averaging methods along with an equation for gas-phase species, equations are derived that describe the rate of change of average flow variables for both gas and particle phases. Numerical schemes are developed and some of the difficulties involved in two-phase flow systems, that are not an issue in single-phase flow, are presented. An internal ballistics application is considered as a test case and the solution discussed.

The other important reaction involved in the combustion cycle, solid gasification, is explored. The model is based on detailed description of interphase mass and energy transfer at the solid-gas interface. This involves the solution of the heat conduction equation with a moving boundary that divides the solid and gas regions. Similar numerical schemes are constructed to solve the equations. Finally, this model is coupled with the equations of gas-phase reaction. This describes the complete cycle whereby increases in gas temperature cause the solid to increase in temperature and gasify. Subsequent gas-phase combustion of the reactant gases produces heat-transfer between the solid and gas and continues to accelerate gasification. Eventually this results in self-sustained combustion of the solid propellant.

ACKNOWLEDGEMENTS

I would like to specially thank Professor J.F. Clarke who created the foundation for the theoretical model and has given excellent guidance throughout the course of this research. His experience in combustion and applied mathematics have been indispensable in the evolution of this work. I would also like to express my appreciation to Professor E.F. Toro, of Manchester Metropolitan University, whom has provided expertise in the area of numerical methods and two-phase flow. His encouragement over the years in which I have been involved in the field of CFD have been valuable.

The program of study would not have been possible without the sponsorship of the DRA Fort Halstead. In particular, Clive Woodley has supported the work and made available experimental data. I am grateful for the input that he has volunteered in both experimental and theoretical interior ballistics.

Finally, I would like to take this public opportunity to thank my husband, John. Many may provide lip service to the concept of the modern man but I am confident that few could have provided, so generously, the encouragement and support throughout my research along with being a patient, caring father to our two girls.

Contents

List of Figures

0.1 Nomenclature

$'$	dimensional quantity
t	time(sec)
x	axial direction along the combustion chamber
y	direction normal to solid surface
ϵ	porosity
ϵ^p	region occupied by solid
ρ	gas temperature(kg/m^3sec)
ρ^p	solid density(kg/m^3sec)
u	gas velocity(m/sec)
u^p	solid particle velocity(m/sec)
κ	gas kinetic energy(J/kg)
κ^p	particle kinetic energy(J/kg)
a	gas-phase sound-speed(m/sec)
a^p	particle sound-speed(m/sec)
p	gas pressure(Pa)
p_0	initial pressure(Pa)
e	gas thermal energy(J/kg)
E	total gas energy(J/m^3)
c	reactant mass-fraction
T	gas temperature(K)
T_0	initial temperature(K)
T_s^p	solid surface temperature(K)
$T^p(y,t)$	solid temperature profile(K)
$\mathbf{U}$	vector of conserved variables
$\mathbf{U}^g$	vector of conserved variables for gas
$\mathbf{U}^p$	vector of conserved variables for solid
$\mathbf{F}$	flux function
$\mathbf{S}$	source function
R	universal gas constant($J/Kkgmole$)
W	molecular weight
b	gas covolume(m/kg)
γ	ratio of specific heats
α^p	solid diffusivity (m^2/sec)
C	specific heat capacity of gas(J/kgK)
C^p	specific heat capacity of solid (J/kgK)
λ^p	solid conductivity ($J/msecK$)
λ	gas conductivity ($J/msecK$)
q	heat flux (J/m^2secK)

R	intergranular stress (Pa)
Q	gas-phase reaction energy of formation (J/kg)
Q^p	solid-phase energy of formation (J/kg)
L	latent heat of gasification of solid (J/kg)
K	rate of reaction (kg/m^3sec)
Ω	chemical frequency (sec^{-1})
$[A]$	concentration of reactant A $(moles/m^3)$
$X(g)$	gaseous oxidant
$F(g)$	gaseous fuel
$P(g)$	gaseous inert product
ν	stoichiometric coefficients
k	rate constant (sec^{-1})
$\mathcal{D}$	Damköhler number
E_A	activation energy of gas-phase reaction $(J/kgmole)$
E_A^p	activation energy of solid-phase surface reaction $(J/kgmole)$
A_g	reaction coefficient of gas-phase reaction $(1/Pasec)$
A_s	reaction coefficient of solid-phase gasification $(kg/Pasec)$
B_{cJ}	burn-rate coefficient $(m/secPa^n)$
n	pressure index
$\dot{r}$	rate of regression of propellant surface (m/sec)
m	mass of propellant grains (kg)
$\dot{m}$	rate of gasification of propellant (kg/sec)
$\dot{m}_{gr}$	rate of gasification of a propellant grain (kg/sec)
m_{ig}	total mass of igniter (kg)
$\dot{m}_{ig}$	rate of addition of igniter gas (kg/sec)
t_{ig}	ignition delay (sec)
e_{ig}	chemical energy of igniter gas (J/kg)
T_c	critical temperature (K)
T_d	decomposition temperature (K)
T_{ig}	ignition temperature (K)
S_p	Surface area of solid grain (m^2)
d_0	outer diameter of the solid grain (m)
d_I	inner diameter of the solid grain (m)
D	size of propellant grain (m)
D_p	effective diameter of propellant grain (m)
V_0	initial volume of propellant grain (m^3)
S	surface area of propellant grain (m^2)
S_0	initial surface area of propellant grain (m^2)

θ	form function
$f(t)$	fraction of D remaining at time t
$z(t)$	fraction of weight remaining at time t
f_s	drag force (N/m^3)
k_D	drag coefficient
ϵ_0	settling porosity
q	heat transfer (J/m^3sec)
W_l	heat loss to the walls (J/m^3sec)
c'	radiation coefficient (J/m^2secK^4)
E	emissivity
ψ	heat-transfer coefficient
l	length of domain (m)
c_{fl}	Courant number
c_D	diffusion number
$ncells$	number of cells in x direction
$msol$	number of cells in y direction

Chapter 1

Introduction

1.1 Internal Ballistics Modelling

Internal ballistics modelling involves the combustion of highly energetic propellant materials. Propellants burn releasing large quantities of chemical energy which explains their use as the highly concentrated fuel that powers rocket motors and ballistic weapons. Propellants differ from explosive materials as the combustion process is much less violent; detonation has been observed during malfunction of arms but is an undesirable phenomena of solid propellant combustion. It is the typical combustion cycle of internal ballistics that will be investigated in this work.

Traditionally propellant is provided in solid form such as granular or stick propellant, although some modern weapons do exploit the various advantages of propellant in liquid form. Figure (1.1) illustrates a typical ballistic weapon configuration and the ballistic cycle extracted from the text by Kuo & Summerfield [1]:

The long cylindrical combustion chamber is filled with propellant material and a projectile is placed at one end. The opposite end of the chamber is called the 'breech'. Combustion is initiated by some igniter stimulus and although there are various modes and configurations that are in operation, specifically this work will concentrate on heating the propellant grains from ambient by the addition of hot 'igniter-gas'. The igniter-gas is vented via the 'primer' tube which runs along the centre of the cross-sectional area. The tube extends over some fraction of the total length of the chamber. The primer is a perforated

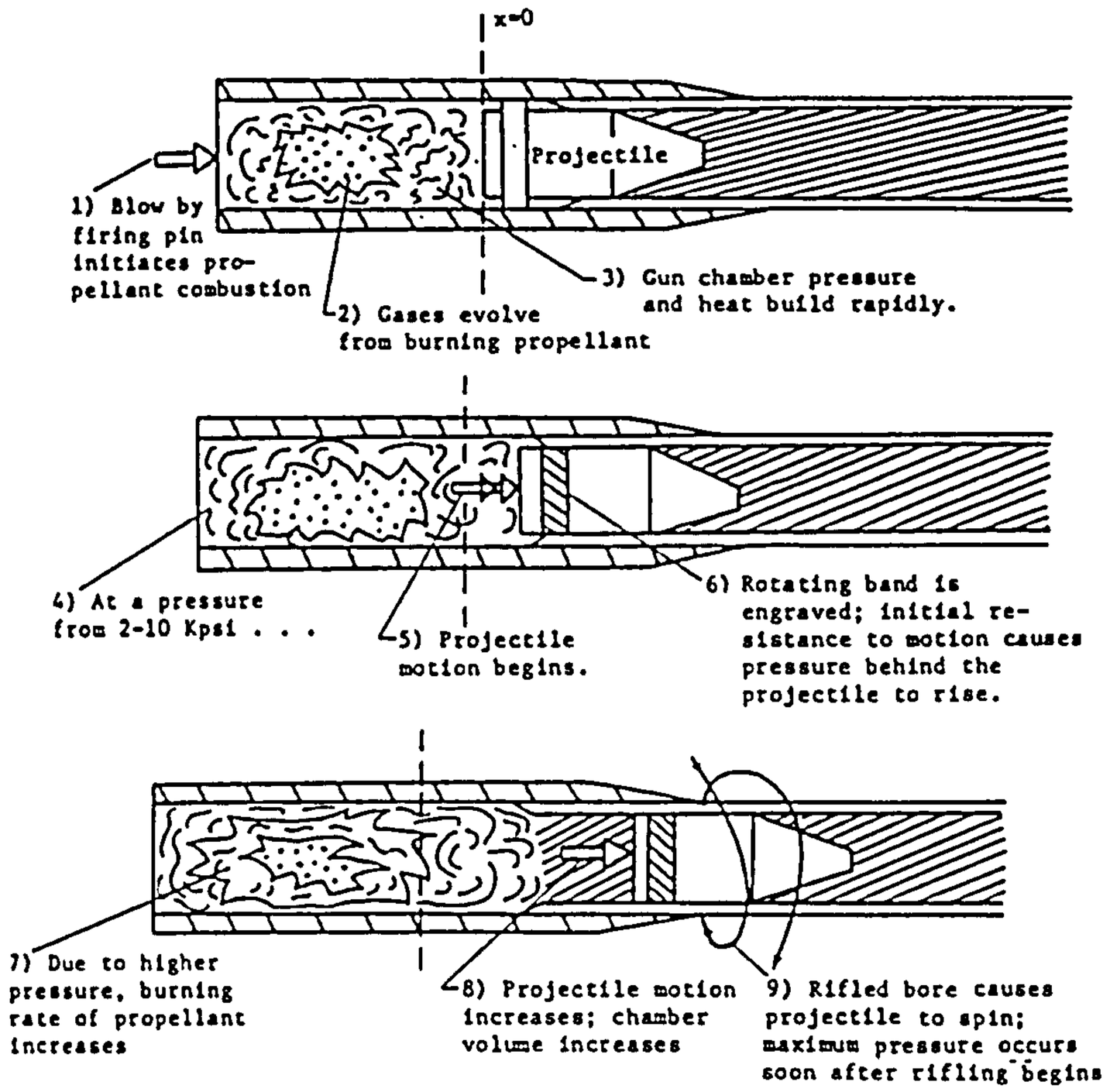

Figure 1.1: Ballistic cycle.

tube through which the igniter-gas passes and penetrates the propellant bed. Energy is transferred from the hot gas to the propellant until the propellant ignites and burns, releasing chemical energy. Once the propellant combusts the chamber will pressurise rapidly transmitting a force onto the projectile-base. The projectile is held in position by an engraving band which does not allow the projectile to move before the pressures behind it are high- a typical value is around $60MPa$. The engraving band is designed so that once the pressure rises above this level, a torque is created causing the projectile and engraving band to spin out of position and travel along the barrel of the gun. The movement of the projectile extends the length of the combustion chamber until finally the projectile leaves through the muzzle into the outside atmosphere. Usually, the propellant will be completely burnt before the projectile leaves the barrel.

Early theoretical work on internal ballistics was primarily concerned with calculation of the exit velocity of the projectile. The force on the projectile is predicted by calculating the pressure history at the projectile-base. Early theory on internal ballistics is well documented in the book by Corner *et al.* [2]. The first models proved to be quite accurate at calculating muzzle velocities and peak pressure but no attempt was made to include flow dynamics in the chamber and the problem was regarded as a 'well-stirred' or 'lumped parameter' system. This means that temporal variation of quantities - such as the bulk pressure- were calculated with no account of position. An early lumped parameter code was written by Baer & Frankle [3].

Piobert's law of burning was recognised at this time which provides a formula for the rate of regression of the solid propellant surface $\dot{r}$ as a function of external gas pressure and a number of empirical constants specific to each propellant type. In addition much effort was devoted towards constructing formulae that would provide the rate of change of burning surface area over time for quite complicated propellant geometries. The idea of the form function was constructed by Corner which provides a relationship between the rate of burning $\dot{r}$ and the exposed surface area S_p. The combination of these two ideas produces a method of measuring the rate of mass-transfer from solid to gas:

$$\dot{m} = \rho^p S_p \dot{r}, \tag{1.1}$$

where $\dot{m}(kg/sec)$ is the rate of gaseous mass addition and ρ^p is the density of the solid propellant. Along with this, an experimentally derived energy of combustion is taken for the propellant $Q(J/kg)$ and the rate of energy and pressure increase in the gas-phase can be deduced. During these studies, it was soon apparent that at high pressures the reactant gas could not be described accurately using the ideal gas equation and a covolume equation

was adopted. Both of Piobert's law and Corner's theory are used in internal ballistics modelling today.

However, this approach could not model some of the very noticeable and undesirable phenomena that were being observed during the operation of ballistics weapons [4]. In particular the presence of longitudinal pressure waves, similar to the combustion instability found in rocket motors, would often cause difficulties and it was crucial to extend the model to at least one-dimension in the axial direction.

Kuo & Summerfield [5] first attempted this by developing a one-dimensional inviscid model that included gas dynamics but assumed that the solid propellant remained stationary. Very soon after this, a number of authors developed multi-phase flow theory to produce models of propellant combustion including Krier [6], Culick [7], Gough [8] and Kuo [9].

However, these were based on different approaches within multi-phase flow. The first two authors adopted the idea that the two-phase mixture acts as a continuum for which equations of mass, momentum and energy can be derived. A thorough documentation of this theory can be found in the book by Soo [10].

The equations produced by the latter two authors were based on separated flow theory allowing each phase to occupy a separate control volume. These average equations can be derived by integrating over regions large in comparison with the scale of heterogeneity of the mixture. This region is large enough to contain many particles but small compared to the overall dimensions of the flow.

The two phases involve a compressible gas and the solid particles may be assumed to be incompressible for typical pressure ranges produced in internal ballistics applications. For the gas-phase, equations of mass, momentum and energy are produced. The solid-phase involves equations for mass and momentum but do not require an energy equation due to the assumption of incompressibility. Additionally an equation for the number of solid particles in the system can be derived which will be conserved assuming that the particles do not fragment or coalesce. All of these flow equations involve an additional variable not involved in single-phase flow called the 'porosity', ϵ, which describes the fraction of volume occupied by gas whilst $(1 - \epsilon)$ describes the fraction occupied by the propellant. Since the solid density is in fact constant, the mass equation in the solid-phase reduces to an equation for ϵ. The covolume equation of state is used to close the system. This provides six equations in six unknowns that can be solved.

The original model of Krier contradicted previous two-phase flow theory and was proved to be incorrect [1]. The equations derived by Gough emerged as the most prominent form for interior ballistics modelling which were adopted by several different research establishments worldwide [11], [12], [13], [14], [15]. However, Gough soon realised that the system of equations were ill-posed, but was not alone; scientists dealing with other fluid flow problems had found that the inviscid two-phase flow equations for two incompressible phases were also ill-posed. Specifically the momentum equations were found to be the cause and proponents of the continuum approach argue that it is due to the neglect of 'inertial' terms, that do not appear in the separated flow theory. More details of this will be described at a more appropriate stage in this work as Gough's equations are used as the base in which a more detailed ignition model is included. Gough *et al.* solved the equations using the MacCormack method [16] in the code NOVA. Several years were spent after this extending the model to accept more general chamber geometries, extending to two-dimensions and modifying the code to allow greater generality of initial propellant distribution [11]. The last of these items included initial propellant distributions that included regions of ullage (no propellant charge) and specifying distinct areas that held different types of propellants. This was achieved by constructing a dynamic mesh routine that tracked internal boundaries of the flow. The code was also developed to include some of the additional detail required for stick propellant modelling.

Kuo *et al.* also developed sets of equations suitable for stick propellant that used a combined Eulerian-Lagrangian [17]. In this work, the possibility of more than one chemical reaction controlling combustion was considered. Combustion was assumed to involve three reactions; solid-surface pyrolysis, an exothermic gas-phase reaction followed by a very exothermic gas-phase reaction. Complementary experiments confirmed numerical results indicating very slow stick velocities. The chemical solutions showed the bulk of chemical energy being released at the breech implying that pyrolysis and energy release occurred at the same location. Following this Kuo also carried out experimental and numerical studies concerning the fracture of stick propellants [18]. In particular, a fluid-dynamic code was coupled with a finite-element code to analyse the effect of combustion on the structure of a single stick. Fragmentation of the propellant grain was observed which is particularly relevant as propellant fragmentation causes a sudden increase in exposed surface area S_p. This increases the rate of burning, described as uncontrolled burning as very rapid pressure increases have proved responsible for causing deflagation-to-detonation transition in the combustion chamber.

[1] This was corrected in later work of the author's

In the late eighties, Gough and associates also extended their work to include gas-phase chemical kinetics contained in the XNOVAXKTC, code [19], [20]. The intention was to explain some of the pressure differences obtained when different igniter gases are used to initiate combustion. For example, increased pressures, of up to thirty percent, were observed when oxygen-rich igniters were adopted. They were also aware of other phenomena that implied the importance of chemical kinetics such as long ignition delays, often followed by unexplained vigorous combustion, and high reactivity observed in gas-only regions. However, the study does not concentrate on the ignition mechanism but more the effect of different igniter materials on the overall energy release throughout the combustion cycle.

Arguably the most recent breakthrough on propellant combustion was made by Baer & Nunziato [21] who brought together some of the ideas developed by researchers over previous years. The equations were developed for deflagation-to-detonation transition and had to include compressibility effects in the solid-phase due to the high pressures that occur. The derivation was based on the continuum approach to multi-phase modelling and the resultant system involves mass, momentum and energy equations for both phases and two equations of states. Along with this there is a compaction equation, that controls the change in porosity, which was developed to satisfy a number of entropy conditions. From this a well-posed and comprehensive model was developed. For many ballistic scenarios the model of Gough is sufficient but it is speculated that the equations of Baer & Nunziato would perform well past the point at which Gough's equations fail.

More recently, the interior ballistics code equations derived by Gough have been extended to include viscous and turbulent effects [22]. The accompanying code has retained the mesh routines of previous versions of the code but adopted new CFD techniques to solve the governing equations specifically developed for the multi-dimensional time-dependent compressible Navier-Stokes equations.

Margolis & Williams have also been investigating the multi-phase flow combustion problem [23]. In particular they study the effect of a deflagation wave through a propellant bed and include the formation of a liquid-phase. The equations have been mathematically analysed in the steady-state by use of activation-energy asymptotics. However, the development of these ideas for a realistic internal ballistics problem has not so far been pursued.

The above review describes the development of interior ballistics combustion models up to the present day. In the next section ignition studies and the

motivation for the work contained in this thesis will be outlined.

1.2 Ignition Theories

Ignition modelling has been quite crude in many internal ballistics codes. Many assumed that once the gas temperature increases above some experimentally measured 'ignition temperature', then the propellant grain would burn at a rate governed by Piobert's law. The weakness of the ignition temperature idea is that it is supposed to encompass all of the intricate heat-transfer processes between the gas and solid, solid thermochemistry, solid-phase reactions and gas-phase reactions. Experiments proved that the formation of pressure waves was highly dependent on the primer configuration and method of ignition providing good reason to look at the ignition process in more detail. A comprehensive review of ignition modelling is contained in the chapter by Hermance in [24] and elements of his work will be used in this review.

Ignition models emerged as early as the 1950's and a review of experiment and theory between then and 1966 was conducted by Price and co-workers [25]. By then a number of ignition theories had developed which will be outlined. Experimental work and the three ignition theories, solid, heterogeneous and gas were discussed in Prices's review. In this, the relationships between experiment and the proposed theories were outlined and the strengths and weaknesses of the various theories compared. In particular, there was a plea to produce ignition by use of an externally applied heat flux so that experiments and theory could be easily repeatable and comparable. As a result, much of the experiment and theory following this report were based on radiation driven thermal ignition.

The earliest solid theory measured the ignition delay by assuming that up to ignition the solid acts similar to an inert material. By solving the one-dimensional heat conduction equation normal to the propellant surface, the rate of rise in solid surface temperature can be predicted. Ignition was assumed to be controlled by a condensed-phase reaction confined to a thin surface region. For surface temperatures below some critical temperature T_c the reaction rate was negligible. However, once the temperature approached empirically derived T_c, then the rapid growth in surface exothermic reaction resulted in ignition.

The very first of these models simply solved the heat-conduction equation

up to T_c at which ignition was assumed to occur. However, these models could not measure whether the propellant had actually attained an ignited state- some sort of exothermic reaction must be involved to do this- and so the inert heating idea is only of use if the duration of initial heating is much longer than the time between the point at which the temperature is equal to T_c until some self-sustaining reaction takes place.

More detailed models followed that included evolution of the condensed-phase reactant (for some order of reaction) and contributions in the energy equation for heat release due to exothermicity, convective heat transfer due to regression of the surface and in-depth absorption of heat. Surface boundary conditions also took into account any energy requirements due to phase change. Merzhanov and Averson [26] produced an excellent review of the solid-phase ignition theory that described many of the analytical and approximate methods used at the time to investigate the nature of the solution.

A most elegant study was produced by Liñan and Williams [27] in the early seventies. By using high activation energy asymptotics, they produced analytical expressions for the relationship between surface energy release, activation energy and ignition delay time that was identical to an empirical expression produced by Bradley [28] in the preceding year. Several papers stemmed from this initial paper to include in-depth radiation absorption and conductive heat losses to an external gas-phase. Although interesting, the first paper was the most notable that introduced the use of high energy activation energy asymptotics as a powerful analytical tool in the study of ignition.

One of the most significant results obtained from the solid-phase theory was the relationship between ignition delay t_{ig} and external heat flux q such that:

$$t_{ig} \propto q^n$$

where $-1.52 < n < -2$ at constant pressure, which agrees with experiment. However, the solid theory also indicates that as the pressure increases, the ignition delay **increases** which is contrary to experiment. In fact, composite propellants, which are composed of ammonium perchlorate oxidiser embedded in a matrix of rubber or polymer, seemed unlikely candidates for ignition based on condensed phase reactions alone as their initiation displayed sensitivity to external pressure and exothermic gas-phase reactions were observed. Experiments had been conducted in which propellant material was ignited on exposure to strong oxidisers without the need for any thermal sources of energy. Indeed, shock-tube experiments were used to ignite propellant material by exposure to stagnant reflected shock conditions. The experiments showed

ignition delays dependent on gas-phase oxidizer content and pressure. So, it can be drawn that the solid-phase theory breaks down due to its inability to include both the effects of external pressure and oxidiser content.

A 'hypergolic' theory was proposed; this claimed that ignition was due to the chemical attack of gaseous oxidiser on the solid surface which produces an exothermic surface reaction. These theories involved transient gas-phase diffusion of chemical species plus heat conduction into the solid. However, the weakness of the hypergolic theory arose from the question of whether such a seemingly volatile material could exist in atmospheric conditions. Furthermore, this did not explain the ignition of composite propellants in inert atmospheres. From this question a heterogeneous theory arose which asserted decomposition on heating to produce a reactive acid followed by surface hypergolic attack. At the time of Prices' review, the study of this was very much at a qualitative stage but many argued that this theory was 'correct' despite the lack of quantitative proof. Other theories were seen as special cases of the heterogeneous theory or unimportant secondary aspects of ignition. Price commented that this complacency led to the neglect of gas-phase theories, which in the light of more recent developments in ignition theory was a rather astute criticism.

Following this, in 1968 Williams [29] produced a heterogeneous ignition model with heat-conduction equations for the solid and the gas and an equation for the evolution of reactant gas. Recall that heterogeneous ignition is controlled by chemical attack on the solid surface; the model links the solid temperature, the surface reaction rate and the quantity of external oxidiser. The study revealed two distinct periods in the ignition event; initially, the surface temperature rises slowly and continually until it arrives at some temperature. During the second period the temperature remains almost constant over some period of time that ends when suddenly the surface temperature rises sharply, characterising ignition. Using these results, a relationship between ignition delay and the partial pressure of the gaseous oxidiser was deduced that was essentially equivalent to the relationship that can be found using the gas-phase ignition theory. However, Williams' work did not include convective effects at the solid surface and so the validity of the model ends once pronounced surface reaction/regression occurs.

Andersen [30] developed the heterogeneous theory using the methodology of Frank-Kamenetskii [31]. On first glance, the work appears to be a solid-phase theory of ignition with in-depth radiation absorption. However, the assumptions made with respect to exothermic energy release mean that this can in fact be classed as a heterogeneous model. The analysis also revealed two

distinct heating periods prior to ignition; the first period comparable to heating of an inert solid where the temperature increases to some critical temperature followed by the second rate-controlling step involving an exothermic surface reaction. The work adopts the criterion that once the rate of temperature rise due to chemical reaction is of the same order as the rate of temperature rise due to the heat source, then ignition occurs. A function of ignition delay versus external heat flux and external gas pressure was deduced that gave good agreement with experiment. In a later paper [32], the time to establish self-sustained burning was included in the ignition model. This involved adding an extra term to account for convective effects due to surface regression. After the exothermic reaction is initiated at the surface the solid starts to regress. This results in energy loss at the surface due to convection. Although the model was lacking in detail it illustrated the importance of including the convective transport.

Liñan & Crespo [33] used asymptotics in a heterogeneous model to produce an analytical expression relating surface energy release to activation energy that is similar to that derived using the solid-phase theory [27]. Convective effects were excluded but added in a later paper,[34]. This provided the interesting result that high rates of surface gasification could actually *inhibit* the ignition process via excessive convective energy loss at the surface.

However, experimental investigation of propellant ignition by radiative heat flux uncovered a time difference between first gasification and ignition. The heterogeneous theory failed to provide an explanation for this.

These observations provoked the development of the gas-phase theory of ignition. The gas-phase ignition assumes that the propellant decomposes on exposure to heat to produce reactant gas. These reactant gases subsequently react exothermically to produce ignition characterised when the gas attains some local temperature or luminosity. At the time of the review by Price, no explanation of the solid/gas interface decomposition was included and investigations were at a very early stage.

Since then, Hermance *et al.* [35] developed the idea based on the results of shock tube experiments, [24], where the initial thermal stimulus was provided by conductive heat transfer from a stagnant high temperature gas. The physical configuration treats gas and solid in a closed vessel with a single interface between solid and gas. Gas-phase energy and gaseous reactant equations plus a solid conduction equation are solved at the interface which is regressing due to endothermic surface pyrolysis. A number of ignition criteria were developed based on gaseous conditions. For example, ignition was assumed to

occur if the gas temperature rose by fifty percent from the initial temperature or if the light intensity, based on the gas temperature, increased to some level. The gas theory was applied to pure fuel [35], homogeneous [36] and heterogeneous [37] propellants. Relations between ignition delay and both pressure and mass-fraction of oxidiser were deduced that compared well with shock tube experiments.

Gas-phase and heterogeneous theories were developed for the problem of propellant-surface decomposition caused by sudden flow of a hot oxidising gas by Kashiwagi and Summerfield. At the time, the problem was a formidable problem in numerical analysis so the gas-flow was assumed to be steady-state. The gas theory [38] produced closer agreement with experiment.

The theory of gas-phase ignition due to radiative heat flux is slightly less developed. Hermance & Kumar [39] show that the ignition criterion used by Andersen [30], for heterogeneous ignition, based on the equality of heat-loss and heat generation is inadequate for radiative ignition. A 'stronger' criterion which also takes into account the time required to establish self-sustained combustion is needed. For low fluxes of radiative heating, a reasonable correlation between the ignition delay and pressure was found but for higher fluxes the agreement was not good. In fact, the numerical calculations implied that the gas-phase chemical times were much lower than the total ignition delay.

Kindelan & Williams once again produced impressive results by exploiting asymptotic methods to analyse the gas/solid equations. The endothermic gasification process produced by a constant radiative heat flux was studied in [40]. This revealed three distinct periods that may be compared with the heterogeneous work of Andersen; inert heating, transition and finally surface gasification. The work found that the time to first gasification versus applied heat flux behaved in the same way as the time taken for thermal runaway derived by heterogeneous ignition theory. The differences between endothermic surface reaction and exothermic reaction (heterogeneous theory) is that the former produces temperature levelling at the surface whilst the latter provides thermal runaway, but apart from this there were more similarities than differences. In [41], exothermic reactions were considered in the gas-phase so that a gas-phase ignition is possible. If it is assumed that the ratio between the gas-phase activation energy and the gasification activation energy is around one, the analysis proved that ignition could occur at earliest at first gasification or at some considerable time later. However, the work on radiative heating could not produce evidence to suggest that the gas-phase reaction was the overall controlling mechanism in the ignition process and it is highly likely to be a combination of slight exothermicity at the surface followed by gas-phase

reaction.

Despite this, the gas-phase theory provides explanation to some of the most indisputable experimental evidence that cannot be explained by either the solid or heterogeneous ignition theories; the influence of pressure, oxidiser concentration and delay between first gasification and ignition. Before more general discussion on practical ignition studies is embarked on, the comments made by Hermance [24] to conclude his review on ignition studies will be stated; the gas-phase ignition theory needs further development and the question of ignition criteria is still unresolved. The convective transport terms from the should not be neglected from the solid-phase energy equation since ultimately ignition is not truly attained until there is established surface regression of the solid. More theoretical and particularly numerical work is needed. He remarks that at its most daunting, ignition is not controlled by one overall mechanism but a combination of gas-phase reactions and solid gasification.

The above studies are very interesting at the solid/gas interface level and can be easily compared to some of the rather artificial experimental work that has been performed. However none of this work encompasses the theories in a realistic gun or rocket combustion chamber.

Kuo *et al.* [42] solve a one-dimensional heat-transfer equation coupled with the gas-phase Euler equations for application to rocket burning. The model does not include a regressing boundary and is designed to measure inert heating in the solid until the surface arrives at some decomposition temperature. After this point combustion is assumed to obey Piobert's law. This is the most simplistic ignition that corresponds to the earliest theory presented in the early fifties. This means ignition and decomposition occur simultaneously at the surface. Heat-transfer is measured using simple boundary layer theory based on Newton's cooling law. However, the attraction of this work is that rather than solving the heat conduction equation into the solid material, an integral method is applied to the equation. By assuming that the solid temperature profile can be described by a third-order polynomial, the partial-differential equation can be transformed to a first-order ordinary-differential equation that describes the rate of surface temperature change in time. This is much faster than solving the partial-differential equation over each time-step and although approximate it is efficient and simple to code. Once the surface temperature reaches some ignition criterion, the equation is no longer utilised.

The ignition studies described above are particularly appropriate for rocket motor configurations and use very similar modelling ideas as 'transient burning' theory. Steady-state burning is combustion which occurs in a constant pressure

atmosphere. For example a strand-burner involves burning of a propellant stick in atmospheric conditions from which a wealth of experimental data can be determined. It was soon apparent that burning rates of the strand-burner did not compare well with those inside a combustion chamber. Transient theory is designed to predict the burn-rate $\dot{r}$ during severe pressure excursions and has been also used as a basis for ignition models.. Most of the work develops methods of using data from so-called 'steady-state' burning regimes to map into the transient environment. The theory concentrates on heat-transfer processes at the solid/gas interface throughout the burning regime not just up to the point of ignition.

One of the earliest transient burn-rate methods was based on small perturbation theory. For small changes of pressure, small changes in the burning rate could be deduced by using steady-state data. This produces very simple explicit expressions for the burn-rate but unfortunately is not suitable for large changes of pressure.

It was soon realised that there was no easy method of mapping from the steady-state to the transient. Many authors considered the solution of the heat-conduction problem with regressing surface in a similar way to those studying ignition, as described above. Assuming that the reaction at the surface is confined to a thin surface layer, the rate of *combustion* was assumed to be controlled by a zeroth order Arrhenius reaction dependent on surface temperature. This procedure effectively replaces Piobert's law of burning with more detailed modelling of interface chemistry. There is a large amount of work along these lines where the approach differs via the method in which the heat-transfer from the gas to the solid is formulated.

Flame models were developed in the late sixties and early seventies that are based on the assumption of 'quasisteady' conditions. By comparing the characteristic times associated with the thermal diffusion processes in the gas, solid-surface and remaining solid, the system is said to be quasisteady if the timescale associated with the pressure excursion is much greater than that of the gas and surface propellant region but of the same order as the bulk of the solid material. The models are produced by integrating the steady-state gas-phase energy equation between the propellant surface and infinity providing an interface boundary condition that can be interpreted as an expression for heat-transfer. The methods differ depending on the assumed distribution of heat release in the gas perpendicular to the solid surface. From this a whole family of different heat-feedback formulations can be defined which are outlined in the book [24] and the review on transient burning by Coates & Kuo [43]. In 1977, Kooker & Nelson [44] compared three different flame models. The study did

not couple gas and solid phase and the external pressure was imposed from empirical data. They concluded all three models gave comparable burning rates and that the burn-rate was very sensitive to the amount of surface heat release.

However, the work by other researchers does not support this. In 1982 Miller [45] produced an interesting study by considering solid propellant burning in atmospheric conditions. Combustion was assumed to be controlled by a surface reaction followed by a gas-phase reaction. A steady-state analysis produced formulations of the burn-rate that agree with Piobert's empirical law. He also obtained an expression to describe the heat-transfer from gas to solid for transient burning. Following this, Miller & Coffee [46] made an extensive comparison of flame-model formulations of heat-feedback to compare with their own. Miller and Coffee report large variations in solutions and conclude that the models are unreliable.

In the late 1970's the transient theory derived by Zeldovich-Novozhilov emerged from the former USSR describing a mapping from the steady-state to the transient to give the heat-transfer. This was outlined by Summerfield and coworkers [47]. The method was widely adopted by many at the time, including Gough who used this as a method of modelling ignition. He installed this into the internal ballistics code based on his two-phase flow equations [48]. The flow equations are coupled to the solid-phase conduction equation with moving boundary at a typical propellant particle surface. By using the Zeldovich formulation for the heat-transfer from gas to solid, the rate of surface combustion is measured. However, the inclusion of this was not particularly fruitful and no validation has been made.

The disadvantage of the Zeldovich method compared to the flame models is that it relies on extensive steady-state burning-rate data and cannot be utilised in conjunction with erosive burning theory [2]. As an ignition model it is treating the process as solid-phase ignition with all the associated limitations.

Despite the huge effort that was devoted to the problem of transient burning, most of the theory developed in the 1970's remains in the area of combustion instability in rocket motors and has not been employed by the interior ballistician. The propellant configuration in rocket motors is quite different from ballistics and the theory is not easily transferred from one application to another.

---

[2] Erosive burning is the phrase used to describe increases in burn-rate due to cross-flow sweeping over the propellant surface

However, the fundamental ideas have provided a base to build on. More recent attempts to model the conditions at the surface abandon the rather complicated mathematical derivation of heat-feedback expression in favor of more conventional expressions for heat-transfer. These are based on the temperature difference $T - T_s$, where T is the gas temperature and T_s is the propellant surface temperature, plus a number of empirical constants. Radiative heat transfer, dependent on fourth powers in temperature, may also be included. For example the work by Loraud & Porterie [15], specifically designed for internal ballistics, base their ignition model on the early work of Kuo *et al* [42], that is, a simple inert heat-up equation for the surface grain until it arrives at some ignition-decomposition temperature. This work solves axisymmetric viscous two-phase flow equations and provides valuable information on how primer geometry can promote the formation of pressure waves. The work by Wildegger-Gaissmaier and Keller [13] perform similar work. Hypothetical configurations are presented which do not assist such pressure waves. Krier & Gokhale [49] do not consider the solid temperature to measure the evolution of ignition in their study of DDT in solid propellants. Instead a certain amount of energy must be absorbed in the solid for ignition to occur.

There is a wealth of detailed experimental evidence in the literature suggesting ignition that is heavily influenced by gas-phase reactions, [24]. This work serves to model two simple observations of realistic ballistic environments. Experiments have been conducted in which there is a region of ullage in the propellant bed. Ignition has often been seen to occur in gas-only regions of the chamber, which implies a homogeneous ignition reaction. As mentioned above, experimentally the solid is found to decompose into gas prior to ignition implying that the solid produces gas which ignites some-time later. In the field of ballistics, information gathered by the ignition theorists has not been exploited and few have actually considered chemical energy release via gas-phase reactions. Those that did, tended to consider the effect on the overall combustion cycle rather than specifically ignition.

Inspired by the work described in the review above, it is anticipated that satisfaction of these two observations must involve a model that includes propellant gasification into reactant gas followed by a model to describe the evolution of the gas-phase chemical ignition. The first of these requirements can be provided by previous theory as given above, the second requires inclusion of gas-phase chemical kinetics in the two-phase flow equations. This thesis derives such a decomposition and gas-phase ignition model. Mathematical analysis of the equations will be undertaken and numerical methods will be validated before the complicated ballistic problem is considered.

1.3 Improved Ignition Theory

The exact definition of 'ignition' has proved to be quite elusive; it is often described as a 'go/no-go' process or 'thermal runaway' with empirical measurements based on this. The mathematical analysis of the proposed ignition model provides a more precise, scientific understanding that agrees well with the physically motivated definition.

Chemical-kinetic theory will be introduced in chapter two and applied to a chemical reaction in the gas-phase. The proposed reaction is assumed to control combustion, in particular, the initiation of combustion, ignition. A model is derived to describe the behavior of a reactant gas that is injected into a closed vessel. The purpose is to mimic a gasifying propellant, initially without the complications of two-phase flow, producing a source of reactant which will combust according to the proposed chemistry. Single-phase inviscid equations of mass, momentum and energy are derived which involve 'source' terms due to addition of gaseous material into the closed chamber. A number of assumptions allow the chemistry to be described by a single reactant species equation. This provides four equations and five unknowns. The system is closed by including an ideal equation of state.

To provide a physical understanding of the equations with chemistry, the system is simplified into its spatially uniform form. Expressions for the time-rate of change of mass, species concentration and energy - in the form of a system of ordinary-differential-equations - are derived. Mathematical analysis can reduce the system onto a phase-plane which depicts how the temperature in the system varies with changes in reactant species concentration. In this context the relationship between ignition, reactant concentration and gas temperature is revealed.

In chapter three, the numerical solution of the spatially uniform system serves to exemplify the analysis in the preceding section and complements the work by allowing a greater degree of generality in the system. The timescales of chemical kinetics are much faster than that of flow dynamics. The manifestation of this means that the ordinary-differential equations are 'stiff' [50]. This disables the use of more conventional solvers, such as explicit Runge-Kutta methods, to solve the equations and an appropriate implicit method is adopted. A parametric analysis of the terms introduced by gas-phase chemistry is performed. Discussion of how the new system of equations, described as the system with non-equilibrium chemistry, fits in with previous models, which assume chemical equilibrium, is included. Finally, the equation of state

is replaced by the more realistic covolume form, in order to cope with very high pressure, and the effect on the equations is explored.

Chapter four describes the numerical scheme developed to solve the system of equations that include one-dimensional effects. The system is a highly non-linear system of partial-differential-equations. Time-operator-splitting is employed which reduces the system into smaller manageable problems. The first involves the Euler equations with chemical effects. Modern shock-capturing methods are used to solve these flow equations which produce accurate solutions of shock propagation. A finite-volume-scheme, based on the original work by Godunov and called the WAF method, is chosen. This is a method which exploits the solution of the Riemann problem and an approximate efficient Riemann solver, called the HLLC method, is introduced. The second part of the operator-split produces a set of ordinary-differential-equations which are solved as in chapter three. The numerical methods are applied to a test problem which has the configuration of a typical combustion chamber. Flow histories are examined which produce valuable information of how the gas-dynamics and chemistry are interrelated.

Chapter five derives the two-phase flow equations with gas-phase chemistry. The averaging process is applied in an identical manner as Gough to produce an internal ballistics model with chemical kinetics. Before proceeding, a discussion is included which outlines some of the difficulties encountered by the author, and previously by other researchers, during the solution procedure of the two-phase flow equations. A remedy to this is suggested and the motivation behind it revealed.

The numerical methods are extended to solve the system which now involves a solid-phase, in particular the Riemann-problem for the solid-phase equations will be discussed. Some of the empirical relations that are required to model two-phase flow are defined. Whilst the above work provides a mechanism for the gas-phase ignition process, in the first instant the solid must gasify to produce a source of reactant gas. As mentioned earlier there are two important contributions required to measure the rate of gasification of the solid propellant, the change in exposed surface area S_p and the gasification at the surface $\dot{r}$.

A description of how S_p is calculated in internal ballistic codes, based on the work by Corner [2], is outlined. Specifications required to model three different propellant geometries are included. The calculation of $\dot{r}$ is more complicated involving detailed modelling of the rate of processes at the propellant surface. In the past the rate has been assumed to be controlled by Piobert's law which

states that $\dot{r}$ is a function of gas-phase pressure and this will be assumed in this chapter. The model is now suitable to apply to a real internal ballistic scenario. Flow variable histories are produced for the problem and the results discussed.

In chapter six, a more detailed model will be outlined to describe the detailed interface heat-transfer processes. This is designed to describe the transition of the propellant from ambient temperature up-to the point at which gasification is assumed to be controlled by Piobert's law. The transition occurs at very early times prior to gas-phase ignition. The burn-rate model involves the solution of the heat-conduction equation at the surface of a typical propellant grain where the rate of regression of the solid interface changes. Expressions are defined for conduction and radiation heat-transfer at the surface.

Numerical methods are developed and validated by application to similar heat conduction problems that have analytical solutions. The model is then applied to a 'closed-bomb' ballistics problem. This involves burning propellant in a bomb which has no dominant spatial direction, again a sort of well-stirred reactor. These are often used to measure pressure history during propellant combustion so that propellant properties can be derived from these experiments. The model aims to predict the changing thermal profile at the solid surface subject to a rapidly varying external gas temperature. As the solid heats and gasifies this will produce higher gas temperatures which will in turn increase heat-transfer from the gas into the solid. The relationships between burn-rate, solid temperature and gas temperature will be explored.

A summary of the work described, conclusions and directions for further work are outlined in chapter seven.

Chapter 2

Gas-Phase Ignition

2.1 Chemical Processes

A general description of chemical reactions and their associated rate mechanism will be given. A more comprehensive description can be found in [51]. The chemical reactions that are considered in the following chapters are very simple idealised systems, however this chapter will outline the fundamentals required to extend the model to any real chain of chemical reactions.

2.1.1 Irreversible Chemical Reactions

An irreversible chemical reaction can be denoted as:

$$\sum_{\alpha=1}^{n} \nu'_\alpha A_\alpha \rightarrow \sum_{\alpha=1}^{n} \nu''_\alpha A_\alpha, \tag{2.1}$$

where A_α are the chemical symbols of the chemical present, ν'_α and ν''_α are the stoichiometric coefficients of the reactants and products respectively.

The rate of production of any species is given by:

$$\text{reaction rate} \left(\frac{moles}{m^3 sec}\right) = k' \prod_{\alpha=1}^{n} [A_\alpha]^{\nu'_\alpha}, \tag{2.2}$$

where $[A_\alpha]'$ denotes the concentration of species A_α in $moles/m^3$ and $k'(sec^{-1})$ is the rate constant of the reaction that is dependent on the gas temperature.

It is usually more convenient to express the reaction rate in terms of mass rather than a molar quantity. Also, rather than concentrating on the removal of species from either side of the chemical equation, the net rate of production of any species in a chemical reaction is a more useful quantity. The number of A_α moles created in reaction 2.1 is $(\nu''_\alpha - \nu'_\alpha)$. This gives the mass rate of production of species A_α, denoted K'_α as:

$$K'_\alpha = W_\alpha[\nu''_\alpha - \nu'_\alpha]k' \prod_{\alpha=1}^{n} [A_\alpha]^{\nu'_\alpha}, \tag{2.3}$$

where W is the molecular weight. Now introduce the mass-fraction c_α which is related to the concentration $[A_\alpha]$ by:

$$[A_\alpha] = \frac{\rho' c_\alpha}{W_\alpha} \tag{2.4}$$

where ρ' denotes the dimensional density. Then (2.3) is given as:

$$K'_\alpha = W_\alpha[\nu''_\alpha - \nu'_\alpha]k' \prod_{\alpha=1}^{n} \left(\frac{\rho' c_\alpha}{W_\alpha}\right)^{\nu'_\alpha}. \tag{2.5}$$

Introduce the *characteristic chemical time*:

$$\tau' = \frac{\rho'}{k \prod_{\alpha=1}^{n} \left(\frac{\rho'}{W_\alpha}\right)^{\nu'_\alpha}}. \tag{2.6}$$

Substitution into (2.5) gives

$$K'_\alpha = \frac{\rho' W_\alpha}{\tau'}[\nu''_\alpha - \nu'_\alpha] \prod_{\alpha=1}^{n} c_\alpha^{\nu'_\alpha}. \tag{2.7}$$

2.1.2 More General Reaction Processes

The above theory is simple to extend to reversible reactions and for a number of reactions occurring simultaneously:

$$\sum_{\alpha=1}^{n} \nu_\alpha^{(r)'} A_\alpha \rightarrow \sum_{\alpha=1}^{n} \nu_\alpha^{(r)''} A_\alpha. \tag{2.8}$$

where $r = 1, 2, ...m$ (the rth reaction).

The net rate of reaction r is the difference between the forward and backward rates.

$$k_f'^{r}[A_\alpha]^{\nu_\alpha^{(r)'}} - k_r'^{r}[A_\alpha]^{\nu_\alpha^{(r)''}}, \tag{2.9}$$

where k'_f is forward reaction rate constant and k'_r is the reverse direction reaction rate.

Similarly the mass-rate of production of species A_α in reaction r is:

$$K'^{(r)}_\alpha = \rho' W_\alpha [\nu^{(r)'}_\alpha - \nu^{(r)''}_\alpha] \left[\frac{1}{\tau'^{(r)}_f} \prod_{\alpha=1}^{n} \rho' c_\alpha^{\nu^{(r)'}_\alpha} - \frac{1}{\tau'^{(r)}_r} \prod_{\alpha=1}^{n} \rho' c_\alpha^{\nu^{(r)''}_\alpha} \right], \quad (2.10)$$

where:

$$\tau'^{(r)}_f = \frac{\rho'}{k'^{(r)}_f \prod_{\alpha=1}^{n} (\frac{\rho'}{W_\alpha})^{\nu^{(r)'}_\alpha}} \quad (2.11)$$

$$\tau'^{(r)}_r = \frac{\rho'}{k'^{(r)}_r \prod_{\alpha=1}^{n} (\frac{\rho'}{W_\alpha})^{\nu^{(r)''}_\alpha}} \quad (2.12)$$

2.1.3 Application to a Simple Chemical Model

The above theory will be used to construct chemical rate expressions for a very simple combustion reaction as described in [52] and [53]. This will be fundamental in the construction of a gas-phase ignition model with chemistry that appears in the following chapters.

Consider an irreversible reaction

$$X(g) + F(g) \longrightarrow 2P(g), \quad (2.13)$$

where $F(g)$ is a fuel, $X(g)$ is an oxidiser and $P(g)$ is an inert product gas.

Then the stoichiometric coefficients as defined in equation (2.1) are:

$$\nu'_X = 1 \quad ; \nu''_X = 0; \quad (2.14)$$

$$\nu'_F = 1 \quad ; \nu''_F = 0; \quad (2.15)$$

$$\nu'_P = 0 \quad ; \nu''_P = 2. \quad (2.16)$$

If the molecular weight of the three species are assumed to be the same and equal to W, then substitution into equation (2.7) gives the following rate equations:

$$K'_X = \frac{\rho' W[-1]}{\tau'} \rho' c_X c_F = -\rho' \Omega' c_X c_F; \quad (2.17)$$

$$K'_F = \frac{\rho' W[-1]}{\tau'} \rho' c_X c_F = -\rho' \Omega' c_X c_F; \quad (2.18)$$

$$K'_P = \frac{\rho W[2]}{\tau'} \rho' c_X c_F = 2\rho' \Omega' c_X c_F \quad (2.19)$$

where $\Omega'(sec^{-1})$ is the chemical frequency. This parameter is independent of mass-fraction and depends on thermodynamic properties of the mixture.

A simple model of gas-phase burning in the presence of solid propellant sources will be described as derived in [52]. The chemical scheme outlined here is adopted to describe the combustion of a gaseous fuel reactant.

2.2 A Gas-Phase Ignition Model

It will be assumed that a solid propellant decomposes into a reactant gas that subsequently burns in the gas-phase. The reactant is fed into the combustion chamber at a rate $\dot{m}'$ along with a hot inert igniter gas fed in at a rate $\dot{m}'_{ig}$.

The Euler equations for this physical scenario will now be developed. The combustion chamber is long and thin with adiabatic walls. All sources are assumed to be distributed uniformly across any cross-section and gravity is neglected. These assumptions are consistent with the idea that the propellant behavior can be modeled as a one dimensional unsteady process.

It is anticipated that discontinuities will occur in the resultant flow. So that these can be adequately simulated the integral form of the conservation equations will be considered.

2.2.1 Equation of State

At this stage, for simplicity, all gases present are considered to be ideal such that:

$$p'v' = \frac{\mathsf{R}'}{W}T' = \mathcal{R}T', \tag{2.20}$$

where p' is the pressure, ν' is the specific volume, W is the molecular weight, R' is the universal gas constant, $\frac{\mathsf{R}'}{W} = \mathcal{R}$ and T' is the temperature.

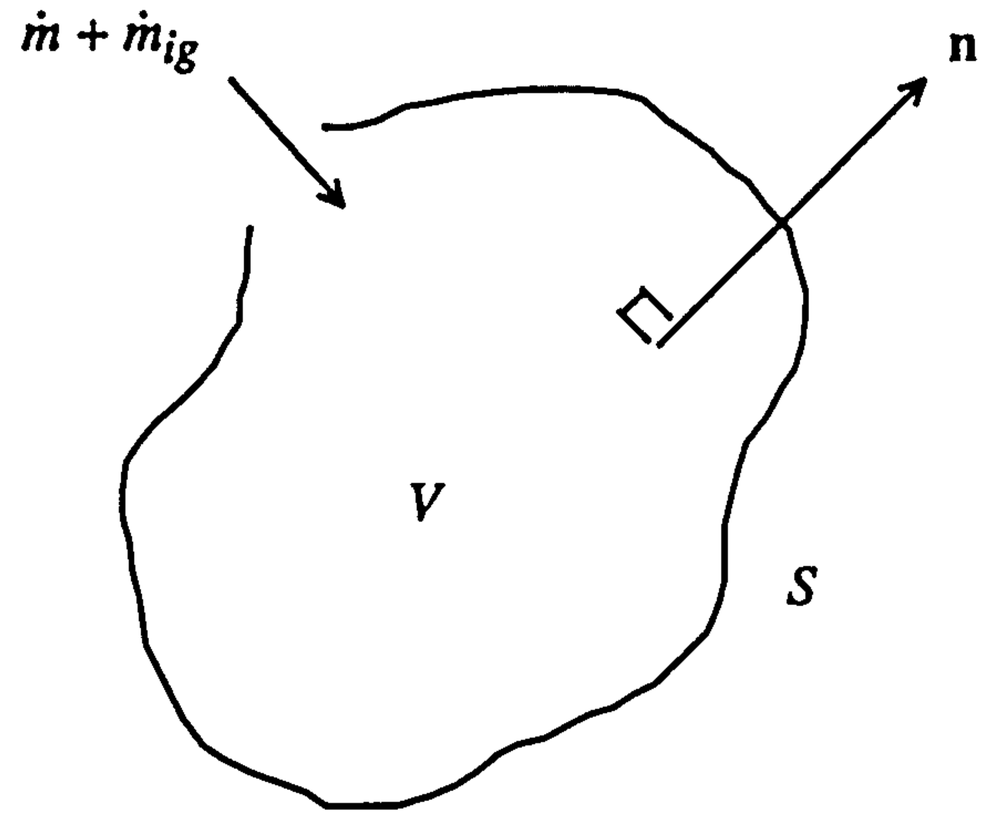

Figure 2.1: Domain of integration with sources.

2.2.2 Conservation of Mass

Mass conservation as applied to the domain in figure (2.1) can be given as:

$$\frac{d}{dt'}\int_{V'}\rho' dV' + \int_{S'}\rho' u'_j n_j dS' = \int_{V'}(\dot{m}' + \dot{m}'_{ig})dV', \tag{2.21}$$

where t' is the time, V' is the volume, S' is the surface area, n_j is the unit vector normal to S', ρ' is the gas density, u'_j is the gas velocity, $\dot{m}'$ is the rate of addition of gas due to propellant decomposition and $\dot{m}'_{ig}$ is the rate of addition of igniter gas. It is assumed for simplicity that the igniter gas is an inert ideal gas so that it is only a source of thermal energy not chemical energy.

The differential equation in conservation form, that is valid in smooth regions of flow, can be derived from equation (2.21) using Gauss's theorem:

$$\frac{\partial \rho'}{\partial t'} + \frac{\partial(\rho' u'_k)}{\partial x'_k} = \dot{m}' + \dot{m}'_{ig}. \tag{2.22}$$

2.2.3 Conservation of Reactant Species

The reactant gas generated by decomposition of the solid propellant is assumed to be composed of a fuel F and an oxidiser X. In general these will exist in concentrations c_F and c_X, respectively, where c_F is the fraction of any unit mass of the whole gas mixture that is fuel and c_X is the fraction of oxidiser.

The conservation of these two species can be given as:

$$\frac{d}{dt'}\int_{V'}\rho' c_\alpha dV' + \int_{S'}\rho' c_\alpha u'_j n_j dS' = \int_{V'}(\dot{m}'_\alpha + K'_\alpha)dV', \tag{2.23}$$

where α is F or X and K'_α is the rate of creation (depletion if negative) of the reactant species, in units of mass per unit volume per unit time.

The combustion process is assumed to be controlled by an irreversible chemical reaction:

$$F(g) + X(g) \longrightarrow 2P(g), \tag{2.24}$$

where $P(g)$ is an inert product gas as described previously in section (2.1.3).

If the molecular weights of X and F are the same, it follows that the molecular weight of P must also be the same. The reaction rate can then be written as:

$$K'_X = K'_F \equiv K' = -\rho'\Omega' c_X c_F. \tag{2.25}$$

$\Omega'(sec^{-1})$ is the chemical frequency which is strongly dependent on the gas temperature and weakly dependent on pressure and will be defined as:

$$\Omega' = A'_g p' \exp\left(-E'_A/\mathcal{R}'T'\right). \tag{2.26}$$

Here A'_g is the frequency of collision and E'_A is the activation energy. Furthermore, it is assumed that the mass that is introduced into the system is half composed of X and the other half is F, then $\dot{m}'_X = \dot{m}'_F = \dot{m}'/2$. Consider the differential form of the conservation equation (2.22), using the simplification described above, this gives:

$$\frac{\partial(\rho' c_\alpha)}{\partial t'} + \frac{\partial(\rho' c_\alpha u'_k)}{\partial x'_k} = K' + \dot{m}'/2. \tag{2.27}$$

These two relations for the species equations of the oxidant and fuel can be subtracted:

$$\frac{\partial(\rho'(c_F - c_X))}{\partial t'} + \frac{\partial(\rho'(c_F - c_X)u'_k)}{\partial x'_k} = 0. \tag{2.28}$$

By using the differential form of the mass equation (2.22) this can be written as:

$$(\dot{m}' + \dot{m}'_{ig})(c_F - c_X) + \rho' \frac{D(c_F - c_X)}{Dt'} = 0, \tag{2.29}$$

where

$$\frac{D}{Dt'}(c_F - c_X) \equiv \frac{\partial(c_F - c_X)}{\partial t'} + u'_k \frac{\partial(c_F - c_X)}{\partial x'_k}, \tag{2.30}$$

signifies the differentiation of $(c_F - c_X)$ following the motion of a fluid particle. Equation (2.29) can be integrated formally to give:

$$(c_F - c_X) = (c_F - c_X)_0 \exp\left(\int_0^{t'} \nu'(\dot{m}' + \dot{m}'_{ig})\partial t'\right), \tag{2.31}$$

where $\partial t'$ indicates integration with respect to t' along a particle path.

One possible solution of this is to make

$$c_X = c_F \equiv c, \tag{2.32}$$

which will be done here and the above equations for the species can be reduced to only one species equation that applies to both X and F

$$\frac{d}{dt'}\int_{V'} \rho' c dV' + \int_{S'} \rho' c u'_j n_j dS' = \int_V (\frac{\dot{m}'}{2} - \rho' \Omega' c^2) dV'. \tag{2.33}$$

2.2.4 Conservation of Momentum

The addition of mass into the closed system also introduces a momentum source term into the volume V'. If there are no other external forces acting on the gases and the reactant gas is assumed to enter the domain with local velocity u'_j, then the momentum equation is:

$$\frac{d}{dt'}\int_{V'} \rho' u'_j dV' + \int_{S'} (\rho u'_j u'_k + p'\delta_{jk}) n_j dS' = \int_{V'} u'_j (\dot{m}' + \dot{m}'_{ig}) dV'. \tag{2.34}$$

2.2.5 Conservation of Energy

Consider the energy in a unit mass of gas: The total energy is the sum of the intrinsic energy of the gas- which is a function of temperature and chemical

composition in the case of non-equilibrium chemistry- plus the kinetic energy. The intrinsic energy of each species is given as:

$$e'_{Ia} = e'_a + c_a Q'_a, \tag{2.35}$$

where e'_{Ia} is the intrinsic energy, e'_a is the specific thermal energy and Q'_a is a constant energy of formation per unit mass of the species. If the kinetic energy per unit mass of the mixture is given as:

$$\kappa' = \frac{1}{2} u'_k u'_k, \tag{2.36}$$

then the total energy per unit mass of the mixture is given as:

$$E' = \rho' \left(\sum (e'_a + c_a Q'_a) + \kappa' \right). \tag{2.37}$$

For simplicity, assume that the energy of formation of the fuel F and oxidant O are the same and that all three species X, F and P have the same specific thermal energy c. Adopting the assumption of equal mass fractions of reactant gases, given in equation (2.32), means the total energy in a unit volume of the mixture is given by

$$E' = \rho' \left(e' + 2cQ' + \kappa' \right). \tag{2.38}$$

Now consider the change in total energy in the system due to the gasification process. The total rate of mass addition of reactant gas $\dot{m}'$ is

$$\dot{m}' = \dot{m}'_X + \dot{m}'_F \tag{2.39}$$

and the rate of mass addition of igniter gas is $\dot{m}'_{ig}$. The reactant gases are assumed to enter the chamber at the local gas temperature and so introduce their own intrinsic energy, e' and Q', and kinetic energy per unit mass. In this simple thermodynamic model, the adiabatic addition of gas to the system from the sources does work on the gas within the system at a rate $\dot{m}'p'v'$ per unit volume. Thus energy is added to the system at a rate, per unit volume,

$$\dot{m}'(e' + \kappa' + p'v' + Q'). \tag{2.40}$$

The inert igniter gas only introduces thermal energy, kinetic energy and work; its contribution to the rate of energy addition per unit volume is therefore:

$$\dot{m}'_{ig}(e' + \kappa' + p'v'). \tag{2.41}$$

Finally the complete conservation law is given as:

$$\begin{aligned} \frac{d}{dt'} \int_{V'} E' dV' + \int_{S'} u'_j (E' + p') n_j dS' &= \int_{V'} (\dot{m}' + \dot{m}_{ig}')(e' + \kappa' + p'v') \\ &+ \dot{m}'(Q' - L') dV'. \end{aligned} \tag{2.42}$$

2.2.6 The Differential Conservative Form

From the above integral forms of the equations the differential form of the equations can be deduced. The conditions for which the differential form of the equations is valid is limited. Specifically, whilst the integral form is valid in regions of discontinuous flow the differential form only prevails in continuous flow. These relation can be derived using the integral equations (2.21), (2.33), (2.34) and (2.42) and Gauss' theorem:

$$\frac{\partial \rho'}{\partial t'} + \frac{\partial(\rho' u_k')}{\partial x_k'} = \dot{m}' + \dot{m}_{ig}'; \tag{2.43}$$

$$\frac{\partial(\rho' c)}{\partial t'} + \frac{\partial(\rho' c u_k)}{\partial x_k'} = K' + \frac{\dot{m}'}{2}; \tag{2.44}$$

$$\frac{\partial(\rho' u_j')}{\partial t'} + \frac{\partial(\rho' u_j' u_k')}{\partial x_k'} + \frac{\partial p'}{\partial x_j'} = u_j'(\dot{m}' + \dot{m}_{ig}'); \tag{2.45}$$

$$\frac{\partial(E')}{\partial t'} + \frac{\partial u_k'(E' + p')}{\partial x_k'} = (\dot{m}' + \dot{m}_{ig}')(e' + \kappa' + p'v') + \dot{m}'(Q' - L'). \tag{2.46}$$

2.3 The Spatially Uniform Problem

To develop an understanding of the consequences of including chemical kinetics and the effect on other flow variables, the spatially uniform problem will be considered as in [54]. This means that the time evolution of the gaseous mixture will be investigated by neglecting all space derivatives.

For further simplification let $\dot{m}_{ig}$ be zero - the propellant is already in gaseous form and so the system does not necessarily require the addition of igniter gas to initiate combustion- which reduces the system to:

$$\frac{d\rho'}{dt'} = \dot{m}'; \tag{2.47}$$

$$\frac{dc}{dt'} = \dot{m}'v'(1/2 - c) - \Omega' c^2; \tag{2.48}$$

$$\frac{dc'}{dt'} = 2Q'\Omega' c^2 - \dot{m}'v'(L' - p'v'). \tag{2.49}$$

Define the independent variable τ via the relation:

$$\frac{d\tau}{dt'} = v'\dot{m}', \tag{2.50}$$

and the following dimensionless variables $\rho = \rho'/\rho'_0$, $\mathcal{D} = \Omega'/v'\dot{m}'$, $e = e'/Q'$ and $L = L'/Q'$. Note that the variable $\mathcal{D} = \Omega'/v'\dot{m}'$, is a local Damköhler number as it is the ratio of the rate of chemical reaction of species to the rate of delivery of reactant species. The reaction rate factor Ω' is a quantity that depends on thermodynamic variables and if the rate of delivery of reactant species is also considered in this way (e.g. internal ballistics theories usually make use of a pressure dependent rate of delivery) then the Damköhler number is a function of thermodynamic variables; assume that $\mathcal{D} = \mathcal{D}(e)$.

Using these relations, the equations for c and e in time can be transformed to equations in the new variable τ:

$$\frac{dc}{d\tau} = \frac{1}{2} - c - \mathcal{D}c^2 \equiv D(e,c); \tag{2.51}$$

$$\frac{de}{d\tau} = 2\mathcal{D}c^2 - L + pv \equiv N(e,c). \tag{2.52}$$

Recall that the gas is assumed to be ideal so that:

$$p'v' = (\gamma - 1)e'. \tag{2.53}$$

Using the above, equations (2.51) and (2.52) can be transformed to the following single autonomous equation:

$$\frac{de}{dc} = \frac{2\mathcal{D}c^2 - (L - (\gamma-1)e)}{\frac{1}{2} - c - \mathcal{D}c^2} \equiv \frac{N(e,c)}{D(e,c)}. \tag{2.54}$$

2.3.1 Analysis in the (e,c)-Phase-Plane

First consider the values of c and c at which the numerator and denominator are equal to zero.

$$N(e,c) = 2\mathcal{D}c^2 - (L - (\gamma-1)e) = 0, \tag{2.55}$$

then:

$$c = c_n = \sqrt{\frac{L - (\gamma-1)e}{2\mathcal{D}}} = \sqrt{\frac{\bar{L}}{2\mathcal{D}}}, \tag{2.56}$$

where

$$\bar{L} = L - (\gamma - 1)e. \tag{2.57}$$

This means that in the (e,c)-plane, an integral curve must have a horizontal tangent if it crosses the locus of c_n. For the denominator:

$$D(e,c) = \frac{1}{2} - c - \mathcal{D}c^2 = 0, \tag{2.58}$$

then:

$$c = c_d = \frac{-1 + \sqrt{1 + 2\mathcal{D}}}{2\mathcal{D}}. \tag{2.59}$$

Similarly, the integral curves will have a vertical tangent at intersection points with the locus of c_d.

These two-locii intersect at a singular point where the values of c and e define conditions at a 'stationary state' as described in [55].

$$c_n = c_d = c_{ss}. \tag{2.60}$$

After some algebra, equating equations (2.56) and (2.59) produces explicit expressions for the value of $\mathcal{D}$ and c at the stationary state:

$$\mathcal{D} = \mathcal{D}_{ss} = \frac{2\bar{L}_{ss}}{(1 - \bar{L}_{ss})^2}; \tag{2.61}$$

$$c = c_{ss} = \frac{1}{2}(1 - \bar{L}_{ss}). \tag{2.62}$$

To investigate the nature of this stationary state, it is necessary to perform a local stability analysis. The idea of such an analysis is to determine how small perturbations around the point behave. For example, if the small perturbations grow the state is unstable, conversely if the perturbations diminish the stationary state is stable. Define such a perturbation via:

$$e = e_{ss} + \Delta e, \qquad \Delta e << e_{ss}; \tag{2.63}$$

$$c = c_{ss} + \Delta c, \qquad \Delta c << c_{ss}. \tag{2.64}$$

Substituting (2.63) and (2.64) into equations (2.52) and(2.51) and expanding the right hand-sides of D and N in the form of a Taylor series gives the result:

$$\begin{aligned} \frac{de}{d\tau} = \frac{d\Delta e}{d\tau} &= N(e_{ss}, c_{ss}) + \left(\frac{\partial N}{\partial e}\right)_{ss} \Delta e + \left(\frac{\partial N}{\partial c}\right)_{ss} \Delta c \\ &+ O(\Delta^2 e, \Delta^2 c); \end{aligned} \tag{2.65}$$

$$\begin{aligned} \frac{dc}{d\tau} = \frac{d\Delta c}{d\tau} &= D(e_{ss}, c_{ss}) + \left(\frac{\partial D}{\partial e}\right)_{ss} \Delta e + \left(\frac{\partial D}{\partial c}\right)_{ss} \Delta c \\ &+ O(\Delta^2 e, \Delta^2 c). \end{aligned} \tag{2.66}$$

Remember that $N(e_{ss}, c_{ss})$ and $D(e_{ss}, c_{ss})$ are by definition identically zero. It is easy to see that:

$$\frac{\partial N}{\partial c} = 4\mathcal{D}_{ss} c_{ss} > 0; \tag{2.67}$$

$$\frac{\partial N}{\partial e} = 2c_{ss}^2\dot{\mathcal{D}}_{ss} + (\gamma - 1) > 0; \tag{2.68}$$

$$\frac{\partial D}{\partial c} = -2\mathcal{D}_{ss}c_{ss} - 1 < 0; \tag{2.69}$$

$$\frac{\partial D}{\partial e} = -c_{ss}^2\dot{\mathcal{D}}_{ss} < 0; \tag{2.70}$$

where the signs are deduced since $\mathcal{D}$, c are by definition always positive and

$$\dot{\mathcal{D}} \equiv \frac{d\mathcal{D}}{de} > 0 \tag{2.71}$$

implying that the rate of chemical reaction increases with increases in thermal energy as would be expected. Using the values of c_{ss}, $\mathcal{D}_{ss}$ given above define the constants:

$$\alpha_{ss} = \frac{4\bar{L}_{ss}}{1 - \bar{L}_{ss}} > 0; \tag{2.72}$$

$$\beta_{ss} = \frac{1}{2}(1 - \bar{L}_{ss})^2\dot{\mathcal{D}}_{ss} + (\gamma - 1) > 0; \tag{2.73}$$

$$\gamma_{ss} = -\frac{1 + \bar{L}_{ss}}{1 - \bar{L}_{ss}} < 0; \tag{2.74}$$

$$\delta_{ss} = -\frac{1}{4}(1 - \bar{L}_{ss})^2\dot{\mathcal{D}}_{ss} < 0. \tag{2.75}$$

It follows from (2.65) and (2.66) that perturbations Δe and Δc satisfy the pair of linear ordinary-differential-equations

$$\frac{d\Delta e}{d\tau} = \alpha_{ss}\Delta e + \beta_{ss}\Delta c; \tag{2.76}$$

$$\frac{d\Delta c}{d\tau} = \gamma_{ss}\Delta e + \delta_{ss}\Delta c. \tag{2.77}$$

The above two equations are simple linear equations. If solutions of the form

$$e = r_n e^{\zeta_n \tau} \quad c = s_n e^{\zeta_n \tau}, \tag{2.78}$$

are tried for arbitrary ζ_n, then (2.76) and (2.77) makes:

$$r_n\zeta_n = \alpha_{ss}r_n + \beta_{ss}s_n; \tag{2.79}$$

$$s_n\zeta_n = \gamma_{ss}r_n + \delta_{ss}s_n; \tag{2.80}$$

or:

$$(\alpha_{ss} - \zeta_n)r_n + \beta_{ss}s_n = 0; \tag{2.81}$$

$$\gamma_{ss}r_n + (\delta_{ss} - \zeta_n)s_n = 0. \tag{2.82}$$

There is a solution for r_n, s_n only if ζ_n satisfies:

$$\det \begin{vmatrix} \alpha_{ss} - \zeta_n & \beta_{ss} \\ \gamma_{ss} & \delta_{ss} - \zeta_n \end{vmatrix} = 0, \tag{2.83}$$

or:

$$(\alpha_{ss} - \zeta_n)(\delta_{ss} - \zeta_n) - \gamma_{ss}\beta_{ss} = \zeta_n^2 - (\gamma_{ss} + \delta_{ss})\zeta_n + \alpha_{ss}\delta_{ss} - \gamma - ss\beta_{ss}. \tag{2.84}$$

Hence two values of ζ_n can be found, namely:

$$2\zeta_1 = (\alpha_{ss} + \delta_{ss}) + \sqrt{(\alpha_{ss} + \delta_{ss})^2 - 4(\alpha_{ss}\delta_{ss} - \gamma_{ss}\beta_{ss})}; \tag{2.85}$$

$$2\zeta_2 = (\alpha_{ss} + \delta_{ss}) - \sqrt{(\alpha_{ss} + \delta_{ss})^2 - 4(\alpha_{ss}\delta_{ss} - \gamma_{ss}\beta_{ss})}. \tag{2.86}$$

A more general solution of the linear equations can be found by multiplying $e = r_1 e^{\zeta_1 \tau}$, $c = s_1 e^{\zeta_1 \tau}$ by a constant C_1 since the result will still satisfy (2.76) and (2.77). Similarly, $e = r_2 e^{\zeta_2 \tau}$, $c = s_2 e^{\zeta_2 \tau}$ can be multiplied by a constant C_2. If these two solutions are added a general solution is given as:

$$\Delta e = C_1 r_1 \exp(\zeta_1 \tau) + C_2 r_2 \exp(\zeta_2 \tau); \tag{2.87}$$

$$\Delta c = C_1 s_1 \exp(\zeta_1 \tau) + C_2 s_2 \exp(\zeta_2 \tau). \tag{2.88}$$

By using the relations given in (2.72), (2.73), (2.74) and (2.75) it can be seen that the signs of ζ_1 and ζ_2 are real and opposite. It can be shown that in the expressions for Δe, equation (2.87), and Δc, equation (2.88), that it is the positive exponential that eventually dominates the expressions indicating an unstable stationary state; this particular type is called a saddle point [55].

Since Δe and Δc are vanishingly small (differential) increments, one can write:

$$\left.\frac{de}{dc}\right|_{ss} = \frac{r_1 + (C_2/C_1) r_2 \exp[(\zeta_2 - \zeta_1)\tau]}{s_1 + (c_2/c_1) s_2 \exp[(\zeta_2 - \zeta_1)\tau]}, \tag{2.89}$$

which, for $C_1 \neq 0$, will give the tangents to integral paths that pass through (c_{ss}, e_{ss}) which can be used to sketch the 'separatrices' of the saddle point. These are integral curves that pass through the stationary state separating regions of different solution behavior.

A sketch, taken from [53], of the integral curves in the phase plane (e, c) can be seen in figure (2.2) which clearly indicates the features described. Only

the segment $0 < c < \frac{1}{2}$, $e > 0$ is of physical interest. For exothermic combustion to occur it is clear from the figure that $\dot{m}'$ must be positive and the ambient conditions must be such that $e > e_1$ where e_1 is defined as the point of intersection of the lower separatrix from (c_{ss}, e_{ss}) with the ordinate axis.

It can easily be seen from equation (2.54) that

$$\left.\frac{de}{dc}\right|_{c=0} = -2\bar{L}, \tag{2.90}$$

which implies that for positive $\bar{L}$, internal energy e decreases with increasing c initially. However, the point of zero gradient is when:

$$\bar{L} = L - (\gamma - 1)e = 0. \tag{2.91}$$

Define this value of internal energy as $e_{11} = L/\gamma - 1$. The physical significance of this point is that if the initial energy is such that $e \geq e_{11}$, then the energy will immediately start to increase with increasing c. For $e_1 < e < e_{11}$ the internal energy will initially decrease to a minimum ($N = 0$) and then start to increase. This implies that providing sufficient propellant is supplied then for $e > e_1$ combustion will be self-sustaining.

These and further physical features will be described in the next section where the numerical solution is investigated. The numerical solution will be validated using the algebra derived above. After this a slightly more general and realistic form of the equations are solved. The influence of chemical parameters in the system will be investigated and the theory compared with more traditional ideas in internal ballistics.

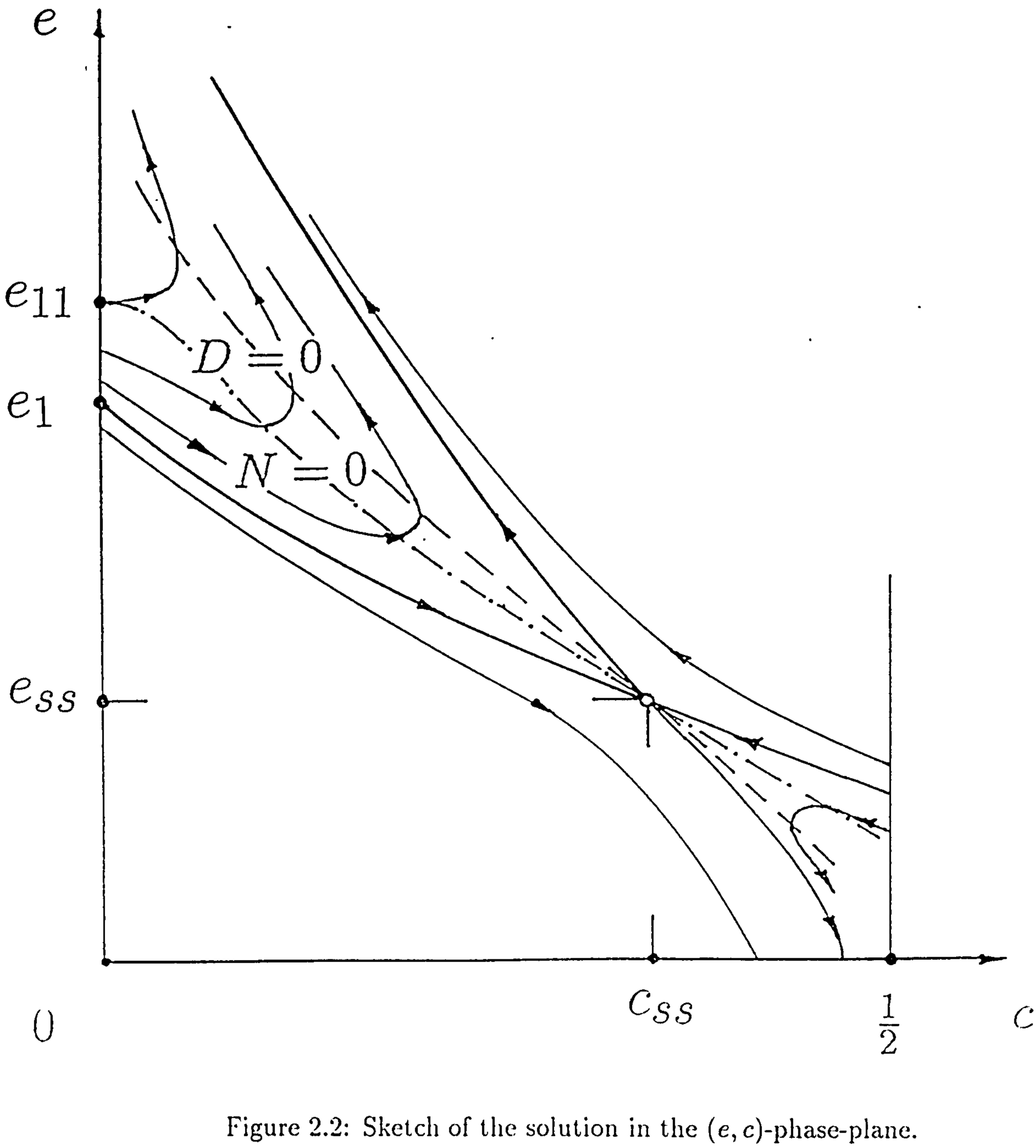

Figure 2.2: Sketch of the solution in the (e, c)-phase-plane.

Chapter 3

Numerical Investigation

The preceding chapter described how an analytical solution for the spatially independent equations could be produced. However, the assumptions for this simple system will not necessarily be valid when applied to internal ballistics problems which will require numerical methods to produce a solution. In this chapter, numerical solutions will be used to compare with the previous analysis for validation purposes. A parametric analysis will then be performed, with ease, using this numerical scheme.

3.1 The Numerical Solution

The system of ordinary-differential-equations derived in the previous section can be summarized as:

$$\frac{d\rho'}{dt'} = \dot{m}'; \tag{3.1}$$

$$\frac{dc}{dt'} = -\Omega' c^2 + (\frac{1}{2} - c)v'\dot{m}'; \tag{3.2}$$

$$\frac{de'}{dt'} = 2Q'\Omega' c^2 - v'\dot{m}'(L' - p'v'). \tag{3.3}$$

The system may be transformed using:

$$\frac{d\tau}{dt'} = v'\dot{m}', \tag{3.4}$$

to give:

$$\frac{d\rho}{d\tau} = \rho; \tag{3.5}$$

$$\frac{dc}{d\tau} = \frac{1}{2} - c - \mathcal{D}c^2; \tag{3.6}$$

$$\frac{de}{d\tau} = 2\mathcal{D}c^2 - L + (\gamma - 1)e, \tag{3.7}$$

where $\rho = \rho'/\rho'_0, \mathcal{D} = \Omega'/v'\dot{m}', e = e'/Q', L = L'/Q'$ and $\dot{m} = \dot{m}'/Q'$ with initial conditions $\tau = 0, t = 0, \rho = 1, c = 0, e = e_0$.

The systems of ordinary-differential-equations are difficult to solve numerically. Standard explicit methods used to solve ordinary-differential-equations, such as Runge-Kutta methods, cannot resolve the radically different timescales of chemical kinetics - compared with other flow variables - without the use of cripplingly small timesteps. Systems that exhibit these characteristics are described as stiff. In a precise mathematical context, if the system is written as $\mathbf{U}_t = \mathbf{f}(\mathbf{U}, t)$, then stiffness can be recognised if the Jacobian of $\mathbf{f}$ possesses a relatively large negative eigenvalue ([50]). Fortunately, the problem of stiffness is not a new one and today numerical methods are well established that deal with these difficulties reliably and accurately.

In particular, Gear [50] developed backward-differentiation-formulae that successfully reduce the system to a set of implicit linear equations that can easily be solved to produce a solution. The timestep is varied depending on the rate of change of flow variables so that accuracy and stability are preserved which explains why the formulae fall into the general class of linear multistep methods. Gear produced a code based on his work which has been developed and improved along with co-worker Hindmarsh [56]. The most recent version LSODE will be used to solve the system of equations described above. Recall, from the previous chapter, if the Damköhler number is defined as a function of internal energy $\mathcal{D}(e)$, then the equations for mass-fraction and energy can be decoupled from the other governing equations. This results in one autonomous equation:

$$\frac{de}{dc} = \frac{2\mathcal{D}c^2 - (L - (\gamma - 1)e)}{\frac{1}{2} - c - \mathcal{D}c^2}. \tag{3.8}$$

The analytical solution of this problem was investigated and pursued in the previous section.

An explicit function will now be given for the Damköhler number using the

chemical rate expressions derived in section 2.1.3:

$$\mathcal{D}(\rho, e) = \frac{\Omega'}{v'\dot{m}'} \equiv \frac{A'_g p' \exp\left(-E'_A/\mathcal{R}'T'\right)}{v'\dot{m}'}. \tag{3.9}$$

The ideal equation of state can then be used to give:

$$\mathcal{D}(\rho, e) = \frac{A'_g \rho'(\gamma-1)e' \exp\left(-E'_A/(\gamma-1)e'\right)}{v'\dot{m}'}. \tag{3.10}$$

If the rate of mass addition $\dot{m}$ is defined as a function of pressure (in combustion this is known as Piobert's law of burning) then again using the ideal equation of state:

$$\dot{m} = \rho'^p S'_p \dot{r}' = \rho'^p S'_p B'_{cf} p' = A'_s \rho'(\gamma-1)e'. \tag{3.11}$$

where ρ'^p is the density of the solid propellant, S'_p is the surface area of the propellant which, will be assumed to be constant in this section, $\dot{r}'(m/sec)$ is the rate of surface regression of the solid and $A'_s = \rho'^p S'_p B'_{cf}$. Finally, the Damköhler number can be given as:

$$\mathcal{D}(\rho, e) = \frac{A'_g}{A'_s}\rho' \exp\left(-E'_A/(\gamma-1)e'\right). \tag{3.12}$$

For simplicity assume that the gas density is constant so that the Damköhler number is a function of internal energy only $\mathcal{D}(e)$, then an analytical solution can be found with all the attributes as described in the previous chapter and in [53].

Figure (3.1) is a numerical solution in the $T'-c$ plane which corresponds to the reduced autonomous equation (3.8) where the ideal equation of state is used to replace the internal energy with perhaps a more physically understandable temperature distribution (since T' is directly proportional to e). The values of the parameters used to produce this solution are given in table 3.1:

The initial value of temperature T'_0 has been varied like a parameter to give a full phase-plane solution. The null-clines

$$N(e, c) = 0; \quad D(e, c) = 0 \tag{3.13}$$

give the loci of minimum internal energy e_{min} and maximum mass-fraction c_{max} corresponding to the formulae (2.56) and (2.59). Clearly the loci correspond to

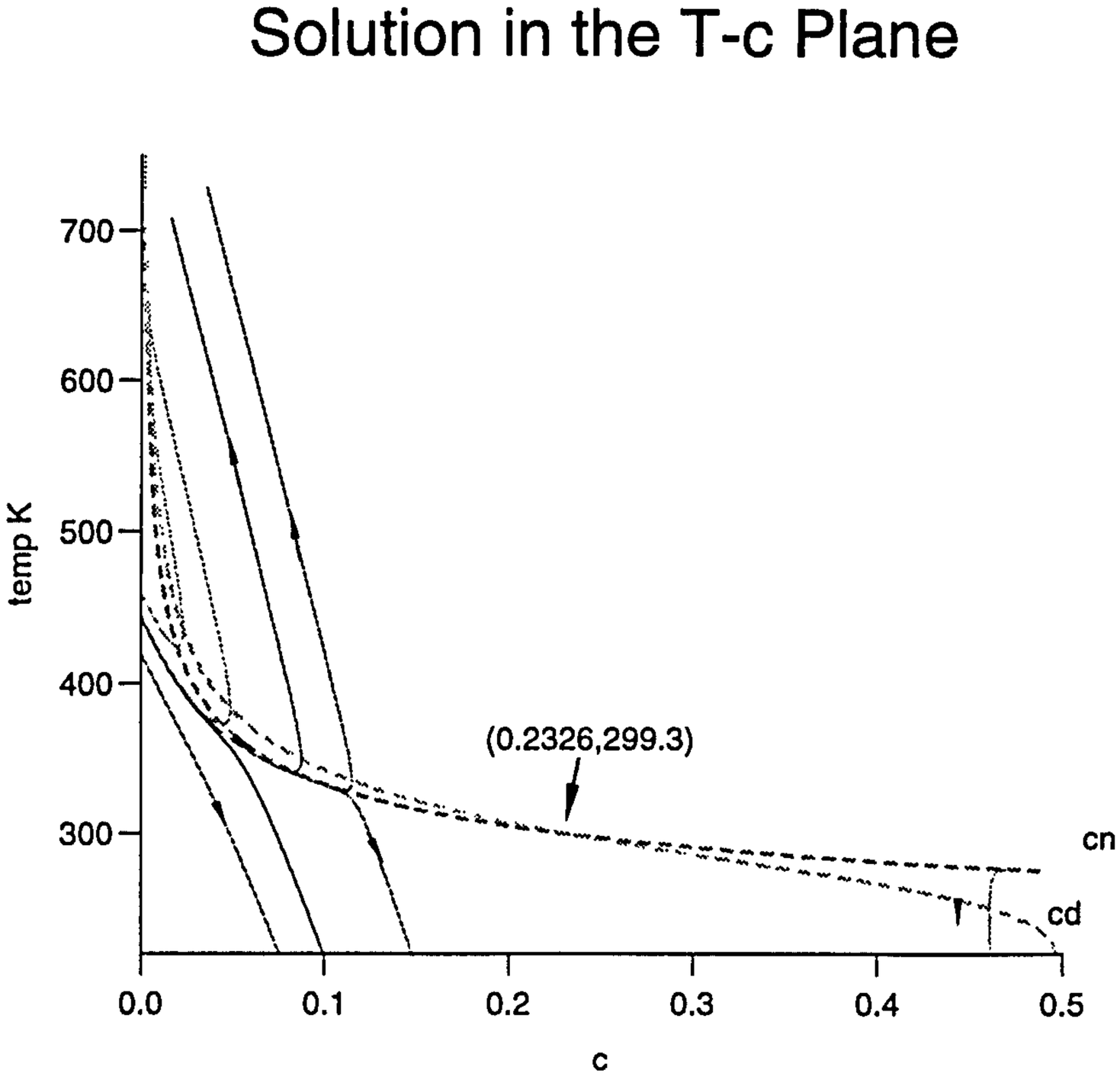

Figure 3.1: Solution in the $T' - c$ plane for different initial temperatures T'_0 and mass fraction c_0.

γ	1.2627	L'	1996100 J/kg
Q'	3512700 J/kg	A'_g	$10^4 1/secPa$
A'_s	$10^{-4} kg/secPa$	ρ'_0	0.88983 kg/m^3
$E'_A/\mathcal{R}'$	$5000K$	W	21.535
R'	$8313.3 J/K kgmole$		

Table 3.1: Parameters for numerical solution of spatially uniform case.

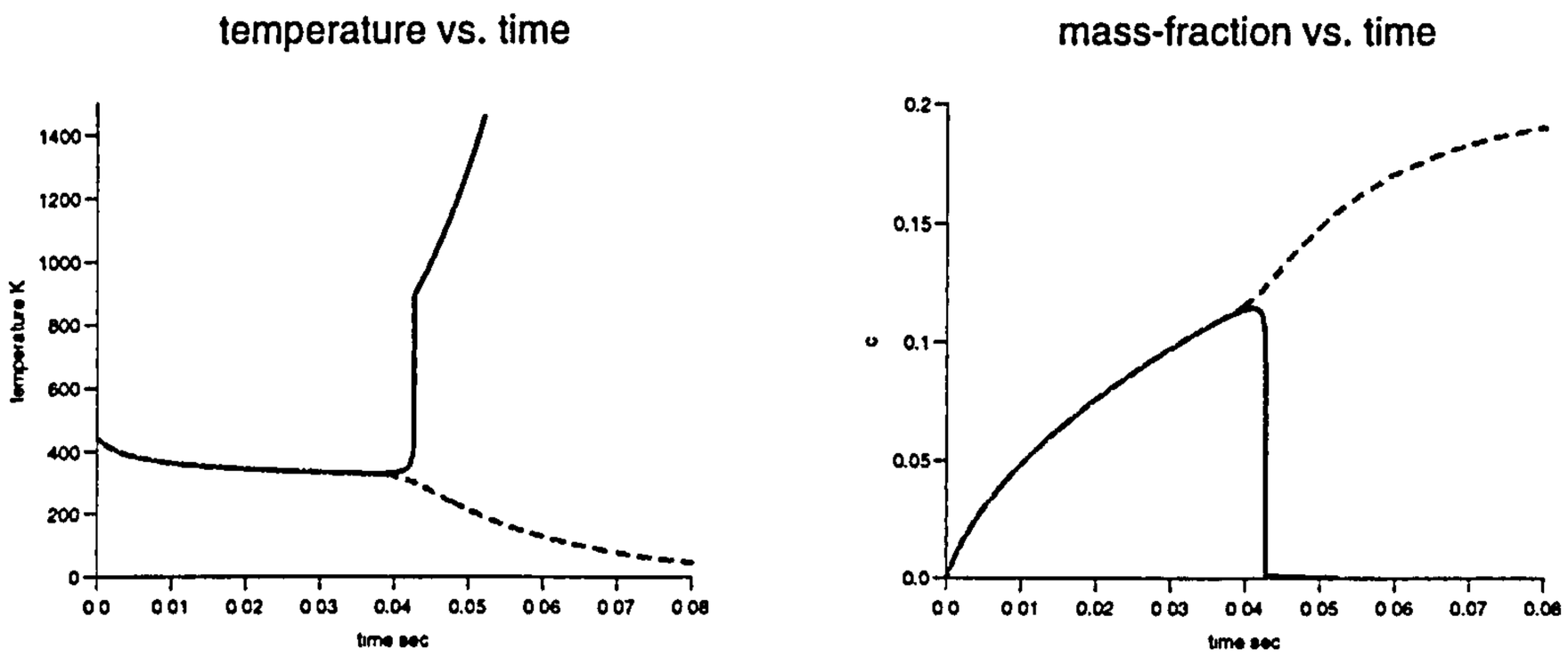

Figure 3.2: Temperature and mass-fraction histories for different $T_0' = 443.5K$ (- - -) and $T_0' = 444K$ (full line).

zero and infinite tangents of the integral curves. These intersect at the saddle point singularity and if the numerical solution passes close to the saddle point the code runs into difficulties. This illustrates how the mathematical analysis can play an important role by identifying conditions that may cause difficulties in the numerics. It is reassuring to see validation of the numerical solution achieved by exploiting the analytical methods.

Now consider some of the features shown in figure (3.1) and the physical interpretation: For values of T_0' below $\approx 444K$, the mass-fraction increases as the internal energy falls and continues to decline. Physically this corresponds to the system that has insufficient energy at the early stages to overcome the energy losses due to latent heat. Reactive species are produced by gasification and, despite the fact that gaseous mass-addition is a source of chemical energy, there is never sufficient thermal energy to trigger an exothermic reaction. The reactive species remains a potential source of energy which cannot be released. In combustion terms ignition cannot occur. This can be seen more clearly in figure (3.2) which gives the temperature T' and mass-fraction c histories independently. The dashed curve represents the situation in which ignition does not occur and where the initial temperature is $443.5K$.

The situation is totally different when T_0' is above this critical level. The

solution starts in the same way, that is the mass-fraction increases, but the temperature now falls to a minimum temperature T'_{min} (again due to latent heat losses). However, the system is now able to sustain this loss and the thermal energy starts to rise. The mass-fraction soon reaches a maximum and then decreases as the temperature rapidly increases. The point at which ignition is attained is somewhat ambiguous: For instance, ignition might be said to occur when the temperature first recovers and starts to increase, that is, when $N(e,c) = 0$ and the temperature is minimum T'_{min}. Alternatively, ignition could be when $D(e,c) = 0$ and $c = c_{max}$, for once the energy of the system rises above this critical level there is an almost discontinuous jump in thermal energy accompanied by a similarly violent consumption of reactant gas. Frequently ignition is described as *thermal runaway* and clearly the second definition might be regarded as such a physical process. The time interval before the mass-fraction attains c_{max} will be described as the ignition delay.

After this, the mass-fraction tends to very small values as the temperature increases dramatically. In these circumstances the solution describes how reactant gas enters the system and is consumed instantaneously releasing all available chemical energy. At these times the combustion cycle is well underway. Again, the full lines in figure (3.2) represent this possible outcome. The solution tends to equilibrium chemistry after the ignition delay as will be seen later in this chapter. The initial conditions mean that the only solutions in the phase-plane that are physically relevant, in this context, are those in which $t' = 0, c = 0$.

Obviously, the above solution is rather non-physical due to the way in which it has been constructed. However, for validation purposes, it is enlightening just how the numerically generated solution fits in with the analytical solution.

Now, consider the full set of equations where for simplicity the rate of addition of gaseous mass $\dot{m}'$ is constant at $60\frac{kg}{m^3}$. The rate of change of density is no longer assumed to be zero so the Damköhler number is now also a function of changing density $\mathcal{D}(\rho, e)$. This means that the equation given in (3.8) will no longer be autonomous so cannot be solved independently from the density variation. However, note that the analysis in the preceding chapter does not insist that the density is constant, only that the Damköhler number is a function of internal energy alone. The density was assumed to be constant only so that typical expressions used in internal ballistics, Piobert's burning law,

could be used to measure the rate of gasification.

The $T' - c$ plane is given in figure (3.3). This picture does not greatly differ from figure (3.1) and the physical interpretation is identical. However, the solution seems to have been displaced vertically so that the critical initial value of T_0' that determines whether exothermic reaction occurs or not is now approximately $486K$.

Figure 3.4 illustrates the flow-variable histories for two different initial values of T_0' where the density is now allowed to vary at a constant rate.

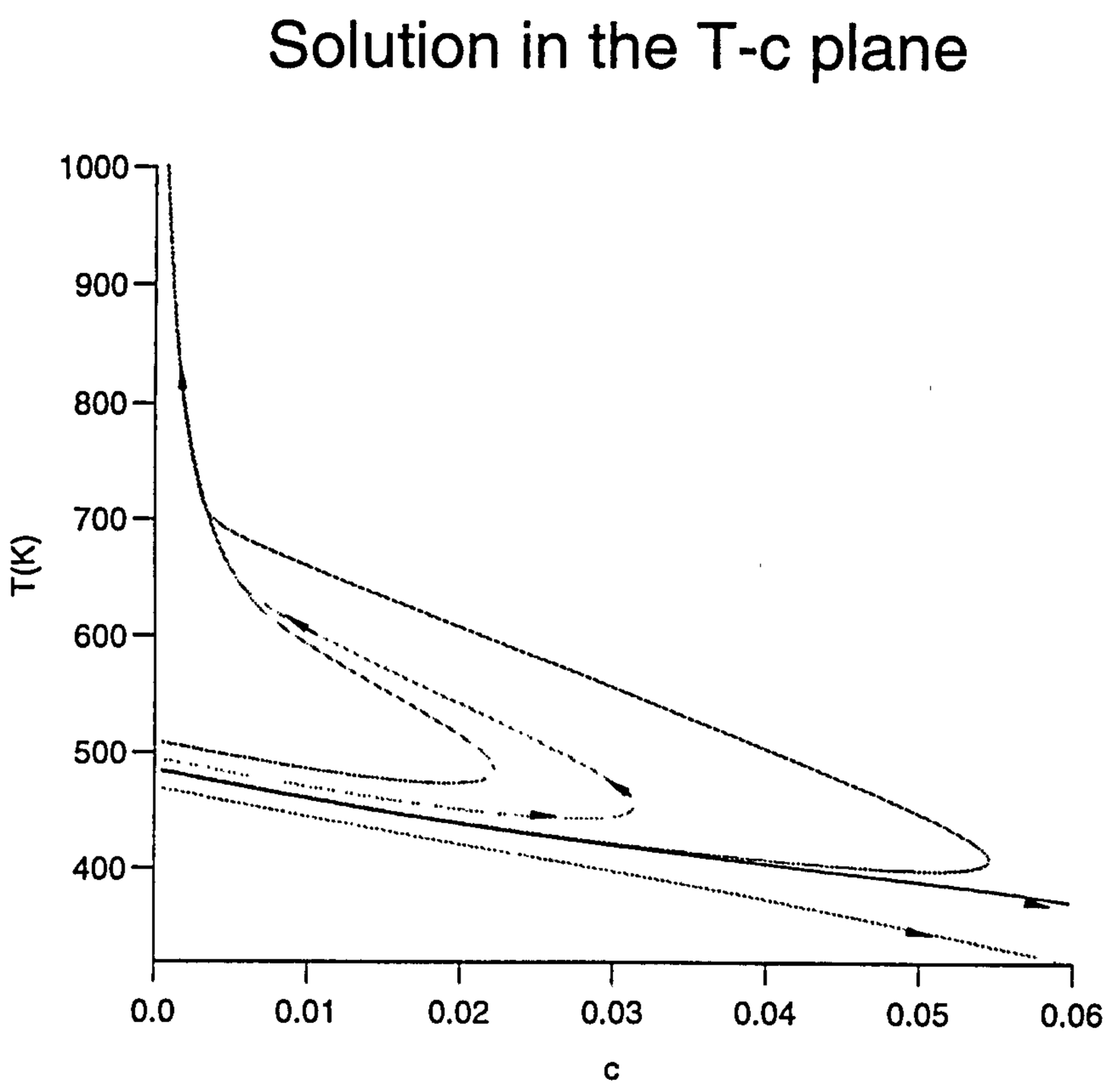

Figure 3.3: $T' - c$ plane with density variation for different values of T'_0.

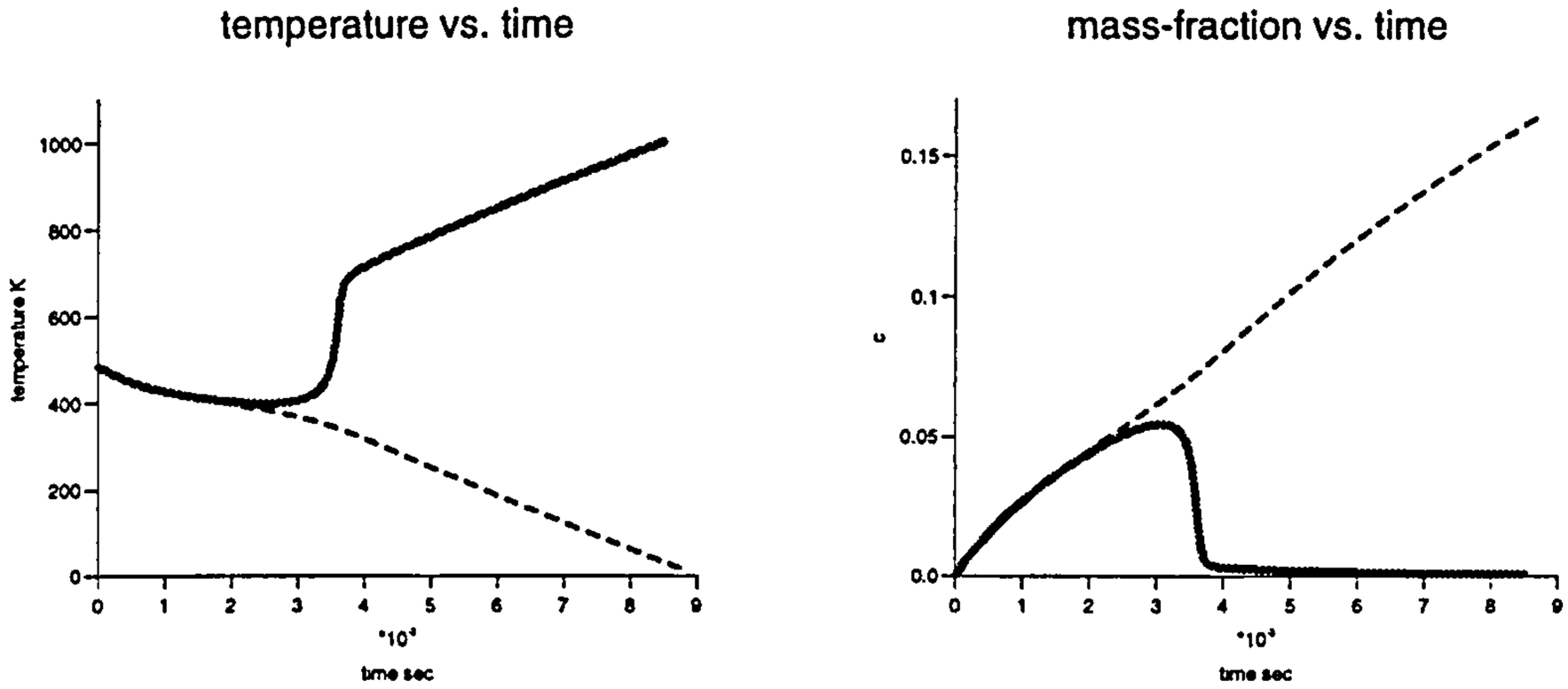

Figure 3.4: Temperature and mass-fraction histories for different $T_0' = 486K$ (full line) and $T_0' = 485K$ (- - -).

3.2 Internal Ballistics with Chemistry

It is informative to see how the inclusion of chemical kinetics effects the solution of the Euler equations with source terms. More conventional flow equations in internal ballistics and this model will be compared.

3.2.1 Equilibrium & Non-Equilibrium Equations

The inclusion of chemical reactions means that it is necessary to consider a species conservation equation as in equation (2.48).

$$\frac{d}{dt'}(\rho' c) = \dot{m}'/2 + K'. \tag{3.14}$$

The equations of mass and energy are formally unchanged by the presence of chemical species, observed from the absence of c in equations (2.47) and (2.49).

However, the definition of total energy in the energy equation has a different form when chemical kinetics are being modeled.

The energy conservation equation is defined as:

$$\frac{d}{dt'}E' = \left(\dot{m}' + \dot{m}'_{ig}\right)(e' + p'v' + \kappa') + \dot{m}'(Q' - L'), \tag{3.15}$$

where e' is the thermal energy and κ' is the kinetic energy per unit mass.

Equilibrium chemistry is established in a a system once the chemical times involved are negligible, as in many standard applications of the inviscid flow equations. In this case, the total energy is defined as:

$$E' = \rho'(e' + \kappa'), \tag{3.16}$$

However, for the non-equilibrium chemistry, defined in the previous chapter, total energy is defined as:

$$E' = \rho'(e' + \kappa' + 2cQ'). \tag{3.17}$$

When these two energy definitions and the transformation

$$\frac{d\tau}{dt'} = v'\dot{m}' \tag{3.18}$$

are substituted into the energy conservation equation (3.15), along with the dimensionless variables, two different equations for the rate of change in pressure appear:

$$\frac{dp}{d\tau} = \gamma p + \rho(\gamma - 1)(Q - L) \quad \text{equilibrium;} \tag{3.19}$$

$$\frac{dp}{d\tau} = \gamma p + \rho(\gamma - 1)(2DQc^2 - L) \quad \text{nonequilibrium.} \tag{3.20}$$

Since chemical equilibrium implies that chemical characteristic times are negligibly small, an alternative definition could be that the chemical frequency is infinitely fast, $\Omega \to \infty$. For physical reasons the chemical rate K' must be bounded so that since $K' = -\rho'\Omega'c^2$ this implies that as chemical equilibrium is approached c must tend to zero. If these ideas are used in the species equation (3.14), one finds that limitingly fast reaction implies the equilibrium conditions:

$$\begin{aligned} K &\to \frac{m}{2}; \\ \Rightarrow 2\mathcal{D}c^2 &\to 1. \end{aligned} \tag{3.21}$$

Figure (3.5) shows plots of temperature, for equilibrium and non-equilibrium chemistry, and $2\mathcal{D}c^2$ vs. t' for the non-equilibrium case only. The dataset

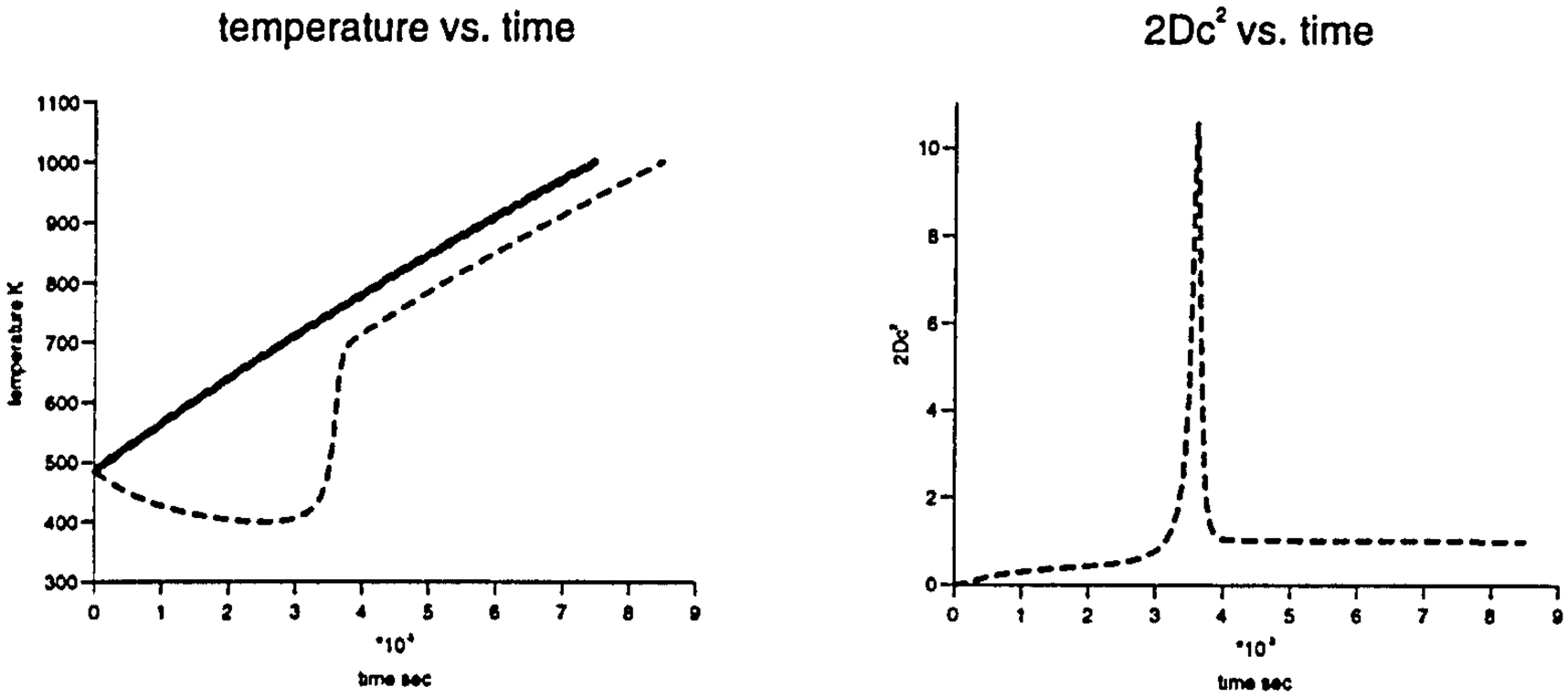

Figure 3.5: Comparison of non-equilibrium (- -) and equilibrium (full line) chemistry.

that was used to produce the earlier plot in figure (3.4) was adopted where the initial gas temperature is $486K$. This clearly displays how the new model with non-equilibrium chemistry approaches the equilibrium model as time progresses as condition (3.21) is satisfied. Similarly, the temperature distribution described by equation (3.19) approaches the temperature distribution for equation (3.20). When equilibrium chemistry is attained the change of temperature will be governed by the rate of gasification of propellant species $\dot{m}$ and the effect of chemical kinetics in the gas-phase are negligible.

This is a clear illustration of how chemical kinetics affect the solution. Now compare the energy equation in equilibrium form given above, and described here as model A, and the conventional form of the gas-phase energy equation, model B, that has been adopted in the old single phase internal ballistic models [2] as originally compared in [57].

The equilibrium form of the energy equation as described above in equation (3.20) is stated in dimensional form:

$$\frac{dp'}{dt'} = v\dot{m}'\gamma p' + \dot{m}'(\gamma - 1)(Q' - L') \quad \text{model A} \tag{3.22}$$

The pressure distribution given in conventional lumped parameter ballistic

models is of the form [2]:

$$\frac{dp'}{dt'} = \dot{m}'(\gamma - 1)(Q' - L') \quad \text{model B} \tag{3.23}$$

Comparison of the new and old expressions clearly indicates the appearance of an extra term; to try and recognise the meaning of this extra term consider a purely investigative limiting case. Gas is fed into the chamber in a chemically neutral manner so there are no latent heat requirements, so L' is zero, nor is the process exothermic, Q' is zero also. It is supposed that no igniter gas is required to initiate such a process, $m'_{ig} = 0$. Obviously the existence of such a volatile solid material that spontaneously gasifies is highly unlikely without the need for some sort of stimulus.

Model B described by equation (3.23) indicates that in such a process although the mass addition $\dot{m}'$ is non zero, the pressure would remain constant since

$$\begin{aligned} \frac{dp'}{dt'} &= 0; \\ \Rightarrow p' &= \text{constant}. \end{aligned} \tag{3.24}$$

Substituting the mass equation (2.47) into the pressure (3.22) produces the relation between pressure and density:

$$\begin{aligned} \frac{dp'}{p'} &= \gamma \frac{d\rho'}{\rho'}; \\ \Rightarrow p &\propto \rho^{\gamma}. \end{aligned} \tag{3.25}$$

This dependence of pressure on density represents simple adiabatic isentropic addition of mass.

Despite the neglect of such a term in model B, equation (3.23) has remained quite satisfactory at predicting rates of pressure rise. To understand why this is the case, it is necessary to understand the energy change that is assumed to occur when the solid propellant gasifies (this will be seen in more detail when the two-phase problem is addressed). In model B, that is essentially the same as described in [58], the change in energy at the propellant/gas interface is described as

$$\dot{m}'e'|_s \equiv \dot{m}'Q'^p|_s\,, \tag{3.26}$$

where s is the interface and a new parameter has been introduced Q^p which is the energy of formation produced by simultaneous gasification and combustion of the propellant. This implies that the rise in gas-phase thermal energy

is equal to the energy released at gasification of propellant which produces a source of mass and exothermic energy simultaneously. Both of these contributions are taken into account in Q'^{p}.

In model A the contributions are split into two recognisable parts; energy increase due to gasification followed by energy increase due to gas-phase combustion:

$$((\dot{m}'(e' + p'v') + \dot{m}'(Q' - L'))| = \dot{m}'Q'^{p})|_{s}\,. \tag{3.27}$$

This new value Q' has been introduced to distinguish it from Q'^{p}. This effectively means that the definition of Q' is different in models A and B. These differences will need to be recognised to fully implement the model with chemistry, where there is a distinguishable term responsible for adiabatic addition of gas, into a real ballistic scenario. Experimental data must be gathered for the net rate of change of energy due to chemical gasification and for the exothermic gas-phase reaction individually. In this gas-phase model presented Q will now be adopted as the energy of formation of the reactant gas.

3.3 Parametric Analysis

To understand the influence of chemical kinetics on the full system and the effect of key chemical parameters on chemical rates, a parametric analysis was necessary. This also ensures that the set of equations represent well understood physical phenomena. The parameters that will be investigated are the latent heat L', rate of addition of gaseous mass $\dot{m}'$ and the two reaction rate parameters- the activation energy E'_A and the frequency of collision A'_g.

3.3.1 Latent Heat

The results of changing the size of L' can be described by varying the dimensionless variable $L = L'/Q'$. Compare the solutions where the dimensionless latent heat L is varied from 0.568, to $L + \Delta L$ and $L - \Delta L$ where ΔL is 0.004.

Figure (3.6) shows the equivalent phase plane as in figure (3.3) but now the temperature T_0 is constant and L is varied. When L is increased to $L + \Delta L$ ignition does not occur since more heat is now lost to gasify the solid propellant. If L is decreased to $L - \Delta L$, less energy is needed for gasification and the initial fall in internal energy decreases. The temperature soon starts to increase. and very rapidly there will be sufficient energy to switch on the ignition reaction. This means the maximum reactant mass fraction c_{max} will be lower than for the original value of L before the mass-fraction plunges down to near zero values.

The equivalent temperature and mass-fraction plots for this event can be seen in figure (3.7)

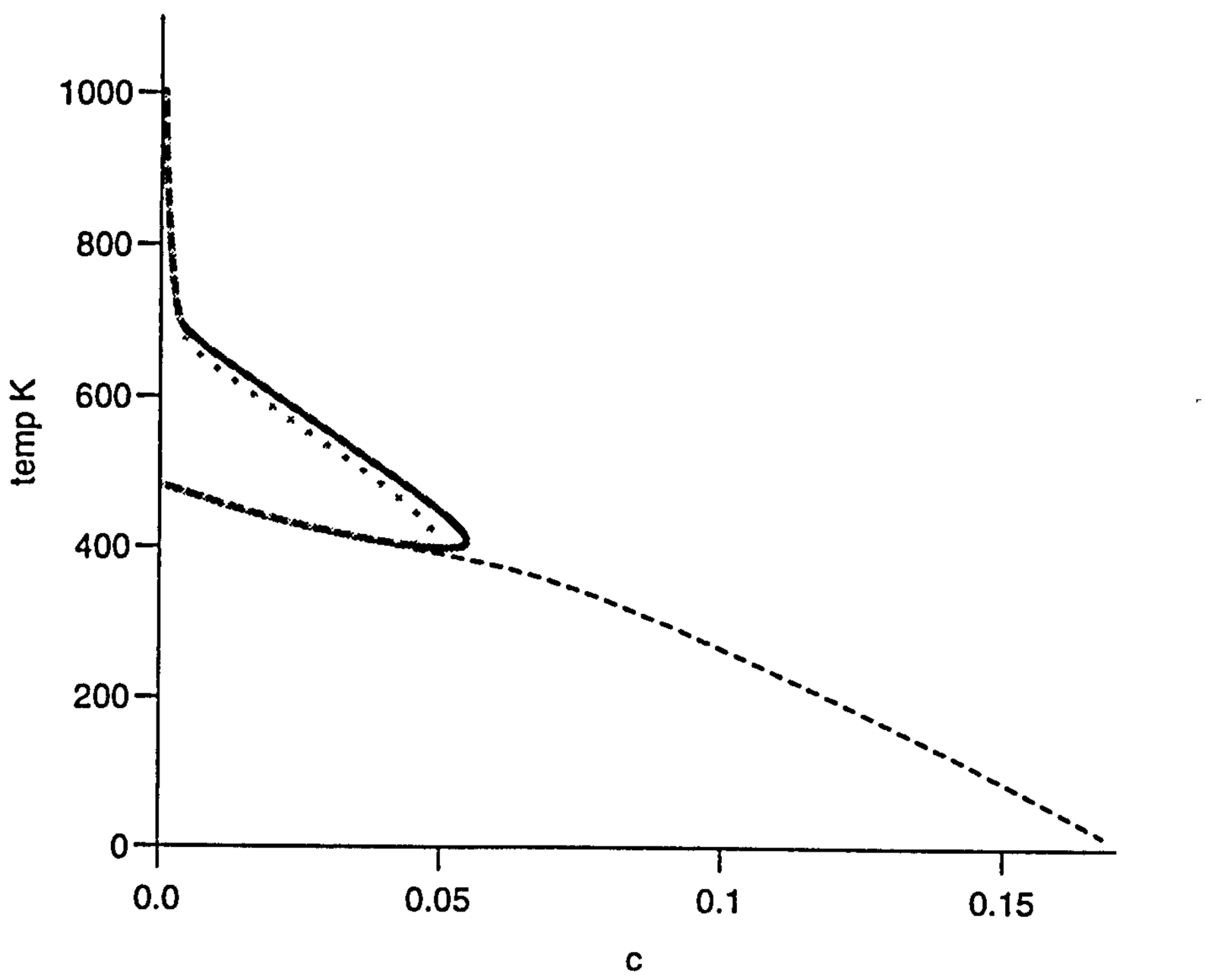

Figure 3.6: Solution in the $T' - c$ plane as L is varied, $L = L + \Delta L$ (dotted line), L (full line) and $L - \Delta L$ (- - -).

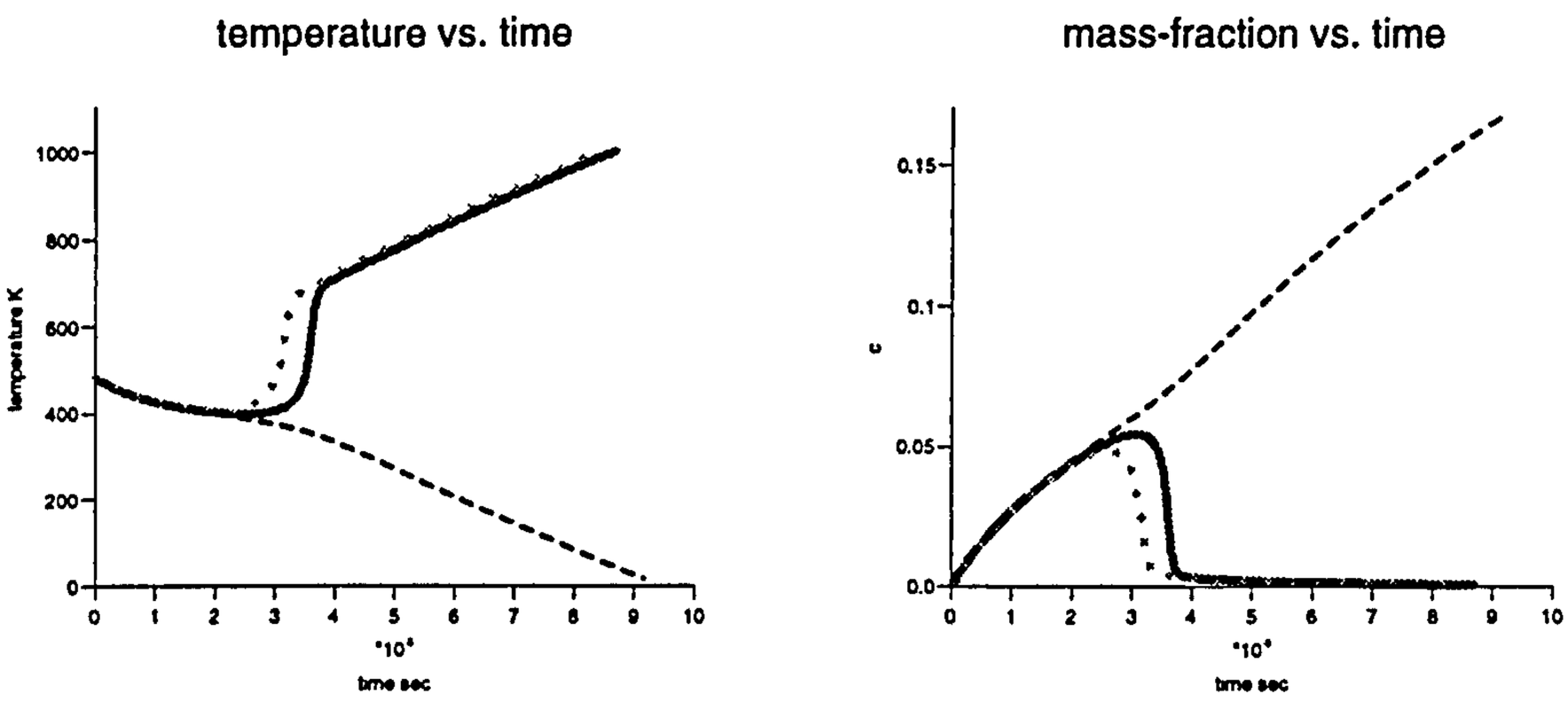

Figure 3.7: Temperature and mass fraction histories as L is varied, $L = L+\Delta L$ (dotted line), L (full line) and $L - \Delta L$ (- - -) is varied.

3.3.2 Rate of Mass Addition $\dot{m}'$

Consider the case in which the rate of addition of mass is varied $\dot{m}' = 30kg/m^3sec$, $60kg/m^3sec$ and $120kg/m^3sec$.

Firstly consider what happens when $\dot{m}$ is increased from $30kg/m^3sec$ to $60kg/m^3sec$: Figure (3.8) gives the temperature and mass-fraction histories. The fall in temperature at early times is more pronounced for the larger value of $\dot{m}$. This is due to the increased requirement of latent heat to gasify the larger mass of solid material. The results is an increased ignition delay and greater accumulation of reactant gas. However, **after** ignition the rate of change of temperature remains higher.

If $\dot{m}$ is further increased to $120kg/m^3sec$ there is insufficient initial energy to sustain an exothermic reaction and ignition does not occur.

For internal ballistics problems there is a point at which the fuel source is completely depleted called *burnout*. Consider what happens when this occurs:

If combustion is well underway at burnout, in this example at $6ms$, figure (3.9) shows how the temperature rapidly settles to a constant and the mass-fraction approaches very small values. However, if burnout occurs during the

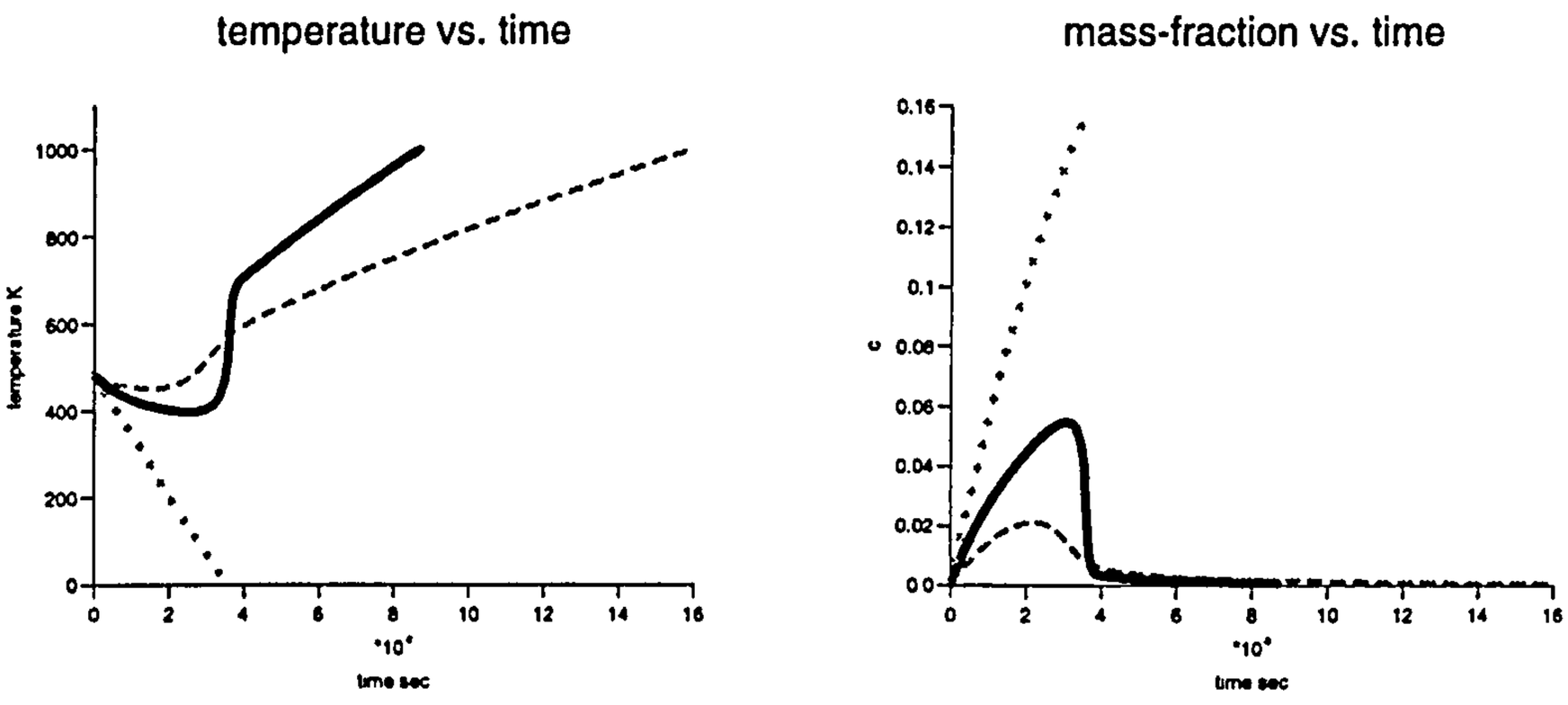

Figure 3.8: Temperature and mass-fraction histories for different rates of mass addition where the dashed line is for $\dot{m}' = 30kg/m^3$, the full line is $\dot{m}' = 60kg/m^3$ and the dotted line is $\dot{m}' = 120kg/m^3$.

ignition delay, prior to approximately $4ms$, at $3ms$, this is not the case as can be seen in figure (3.9). Although the mass addition is zero, the internal energy increases before levelling off. The differences can be understood by studying the reduced form of the equations given in section 2.3 when $\dot{m}'$ becomes zero:

$$\frac{d\rho'}{dt'} = 0; \tag{3.28}$$

$$\frac{dc}{dt'} = -\Omega' c^2; \tag{3.29}$$

$$\frac{de'}{dt'} = 2Q'\Omega' c^2. \tag{3.30}$$

If burnout occurs after the ignition event, then the chemistry is approaching equilibrium as described in section 3.2.1. According to equation (3.21), and the conditions for burnout, this means that:

$$\rho'\Omega' c^2 \rightarrow \dot{m}'/2 = 0. \tag{3.31}$$

Substitution into equations (3.29) and (3.30) implies that the change in mass-fraction and internal energy will be zero.

Alternatively, for burnout prior to ignition, non-equilibrium effects are still

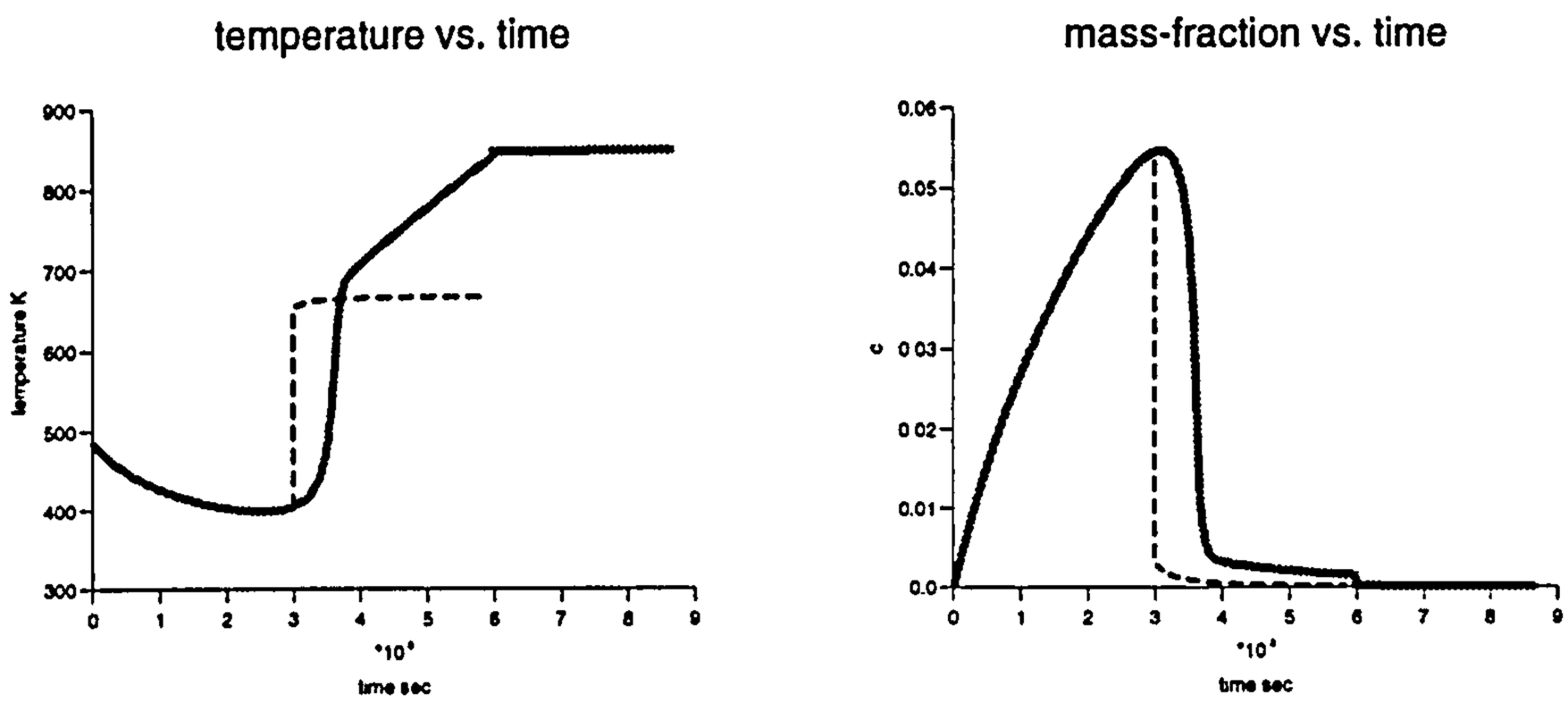

Figure 3.9: Temperature and mass-fraction histories for burnout at $3ms$(dotted line) and $6ms$ (full-line).

important. This implies that:

$$\rho'\Omega'c^2 > \dot{m}/2. \tag{3.32}$$

The gas density is real and positive throughout which implies that:

$$\Omega'c^2 > 0. \tag{3.33}$$

Substitution of equation (3.33) into the mass-fraction equation (3.29) means that the mass-fraction will immediately decrease and the internal energy will continue to rise, according to equation (3.30), until equilibrium chemistry is attained. This makes good physical sense; for non-zero $\dot{m}$ during the ignition delay the internal temperature of the system is reduced due to latent heat requirements outweighing any energy increases due to isentropic mass addition. Decreasing temperatures mean exothermicity is negligible. When burnout occurs and $\dot{m}$ is zero, although there is no *more* addition of reactant mass, there is an increased availability of energy due to absence of latent heat requirements. This means that the reactant gas present can be immediately consumed releasing chemical energy into the system. Once all of this chemical energy has been released there are no other energy sources and the internal energy can increase no more.

The assumption of a constant value of $\dot{m}'$ is completely unrealistic in the ballistic cycle. However, it can be quite accurately calculated as a function of pressure alone if the exposed surface area of the propellant is assumed to be constant:

$$\dot{m}' = A'_s p'^n \tag{3.34}$$

where $A'_s = \rho'^p S'_p B'_{cf}$ is the burn-rate coefficient and n is a constant called the pressure index that are measured empirically. Let equation (3.34) be used to calculate the mass addition where two different coefficients A'_s are adopted, A_1 and A_2 where A_1 is greater than A_2, 10^{-4} and 3×10^{-4} respectively, are chosen for comparison.

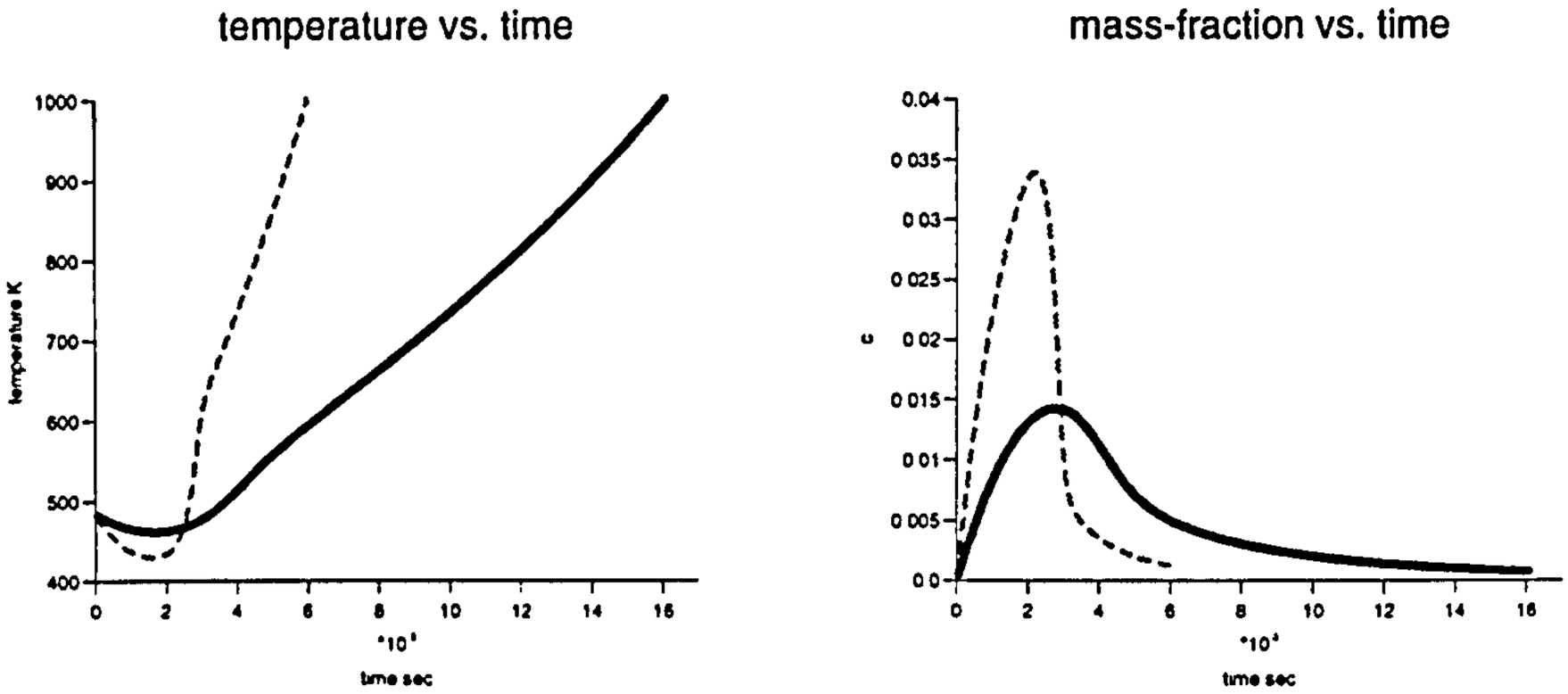

Figure 3.10: Temperature and mass-fraction histories where the rate of mass addition is proportional to pressure with constant of proportionality A_1 (full line) and A_2 (- - -).

The pressure and mass-fraction histories can be seen in figure (3.10). Ignition occurs at different times, approximately $3ms$ for the higher constant A_2 and $4ms$ for A_1. Previously, after ignition the rate of rise of temperature tended to a constant. It can be clearly seen that the *rate* of temperature rise now increases with time.

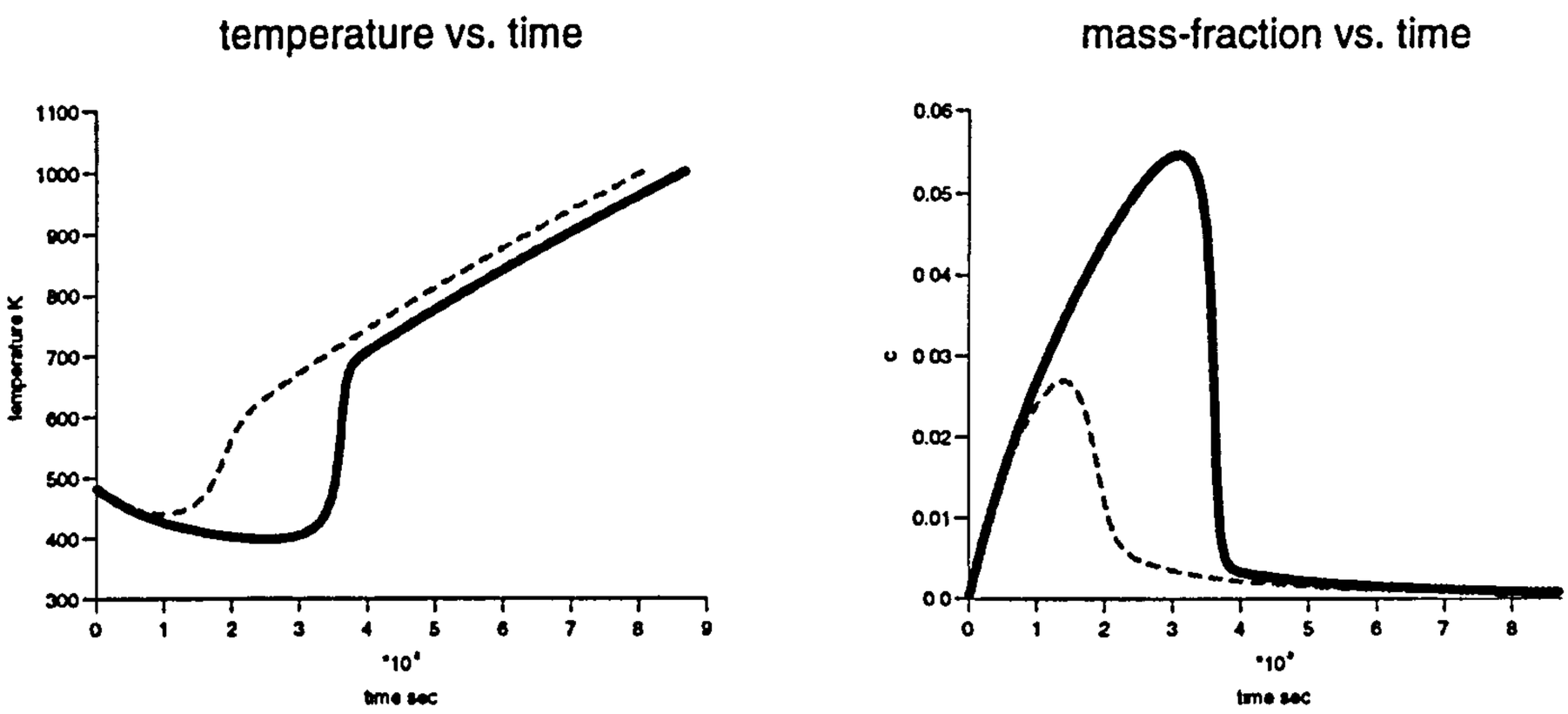

Figure 3.11: The effect of A_g on the flow histories; $A'_g = 10000(secPa)^{-1}$ (full line) and $A'_g = 15000(secPa)^{-1}$ (- - -).

3.3.3 Chemical Rate Parameters

Now consider the two parameters associated with the rate of chemical reaction:

$$\Omega' = A'_g p' \exp\left(-E'_A/\mathcal{R}'T'\right). \tag{3.35}$$

A'_g is related to the frequency of collision which is a measure of the number of molecule-molecule collisions. E'_A is the activation energy of the reaction, a measure of the amount of energy required before two molecules will react. This controls how the temperature will affect the rate of reaction. If the exponential term is negligibly small, it will dominate Ω' which will also be approximately zero. During the reaction, the exponential can rapidly change with small increases in temperature. If the exponential is close to the maximum value of 1 then it is said to be saturated and the reaction rate is very weakly dependent on further increases in temperature.

Consider the effect of multiplying A'_g by 1.5; figure (3.11) shows how this increase speeds up the rate of reaction as would be expected.

Next the activation energy is varied as displayed in figure (3.12). E'_A is now only multiplied by 0.9 and 1.1 and yet this radically changes the reaction time. In fact for the higher activation energy this prevents ignition occurring at all.

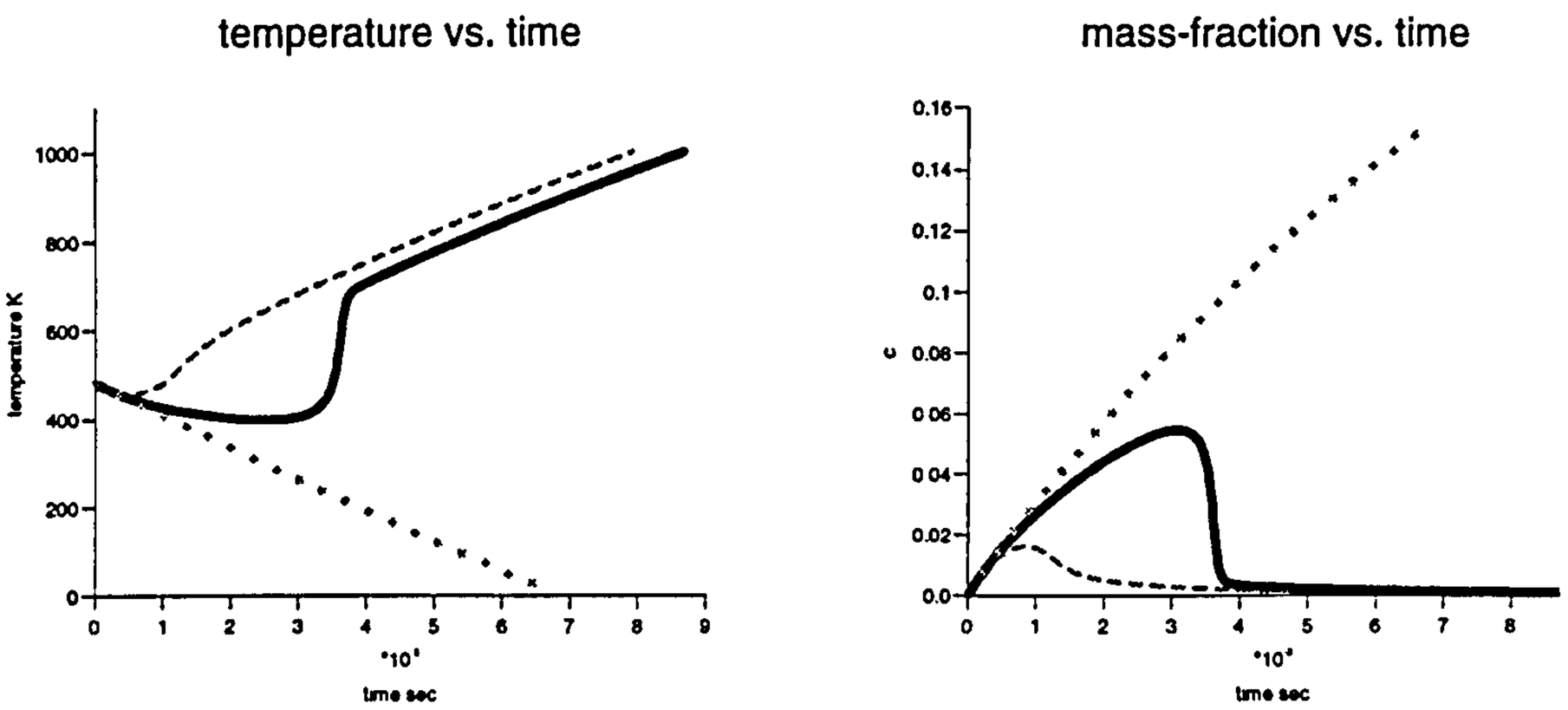

Figure 3.12: The effect of E'_A on the flow histories; $E'_A = 5000K$ (full line), $E'_A = 0.9 \times 5000K$ (- - -) and $E'_A = 1.1 \times 5000K$ (dotted line).

The reduction of E'_A causes halving of the ignition delay. Once again this result makes good physical sense from the definition of the activation energy. The activation energy is the dominant parameter in the chemical rate parameters.

3.4 A Covolume Equation of State

Particularly at high densities, the ideal equation of state is inaccurate for the gaseous products of combustion. A more appropriate equation of state is the covolume equation:

$$e' = \frac{p'(1-\rho' b')}{\rho'(\gamma-1)} = \frac{\mathsf{R}'T'}{W(\gamma-1)} \tag{3.36}$$

where $b'(m/kg)$ is a constant.

The form of the equations for mass, mass-fraction, momentum and energy conservation do not change. However when the pressure is substituted into the energy equation (2.46), transformed from t' to τ and the dimensionless variables adopted, the pressure variation is:

$$\frac{dp}{d\tau} = \frac{\gamma p + (\gamma-1)2\rho D c^2 Q}{1-\rho b'} \tag{3.37}$$

or in equilibrium form:

$$\frac{dp}{d\tau} = \frac{\gamma p + (\gamma - 1)\rho Q}{1 - \rho b'} \tag{3.38}$$

Equation (3.38) can be approximately integrated analytically but the process is not elegant and it is easier to resort to numerical methods. However, since both ρ and b' are positive, the effect of this modification is to increase the rate of change in pressure over time as the density ρ increases.

An enlightening study of the spatially uniform problem has been undertaken. This has given precise meaning to some of the new parameters that have been introduced in a model that includes chemical kinetics. The predictions produced make physical sense and can be firmly placed in context with past combustion models. The definition of ignition has been discussed; a proposal has been put forward that gives the term a mathematical interpretation which also ties up well with the observed phenomena. With the wealth of information and understanding that has been gained, the more complex problem that deals with the interrelation of flow and chemistry will be pursued. This means solving the complete set of conservation equations given at the start of this chapter.

Chapter 4

The One-Dimensional Problem

The single-phase equations are given as:

$$\frac{d}{dt'}\int_{V'}\rho' dV' + \int_{S'}\rho' u'_j n_j dS' = \int_{V'}(\dot{m}' + \dot{m}'_{ig})dV'; \tag{4.1}$$

$$\frac{d}{dt'}\int_{V'}\rho' c dV' + \int_{S'}\rho' c u'_j n_j dS' = \int_{V'}(\dot{m}'/2 + K')dV'; \tag{4.2}$$

$$\frac{d}{dt'}\int_{V'}\rho' u'_j dV' + \int_{S'}(\rho' u'_j u'_k + p'\delta_{jk})n_j dS' = \int_{V'} u'_j(\dot{m}' + \dot{m}'_{ig})dV'; \tag{4.3}$$

$$\frac{d}{dt'}\int_{V'}E' dV' + \int_{S'} u'_j(E' + p')n_j dS' = \int_{V'}(\dot{m}' + \dot{m}'_{ig})(e' + \kappa' + p'v') + \dot{m}'(Q' - L')dV'; \tag{4.4}$$

where the gas will be assumed to be a covolume gas such that:

$$e' = \frac{p'(1 - \rho' b')}{\rho'(\gamma - 1)}. \tag{4.5}$$

and the total energy is defined as:

$$E' = \rho'\left(e' + \kappa' + 2cQ'\right). \tag{4.6}$$

For brevity, from now on, in this thesis, all quantities are dimensional, and " ' will be dropped . For smooth solutions the equations can be rewritten in

one-dimensional, differential form as:

$$\begin{pmatrix} \rho \\ \rho c \\ \rho u \\ E \end{pmatrix}_t + \begin{pmatrix} \rho u \\ \rho c u \\ \rho u^2 + p \\ \rho u(E+p) \end{pmatrix}_x = \begin{pmatrix} \dot{m} + \dot{m}_{ig} \\ \dot{m}/2 - \rho\Omega c^2 \\ u(\dot{m} + \dot{m}_{ig}) \\ (\dot{m} + \dot{m}_{ig})(e + pv + \kappa) + \dot{m}(Q - L) \end{pmatrix} \quad (4.7)$$

that is

$$\mathbf{U}_t + [\mathbf{F}(\mathbf{U})]_x = \mathbf{S}(\mathbf{U}), \quad (4.8)$$

where

$$\mathbf{U} = \begin{pmatrix} \rho \\ \rho c \\ \rho u \\ E \end{pmatrix}; \quad \mathbf{F}(\mathbf{U}) = \begin{pmatrix} \rho u \\ \rho c \\ \rho u^2 + p \\ u(E+p) \end{pmatrix}; \quad (4.9)$$

$$\mathbf{S}(\mathbf{U}) = \begin{pmatrix} \dot{m} + \dot{m}_{ig} \\ \dot{m}/2 - \rho\Omega c^2 \\ u(\dot{m} + \dot{m}_{ig}) \\ (\dot{m} + \dot{m}_{ig})(e + pv + \kappa) + \dot{m}(Q - L) \end{pmatrix}. \quad (4.10)$$

where u is the component of velocity in the x direction. The initial-value-problem is defined by specifying:

$$\mathbf{U}(x, 0) = \mathbf{U}_0(x). \quad (4.11)$$

The physical boundary conditions for the inviscid flow equations at the fixed boundaries of the domain $x = 0$ and $x = l$ are:

$$u(0, t) = 0; \qquad u(l, t) = 0. \quad (4.12)$$

The system of equations are hyperbolic and will be solved using the method of fractional steps that transforms the single problem into two successive problems - a homogeneous hyperbolic problem followed by a system of stiff ordinary-differential-equations. This will be described together with the numerical methods used to solve each individual problem. Following this, flow variable histories will be examined to investigate the consequences of including simple kinetic theory into the model.

4.1 Numerical Methods

4.1.1 The Method of Fractional Steps

The method of fractional steps is based on the ideas by Yanenko [59]. This involves splitting the problem as given:

$$\mathbf{U}_t + \mathbf{F}(\mathbf{U})_x = \mathbf{S}(\mathbf{U}), \tag{4.13}$$

with initial conditions

$$\mathbf{U}(x,0) = \mathbf{U}_0(x), \tag{4.14}$$

into two subproblems. Firstly the homogeneous hyperbolic conservation law is solved

$$\mathbf{U}_t + \mathbf{F}(\mathbf{U})_x = 0, \tag{4.15}$$

followed by a system of ordinary-differential-equations:

$$\mathbf{U}_t = \mathbf{S}(\mathbf{U}). \tag{4.16}$$

Let $L(t)$ be the exact solution operator of equation (4.13). The solution of this in conjunction with initial conditions (4.14) can be expressed in the form

$$\mathbf{U}(x,t) = L(t)\mathbf{U}_0. \tag{4.17}$$

Similarly let $L_1(t)$ and $L_2(t)$ be the solution operators of (4.15) and (4.16), respectively. The first order fractional step method is based on the approximation:

$$L(t_n)\mathbf{U}_0 \approx (L_2(\Delta t)L_1(\Delta t))^n\mathbf{U}_0, \tag{4.18}$$

or equivalently with L_1 and L_2 reversed where Δt is the splitting step and L_1 and L_2 are at least first-order solutions of equations (4.15) and (4.16). A second-order solution was developed by Strang [60] and is given by

$$L(t_n)\mathbf{U}_0 \approx (L_2(\frac{\Delta t}{2})L_1(\Delta t)L_2(\frac{\Delta t}{2}))^n\mathbf{U}_0, \tag{4.19}$$

where L_1 and L_2 are at least second-order solutions of equations (4.15) and (4.16).

However it should be noted, for discontinuous solutions of conservation laws both methods have been shown to be only at most first order accurate [61]. The method can be extended to multi-dimensional systems as done by Godunov [62] and Strang [60]. A recent paper by Tang & Teng [63] look at the non-homogeneous problem as defined above. They show that (4.18) converges to the unique weak entropy satisfying solution of (4.15), (4.14) and that errors produced by the splitting are bounded so the method is stable. This splitting technique will be used in the following work.

4.1.2 The Homogeneous Hyperbolic System

The homogeneous hyperbolic problem derived from the time-operator-splitting process described above is

$$\mathbf{U}_t + \mathbf{F}(\mathbf{U})_x = 0. \tag{4.20}$$

The system has been written in conservative form where $\mathbf{U}$ is the vector of conserved variables of mass, mass-fraction, momentum and energy. The physical problem that is being considered involves high speeds and it is highly probable that shocks will be an important flow phenomena. The system of partial differential equations above can only produce solutions that include discontinuities, such as shocks, if the more general integral form of the equations is considered. This is given as

$$\oint \mathbf{U}dx - \mathbf{F}dt = 0. \tag{4.21}$$

This integral form (4.92) can be solved using finite volume methods.

4.1.3 The Finite Volume Method

The finite volume method that will be used is the weighted-average-flux (WAF) [64]. This is a second order extension of the original ideas pioneered by Godunov. In this section, the general ideas behind the use of finite-volume schemes to provide conservative methods of solution will be introduced.

Let the domain in x space and t time be discretised into m regular cells of size $\Delta x \times \Delta t$ as seen in figure (4.1). Consider a typical cell i of volume V; the vector of conserved variable at time n in cell i can be denoted as $\mathbf{U}_i^n$. Assume that the vector $\mathbf{U}_i^n$ is known for all i, the timemarching procedure is used to approximate the vector of conserved variables at the next time-level t_{n+1} by using information at t_n and information from the governing equations to give $\mathbf{U}_i^{n+1}$.

Equation (4.21) can be evaluated by integrating in space around the closed volume V between $x_{i-\frac{1}{2}}$ and $x_{i+\frac{1}{2}}$:

$$\oint \mathbf{U}dx - \mathbf{F}dt = 0 \tag{4.22}$$

$$\Rightarrow \int_{x_{i-\frac{1}{2}}}^{x_{i+\frac{1}{2}}} \int_{t_n}^{t_{n+1}} \mathbf{U}(x,t)dx - \mathbf{F}(x,t)dt = 0 \tag{4.23}$$

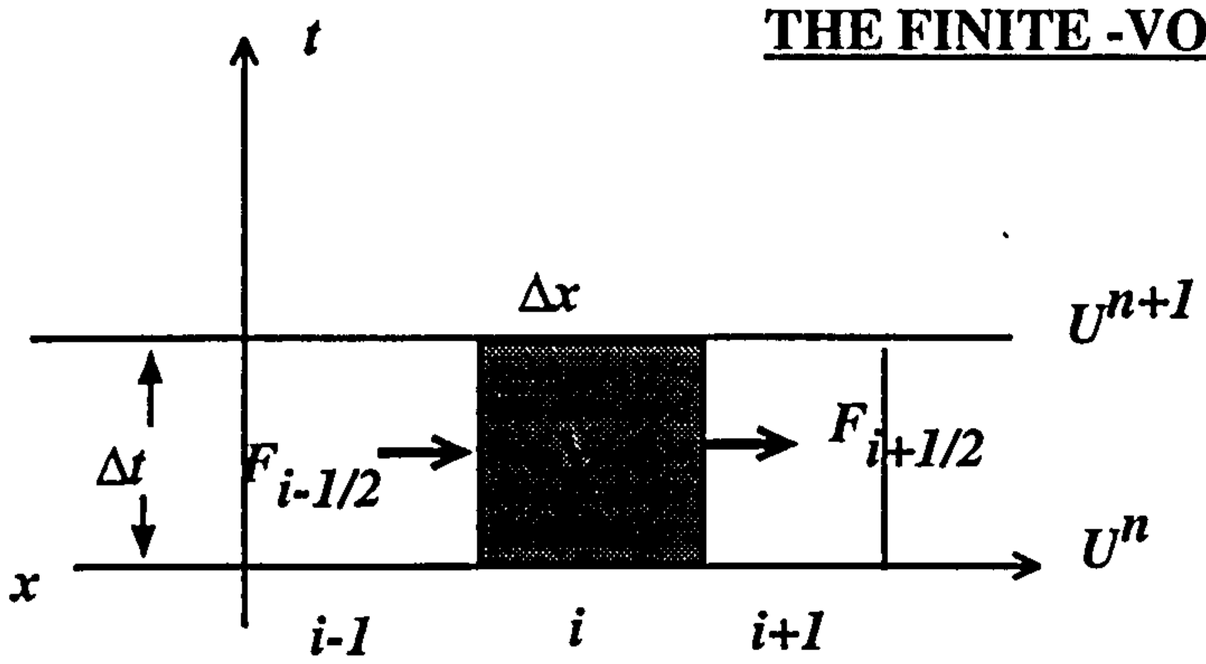

THE FINITE -VOLUME METHOD

Figure 4.1: The discretisation of the domain into finite-volume cells.

$$\Rightarrow \int_{x_{i-\frac{1}{2}}}^{x_{i+\frac{1}{2}}} \mathbf{U}(x,t_{n+1})dx = \int_{x_{i-\frac{1}{2}}}^{x_{i+\frac{1}{2}}} \mathbf{U}(x,t_n)dx + \int_{t_n}^{t_{n+1}} \mathbf{F}(\mathbf{U}(x_{i-\frac{1}{2}},t))dt - \int_{t^n}^{t_{n+1}} \mathbf{F}(\mathbf{U}(x_{i+\frac{1}{2}},t))dt. \quad (4.24)$$

Let the pointwise values of the true solution be denoted by:

$$\mathbf{U}_i^n = \mathbf{U}(x_i,t_n). \quad (4.25)$$

Then the cell average is defined as:

$$\bar{\mathbf{U}}_i^n \equiv \frac{1}{\Delta x}\int_{x_{i-\frac{1}{2}}}^{x_{i+\frac{1}{2}}} \mathbf{U}(x,t_n)dx. \quad (4.26)$$

Substituting the cell average into equation (4.24) and dividing by Δx gives:

$$\bar{\mathbf{U}}_i^{n+1} = \bar{\mathbf{U}}_i^n - \frac{1}{\Delta x}\left[\int_{t_n}^{t_{n+1}} \mathbf{F}(\mathbf{U}(x_{i+\frac{1}{2}},t) - \mathbf{F}(\mathbf{U}(x_{i-\frac{1}{2}},t))dt\right]. \quad (4.27)$$

Numerical methods estimate the exact solution to some defined accuracy where the approximation is introduced via averaging and flux functions on the right-hand-side of equation (4.27). Denoting as $\mathbf{U}'^n_i$ an approximation to the exact average solution $\bar{\mathbf{U}}_i^n$ in cell i, equation (4.27) can be approximated as:

$$\mathbf{U}'^{n+1}_i = \mathbf{U}'^n_i - \frac{\Delta t}{\Delta x}\left[\mathbf{F}'_{i+1/2} - \mathbf{F}'_{i-1/2}\right]; \quad (4.28)$$

where

$$\mathbf{F'}_{i+1/2} \approx \frac{1}{\Delta t} \int_{t_n}^{t_{n+1}} \mathbf{F}\left(\mathbf{U}(x_{i+1/2}, t)\right) dt. \tag{4.29}$$

By using this algorithm, the approximate solution at time $n+1$, given as $\mathbf{U'}_i^{n+1}$, can be obtained over all cells m in the domain. Note that the numerical solution $\mathbf{U'}_i{}^n$ is not only an approximation to the true solution but differs in nature from this since it remains constant over space Δx and time Δt in cell i. The flux function $\mathbf{F'}_{i+1/2}$ is an approximation of the average flux which is a function of any number of elements of the vector $\mathbf{U'}^n$ centered around cell i. Generally, if higher accuracy is required, more of the elements of the vector $\mathbf{U'}^n$ are used in constructing the flux function. Pictorially equation (4.28) is illustrated in figure (4.1).

The final step that is required to calculate the cell average at the new time is the formulation of the flux functions. There are a whole range of discretisation methods that will do this and if the method satisfies (4.28), then it is a conservative method. Two such methods, the Godunov and WAF methods, will be described below.

4.1.4 Introduction to the Riemann Problem

Before the Godunov and WAF methods are described, the concept of a Riemann problem must be introduced. The Riemann problem is the conservation law with simplified initial conditions from which an exact solution may be found. It can provide a wealth of characteristic information that can be used in the construction of conservative methods for the full problem. The Godunov and WAF methods use this information to approximate the flux functions $\mathbf{F'}$. Unfortunately, the exact solution of a single Riemann problem is expensive, computationally, and in any one timestep of a numerical computation hundreds of individual Riemann problems may need to be solved. This expense has prompted the development of more efficient approximate solutions to the Riemann problem a few of which are described in [65],[66],[67] and [68]. The HLLC method [68] is the method that will be used in the following work.

The conservation law with piecewise constant data having a single discontinuity is the Riemann problem as depicted in figure (4.2).

For this system the Riemann problem is given as:

$$\mathbf{U}_t + [\mathbf{F}(\mathbf{U})]_x = 0; \tag{4.30}$$

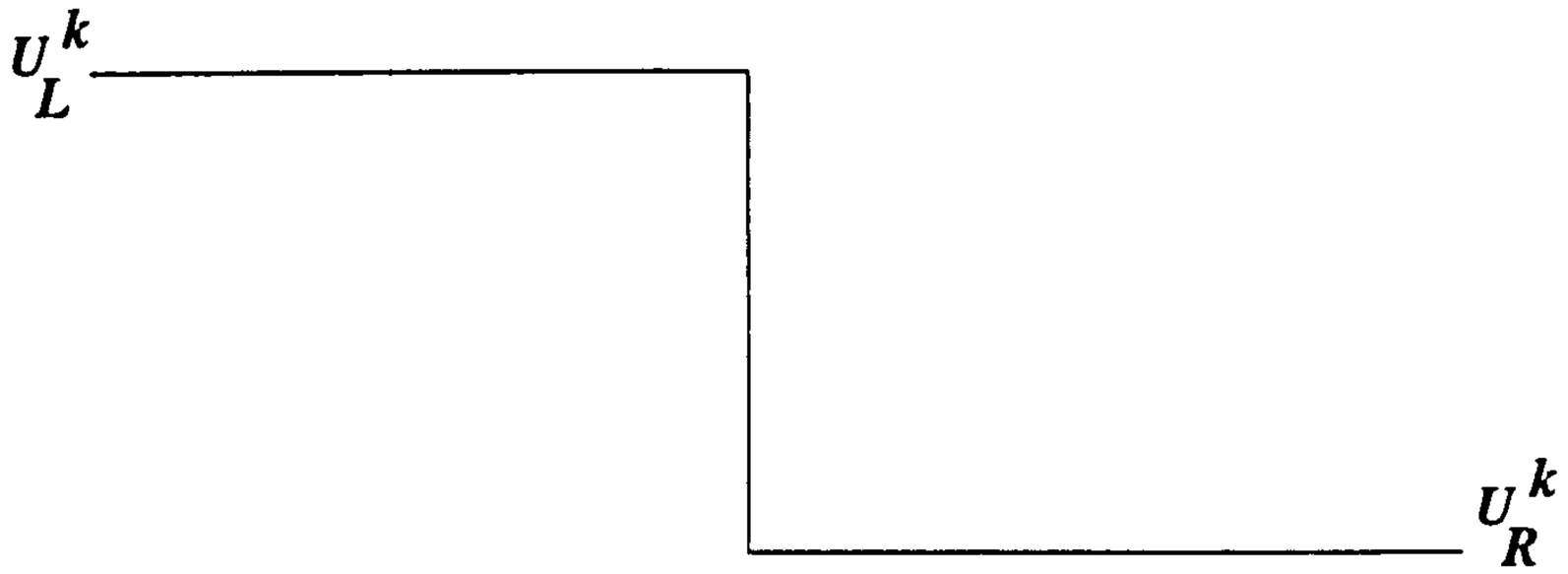

Figure 4.2: Initial conditions for the Riemann problem where U_L^k and U_R^k are two initial left and right components of the vector of conserved variables $\mathbf{U}$.

with initial conditions:

$$\mathbf{U}(x,0) = \begin{cases} \mathbf{U}_L & x < 0 \\ \mathbf{U}_R & x > 0. \end{cases} \tag{4.31}$$

The system of equations (4.30) is said to be *totally hyperbolic* if the eigenvalues of the system are real and distinct. For the system of equations that are being considered, the eigenvalues are:

$$\lambda^{(1)} = u - a,\ \lambda^{(2)} = u,\ \lambda^{(3)} = u,\ \lambda^{(4)} = u + a, \tag{4.32}$$

where a is the gas sound-speed:

$$a = \sqrt{\frac{\gamma p}{\rho(1-\rho b)}}. \tag{4.33}$$

Clearly the eigenvalues are real but not distinct meaning the equations are hyperbolic but not totally hyperbolic.

The solution structure of the Riemann problem given in equations (4.30) and (4.31) consists of four waves that correspond to each of the eigenvalues. Two of the waves are identical and the waves separate four constant regions which can be seen in figure (4.3). The two outer regions contain the initial left and right states whilst the region inside the two nonlinear (outer) waves is called the star state in which flow variables need to be deduced from the governing equations.

The waves that travel at the same speed as the gas $\lambda^{(2)}$ and $\lambda^{(3)}$ advect the density and mass-fraction in the fluid at speed u^*. These two waves are called 'contact discontinuities' and the pressure and velocity remain constant across

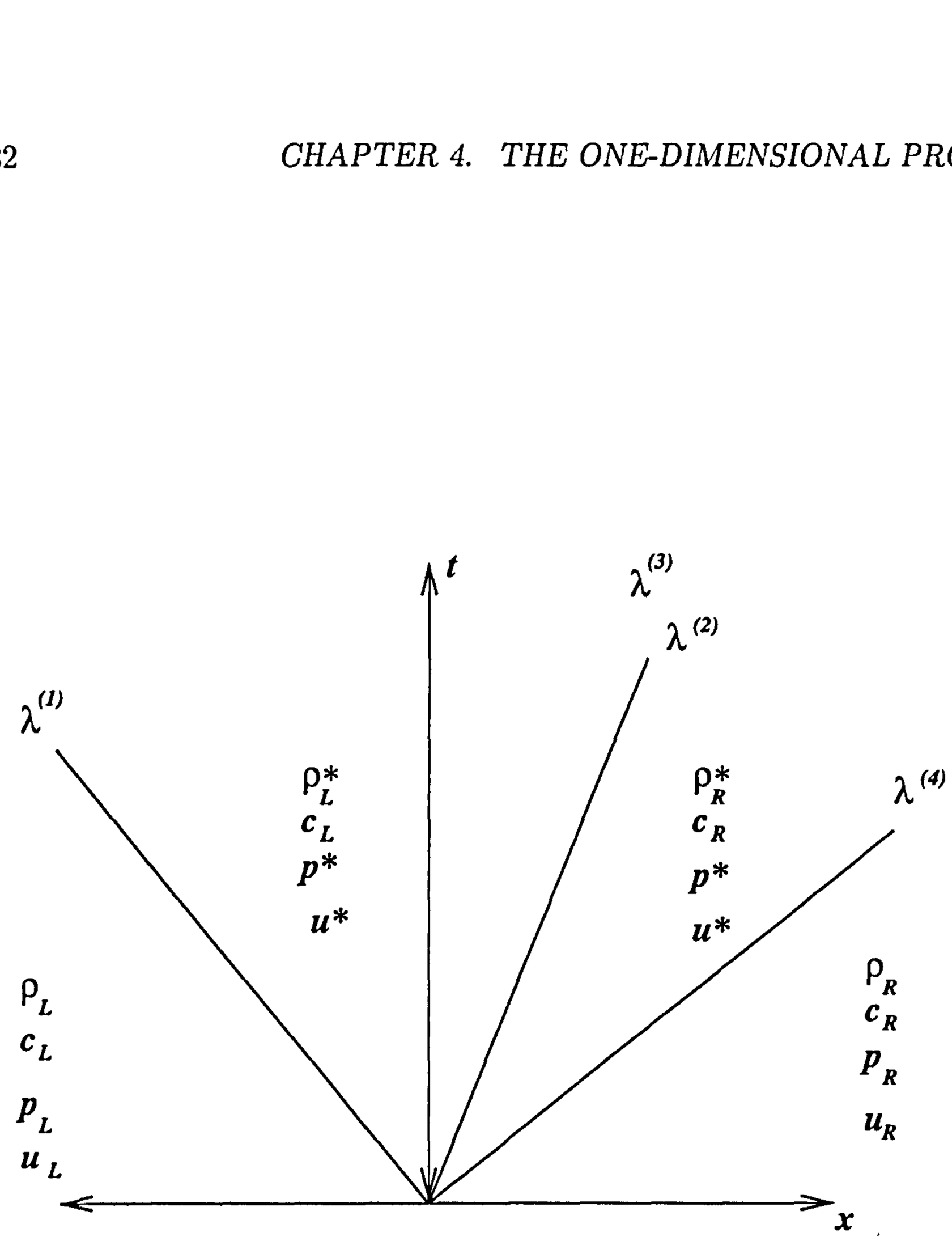

Figure 4.3: Solution structure of the Riemann problem.

them. Across the two nonlinear waves $\lambda^{(1)}$ and $\lambda^{(4)}$, the fraction of reactant c remains constant whilst the velocity, pressure and density all change. The methods that reveal how this particular wave structure, as depicted in figure (4.3), is deduced are outlined below.

The nonlinear waves can be either 'rarefaction waves' or 'shock' waves depending on the flow conditions. A brief description of how to distinguish between the two wave types and methods that will lead to the precise properties of the two will be given.

4.1.5 Rarefaction Waves

Rarefactions are continuous solutions of the equations. Figure (4.4) describes the solution of the Riemann problem where the two non-linear waves are rarefactions. Each wave consists of a rarefaction fan that consists of a continuous solution that connects the outer regions to the star region. Since the solution is continuous the equations may be re-written in non-conservative form:

$$\mathbf{W}_t + \mathbf{A}\mathbf{W}_x = 0, \tag{4.34}$$

where:

$$\mathbf{W} = \begin{pmatrix} \rho \\ c \\ u \\ p \end{pmatrix}, \quad \mathbf{A} = \begin{pmatrix} u & 0 & \rho & 0 \\ 0 & u & 0 & 0 \\ 0 & 0 & u & \frac{1}{\rho} \\ 0 & 0 & \rho a^2 & u \end{pmatrix}. \tag{4.35}$$

The wave-speeds can be found by calculating the eigenvalues of $\mathbf{A}$ for all wave types:

$$\begin{aligned} &Det \quad |\mathbf{A} - \lambda \mathbf{I}| = 0 \\ &\Rightarrow \quad \lambda^{(1)} = u - a,\ \lambda^{(2)} = u,\ \lambda^{(3)} = u,\ \lambda^{(4)} = u + a \end{aligned}$$

which validates equation (4.32) where the corresponding right eigenvectors are:

$$R_1 = \begin{bmatrix} \rho \\ 0 \\ -a \\ \rho a^2 \end{bmatrix}, \quad R_2 = \begin{bmatrix} \rho \\ c \\ 0 \\ 0 \end{bmatrix}, \quad R_3 = \begin{bmatrix} \rho \\ c \\ 0 \\ 0 \end{bmatrix}, \quad R_4 = \begin{bmatrix} \rho \\ 0 \\ a \\ \rho a^2 \end{bmatrix}. \tag{4.36}$$

The formation of what are described as 'generalised Riemann invariants' [69] produce relations that hold across rarefaction waves. Details of the derivation of these is given in appendix (A). The method reveals the complete flow

variable distribution across each rarefaction wave. The generalised Riemann invariants are solutions to the o.d.e.'s

$$\frac{dw_1}{r_1^{(i)}} = \frac{dw_2}{r_2^{(i)}} = ... = \frac{dw_m}{r_m^{(i)}}, \tag{4.37}$$

for each eigenvector $R_i = [r_1^{(i)}, r_2^{(i)}, ..., r_m^{(i)}]^T$ associated with eigenvalue $\lambda^{(i)}$ where w_k is the vector of variables being considered. In short, equation (4.37) describes a relationship between the rate of change of each variable across the wave i.

For the waves described above this gives:

For $\lambda^{(1)}$:

$$\frac{d\rho}{\rho} = \frac{dc}{0} = \frac{-du}{a} = \frac{dp}{\rho a^2}; \tag{4.38}$$

For $\lambda^{(2)}$ and $\lambda^{(3)}$:

$$\frac{d\rho}{\rho} = \frac{dc}{c} = \frac{du}{0} = \frac{dp}{0}; \tag{4.39}$$

For $\lambda^{(4)}$:

$$\frac{d\rho}{\rho} = \frac{dc}{0} = \frac{du}{a} = \frac{dp}{\rho a^2}. \tag{4.40}$$

Firstly consider the center waves $\lambda^{(2)}$ and $\lambda^{(3)}$:

$$\frac{d\rho}{\rho} = \frac{dc}{c}; \quad du = 0; \quad dp = 0. \tag{4.41}$$

This means that the velocity and pressure do not change across the central waves:

$$u_l^* = u_r^* = u*, \quad p_l^* = p_r^* = p* \ . \tag{4.42}$$

This describes the characteristics of a contact discontinuity where the density ρ and fraction of reactant c change discontinuously but the velocity and pressure remain constant as can be seen in figure (4.3).

For $\lambda^{(1)}$ this translates to the results:

$$dc = 0; \quad \frac{d\rho}{\rho} = -\frac{du}{a}; \quad \frac{du}{1} = -\frac{dp}{\rho a}, \tag{4.43}$$

which gives the following relations:

$$c_l = c_l^*; \tag{4.44}$$

$$u_l + \frac{2a_l}{\gamma - 1}(1 - \rho_l b) = u^* + \frac{2a_l^*}{\gamma - 1}(1 - \rho_l^* b). \tag{4.45}$$

Equation (4.44) indicates that the mass-fraction does not change across the wave $\lambda^{(1)}$. For this type of flow where entropy is constant along particle paths, the isentropic condition can be used to connect left and right density and pressure that is:

$$p \propto \rho^{\gamma}. \tag{4.46}$$

This implies that

$$\frac{\rho_l^*}{(1-b\rho_l^*)} = \frac{\rho_l}{(1-b\rho_l)}[\frac{p^*}{p_l}]^{\frac{1}{\gamma}}. \tag{4.47}$$

Use of equations (4.45) and (4.47) provide an expression for the star velocity in terms of the star pressure and initial left-side data:

$$u^* = u_l - \frac{p_l - p^*}{M_l}, \tag{4.48}$$

where

$$M_l = \frac{1-\gamma}{2}\sqrt{\frac{\rho_l p_l}{\gamma(1-b\rho_l)}}\frac{1-(p_*/p_l)}{1-(p_*/p_l)^{(\gamma-1)/2\gamma}}. \tag{4.49}$$

Then u^* can be written in the form:

$$u^* = u_l - f_l(p^*, \mathbf{U}_l). \tag{4.50}$$

Similarly for $\lambda^{(4)}$ it can be shown:

$$c_r = c_r^*; \tag{4.51}$$

$$u_r - \frac{2a_r}{\gamma-1}(1-\rho_r b) = u^* - \frac{2a_r^*}{\gamma-1}(1-\rho_r^* b); \tag{4.52}$$

$$\frac{\rho_r^*}{(1-b\rho_r^*)} = \frac{\rho_r}{(1-b\rho_r)}[\frac{p^*}{p_r}]^{\frac{1}{\gamma}}; \tag{4.53}$$

Use of equations (4.52) and (4.53) provide an expression for the star velocity in terms of the star pressure and initial right-side data:

$$u^* = u_r + \frac{p_r - p^*}{M_r}, \tag{4.54}$$

where

$$M_r = \frac{1-\gamma}{2}\sqrt{\frac{\rho_r p_r}{\gamma(1-b\rho_r)}}\frac{1-(p_*/p_r)}{1-(p_*/p_r)^{(\gamma-1)/2\gamma}}. \tag{4.55}$$

Then u^* can be written in the form:

$$u^* = u_r + f_r(p^*, \mathbf{U}_r). \tag{4.56}$$

Note that if the pressure in the star region is known p^*, then all other flow variables can be calculated and the exact solution can be found with ease.

The Two Rarefaction Wave Structure

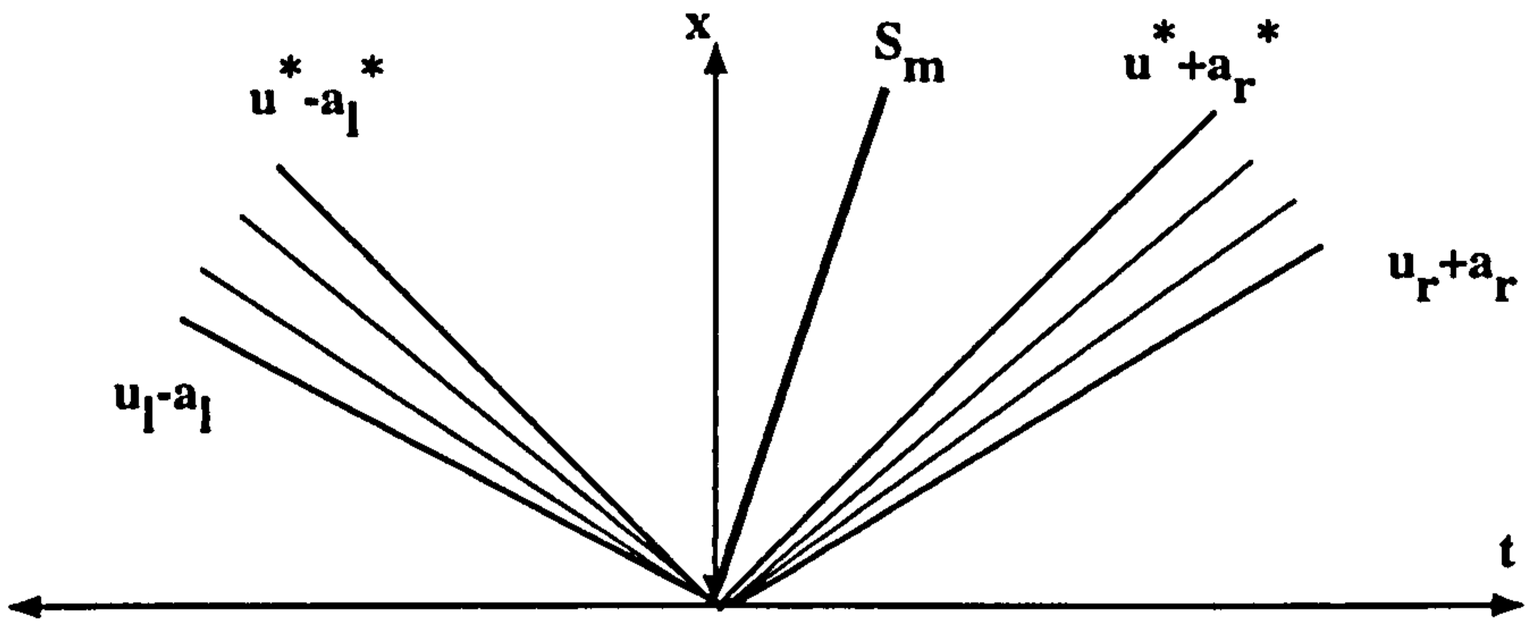

Figure 4.4: Wave solution of the Riemann problem with two rarefactions.

4.1.6 Two Rarefaction Approximation

If the two non-linear waves of the flow are two rarefactions as depicted in figure (4.1.6), then equations (4.50) and (4.56) can be manipulated to give a closed form for the pressure and velocity and use of equations (4.47) and(4.53) give the left and right star density, [67],:

$$p^*_{tr} = \left[\frac{(1-b\rho_l)a_l + (1-b\rho_r)a_r + (u_l-u_r)\frac{(\gamma-1)}{2}}{(1-b\rho_l)\frac{a_l}{p_l^m} + (1-b\rho_r)\frac{a_r}{p_r^m}}\right]^{\frac{1}{m}}; \quad (4.57)$$

$$u^* = u_\alpha \pm \left[\frac{2(1-\rho_\alpha b)a_\alpha(1-[\frac{p^*}{p_\alpha}]^{\frac{2}{m}})}{\gamma-1}\right]; \quad (4.58)$$

$$\frac{\rho^*_\alpha}{(1-b\rho^*_\alpha)} = \frac{\rho_\alpha}{(1-b\rho_\alpha)}[\frac{p^*}{p_\alpha}]^{\frac{1}{gamma}}, \quad (4.59)$$

where $\alpha = \mathrm{L/R}$ and $m = \frac{2\gamma}{\gamma-1}$.

4.1.7 Rarefaction Wave Speeds

A rarefaction wave produces a continuous change in flow variables across the nonlinear waves. This creates the structure illustrated in figure (4.1.6) where a rarefaction fan divides the constant states. The wave speed varies across the fan. The outer extent of the fan travels at the fastest speed - the *head* - and the inner part is called the *tail.* For a right rarefaction the head and tail speed are

$$S_R(head) = u_r + a_r; \tag{4.60}$$
$$S_R(tail) = u^* + a^*_r. \tag{4.61}$$

Similarly for the left rarefaction

$$S_L(head) = u_l - a_l; \tag{4.62}$$
$$S_L(tail) = u^* - a^*_l. \tag{4.63}$$

Summarizing these results validates some of the features seen in figure (4.3) if the two outer waves are assumed to be rarefaction waves.

4.1.8 Shock Waves

As mentioned above, the equations must be written in conservative form to properly account for discontinuous solutions. Rankine-Hugoniot jump conditions can give the wave-speeds of propagating shocks. In this problem there are four waves dividing four constant regions- the right and left initial conditions and the right and left star regions. Jump conditions provide relations that hold across discontinuous changes in the vector of conserved variable:

$$\mathbf{F}(\mathbf{U}_{left}) - \mathbf{F}(\mathbf{U}_{right}) = S(\mathbf{U}_{left} - \mathbf{U}_{right}) \tag{4.64}$$

where S is the shock speed, $\mathbf{F}$ is any flux of the conservation law and $\mathbf{U}_{left}$, $\mathbf{U}_{right}$ are the conditions to the left and right of the discontinuity. This gives:

$$S = \frac{[\mathbf{F}]}{[\mathbf{U}]} \tag{4.65}$$

where [.] indicates the jump in any quantity across a discontinuity. For the system of equations (4.30), then if the outer waves $\lambda^{(1)}$ and $\lambda^{(4)}$ are shocks,

this expands to

$$S_\alpha \begin{bmatrix} \rho_\alpha - \rho^*_\alpha \\ \rho_\alpha c_\alpha - \rho^*_\alpha c^*_\alpha \\ \rho_\alpha u_\alpha - \rho^*_\alpha u^* \\ \rho_\alpha E_\alpha - \rho^*_\alpha E^*_\alpha \end{bmatrix} = \begin{bmatrix} \rho_\alpha u_\alpha - \rho^*_\alpha u^* \\ \rho_\alpha c_\alpha u_\alpha - \rho^*_\alpha c^*_\alpha u^* \\ (\rho_\alpha u^2_\alpha + p_\alpha) - (\rho^*_\alpha u^{*2} + p^*) \\ \rho_\alpha u_\alpha (E_\alpha + p_\alpha v_\alpha) - \rho^*_\alpha u^* (E^*_\alpha + p^* v^*_\alpha) \end{bmatrix} \tag{4.66}$$

where $\alpha = l$ for wave $\lambda^{(1)}$ and $\alpha = r$ for wave $\lambda^{(4)}$. Manipulation of the equations defined in (4.66) reveals valuable information about the structure of the shock. Use of the equations controlling the change in mass and change in mass-fraction produce the results:

$$c_l = c^*_l; \tag{4.67}$$

$$c_r = c^*_r; \tag{4.68}$$

so the mass-fraction does not change across the outer nonlinear waves if these are shock waves, as illustrated in figure (4.3).

The appendix (B) shows how further manipulation of equations (4.66) provide explicit forms for the shock speeds:

$$S_L = u_l - a_l \sqrt{1 + \frac{\gamma + 1}{2\gamma}(\frac{p^*}{p_l} - 1)} \tag{4.69}$$

$$S_R = u_r - a_r \sqrt{1 + \frac{\gamma + 1}{2\gamma}(\frac{p^*}{p_r} - 1)} \tag{4.70}$$

where p^* is still to be determined.

If the Rankine-Hugoniot conditions are applied to the central waves $\lambda^{(2)}$ and $\lambda^{(3)}$, one possible solution to satisfy the momentum and energy condition is that pressure and velocity remain constant across the waves, confirming once again that the structure of the central waves corresponds to that of a contact discontinuity.

Just as for the rarefaction waves, the star velocity u^* and the unknown densities ρ^*_l and ρ^*_r can also be found as explicit functions of the initial conditions and p^*. The derivation of these expressions is also through the manipulation of the Rankine-Hugoniot jump conditions. The star velocity is given in terms of the left and right initial data and the star pressure as given in appendix (B):

$$u^* = u_l - f_l(p^*, \mathbf{U}_l), \tag{4.71}$$

$$u^* = u_r + f_r(p^*, \mathbf{U}_r). \tag{4.72}$$

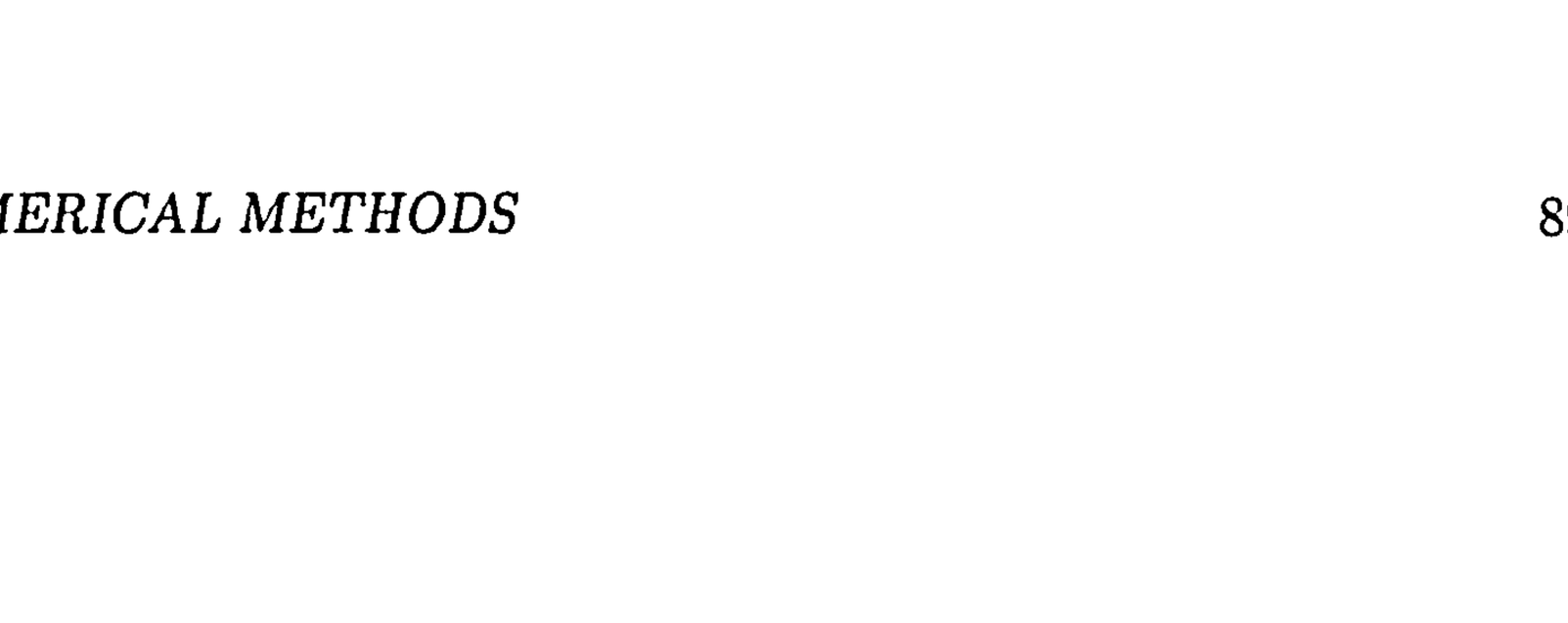

Figure 4.5: Wave solution of the Riemann problem with two shocks.

4.1.9 Two-Shock Approximation

Although no explicit expression can be given for this solution -as in the case of the two rarefaction waves- an approximate closed solution can be given as developed by Toro [70] for an ideal equation of state and extended for a covolume equation of state in [71]. The unknown pressure p^* and velocity u^* can be given as:

$$p^* = \frac{p_l g_l(p_0) + p_r g_r(p_0) + u_l - u_r}{g_l(p_0) + g_r(p_0)}, \tag{4.73}$$

$$u^* = \frac{1}{2}\left((u_l + u_r) + (p^* - p_r)g_r(p_0) - (p^* - p_l)g_l(p_0)\right), \tag{4.74}$$

where

$$g_\alpha(p) = \sqrt{\frac{A_\alpha}{p + B_\alpha}}, \tag{4.75}$$

$$A_\alpha = \frac{2(1 - b\rho_\alpha)}{(\gamma + 1)\rho_\alpha}, \tag{4.76}$$

$$B_\alpha = (\frac{\gamma - 1}{\gamma + 1})p_\alpha, \quad \alpha = l, r \tag{4.77}$$

where p_0 is some initial estimate for the star pressure.

4.1.10 The Exact Solution

The above has described how the structure of the waves is determined. From the analysis of rarefaction waves in section 4.1.5 and shock waves in section 4.1.8, it is apparent that the solution to the Riemann problem reduces to solving equations of the form

$$u^* = u_l - f_l(p^*, \mathbf{U}_l), \tag{4.78}$$
$$u^* = u_r + f_r(p^*, \mathbf{U}_r). \tag{4.79}$$

where the functions f_l and f_r are functions of the initial left and right states and the star pressure p^*. The form of these functions depends on whether the waves are rarefaction or shock waves. By subtracting equations (4.78) and (4.79) a single algebraic equation for the unknown p^* can be solved:

$$F(p^*, \mathbf{U_L}, \mathbf{U_R}) = 0. \tag{4.80}$$

If the solution consists of two rarefactions then the full solution structure can be determined explicitly as seen. For the two-shock case an approximate expression can be derived to give the solution explicitly. However, the above expressions do not give the solution with such ease if the solution consists of both a rarefaction and a shock wave. In this case an exact solution of the Riemann problem can be found iteratively using some initial guess for p^*. At each step the ratio of p^*/p_α is tested to see which form of f_l and f_r should be used in equations (4.78) and (4.79) to form the single equation $F(p^*, \mathbf{U_L}, \mathbf{U_R})$:

$$p^*/p_\alpha \geq 1, \qquad \text{shock}, \tag{4.81}$$
$$p^*/p_\alpha < 1, \qquad \text{rarefaction}. \tag{4.82}$$

The iterative procedure is repeated until the star pressure is calculated within a specified error bound. The value of p^* is then substituted into the formulae to obtain the other unknown variables such as star velocities and densities.

However, this iterative procedure can be very expensive which has prompted the development of an adaptive method of solution that uses different solution strategies depending on the severity of local conditions. Some of these methods that are adopted will be outlined.

4.1.11 Linearised Solver

For regions of small change it can be shown [65] that the non-conservative form of the equations can be approximated by:

$$\mathbf{W}_t + \mathbf{A}(\tilde{\mathbf{W}})\mathbf{W}_x = 0 \tag{4.83}$$

where $\tilde{\mathbf{W}}$ is an average vector written in terms of $\mathbf{W_l}, \mathbf{W_r}$ the initial right and left values of the primitive variables. Using this new formulation, the Riemann invariants give the four equations in four unknowns for this system:

$$u_l + \frac{\bar{a}\rho_l}{\bar{\rho}} = u^* + \frac{\bar{a}\rho_l^*}{\bar{\rho}}; \tag{4.84}$$

$$u_l + \frac{p_l}{\bar{a}\bar{\rho}} = u^* + \frac{p^*}{\bar{a}\bar{\rho}}; \tag{4.85}$$

$$u_l - \frac{\bar{a}\rho_r}{\bar{\rho}} = u^* + \frac{\bar{a}\rho_r^*}{\bar{\rho}}; \tag{4.86}$$

$$u_l - \frac{p_r}{\bar{a}\bar{\rho}} = u^* - \frac{p^*}{\bar{a}\bar{\rho}}. \tag{4.87}$$

The simple closed solution of this problem is

$$p^* = \frac{1}{2}\left[\bar{\rho}\bar{a}(u_l - u_r) + p_r + p_l\right]; \tag{4.88}$$

$$u^* = \frac{1}{2}\left[(u_l + u_r) + \frac{(p_l - p_r)}{\bar{\rho}\bar{a}}\right]; \tag{4.89}$$

$$\rho_l{}^* = \rho_l + \bar{\rho}\frac{(u_l - u^*)}{\bar{a}}; \tag{4.90}$$

$$\rho_r{}^* = \rho_r + \bar{\rho}\frac{(u^* - u_r)}{\bar{a}}; \tag{4.91}$$

where the average states are taken to be $\bar{\rho} = \sqrt{\rho_l \rho_r}$ and $\bar{a} = \frac{a_l + a_r}{2}$.

4.1.12 The HLLC Method

This approximate solution was first devised by Harten, Lax and Van-Leer [72]. Although the method was quite accurate for two-wave problems such as the shallow water equations or isentropic gas dynamics, the contact discontinuity present in the Euler equations was not captured well. The simple reason for this was that the approximate method was based on the assumption of a two-wave structure. The method was extended by Toro, Speares and Spruce [68] and assumes a three-wave initial wave structure.

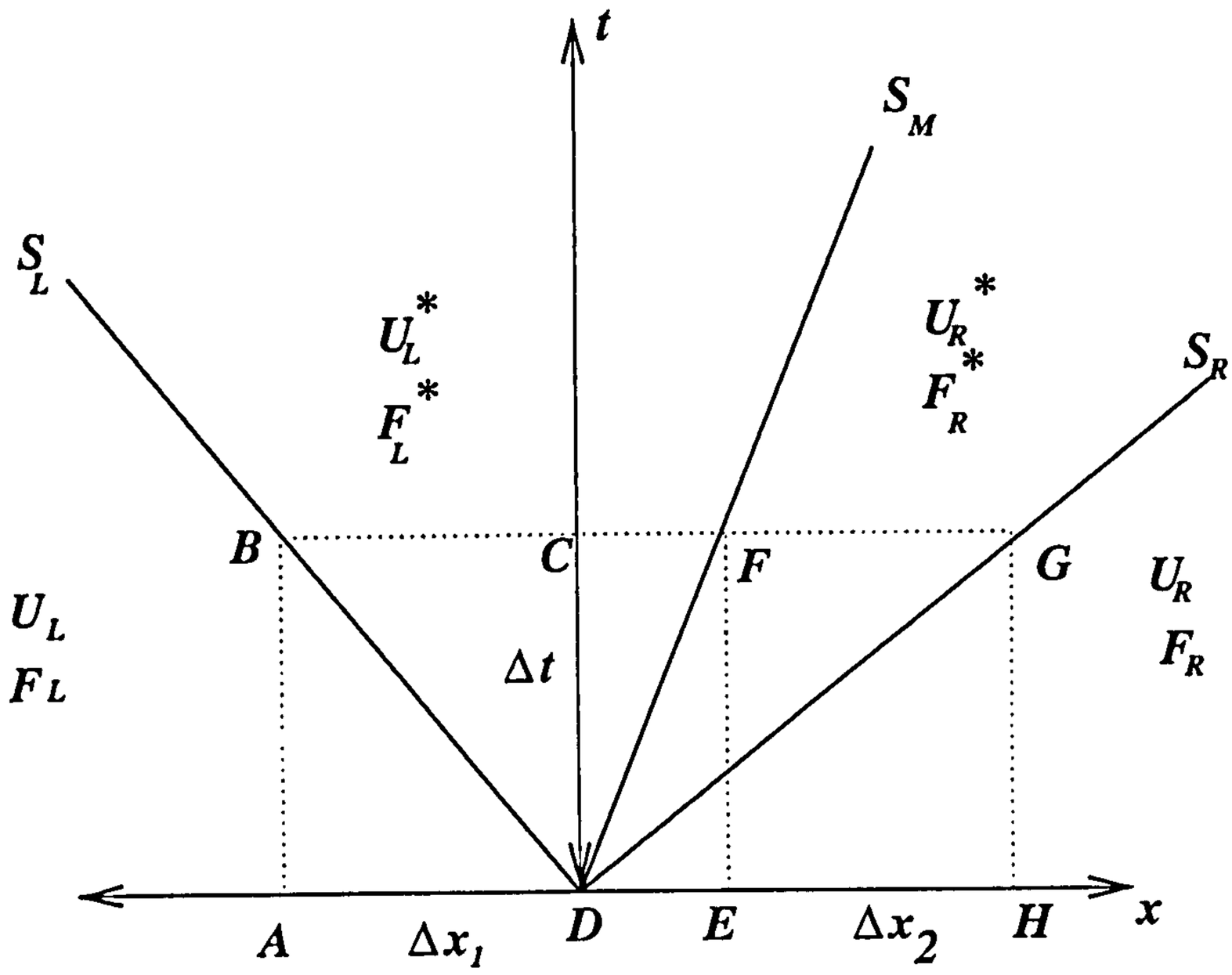

Figure 4.6: The HLLC wave structure.

The wave structure is assumed to be as in figure (4.6):

Three waves of speed S_L, S_M, S_R separate four constant regions. In this approximate solution it is not necessary to consider the fourth wave also of speed u^*. These speeds are regarded as **known** information. The integral form of the conservation law is:

$$\oint \mathbf{U}dx - \mathbf{F}dt = 0. \tag{4.92}$$

Evaluation of equation (4.92) around ABCD gives the result:

$$-\Delta x_1 \mathbf{U}_L + \Delta t \mathbf{F}_L + \Delta x_1 \mathbf{U}^*_L + \Delta t \mathbf{F}^*_L = 0, \tag{4.93}$$

but $\Delta x_1 \equiv S_L \Delta t$ and so this can be written as

$$\mathbf{F}^*{}_L = \mathbf{F}_L + S_L(\mathbf{U}^*_L - \mathbf{U}_L). \tag{4.94}$$

Integrating around EFGH similarly gives

$$\mathbf{F}^*{}_R = \mathbf{F}_R + S_R(\mathbf{U}^*_R - \mathbf{U}_R). \tag{4.95}$$

So if the vector of conserved variables in the star region $\mathbf{U}^*_l$ and $\mathbf{U}^*_r$ can be calculated, then the flux functions in the star region can be found. If equation (4.94) is rewritten in the form:

$$S_L \mathbf{U}^*_L - \mathbf{F}^*{}_L = S_L \mathbf{U}_L - \mathbf{F}_L = \mathbf{Q}, \tag{4.96}$$

where $\mathbf{Q}$ is the vector $(q_1, q_2, q_3)^T$. The value of $\mathbf{Q}$ can be calculated using the relationship of equation (4.96) that consists of known initial data. Recall that the value of the star flux flow variable u^* is identically equal to the central wave speed S_M. This is assumed to be known information so that substitution into the right-hand-side of equation (4.96) gives:

$$S_L \rho^*_l - S_M \rho^*_l = q_1; \tag{4.97}$$

$$S_L \rho^*_l S_M - \rho^*_l S^2_M - p^* = q_2; \tag{4.98}$$

$$S_L E^*_l - S_M(E^*_l + p^*) = q_3. \tag{4.99}$$

This is a system of three equations with three unknowns which can be solved to give:

$$\rho^*_l = q_1/(S_L - S_M) \tag{4.100}$$

$$p^* = S_M q_1 - q_2 \tag{4.101}$$

$$E^*_l = \frac{q_3 p^* + S_M}{S_L - S_M} \tag{4.102}$$

From these expressions the value of $\mathbf{U}_L^*$ can be found. Similarly $\mathbf{U}_R^*$ can be calculated in an identical manner. Substitution into equations (4.94) and (4.95) give the star fluxes that are needed to formulate the WAF method.

4.1.13 Wave-Speed Estimates

The above integral produces an average solution of the problem in terms of the wave-speeds. However, since these are not known, the approximate nature of the method is due to the necessity to estimate wave-speeds. This is where the algebraic expressions that describe the solution of rarefactions and shocks can serve to aid these approximations.

Hybrid wave-speed estimates are used which use approximations for the pressure p^* and velocity u^* to substitute into the exact formulations of the wavespeeds. The exact relations for the wavespeeds are:

$$S_L = u_l - q_l a_l; \quad S_M = u^*; \quad S_R = u_r + q_r a_r; \tag{4.103}$$

$$q_\alpha = \begin{cases} 1 & \frac{p^*}{p_\alpha} < 1 : rarefaction, \\ \sqrt{1 + \frac{\gamma+1}{2\gamma}\left(\frac{p^*}{p_\alpha}\right)} & \frac{p^*}{p_\alpha} > 1 : shock. \end{cases} \tag{4.104}$$

where α is left or right. These solutions are identical to those given in equations (4.60), (4.62), (4.70) and (4.69) where all that is required to calculate the wavespeeds are values for p^* and u^*. The value of p^* and the central wave u^* are selected adaptively depending on the local flow conditions. In regions of small change the linearized estimates given in equations (4.88) and (4.89) are used. This is tested, as a-priori, by calculating the pressure estimate p^* given in equation (4.88). Let,

$$p_{min} = min(p_l, p_r), \quad p_{max} = max(p_l, p_r). \tag{4.105}$$

The linear estimates are used if

$$p_{min} < p^* < p_{max} \quad . \tag{4.106}$$

(4.107)

However, if the initial guess for p^* that is obtained from the linear estimates is greater than the left and right pressures p_l and p_r, then a two-shock approximation is adopted for p^*, using equation (4.73), and u^*, given from equation (4.74). Alternatively, if the initial estimate for p^* is less than both p_l and p_r, then the two-rarefaction approximation is used for the pressure given in equation (4.57) and the velocity is calculated from equation (4.58). This adaptive

method of solution reflects the likelihood of any specific wave pattern emerging using information gleaned from the initial conditions.

To sum up, the method of solution of the Riemann problem: The approximate HLLC method is used throughout the solution procedure. The wave-speed estimates that are required in the HLLC method are the exact formulations but require approximations for the star pressure and velocity. These are selected adaptively so that either a linearised solver is used as described in section (4.1.11), two shock, from section (4.1.9), or two rarefaction, from section (4.1.6), approximations depending on the local flow conditions.

The solution to the Riemann problem will be used in the construction of intercell fluxes in the finite volume methods that are outlined below.

4.1.14 Godunov Type Methods

The solution of the Riemann problem reveals valuable information about characteristic information within the framework of a conservative method. Godunov first devised the idea in 1959 [62] to exploit the Riemann problem, which is an exact solution of a conservative law with simple initial conditions, to provide a general class of conservative methods to solve any system of conservative equations with general initial conditions. The construction of these ideas is outlined below where further detail about the method is given in [73].

Consider the conservation equations with general initial conditions at time t_n given as $\mathbf{U}(x, t_n)$. The domain L is divided into m cells of length Δx. Boundary conditions are given at each extreme of the domain $x = 0$ and $x = L$.

The Godunov method constructs the numerical solution at time t_n in cell i, denoted as $\mathbf{U}'^n_i$, by assuming a piecewise constant distribution of the initial data $\mathbf{U}(x, t_n)$, that is:

$$\mathbf{U}'^n_i \equiv \frac{1}{\Delta x} \int_{x_{i-\frac{1}{2}}}^{x_{i+\frac{1}{2}}} \mathbf{U}(x, t_n) dx. \tag{4.108}$$

This is illustrated in figure (4.7) which indicates how the numerical solution at time t_n is an *approximation* to the initial conditions at t_n.

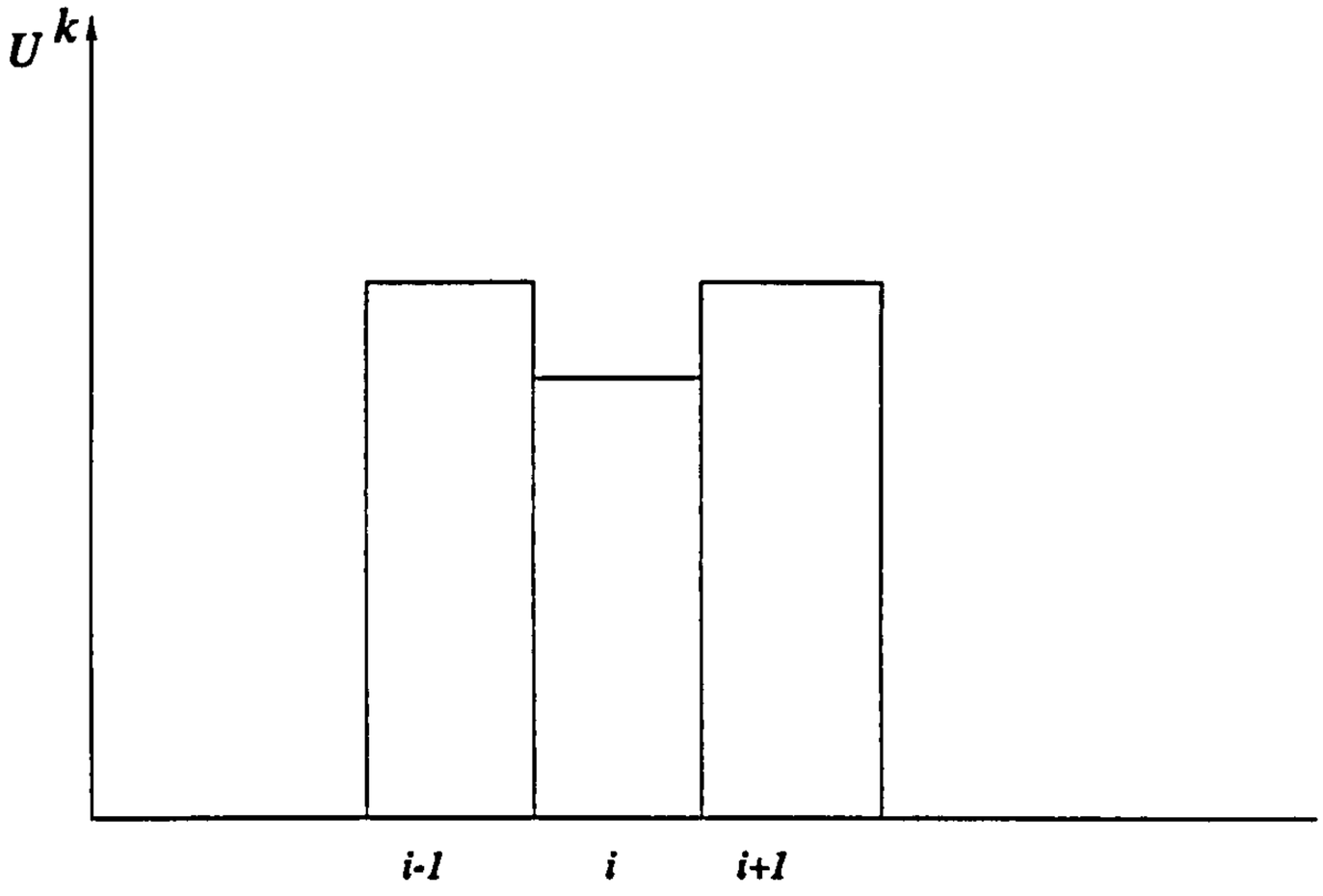

Figure 4.7: The piecewise constant numerical data.

The method proceeds to define a piecewise constant function which is identically equal to the numerical solution at $x = x_i$ and $t = t_n$, that is

$$\tilde{\mathbf{U}}(x_i, t_n) \equiv \mathbf{U}_i'^n; \qquad x_{i-1/2} \leq x \leq x_{i+1/2}. \tag{4.109}$$

Since $\tilde{\mathbf{U}}(x, t_n)$ is piecewise constant, this function and the conservation law

$$\mathbf{U}_t + [\mathbf{F}(\mathbf{U})]_x = 0$$

can define a series of $m + 1$ Riemann problems where each Riemann problem with left and right data, $\tilde{\mathbf{U}}(x_i, t_n)$ and $\tilde{\mathbf{U}}(x_{i+1}, t_n)$ respectively, centred around the intercell boundary $i + 1/2$ is denoted as $RP(i, i + 1)$ for $i = 0, m$. The idea is to solve each Riemann problem $RP(i, i + 1)$ individually.

Consider how the solution at time $t^n + \Delta t$, where Δt is the timestep that has not yet been defined, is constructed. By solving the sequence of Riemann problems over the whole domain, the exact solution in the interval $t_n \leq t \leq t_{n+1}$, $\tilde{\mathbf{U}}(x, t)$ can be found. The approximate numerical solution at the new time t_{n+1} can then be given by averaging the exact solution:

$$\mathbf{U}_i'^{n+1} = \frac{1}{\Delta x} \int_{x_{i-1/2}}^{x_{i+1/2}} \tilde{\mathbf{U}}(x_i, t_{n+1}) dx. \tag{4.110}$$

The process is then repeated using this function as new piecewise constant initial data. Consider how this process is used to mathematically construct intercell fluxes to provide an algorithm for the updating procedure.

Since the function $\tilde{\mathbf{U}}(x_i, t)$ is an exact solution of the Riemann problem over the interval $(i - 1/2 \geq x \geq i + 1/2, t_n \geq t \geq t_{n+1})$ then this must satisfy the conservation law:

$$\begin{aligned}\int_{x_{i-1/2}}^{x_{i+1/2}} \tilde{\mathbf{U}}(x, t_{n+1})dx &= \int_{x_{i-1/2}}^{x_{i+1/2}} \tilde{\mathbf{U}}(x, t_n)dx + \int_{t_n}^{t_{n+1}} \mathbf{F}(\tilde{\mathbf{U}}(x_{i-1/2}, t))dt \\ &- \int_{t^n}^{t_{n+1}} \mathbf{F}(\tilde{\mathbf{U}}(x_{i+1/2}, t))dt. \end{aligned} \tag{4.111}$$

By substituting expressions (4.109) and (4.110) into equation (4.111) the approximate conservative algorithm for this process is given:

$$\mathbf{U}'^{n+1}_i = \mathbf{U}'^n_i - \frac{\Delta x}{\Delta t}\left[\mathbf{F}'_{i+1/2} - \mathbf{F}'_{i-1/2}\right] \tag{4.112}$$

where

$$\mathbf{F}'_{i+1/2} \approx \frac{1}{\Delta t}\int_{t_n}^{t_{n+1}} \mathbf{F}(\tilde{\mathbf{U}}(x_{i+1/2}, t))dt \tag{4.113}$$

The exact solution along any intercell boundary $i + 1/2$ is identically equal to the solution to the Riemann problem between adjacent cells i and $i + 1$. From equation (4.80), at time t^n, this is a function of the two initial states $\mathbf{U}'^n_i$ and $\mathbf{U}'^n_{i+1}$ only, that is

$$\tilde{\mathbf{U}}(x_{i+1/2}, t) \equiv \mathbf{U}'^*_{i+1/2}(\mathbf{U}'^n_i, \mathbf{U}'^n_{i+1}), \tag{4.114}$$

where $\mathbf{U}'^*_{i+1/2}$ is the solution of the Riemann problem along the boundary $i + 1/2$ as depicted in figure (4.8).

Conservative schemes differ in the way in which the flux function, given in equation (4.113) is specified. However, due to the simple structure of the Riemann solution prior to wave interaction, the function $\mathbf{F}(\tilde{\mathbf{U}}(x_{i+1/2}, t))$ at this intercell boundary is seen from figure (4.8) to be constant over time and from equation (4.114) a function of the initial constant left and right data. This constant integration in equation (4.113) gives the result:

$$\mathbf{F}'_{i+1/2} = \mathbf{F}(\mathbf{U}'^*_{i+1/2}(\mathbf{U}'^n_i, \mathbf{U}'^n_{i+1})) \tag{4.115}$$

This means that Godunov's method can be given as:

$$\mathbf{U}'^{n+1}_i = \mathbf{U}'^n_i - \frac{\Delta t}{\Delta x}\left[\mathbf{F}'(\mathbf{U}'^*_{i+1/2}(\mathbf{U}'^n_i, \mathbf{U}'^n_{i+1})) - \mathbf{F}'(\mathbf{U}'^*_{i-1/2}(\mathbf{U}'^n_{i-1}, \mathbf{U}'^n_i))\right] \tag{4.116}$$

Godunov's method is first-order accurate where the approximate nature of the method is in the construction of piecewise constant data from what is actually a smooth solution.

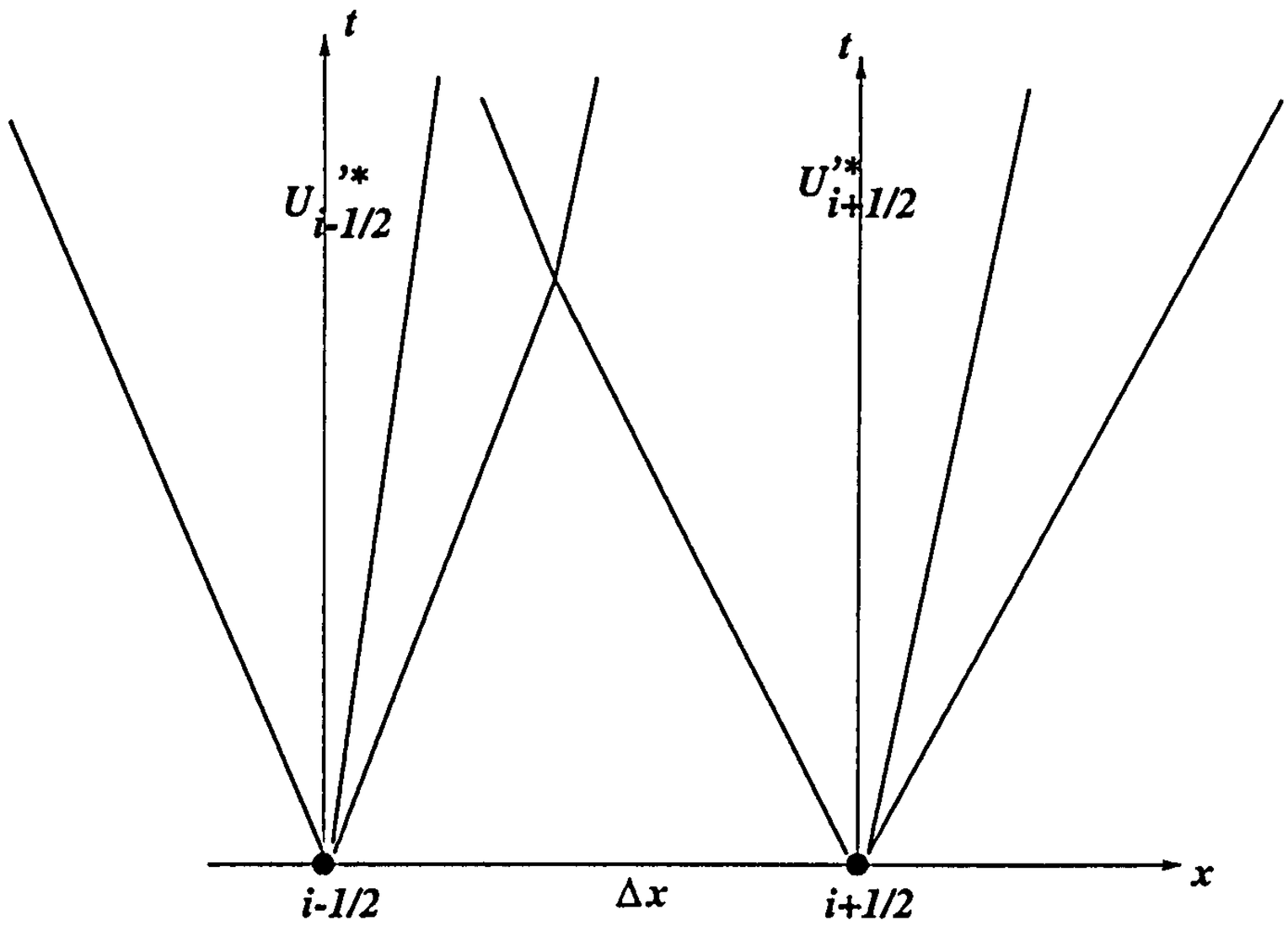

Figure 4.8: Solution to the Riemann problems $RP(i-1,i)$ and $RP(i,i+1)$.

However, to preserve the simple solution structure indicated in figure (4.8) so that, for example, the star state remains constant over the time interval, t must not be too large for the waves arising from neighboring Riemann problems to modify this structure. To ensure this does not occur, $\Delta t = t_{n+1} - t_n$ must be sufficiently small.

It can be shown that the wavespeeds are bounded by the eigenvalues, [74]. Since the neighboring Riemann problems are Δx away, the condition on t is:

$$\left|\frac{\Delta t}{\Delta x}\lambda^{(k)}\right| < 1, \tag{4.117}$$

for all k where $\lambda^{(k)}$ are the eigenvalues of the system.

Condition (4.117) actually allows interaction between Riemann problems provided that these are contained within a mesh cell. Figure (4.8) illustrates how the exact solution at later times $\tilde{\mathbf{U}}(x,t)$ would be very difficult to calculate after wave interaction. However, Godunov's method does not calculate the exact solution but the cell average. The method relies only on the fact that the star state solution along the intercell boundary remains constant during the time interval.

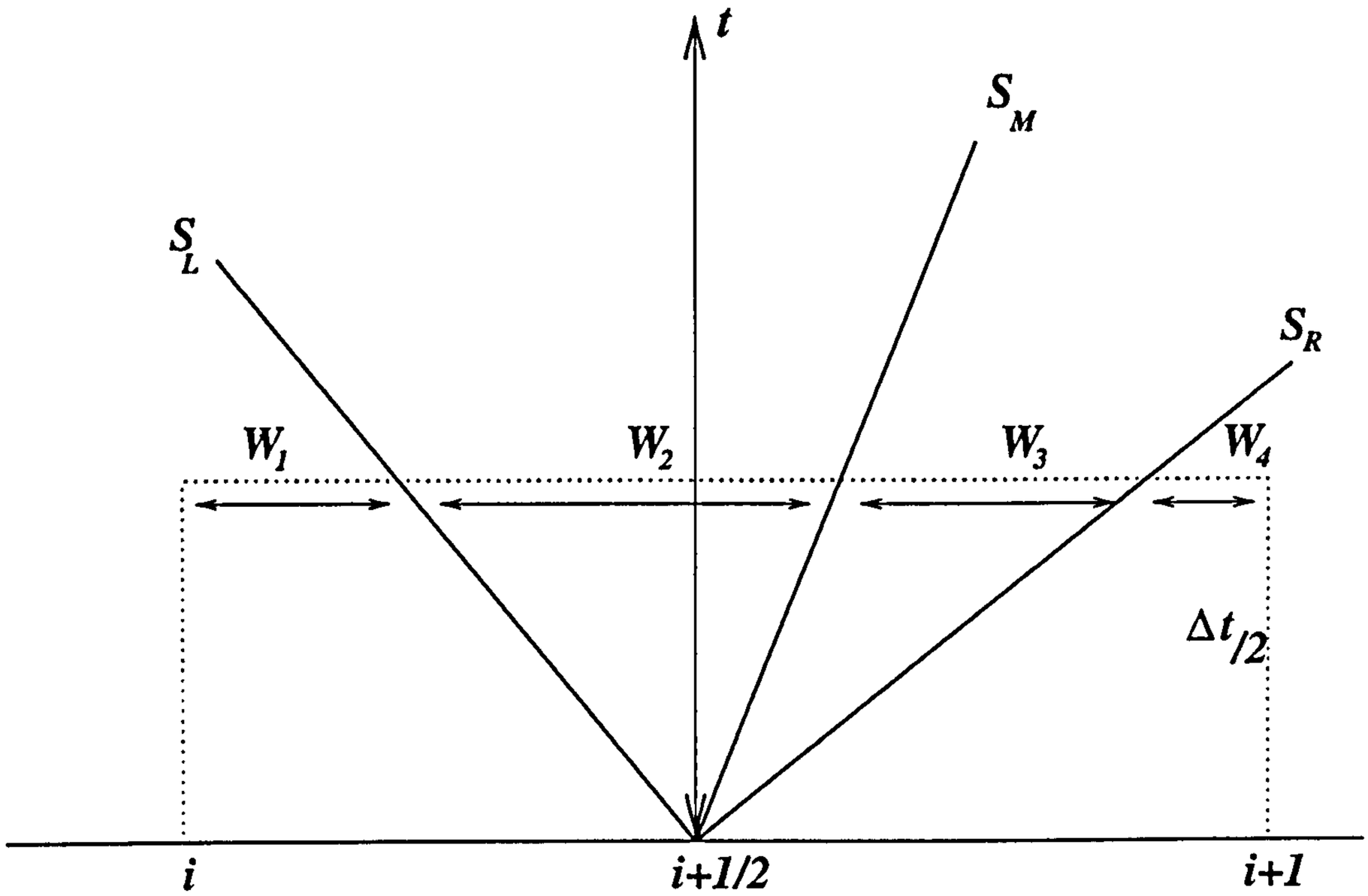

Figure 4.9: The formulation of the WAF method.

4.1.15 The WAF method

The Godunov method utilises the solution of the Riemann problem between cells $(i, i+1)$ only along the intercell boundaries $i+1/2$. This produces a first order solution which badly smears discontinuous waves. The weighted average flux method (WAF), is a high resolution method that was created by Toro [64]. This takes an integral in space over the solution to the Riemann problem at time $t_n + \frac{\Delta t}{2}$ to produce an average flux as depicted in figure (4.9).

As opposed to equation (4.113), the flux is defined as:

$$\mathbf{F}(\mathbf{U}_j^n, \mathbf{U}_{j+1}^n) = \frac{1}{\Delta x} \int_{x_{i-1/2}}^{x_{i+1/2}} \mathbf{F}(\tilde{\mathbf{U}}^n(x, \frac{\Delta t}{2}))dx \tag{4.118}$$

By doing this the accuracy of WAF is extended to second-order accuracy by using more of the information contained in the solution to the Riemann problem.

For the Riemann problem with N wave speeds $S^{(k)}$ and $N+1$ constant states, then the integral in space is trivial and the total flux can be represented as a weighted average of the flux in each constant region:

$$\mathbf{F}(\mathbf{U}_j^n, \mathbf{U}_{j+1}^n) = \sum_{k=1}^{N+1} W_k \mathbf{F}^k(\mathbf{U}^*(\mathbf{U}_j^n, \mathbf{U}_{j+1}^n)). \tag{4.119}$$

This is illustrated in figure (4.9) where the weights W_k are the geometric extents of the constant states in the integral. Define the Courant number as:

$$\nu_k = \frac{S^{(k)}}{(\Delta x/\Delta t)}, \tag{4.120}$$

the ratio of the wave speed over the speed associated with the mesh dimensions.

Simple geometry shows that the weights are given in terms of the Courant numbers:

$$W_k = \frac{1}{2}(\nu_k - \nu_{k-1}), \quad \nu_0 = -1, \quad \nu_{n+1} = 1, \tag{4.121}$$

for $k = 1, n+1$.

4.1.16 Oscillations & TVD Regions

In 1959 Godunov proved that a second-order method would create spurious oscillations behind discontinuities [62]. The WAF method removes these oscillations by constructing total variation diminishing (TVD) constraints on the solution- which effectively reverts the solution to first order accuracy near discontinuities. The TVD region achieves this by modifying the upwind and downwind contribution to the intercell flux. Consider the Riemann problem between cells $(i, i+1)$; the weights W_k control the flux contributions between each wave k of the solution. These are explicit functions of the Courant numbers ν_k associated with each wave. The distribution can be altered by replacing the Courant numbers with 'modified' Courant numbers ν_k':

$$W_k = \frac{1}{2}(\nu_k' - \nu_{k-1}'). \tag{4.122}$$

Since generally ν_k' are greater than ν_k, ν_k' is called the amplified Courant number. The effect of this is to increase the upwind contribution and decrease the downwind contribution in the flux formulation. The amplified Courant numbers are a function of the original Courant numbers and a parameter $r_{i+1/2}$.

This parameter measures the ratio between the change in the flow-field upwind compared with local change in flow variables: The parameter $r_{i+1/2}$ is given as

$$r_{i+1/2} = \frac{(\Delta q)_{upw}}{(\Delta q)_{loc}}, \tag{4.123}$$

where the local change $\Delta q_{loc} = q_{i+1} - q_i$ and the upwind change depends on the sign of the wave speed:

$$(\Delta q)_{upw} = \begin{cases} (\Delta q)_{i-1/2} = q_i - q_{i-1}; & \lambda^{(k)} > 0, \\ (\Delta q)_{i+3/2} = q_{i+2} - q_{i+1}; & \lambda^{(k)} < 0. \end{cases} \tag{4.124}$$

Then the amplified Courant numbers are

$$\nu'_k = A_k \nu_k, \tag{4.125}$$

where

$$A_k = A(\nu_k, r_{i+1/2}). \tag{4.126}$$

For some simple scalar equations a rigorous derivation of the TVD region can be carried out. However, for systems of non-linear equations the TVD region is *empirical* but nevertheless performs very well and has been extensively used. The function in equation (4.126) can be defined in a number of different ways. The two amplifiers that are given as options here are the Minbee amplifier and Van-Leer's amplifier. Van-Leer's captures discontinuities more sharply but the Minbee produces better resolution of smooth waves. The Courant number amplifiers are given by:

$$A_k = \frac{1 - (1 - |\nu_k|)B_k}{|\nu_k|}, \tag{4.127}$$

where the constant B_k is a standard flux limiter function.

Minbee

$$B = \begin{cases} 0 & r_{i+1/2} < 0; \\ r_{i+1/2} & 0 < r_{i+1/2} < 1; \\ 1 & r_{i+1/2} > 1 \end{cases} \tag{4.128}$$

Van-Leer

$$B = \begin{cases} 0 & r_{i+1/2} < 0; \\ \frac{2r_{i+1/2}}{1+r_{i+1/2}} & r_{i+1/2} > 0 \end{cases} \tag{4.129}$$

4.1.17 Boundary Conditions

The inviscid Euler equations have only one physical boundary condition at fixed walls. This states that the velocity normal to the wall must be zero. For the one dimensional problem this implies that at the fixed boundaries of the domain $x = 0$ and $x = l$:

$$u(0,t) = 0; \qquad u(l,t) = 0. \tag{4.130}$$

However, the solution structure of the Euler equations also provides sets of numerical boundary conditions that must be implemented into the solution methodology to provide a correct solution. For Riemann-type methods this involves solving a Riemann problem across the fixed boundary $x = 0$ where the left-side, that is outside the domain, has imposed initial data:

$$u_L = -u_0|_{0+}; \qquad u_R = u_0|_{0+}; \tag{4.131}$$
$$p_L = p_0|_{0+}; \qquad p_R = p_0|_{0+}; \tag{4.132}$$
$$\rho_L = \rho_0|_{0+}; \qquad \rho_R = \rho_0|_{0+}; \tag{4.133}$$
$$c_L = c_0|_{0+}; \qquad c_R = c_0|_{0+}, \tag{4.134}$$

where $0+$ denotes known initial data inside the domain adjacent to the fixed wall at $x = 0$. Similarly at $x = l$ information is required for the right-hand state:

$$u_L = u_0|_{l-}; \qquad u_R = -u_0|_{l-}; \tag{4.135}$$
$$p_L = p_0|_{l-}; \qquad p_R = p_0|_{l-}; \tag{4.136}$$
$$\rho_L = \rho_0|_{l-}; \qquad \rho_R = \rho_0|_{l-}; \tag{4.137}$$
$$c_L = c_0|_{l-}; \qquad c_R = c_0|_{l-}, \tag{4.138}$$

where $l-$ denotes known initial data inside the domain adjacent to the fixed wall at $x = l$. This means that Riemann problems are solved with equal left and right data for the pressure, density and mass-fraction and $u_L = -u_R$ for the velocity. These choices are based on the simple structure of the solution to the Riemann problem. By using this set of initial data for any fluid velocity, at the cell centres of the cells adjacent to the boundaries, the solution to the Riemann problem will give zero velocity along the boundaries which will satisfy the physical boundary conditions. A more general description of the derivation of boundary conditions can be found in [75].

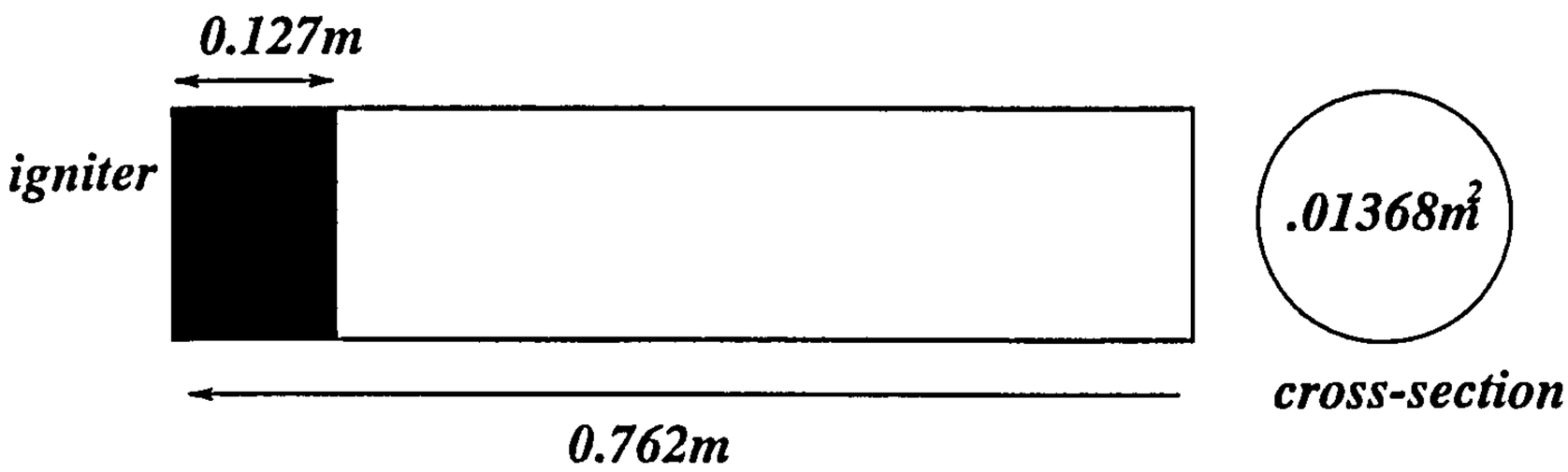

Figure 4.10: A test model.

4.1.18 Summary

The WAF finite-volume scheme will be used to solve the governing equations. This requires the solution to the Riemann problems between adjacent cells. The structure of the Riemann problem for this set of equations has been outlined above. The HLLC method will be used to give an approximate solution to the Riemann problem. This numerical method should produce an accurate solution to the homogeneous hyperbolic problem over some time interval.

4.2 System of Stiff O.D.E.'s

As described in the previous chapter, a stiff ordinary-differential- equation package, written by Hindmarsh [56], is used to solve the second part of the operator split. The solution from the homogeneous hyperbolic problem is used as initial conditions for the ordinary differential equation. The final solution that is produced by solving this initial value problem is the full solution of the complete set of equations

4.3 A Test Problem

A very simple test problem will be considered as described in [76]. This configuration is frequently used to compare interior ballistics CFD codes.

Figure (4.10) shows a cylindrical combustion chamber which is $0.762m$ long

and has a uniform cross-sectional area of $0.01368m^2$. A projectile is placed at one end of the chamber which, in a ballistic simulation, can move. However, not to further complicate the problem, a very high resistance pressure is placed here that prevents movement of the projectile so that the chamber volume is fixed. The opposite end of the chamber is called the breech. The initial gas in the chamber is at ambient conditions. In a typical two-phase simulation the vessel will be full of propellant particles which will start to burn. However, since this model does not include a solid phase, reactant gas (produced by gasification of propellant) is fed into the chamber via a tube that runs down the axial length. Gasification is initiated once the local temperature in the chamber rises above the solid decomposition temperature T_d and a typical value of $444K$ is assumed. The temperature in the chamber raises from ambient to the decomposition temperature due to a constant supply of inert igniter gas also fed through the tube. Whilst reactant gas can be fed along the entire length of the chamber, the igniter gas is only vented along a sixth of the axial length, $0.127m$, starting at the breech. The reactant gas has the capacity to release large quantities of chemical energy but the igniter gas is assumed to be inert. This means that the igniter does not have any chemistry associated with it and only introduces thermal and kinetic energy into the chamber. The rate of addition of reactant gas $\dot{m}$ and the rate of addition of igniter gas $\dot{m}_{ig}$ can be seen in the table (4.1). Initially there would appear to be a large disparity between the two which may seem to be unrealistic since it is the propellant that eventually drives the entire combustion process. In present ignition models once the temperature rises to decomposition, gasification proceeds using the law $\dot{m} \propto p^n$. This produces a discontinuous jump in $\dot{m}$ which is highly unlikely- it is more plausible to expect that once the local gas temperature approaches the decomposition temperature, the gasification $\dot{m}$ will increase slowly from zero. In this case only very small quantities of reactant mass will be introduced into the chamber, so initially a relatively low value of $\dot{m}$ is realistic.

There are no heat losses from the chamber walls and gravity is neglected. All sources of mass are assumed to be constantly distributed over the cross-sectional area so that the problem is one-dimensional. Other necessary parameters are given in table (4.1).

T_0 and p_0 are the ambient temperature and pressure; γ is the ratio of specific heats; R is the universal gas constant; W is the molecular weight of the gas; b is the covolume; Q is the heat of formation; L is the latent heat; $\dot{m}$ is the rate of addition of reactant gas; $\dot{m}_{ig}$ is the rate of addition of igniter gas, A_g is the frequency of collision and *ncell* are the number of cells in the domain.

T_0	$298K$	p_0	$101400Pa$
γ	1.2627	R	$8313.3\frac{T}{Kkgmole}$
W	21.13	b	$0.0010838\frac{m}{kg}$
Q	$3736300\frac{Joules}{kg}$	L	$100000\frac{Joules}{kg}$
$\dot{m}$	$0.8\frac{kg}{msec}$	$\dot{m}_{ig}$	$180\frac{kg}{msec}$
A_g	$10^4\frac{1}{Pasec}$	$ncell$	500

Table 4.1: A model one-dimensional problem.

The most influential chemical parameter, as found in the parametric analysis in the previous chapter, is the activation energy. To illustrate the effect of chemistry on the combustion cycle, two widely different values of the activation energy will be chosen. Firstly a 'low' value for $E_A/\mathcal{R}$ equal to $5000K$, followed by a higher value of $15000K$. Flow variable histories are shown that were produced using the numerical methods described above. These were performed on a very fine five hundred cell mesh. Solutions for the low activation energy will be considered and compared with the high activation energy solutions.

4.3.1 Flow Variable Histories for $E_A/\mathcal{R} = 5000K$

The figures (4.11) to (4.16) illustrate the pressure, gas velocity, temperature, mass-fraction and reaction rate, respectively, over the whole combustion chamber over the first $4ms$. Figures (4.17), (4.18), (4.19) show profiles of flow variables at times $0.75ms$, $1ms$, $1.5ms$ and figures (4.20), (4.21), (4.22) show profiles at $4ms$.

The venting of igniter gas over the first sixth $0 \leq x \leq 0.127m$ of the chamber length causes a rapid increase in the pressure, density and temperature in this region illustrated in figures (4.17) and (4.18). A compression wave forms at the end of the igniter length which travels towards rthe projectile base shown in the pressure history in figure (4.11). The fine mesh produces very good resolution of this shock wave illustrated in the full flow histories and in the pressure profile in figure (4.17). At $0.75ms$ the shock has traveled to $0.525m$. and the expansion fan is also seen in the region of the igniter. Temperatures between $0 \leq x \leq 0.127m$ quickly rise above the decomposition temperature $444K$, seen in figure (4.17), which causes high velocity gradients due to the passage of gas into colder regions towards the projectile base demonstrated in figure (4.18). Once the local temperature rises above the decomposition temperature, reactant gas is fed into the chamber due to gasification of the

propellant. The introduction of reactant gas can be clearly seen in the early time mass-fraction profile in figure (4.19) and in the history in figure (4.15). There is a straight line feature in the mass-fraction history that lags behind the shock wave extending between $(0.02m, 0.2ms)$ to $(0.64m, 1.5ms)$. By consulting the mass-fraction profile the plot displays non-zero mass-fraction between $0.127m \leq x \leq 0.26m$ at time $0.75ms$. Since the temperature over this interval, away from the igniter region, is lower than the decomposition temperature, why does mass-fraction appear in these regions since it cannot be produced locally? By comparing the speed of the shock wave and this feature, it can be easily seen that this is a path of particle paths as in [77]; the reactant is being convected from the hot region into the cold region by the high velocity gas. The change $[u]$ in the flow velocity across a shock of Mach number M_0 is given by [78]

$$\frac{[u]}{a_0} = \frac{2}{\gamma + 1}(M_0 - M_0^{-1}) \tag{4.139}$$

where a_0 is the sound speed ahead of the wave. When the flow speed ahead of the shock is zero, as it is in the case of the primary shock shown in figures (4.11) and (4.13), $[u]$ is actually *equal* to the flow speed behind the shock.

Figure (4.11) shows that the pressure ratio across the primary shock at $0.762m$ is about 4.55. Since the connection between pressure ratio and Mach number for a normal shock is

$$\frac{p}{p_0} = \frac{2\gamma}{\gamma + 1}(M_0^2 - 1), \tag{4.140}$$

it follows that, with the value for γ of 1.2627, the primary shock in figure (4.11) has a Mach number $M_0 \simeq 2.04$. From the formula for $[u]$ we see that, as a consequence, $[u]/a_0 \simeq 1.37$.

The time for the primary shock to travel $0.762m$ is determined from figure (4.11) to be about $1.03ms$. The time for the 'reactant-wave' to travel the same distance is determined from figure (4.15) to be roughly $1.48ms$, i.e. about 1.42 times longer than it takes the primary shock to travel the same distance. The ratio of M_0 to $[u]/a_0$ is equal to $2.04/1.37 \simeq 1.49$, which is close enough in the circumstances to 1.42 for us to conclude that the 'reactant-wave' is indeed following a particle path.

Since reactant mass-fraction rises sharply across this feature it will be called a 'reactant wave'. The gradual build up of reactant gas indicates that the

temperatures are still too low to provoke any large consumption of reactant gases and temperature increases at this stage are mainly due to the adiabatic addition of gas. This can be seen from the rate of reaction plot in figure (4.16) which remains low over the first $1.05ms$ although marginally higher in the hotter igniter region seen in figure (4.19). Now consider what happens at a later time $\approx 1.25ms$. The primary shock travels down the chamber and strikes the fixed projectile base at approximately $1ms$. The shock reflects producing a large jump in temperature displayed in figure (4.17) behind it to above $444K$. This switches on gasification behind the shock explaining the sudden growth of mass-fraction in figure (4.19) and density in figure (4.18). The shock causes rapid deceleration of gas velocity. At $(0.64m, 1.5ms)$ the reflected shock intersects with the reactant wave that is travelling towards the projectile base. The combination of high concentration of reactant mass and high temperature switches on the exothermic reaction (which is controlled by the rate $-\rho\Omega c^2$ where $\Omega = A_g p \exp(-E_A/\mathcal{R}T)$. The reaction causes further increase in temperature and the consumption of mass-fraction is indicated by the low values of mass-fraction that can be seen at this point. If the definition of ignition is taken, from the previous chapter, as being a point of temperature increase along with the initiation of a runaway very exothermic reaction, then this point of intersection can be seen as the precise time and location of ignition. Since it is the igniter configuration that determines the flow field in the above example and the chemical rate parameters that describe the relationship between temperature and release of chemical energy, these are two of the major factors that influence the location of ignition (this will be further illustrated in the following example with $E_A/\mathcal{R} = 15000K$). The reflected shock bends as it travels towards the breech indicating that the shock is accelerating due to the addition of mass and release of chemical energy. Any reactant mass in its path is consumed figures as illustrated in figure (4.15) which continues to feed the shock wave. Once the shock reflects off the breech the mass-fraction remains low.

By using the spatially independent analysis of chapter one, it can be seen that equilibrium conditions are approached once:

$$\rho\Omega c^2 \rightarrow \frac{\dot{m}}{2} = 29.2kg/m^3sec. \tag{4.141}$$

The reaction rate plot at $4ms$ displays reaction rates much higher than this implying that equilibrium conditions have not been attained. In fact the plot shows a sharp peak at $x = 0.4m$ corresponding to conditions of high reactant concentration and temperature. This is precisely the position of the shock front which is again travelling towards the base as illustrated in figure (4.20). The continued effect of the igniter gas is still apparent.

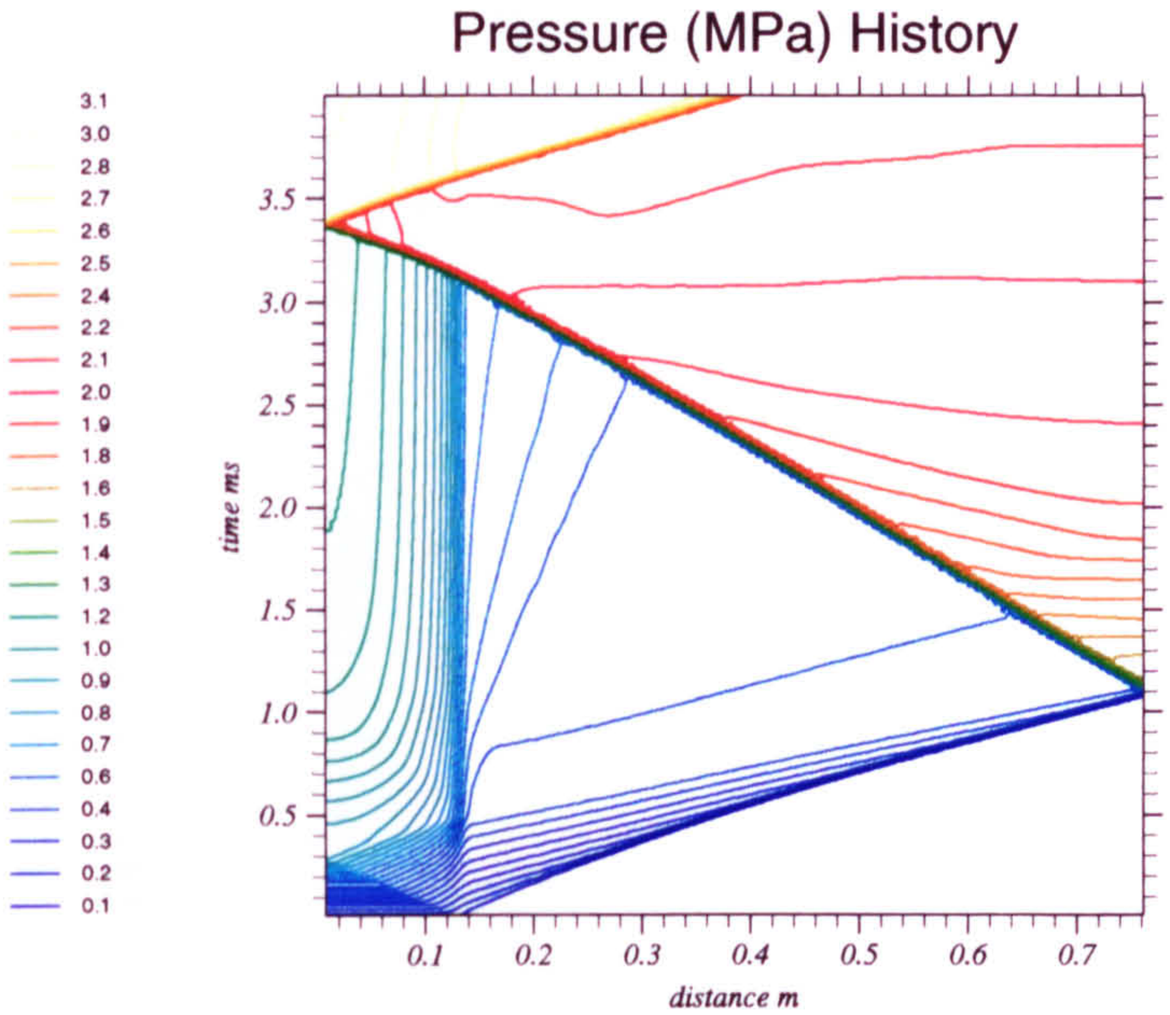

Figure 4.11: Pressure history for $E_A/\mathcal{R} = 5000K$ over the first $4ms$.

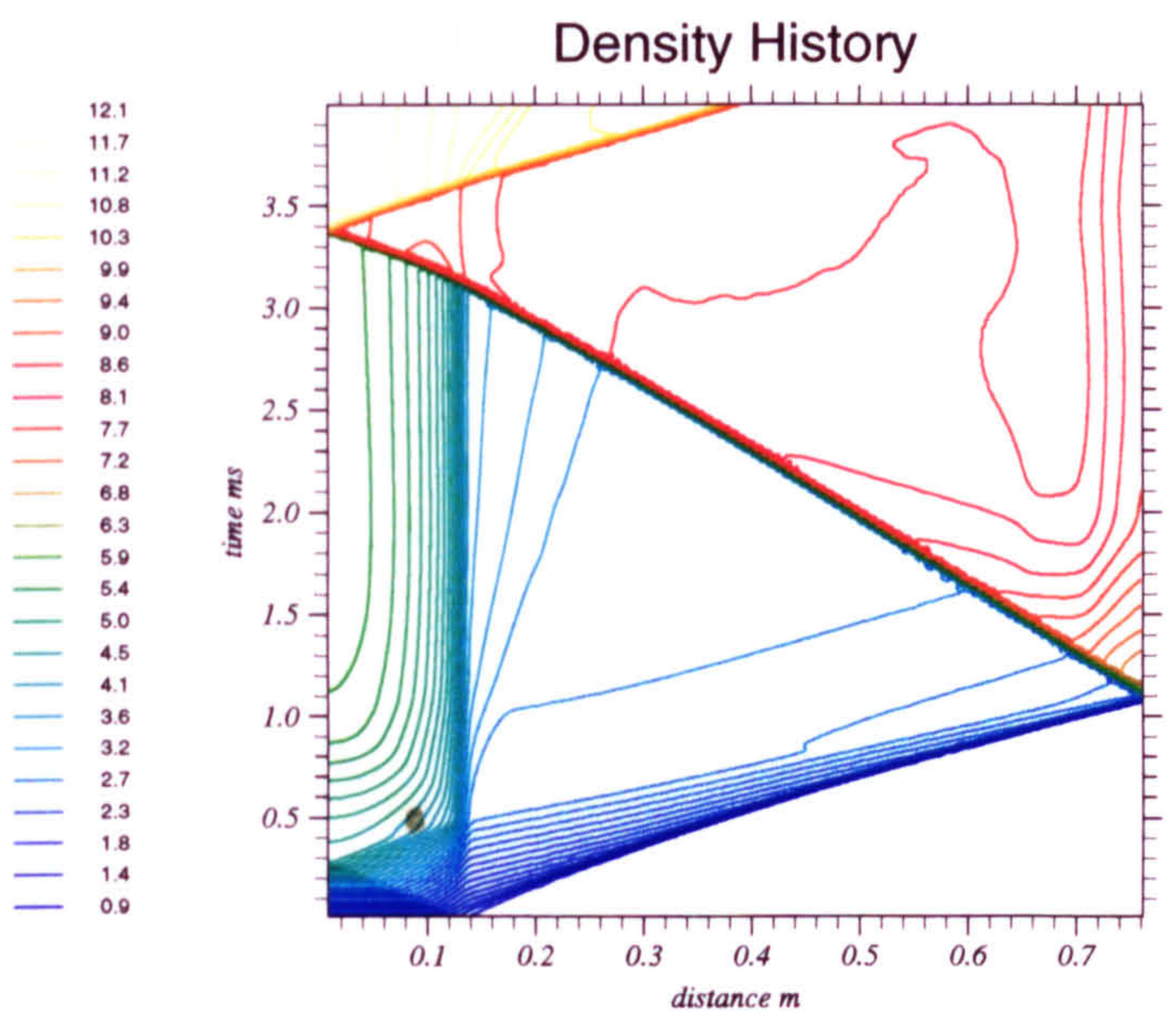

Figure 4.12: Density history for $E_A/\mathcal{R} = 5000K$ over the first $4ms$.

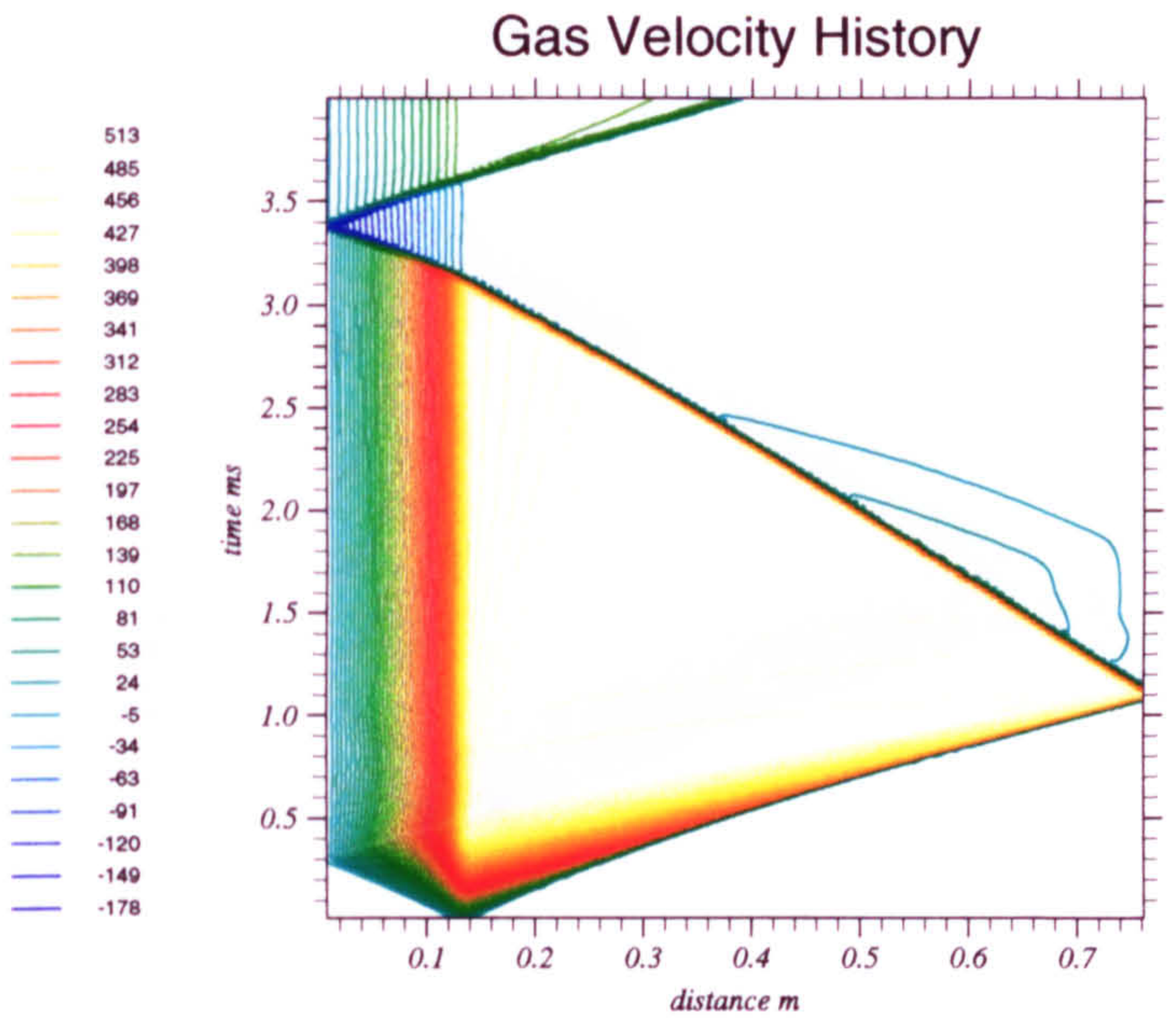

Figure 4.13: Gas velocity history for $E_A/\mathcal{R} = 5000K$ over the first $4ms$.

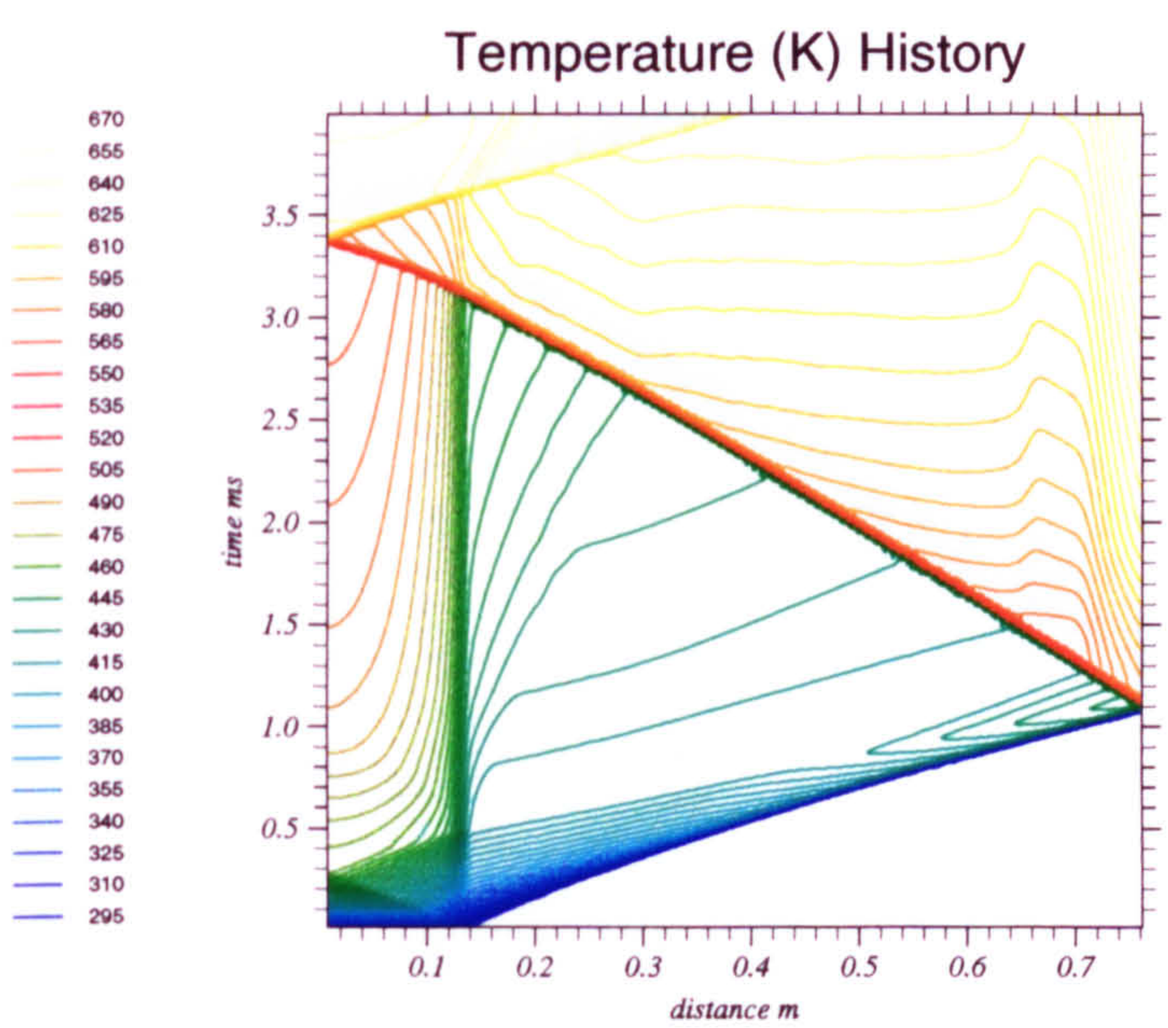

Figure 4.14: Temperature history for $E_A/\mathcal{R} = 5000K$ over the first $4ms$.

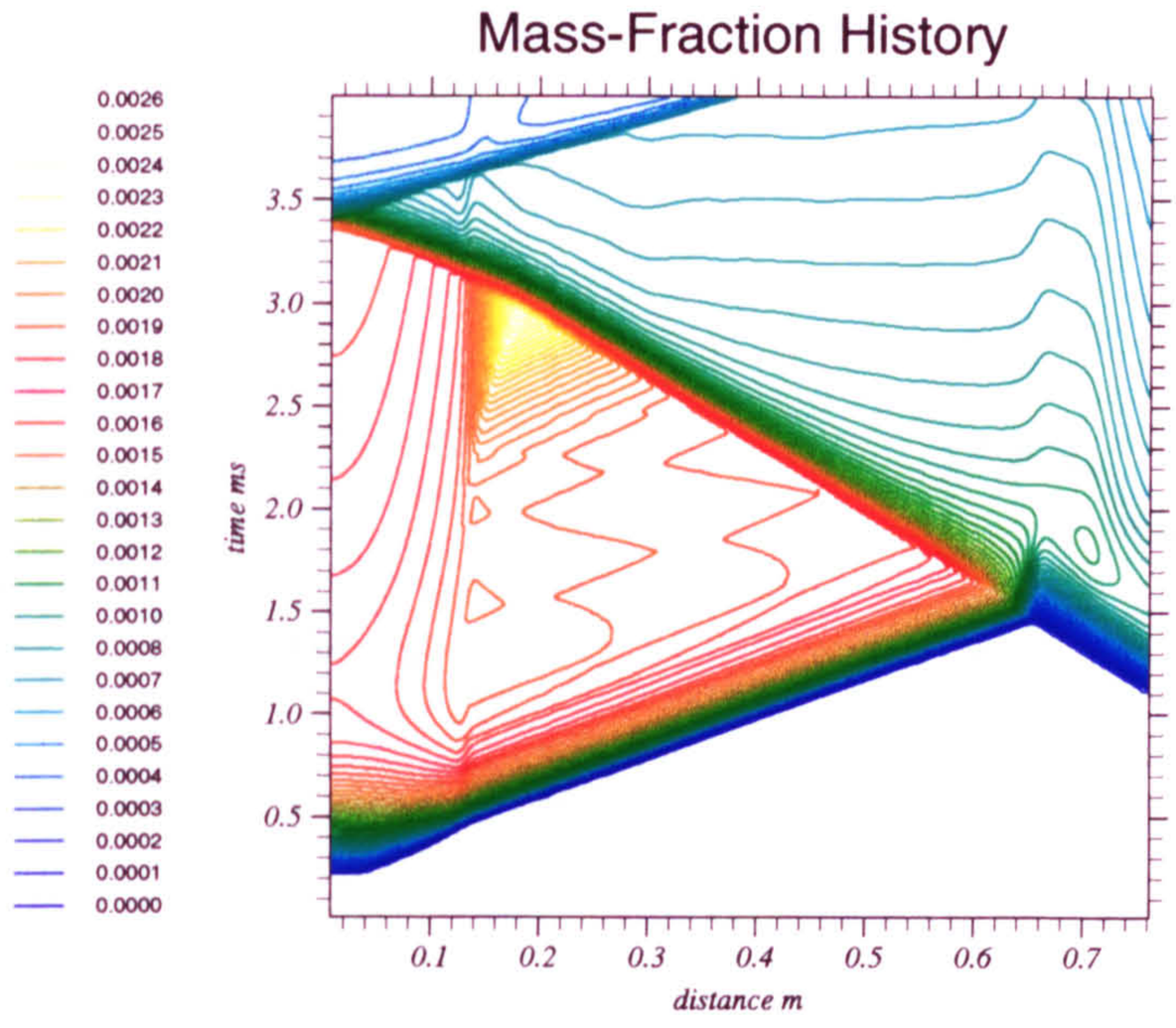

Figure 4.15: Mass-fraction history for $E_A/\mathcal{R} = 5000K$ over the first $4ms$.

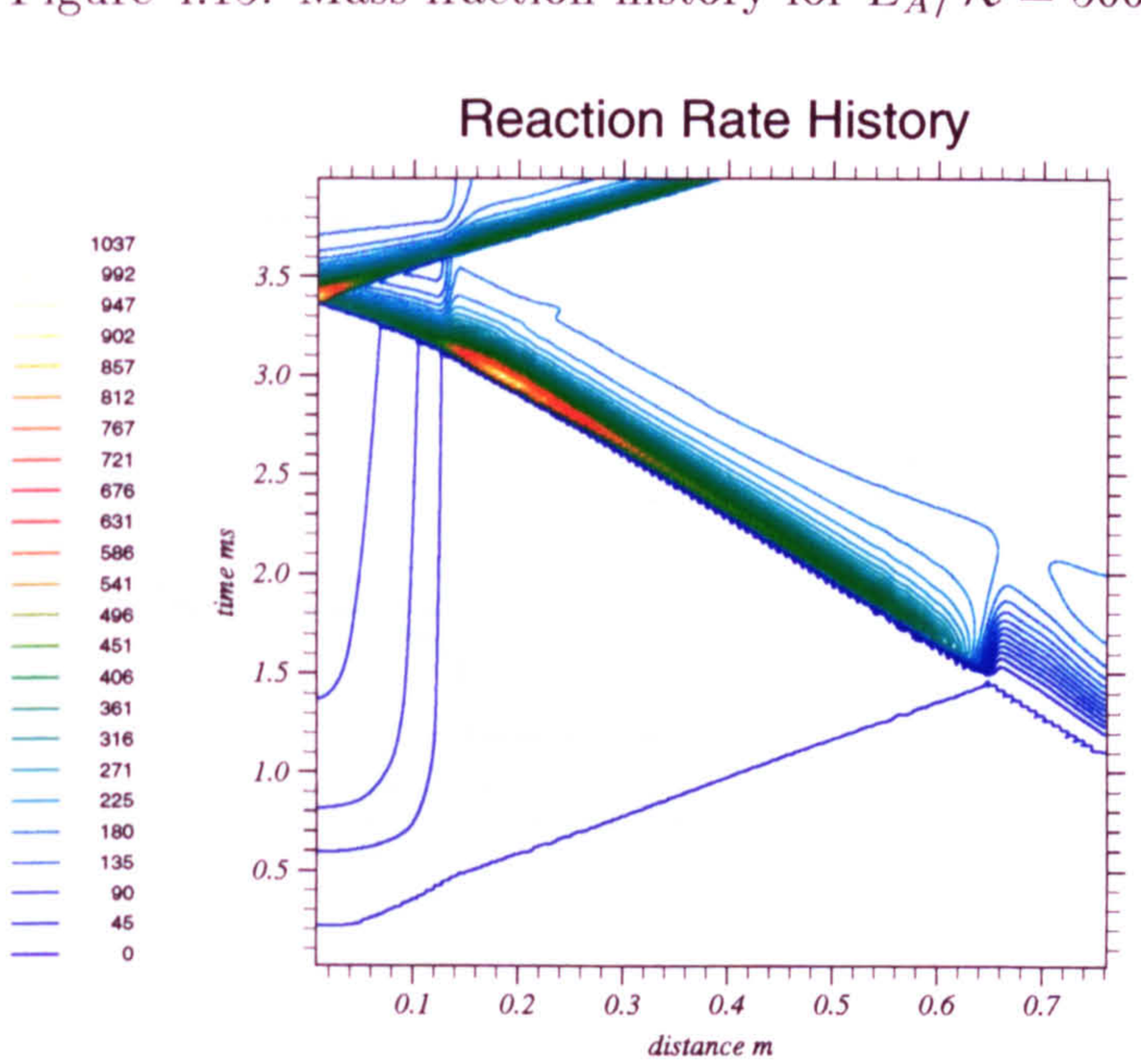

Figure 4.16: Reaction rate history for $E_A/\mathcal{R} = 5000K$ over the first $4ms$.

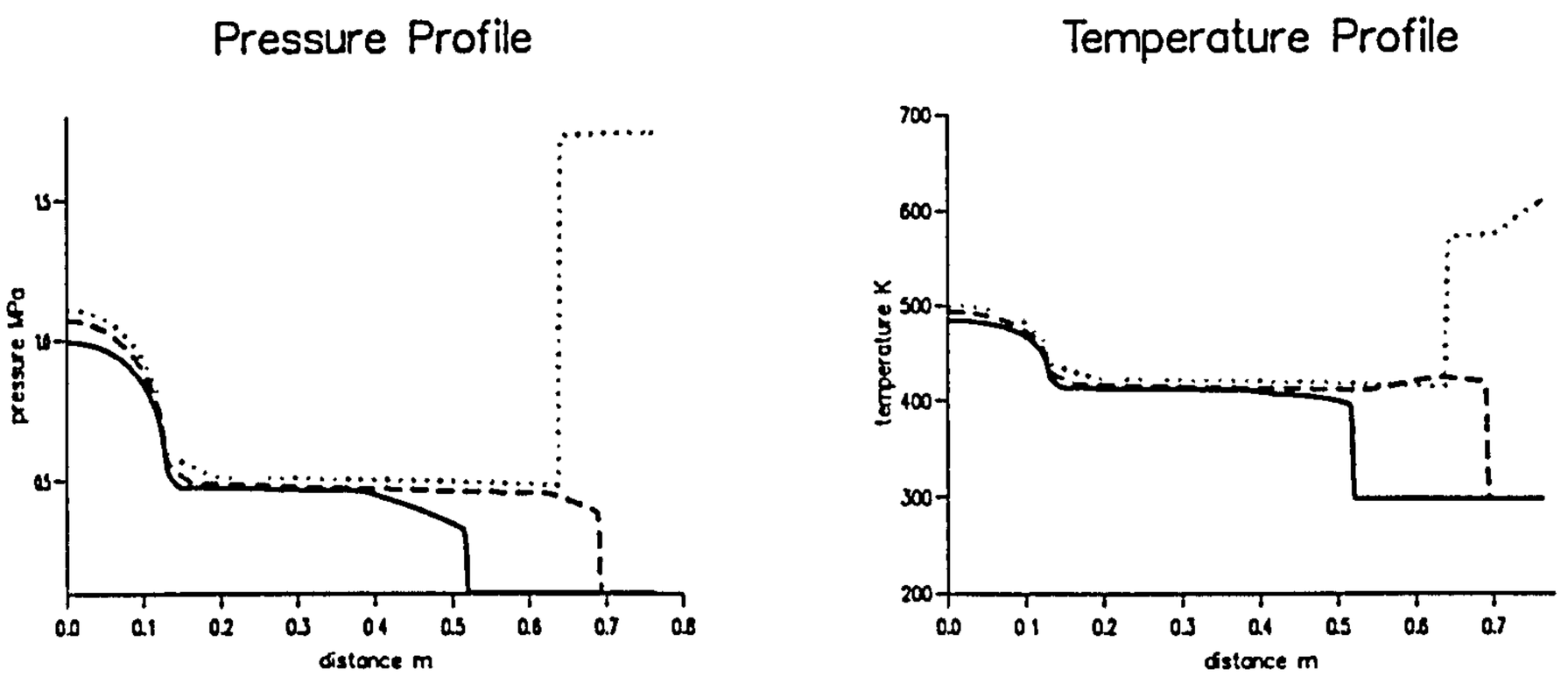

Figure 4.17: Pressure and temperature profiles at $t = 0.75ms$ (full line), $t = 1ms$ (dashed line) and $t = 1.5ms$ (dotted line).

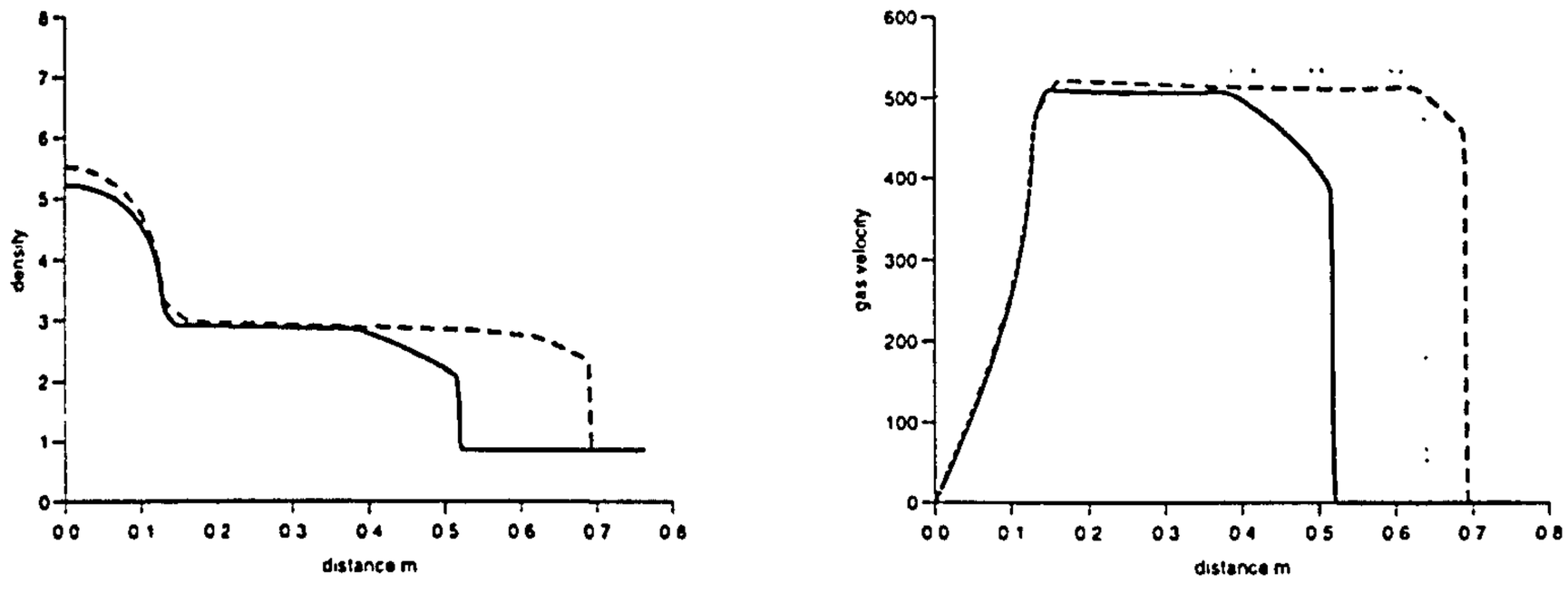

Figure 4.18: Density and gas velocity profiles at $t = 0.75ms$ (full line), $t = 1ms$ (dashed line) and $t = 1.5ms$ (dotted line).

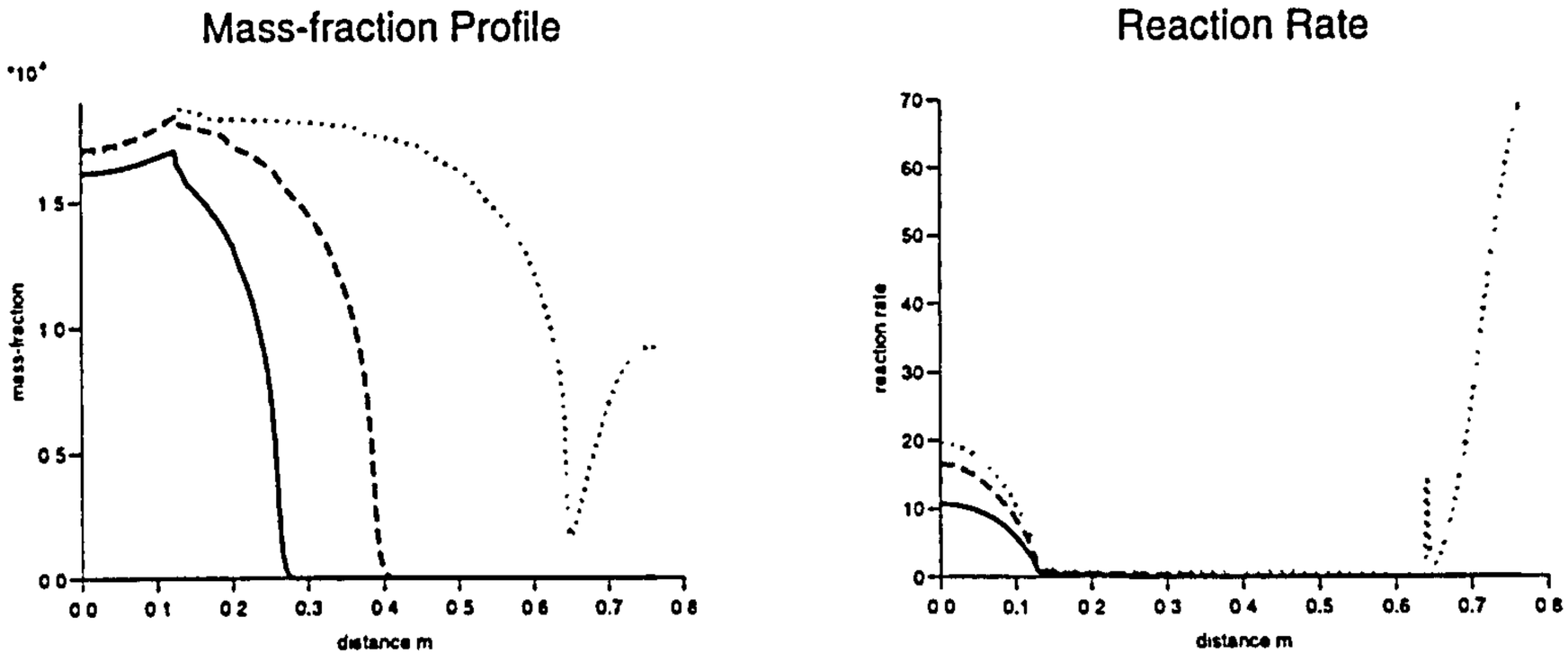

Figure 4.19: Mass-fraction and reaction rate profiles at $t = 0.75ms$ (full line), $t = 1ms$ (dashed line) and $t = 1.5ms$ (dotted line).

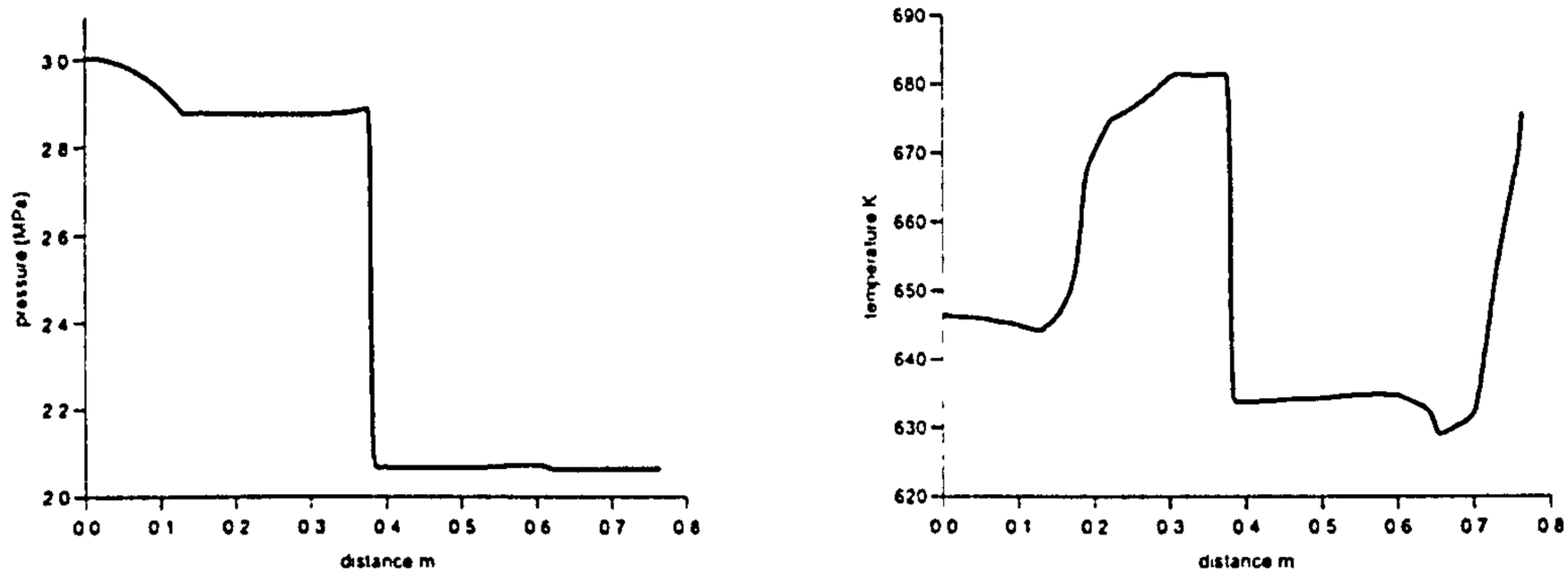

Figure 4.20: Pressure and temperature profiles at $t = 4ms$.

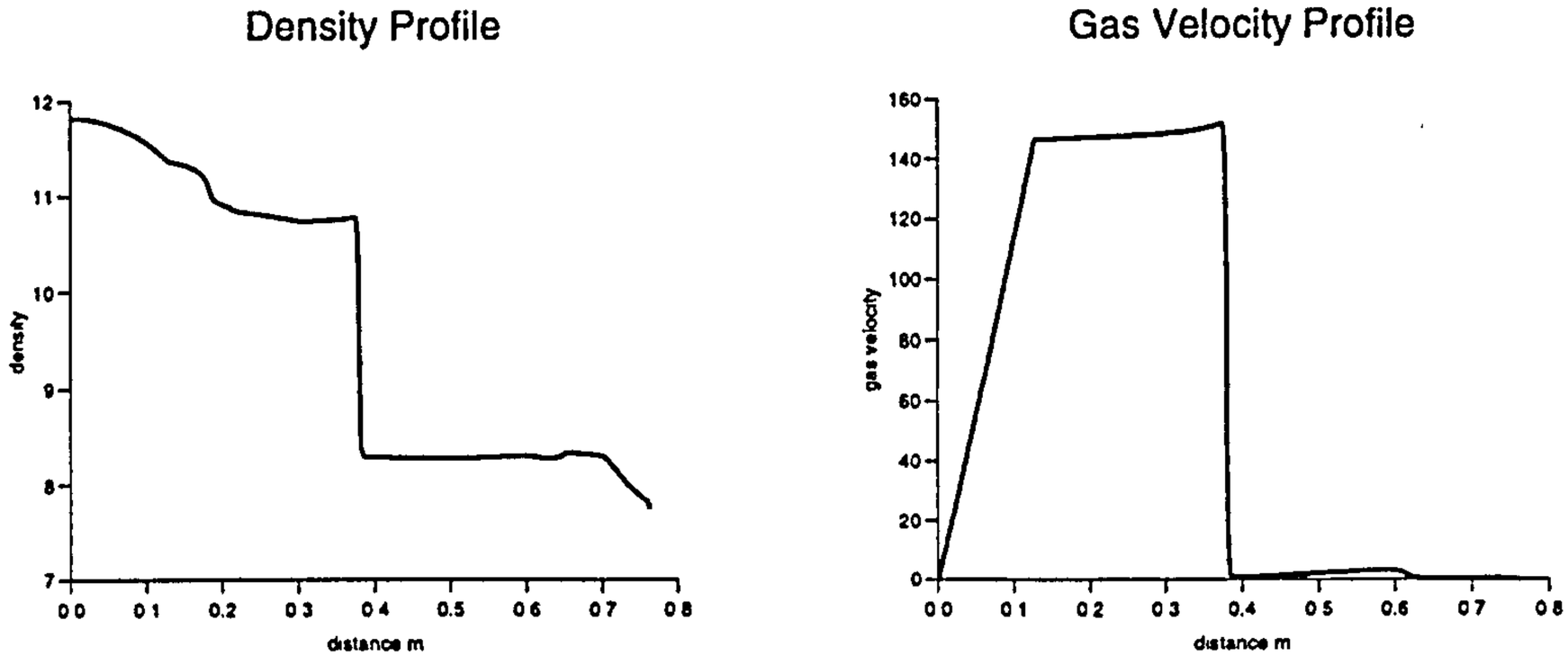

Figure 4.21: Density and gas velocity profiles at $t = 4ms$.

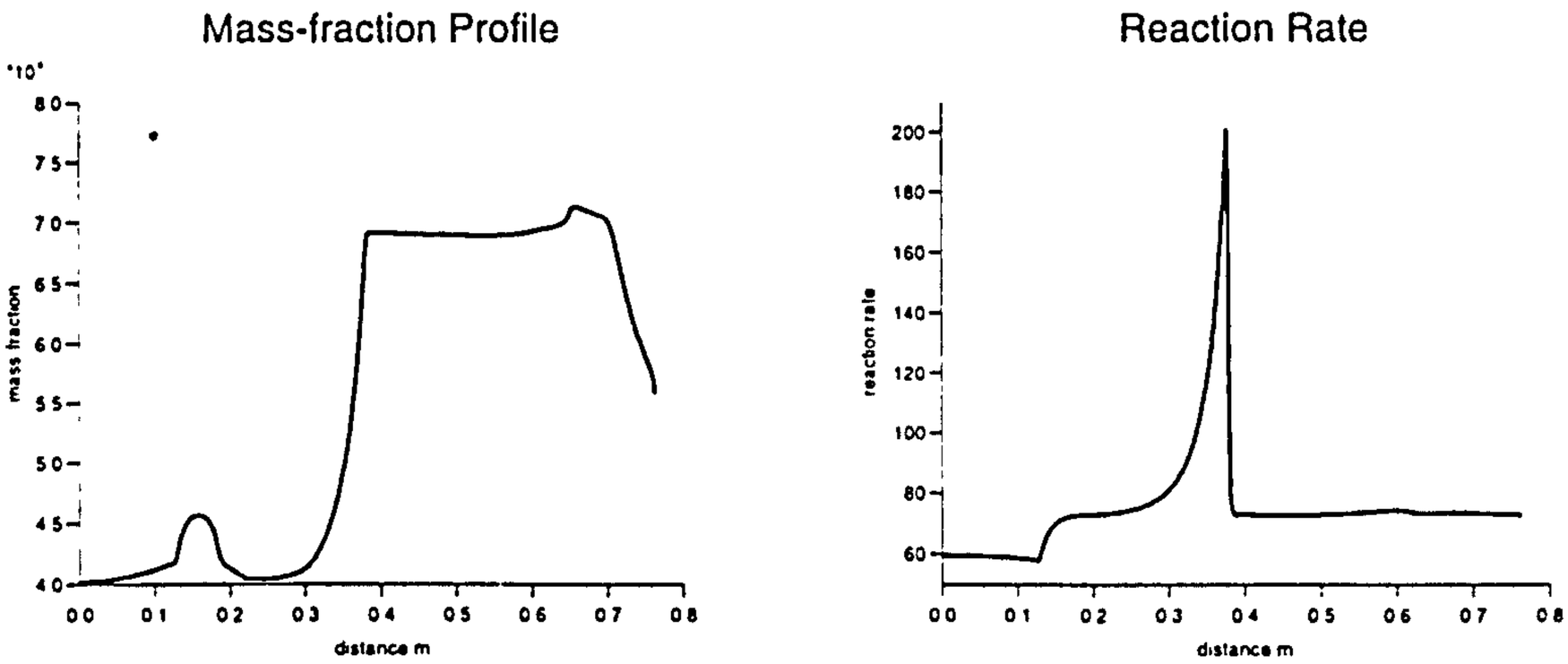

Figure 4.22: Mass-fraction and reaction rate profiles at $t = 4ms$.

4.3.2 Flow Variable Histories for $E_A/\mathcal{R}T = 15000K$

At the early stages there is little difference in the histories for pressure, density, velocity and temperature- igniter gas heats up the breech producing a shock wave and rarefaction fan.

However, consultation of the profile at $0.75ms$ in figure (4.31), differs from the lower activation energy picture in figure (4.19), due to a greater build up of c. This is because the high value of activation energy means there is insufficient thermal energy to produce significant consumption of reactant. This idea is reinforced by comparing the reaction rate plots for the two activation energies which significantly differ. Since relatively small quantities of mass-reaction are being consumed the total energy increase is due to mass addition and negligible chemical energy is being released into the system. A reactant wave forms also due to the convection of reactant gas from the hot igniter regions displayed in figure (4.27). The shock reflects, as before, switching on gasification behind it. However, when the reflected shock and reactant wave intersect, the mass-fraction history shows that c does not decline indicating that ignition has not occurred. In fact the higher temperature behind the shock simply induces more gasification without any chemical energy release so that c increases. This can be confirmed by consulting the reaction rate profile which remains low during these early times in figure (4.31). The intersection of the shock and reactant wave do however produce a feature that indicates a **minimum** in mass-fraction. This is since *additional* reactant is created at $(0.64m, 1.5ms)$ and after this time, the reactant is least for the particle paths at this point. As the shock travels towards the breech the high temperatures gasify propellant introducing more reactant but the high activation energy means that the reaction rate remains low and little reactant is consumed.

At $4ms$ the manifestation of this can be seen by comparing the pressure and temperature in figures (4.20) and (4.32). The temperature plots shows a difference in magnitude of approximately $50K$ that is a result of the difference in chemical energy release. The shock for the lower activation energy is also travelling faster. The difference in the reaction rates is also significant from figures (4.22) and (4.34).

For this second case, one interesting observation is that throughout the combustion cycle the mass-fraction in the igniter region remains at approximately 0.0022 as seen in figure (4.34). This can be explained by considering the density and mass-fraction equations.

$$\frac{\partial}{\partial t}(\rho) + \frac{\partial}{\partial x}(\rho u) = \dot{m} + \dot{m}_{ig} \tag{4.142}$$

$$\frac{\partial}{\partial t}(\rho c) + \frac{\partial}{\partial x}(\rho u c) = \frac{\dot{m}}{2} + K \tag{4.143}$$

As explained above, at this activation energy and temperature range the reaction rate is very small i.e. $\Omega \approx 0$ and thus K is almost zero. The mass-fraction (4.143) equation can be expanded and written as:

$$\rho\frac{\partial c}{\partial t} + \rho u\frac{\partial c}{\partial x} + c.\left[\frac{\partial}{\partial t}\rho + \frac{\partial}{\partial x}\rho u\right] \approx \frac{\dot{m}}{2} \tag{4.144}$$

By using the density equation (4.142) this can be written as:

$$\frac{Dc}{Dt} = \frac{\dot{m}}{\rho}(\frac{1}{2} - c) - \frac{c\dot{m}_{ig}}{\rho} \tag{4.145}$$

The steady-state solution is given as:

$$\frac{Dc}{Dt} = 0$$

$$\Rightarrow c = \frac{\dot{m}}{2(\dot{m} + \dot{m}_{ig})} \tag{4.146}$$

If this value of mass-fraction has been attained it will remain constant in time. Substituting the parameter values $\dot{m} = 0.8kg/msec; \dot{m}_{ig} = 178.81kg/msec$ gives:

$$c = 2.29 \times 10^{-3} \tag{4.147}$$

This shows that the mass-fraction remains almost constant in this region over time because the steady-state has been attained.

The figures from (4.23) to (4.28) illustrate the pressure, density, gas velocity, temperature, mass-fraction and reaction rate, respectively, over the whole combustion chamber over the first 4ms.

Figures (4.29), (4.30), (4.31) show profiles of flow variables at times $0.75ms$, $1ms$, $1.5ms$ and figure (4.32), (4.33), (4.34) show profiles at $4ms$.

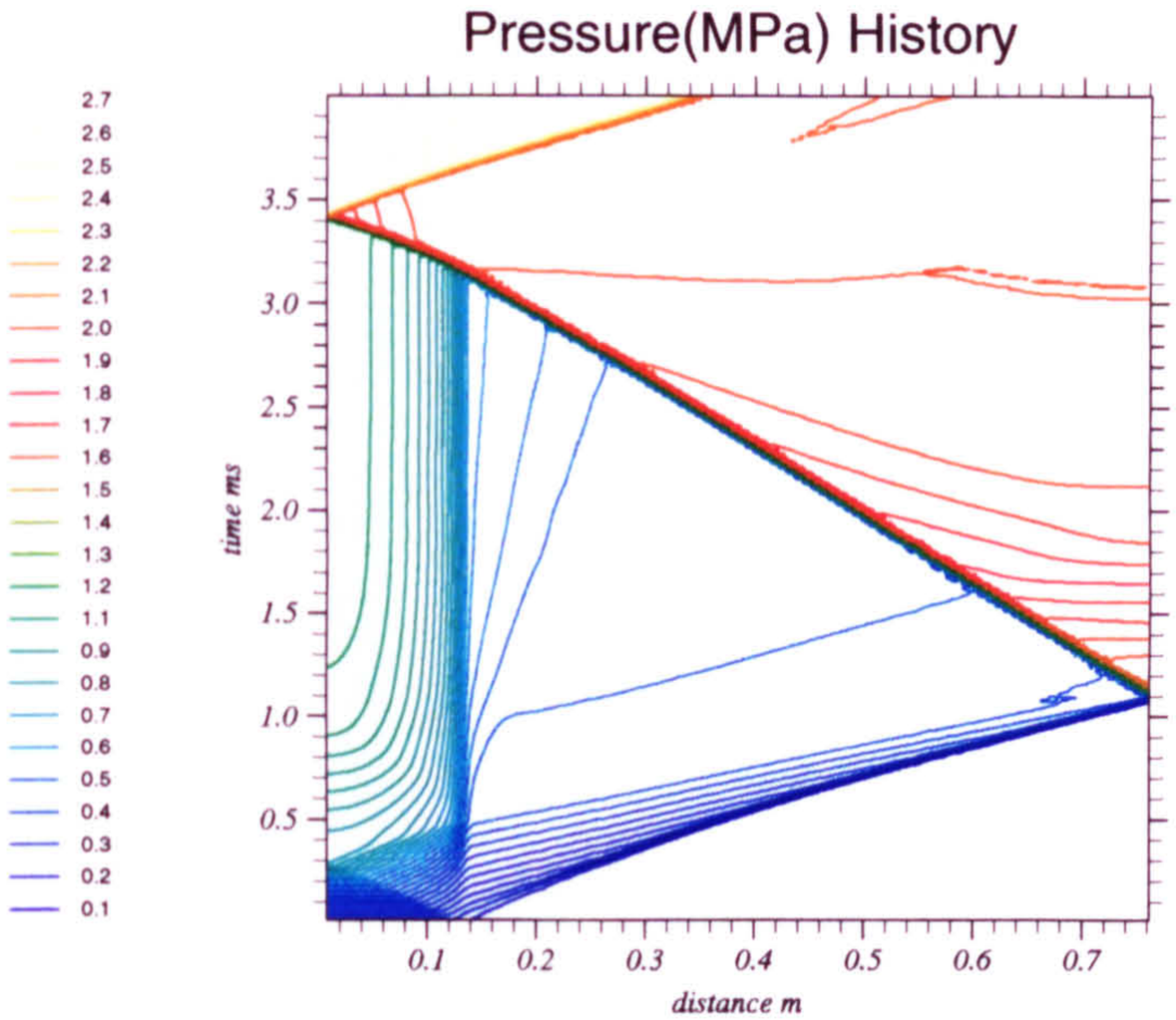

Figure 4.23: Pressure history for $E_A/\mathcal{R} = 15000K$ over the first $4ms$.

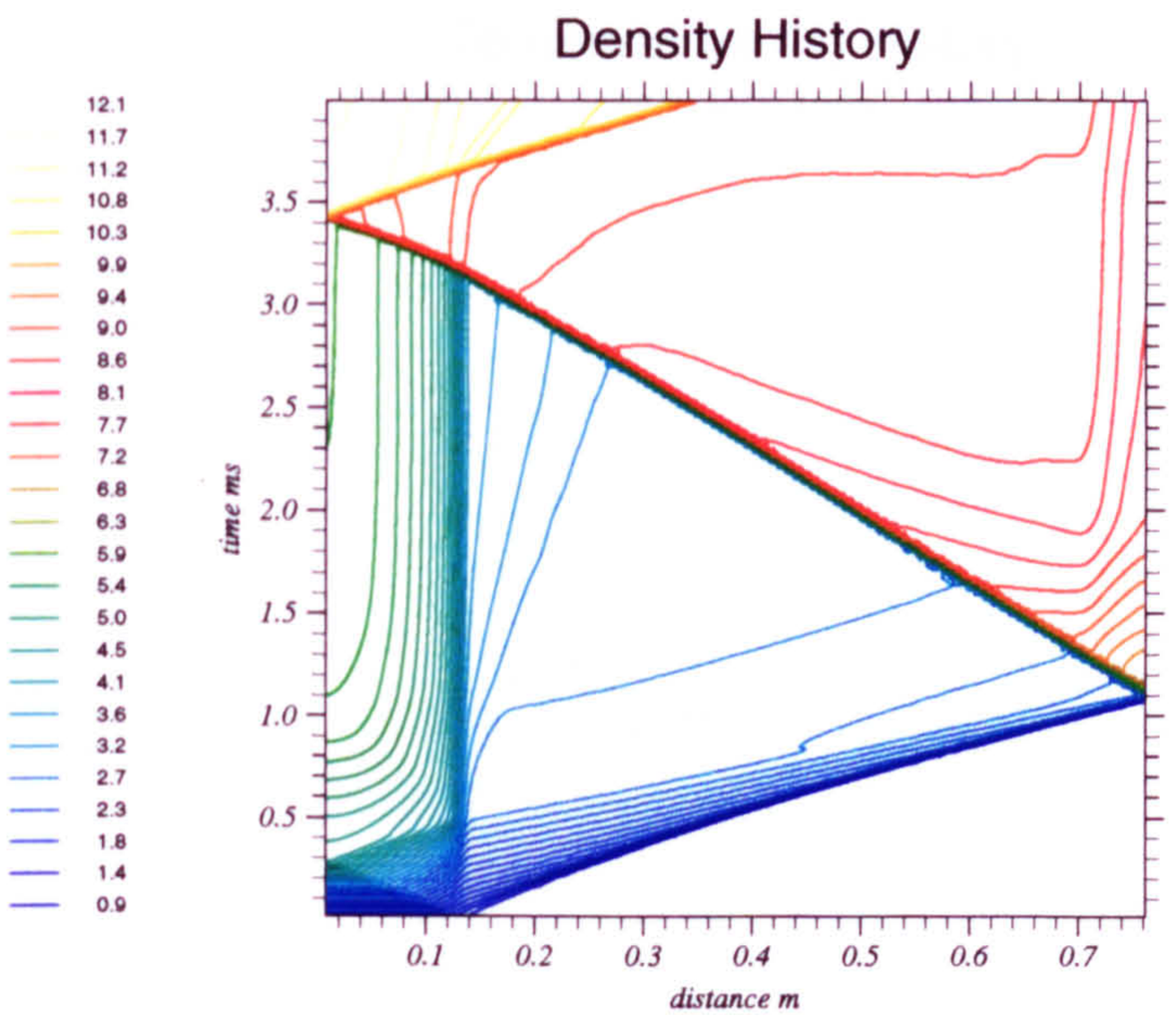

Figure 4.24: Density history for $E_A/\mathcal{R} = 15000K$ over the first $4ms$.

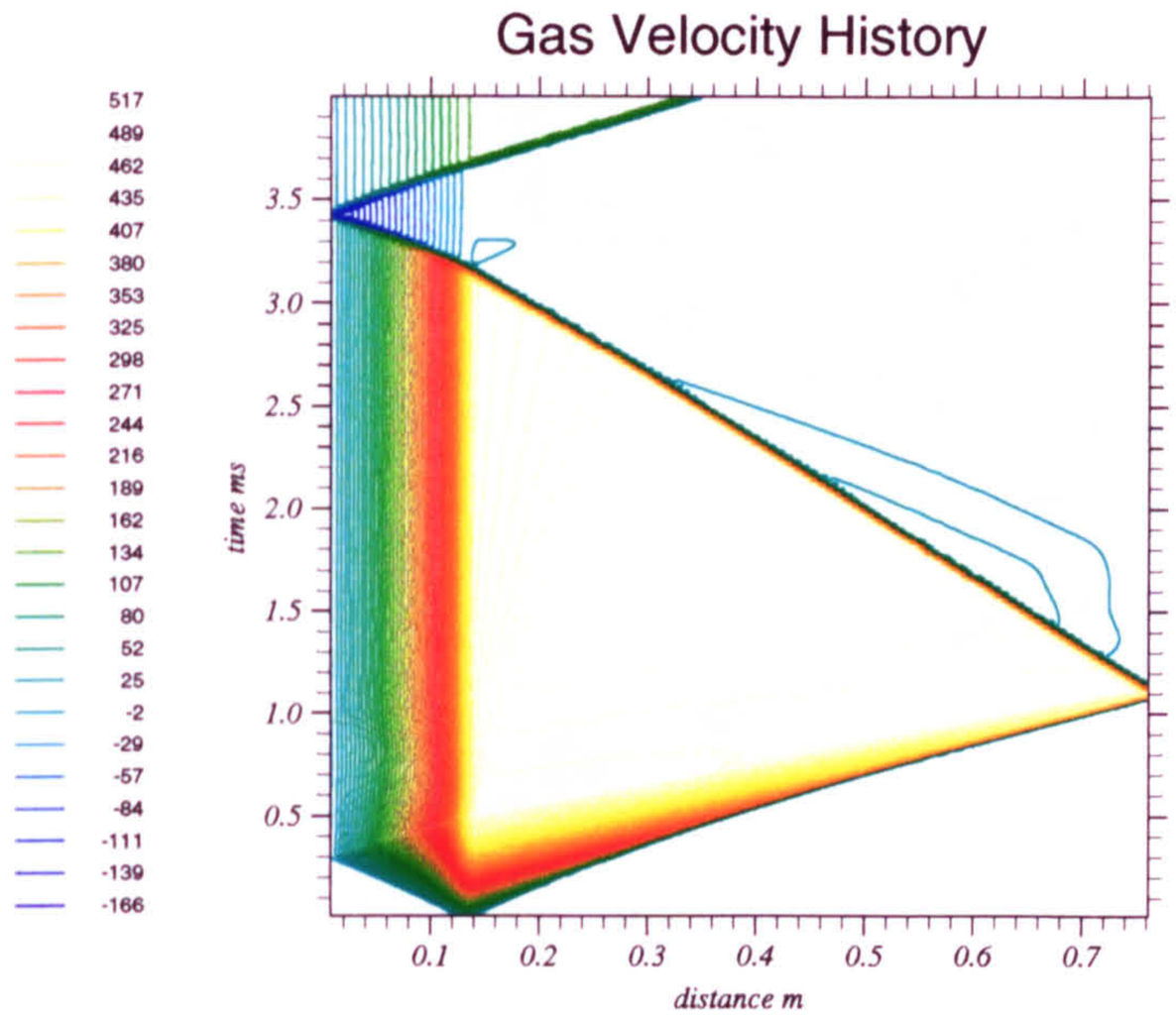

Figure 4.25: Gas velocity history for $E_A/\mathcal{R} = 15000K$ over the first $4ms$.

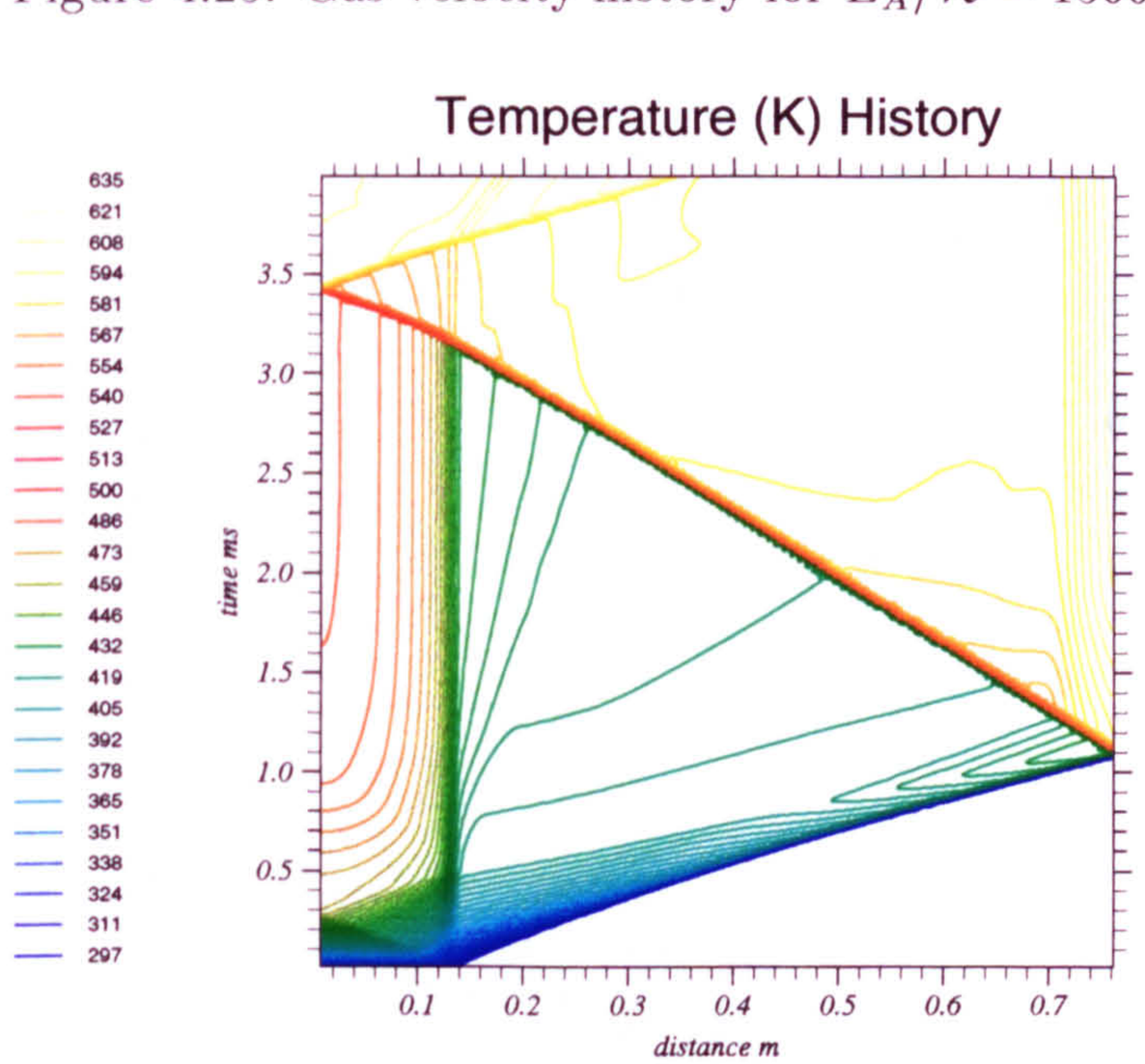

Figure 4.26: Temperature history for $E_A/\mathcal{R} = 15000K$ over the first $4ms$.

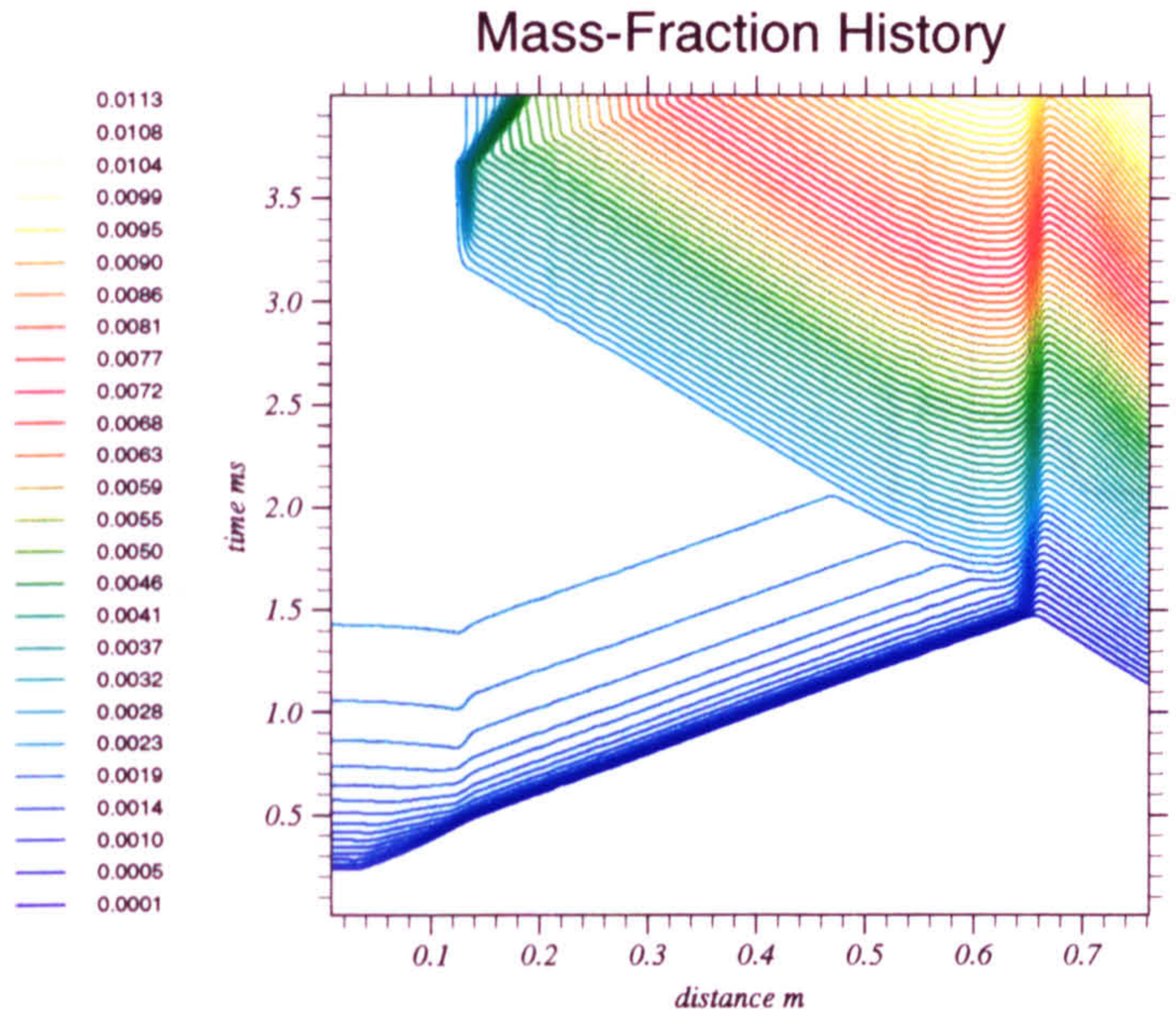

Figure 4.27: Mass-fraction history for $E_A/\mathcal{R} = 15000K$ over the first $4ms$.

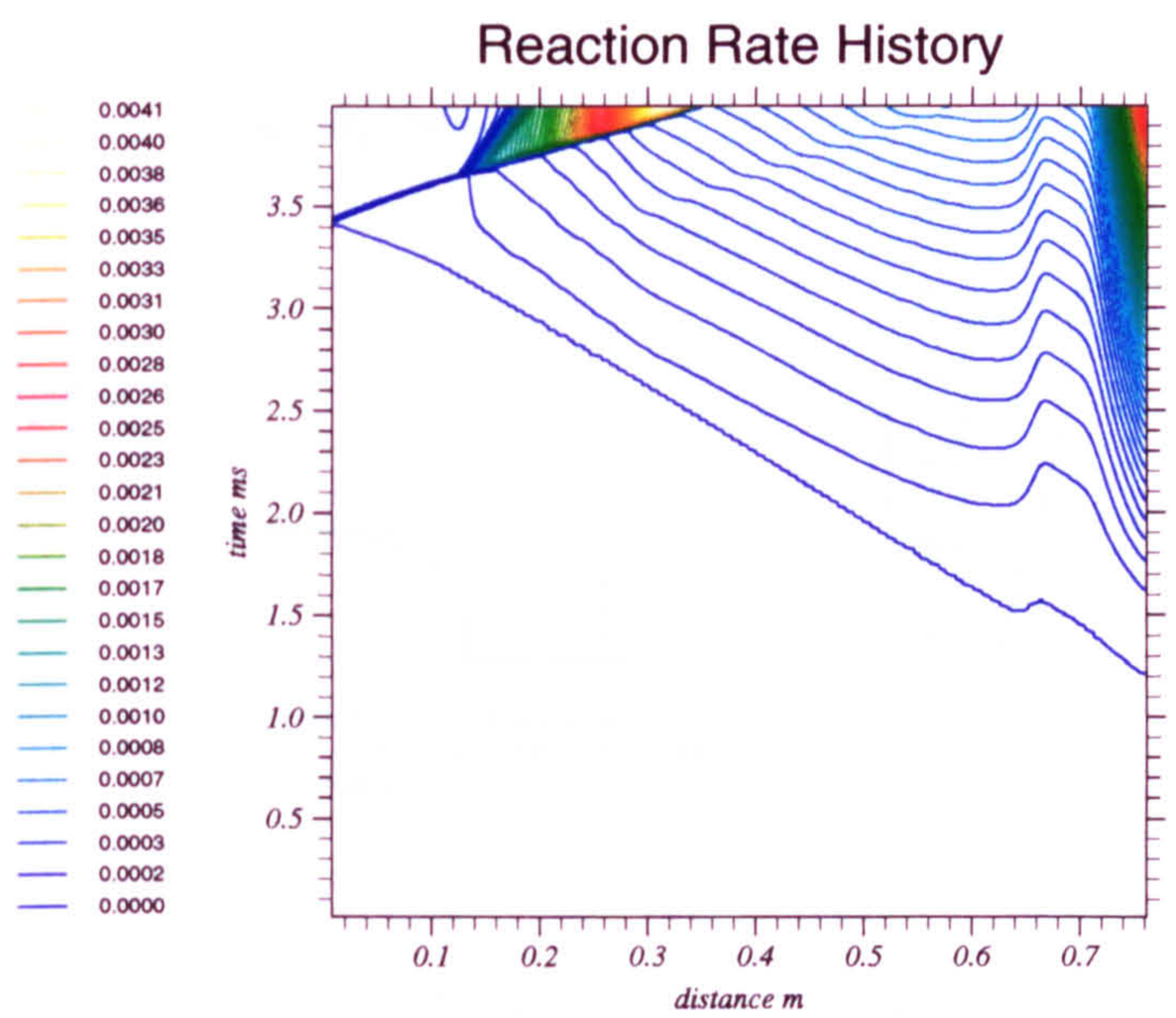

Figure 4.28: Reaction rate history for $E_A/\mathcal{R} = 15000K$ over the first $4ms$.

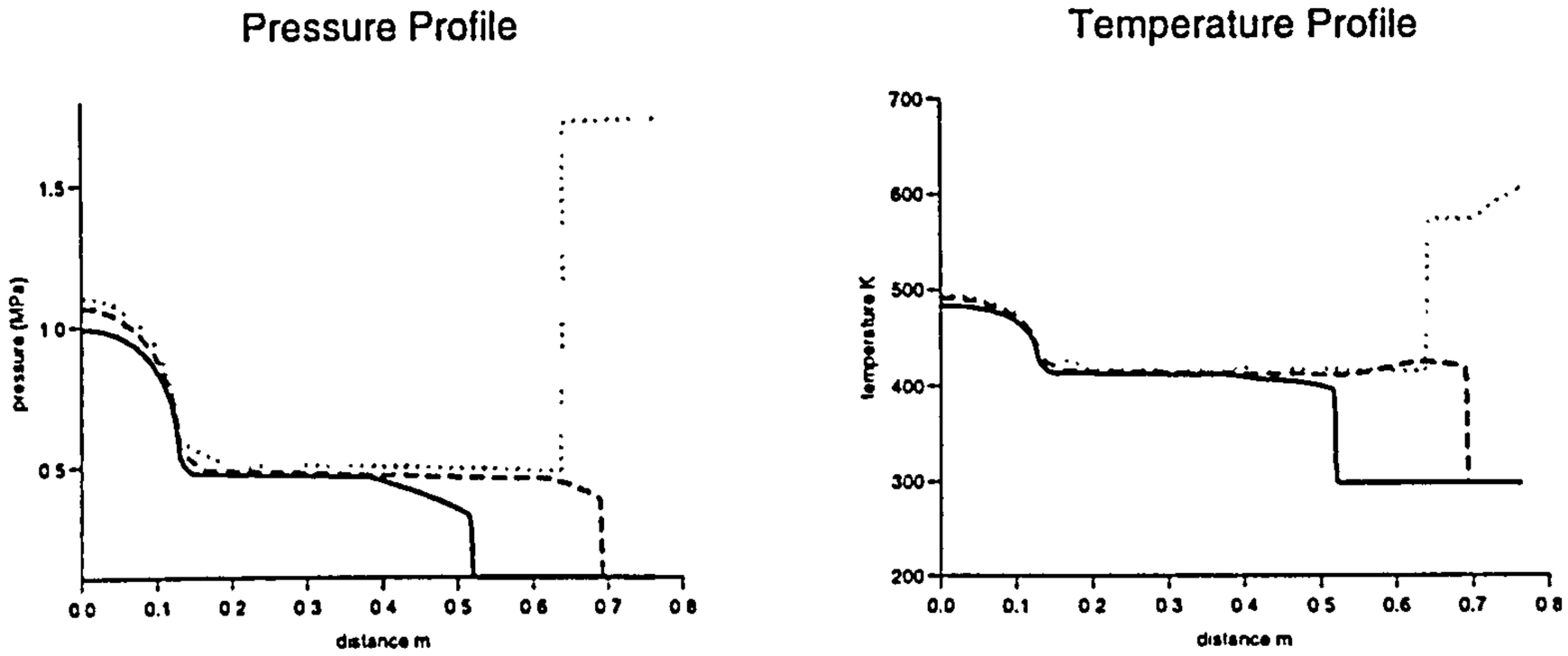

Figure 4.29: Pressure and temperature profiles at $t = 0.75ms$ (full line), $t = 1ms$ (dashed line) and $t = 1.5ms$ (dotted line).

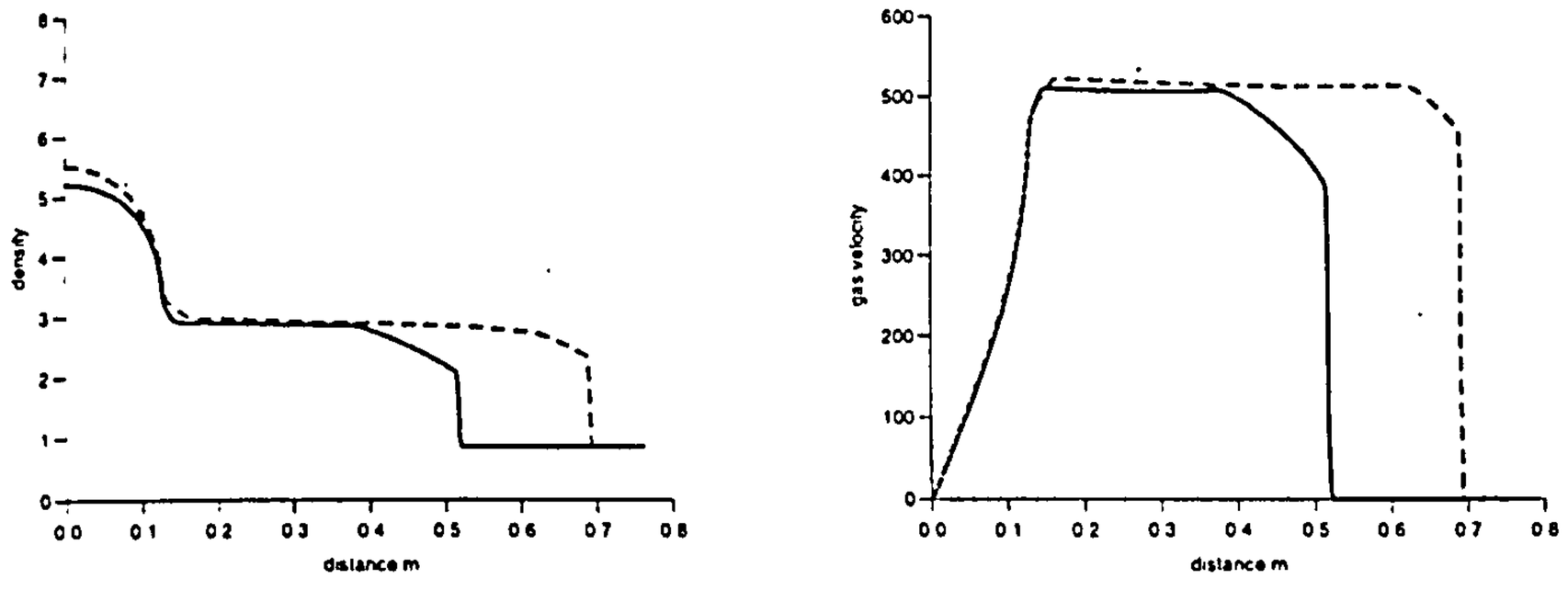

Figure 4.30: Density and gas velocity profiles at $t = 0.75ms$ (full line), $t = 1ms$ (dashed line) and $t = 1.5ms$ (dotted line).

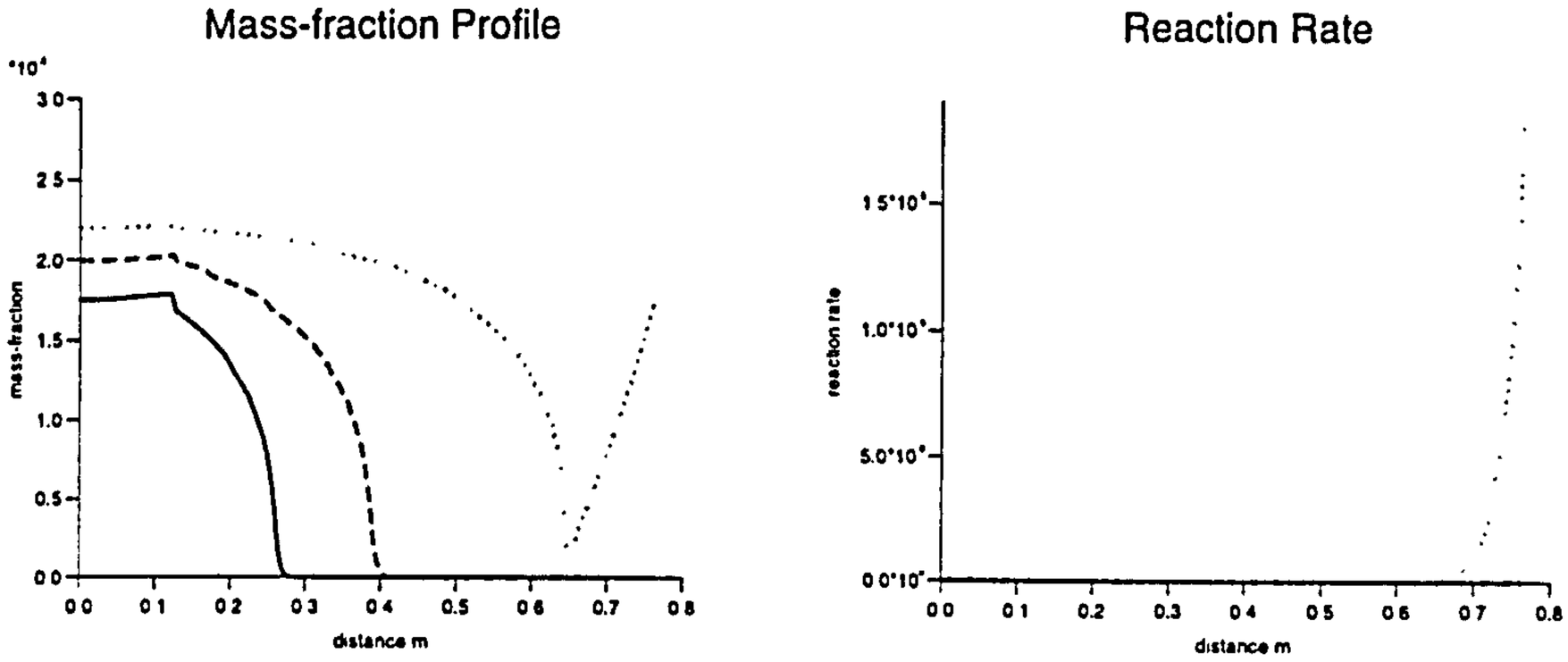

Figure 4.31: Mass-fraction and reaction rate profiles at $t = 0.75ms$ (full line), $t = 1ms$ (dashed line) and $t = 1.5ms$ (dotted line).

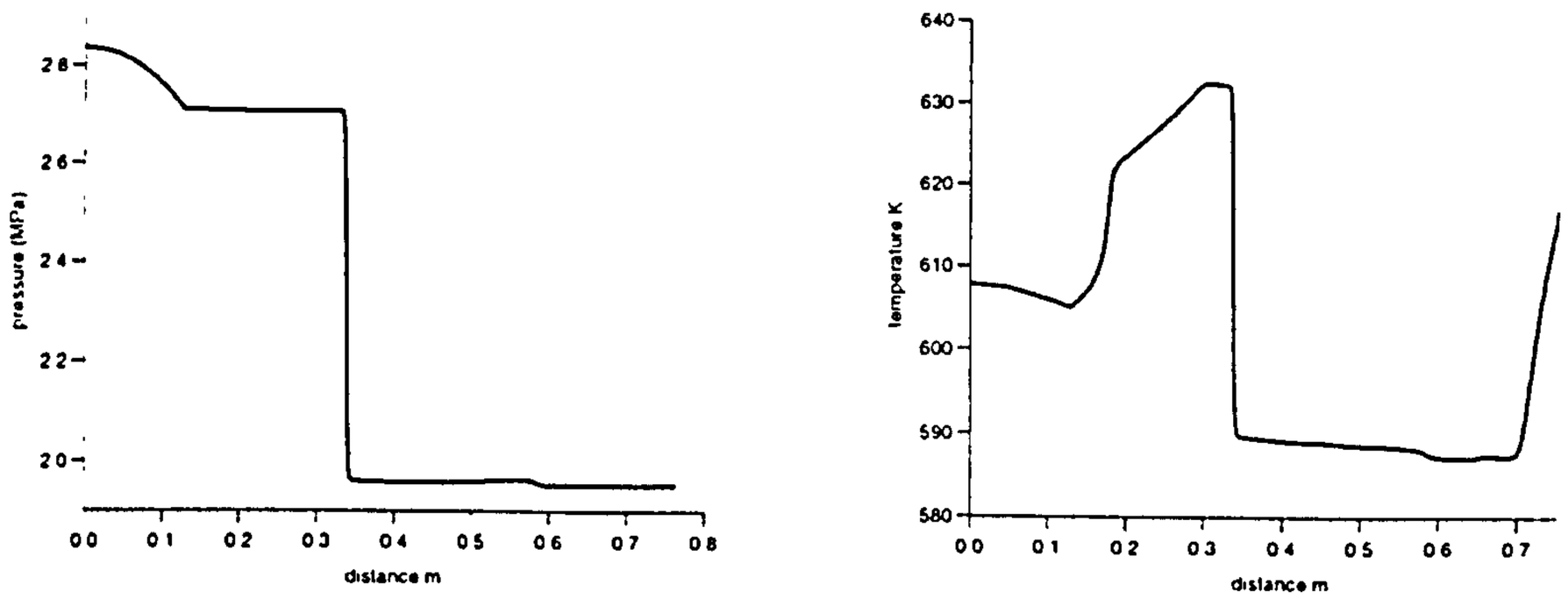

Figure 4.32: Pressure and temperature profiles at $t = 4ms$.

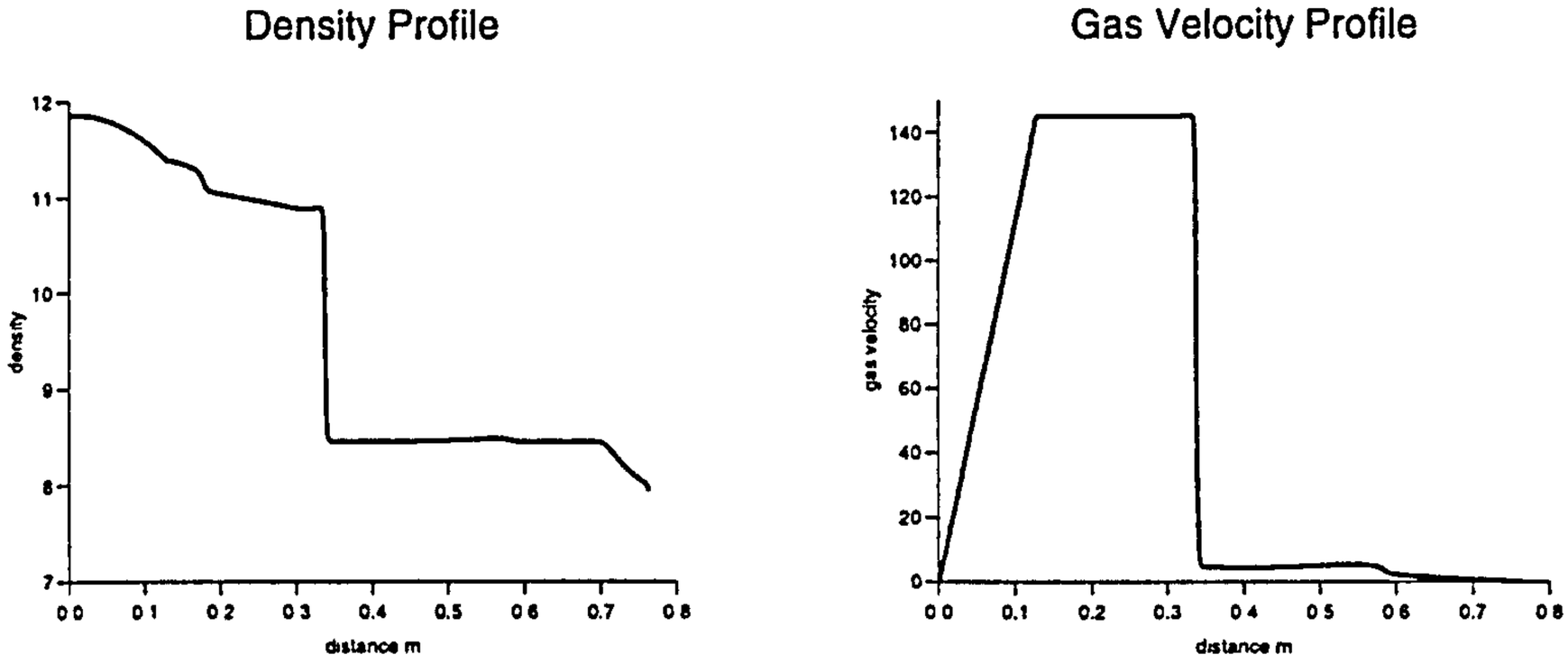

Figure 4.33: Density and gas velocity profile at $t = 4ms$.

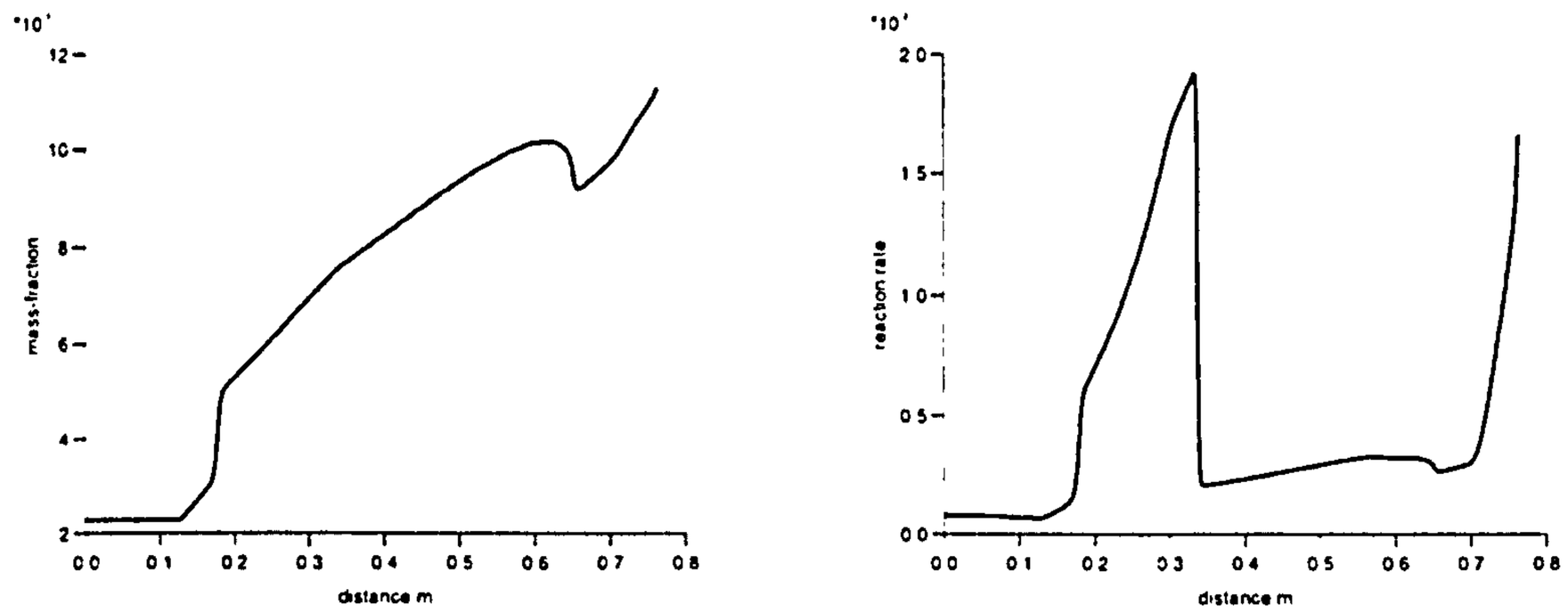

Figure 4.34: Mass-fraction and reaction rate profiles at $t = 4ms$.

4.4 Summary

Just as the previous section gave us a sound understanding of the evolution of chemistry in time, here important relations between fluid flow properties and chemistry have been illustrated. Some of the controlling factors that can influence the time and place of ignition have been deduced. Most equilibrium models can only model the ignition process by assuming combustion is initiated once the local temperature has risen above a critical temperature. This means, in the case illustrated above, ignition occurs in the region in which igniter gas is being fed - at the breech end. However, ignition has often been observed to occur towards the projectile base and most interior ballistic models have been unable to predict this. The solution of the chemical equations presented above can give one possible mechanism of how this can occur and clearly this could not be predicted without tracking the movement and evolution of gas-phase reactant species.

The example problem posed is rather artificial since the effect of the solid motion has been completely neglected. However, by considering the gas alone some clear ideas have been developed which may have become obscured if the more complicated problem was considered. Later, two-phase flow equations will be derived that include the chemistry described above. Perhaps some of the features observed above will not be so different in the more complicated flow regime.

Chapter 5

Two-Phase Flow

There are numerous two-phase flow sets of equations that have been developed for propellant systems [6], [9], [21] which use slightly different approaches. In this work, the equilibrium two-phase flow equations that were derived by Gough [8] will be developed to include the non-equilibrium chemistry that was described in chapter 2. Gough takes mathematical averages of flow variables, for the two-phase mixture, in space and time to develop a set of average two-phase flow equations. In multiphase flow theory, the approach is based on the idea of separated flow as opposed to the continuum approach, adopted for example, by Soo [79]. A full account of the derivation without chemistry can be found in [8].

5.1 Definition of the Average

Consider the domain given in figure (5.1) that consists of a mixture of gas and propellant. The domain is of volume V, the surface area of the domain is S and the vector normal to S is given as $\mathbf{n}$. The idea behind the averaging process is to average the point variables over regions that are large compared to the scale of heterogeneity of the mixture. In this way the averaging acts as low pass filtering which eliminates unwanted high frequency signals from local instant fluctuations of variables. The statistical properties of these fluctuations are taken into account during the derivation of the equations.

To formally average the two-phase flow mixture it is necessary to define a weighting function $g(\mathbf{y} - \mathbf{x}, \tau - t)$ that reflects the influence of remote

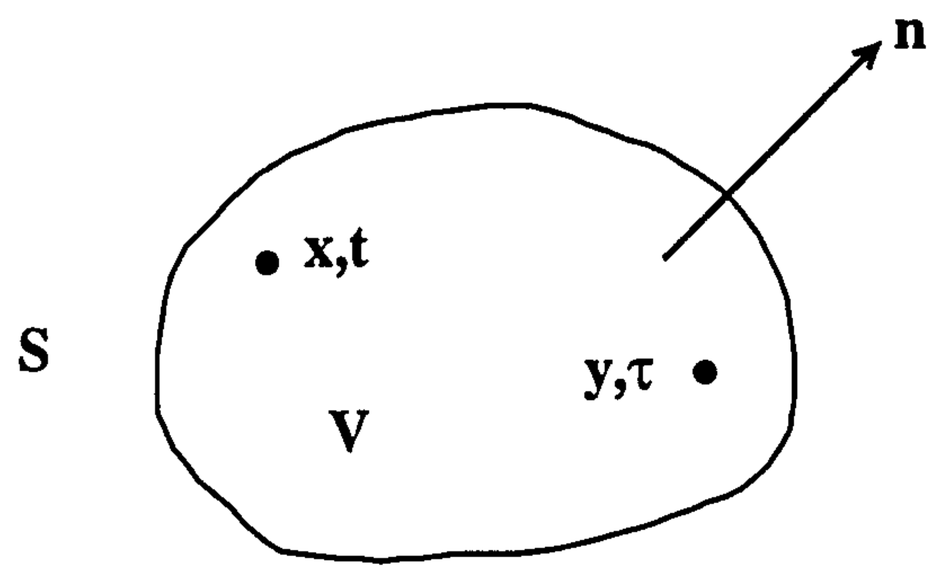

Figure 5.1: Domain

points $(\mathbf{y}, \tau)$ on the average that is formed at $(\mathbf{x}, t)$, where $\mathbf{x}$ and $\mathbf{y}$ are three-dimensional vectors. The requirements on g are identical to those described in [80]; g must be non-negative and the integral of it over all space and time must exist. Then g can be assumed to be normalized such that:

$$\int_{space,time} g(\mathbf{r}, t) dV dt = 1. \tag{5.1}$$

Without going into unnecessary detail about the nature of the weighting function, it is important to highlight some physical aspects associated with this. The weighting function has a 'radius' associated with the region over which the averaging takes place. This radius must be large compared to the particle spacing but small relative to the size of the physical dimensions of the vessel containing the two-phase mixture. In this case, the averaged variables, derived below, are insensitive to the detailed form of the weighting function and are uniquely determined. This statement provides a lower limit on the computational mesh, below which the validity of the average equations fails.

The void fraction or porosity may be defined in terms of g according to

$$\epsilon(\mathbf{x}, t) = \int_R g(\mathbf{y} - \mathbf{x}, \tau - t) dV d\tau, \tag{5.2}$$

where R is the region occupied by the gas. The porosity defines the fraction of the total volume that is occupied by gas at $(\mathbf{x}, t)$. An average value of any gas property ψ can be defined using the above relations:

$$\langle \psi(\mathbf{x}, t) \rangle = \frac{1}{\epsilon(\mathbf{x}, t)} \int_R g(\mathbf{y} - \mathbf{x}, \tau - t) \psi(\mathbf{y}, \tau) dV d\tau. \tag{5.3}$$

The average properties in the solid phase are determined in an analogous manner. Note that the equations are integrated over all time and space.

The averaging procedure is applied to the microscopic equations. These equations contain derivatives and so a commutation principle is required to describe the effect of the order in which differentiation and averaging are performed. The following identities describe this:

Let x_i be a component of $\mathbf{x}$ at which the average is formed. Since the region of integration depends on $\mathbf{x}$ then:

$$\frac{\partial}{\partial x_i}\epsilon(\mathbf{x},t)\langle\psi(\mathbf{x},t)\rangle = \int_R \frac{\partial}{\partial x_i}[g(\mathbf{y}-\mathbf{x},\tau-t)\psi(\mathbf{y},\tau)]dVd\tau. \tag{5.4}$$

Now the integrand on the right-hand-side can be written as:

$$\frac{\partial}{\partial x_i}[g(\mathbf{y}-\mathbf{x},\tau-t)\psi(\mathbf{y},\tau)] = g(\mathbf{y}-\mathbf{x},\tau-t)\frac{\partial\psi}{\partial y_i}(\mathbf{y},\tau) - \frac{\partial}{\partial y_i}[g(\mathbf{y}-\mathbf{x},\tau-t)\psi(\mathbf{y},t)] \tag{5.5}$$

Accordingly an application of the divergence theory yields:

$$\frac{\partial}{\partial x_i}\epsilon(\mathbf{x},t)\langle\psi(x,t)\rangle = \epsilon(\mathbf{x},t)\langle\frac{\partial}{\partial x_i}\psi(\mathbf{x},t)\rangle - \int_\Sigma \psi(\mathbf{y},\tau)g(\mathbf{y}-\mathbf{x},\tau-t)n_i dA, \tag{5.6}$$

where Σ is the region of integration defined by the interface between the media and all time, $\mathbf{w}$ is the velocity of the interface and $\mathbf{n}$ is the normal to the interface taken as positive out of the medium for which the average is being formed.

Similarly we have:

$$\frac{\partial}{\partial t}\epsilon(\mathbf{x},t)\langle\psi(\mathbf{x},t)\rangle = \epsilon(\mathbf{x},t)\langle\frac{\partial}{\partial t}\psi(\mathbf{x},t)\rangle + \int_\Sigma \psi(\mathbf{y},\tau)g(\mathbf{y}-\mathbf{x},\tau-t)\mathbf{w}.\mathbf{n}dA. \tag{5.7}$$

The above identities, in particular (5.6) and (5.7), are key to the formal replacement of the microscopic equations by the governing equations for the average properties.

The surface integrals that will appear in the following averaging procedure can be interpreted in a more physically meaningful manner if they are simplified:

- The term $\int_\Sigma g dA$ is the average surface area per unit volume. Let V^p and S^p be the volume and surface area, respectively, occupied by the propellant Providing that V^p and area S^p have locally similar volume, it can be shown that:

$$\int_\Sigma g dA = (1-\epsilon)\frac{S^p}{V^p}. \tag{5.8}$$

- The velocity of the interface can be expressed as:

$$\mathbf{w} = \mathbf{u}^p + \mathbf{n}\dot{r}, \tag{5.9}$$

where $\mathbf{u}^p$ is the particle velocity and $\dot{r}$ is the rate of regression of the propellant surface.

- The term $\int_\Sigma g\psi dA$ is in effect the definition of the average ψ over the interface Σ apart from the normalizing factor given in equation (5.8). Many of the important transfer processes between the solid and gas such as mass, heat and friction losses can be quite naturally expressed in terms of surface averages. Define the surface average of ψ as:

$$\langle\psi\rangle^i = \frac{\int_\Sigma g\psi dA}{\int_\Sigma g dA}. \tag{5.10}$$

- Since this surface average is in general not equal to the overall average, define the fluctuation field associated with the tensor ψ :

$$\psi'' = \psi - \langle\psi\rangle. \tag{5.11}$$

Provided that

$$\langle\langle\psi\rangle\rangle = \langle\psi\rangle, \tag{5.12}$$

then it follows that $\langle\psi''\rangle = 0$. Physically this means that only the characteristics of the flow that are large compared with the domain of influence of g are embedded in the theory.

- From this it follows that:

$$\langle\phi\psi\rangle = \langle\phi\rangle\langle\psi\rangle + \langle\phi''\psi''\rangle. \tag{5.13}$$

- Finally two more identities will be stated; for the surface average

$$\int_\Sigma \langle\psi\rangle g dA = \langle\psi\rangle \int_\Sigma g dA, \tag{5.14}$$

and

$$\int_R \langle\psi\rangle \nabla g dV d\tau = -\nabla\epsilon\langle\psi\rangle. \tag{5.15}$$

This last equation is identical for the integration over the region occupied by the solid.

A fuller explanation of the above items are given in the thesis of Gough and are included here only for completeness of the following mathematical derivation.

5.1.1 The Microscopic Equations for the Gas-Phase

Equations of motion can be given for each individual phase in the two-phase flow mixture. The Euler equations for the gas-phase are given as:

$$\frac{\partial}{\partial t}\rho + \nabla.\rho\mathbf{u} = 0; \tag{5.16}$$

$$\frac{\partial}{\partial t}\rho c + \nabla.\rho c\mathbf{u} = K; \tag{5.17}$$

$$\frac{\partial}{\partial t}\rho\mathbf{u} + \nabla.(\rho\mathbf{u}\mathbf{u} + \bar{\mathbf{T}}) = 0; \tag{5.18}$$

$$\frac{\partial}{\partial t}\rho(e + \frac{\mathbf{u}.\mathbf{u}}{2} + 2cQ) + \nabla.\left(\rho\mathbf{u}(e + \frac{\mathbf{u}.\mathbf{u}}{2} + 2cQ) + \mathbf{u}.\bar{\mathbf{T}} + \mathbf{q}\right) = 0; \tag{5.19}$$

where ρ is the gas density, $\mathbf{u}$ is the gas-velocity, c is the mass-fraction, e is the internal energy of the gas, K is the rate of reaction, Q is the energy of combustion in the gas-phase and $\mathbf{q}$ is the heat flux. $\bar{\mathbf{T}}$ is the stress tensor which is positive in compression and assumed to be symmetrical. The expression $\mathbf{u}.\mathbf{u}$ signifies the outer product of $\mathbf{u}$ with itself.

These are identical to Gough's equations apart from the inclusion of a mass-fraction equation which also introduces a further term into the total energy formulation.

5.1.2 Boundary Conditions

The boundary conditions for the two-phase reactive flow are given at the gas solid interface by:

$$\rho(\mathbf{u}-\mathbf{w}).\mathbf{n} = \rho^p(\mathbf{u}^p-\mathbf{w}).\mathbf{n}; \tag{5.20}$$

$$\rho c(\mathbf{u}-\mathbf{w}).\mathbf{n} = \frac{\rho^p}{2}(\mathbf{u}^p-\mathbf{w}).\mathbf{n}; \tag{5.21}$$

$$\left[\bar{\mathbf{T}}+\rho\mathbf{u}(\mathbf{u}-\mathbf{w})\right].\mathbf{n} = \left[\bar{\mathbf{T}}^p+\rho^p\mathbf{u}^p(\mathbf{u}^p-\mathbf{w})\right].\mathbf{n}; \tag{5.22}$$

$$\left[\bar{\mathbf{T}}.\mathbf{u}+\rho(\mathbf{u}-\mathbf{w})(e+\frac{\mathbf{u}.\mathbf{u}}{2}+2cQ)\right].\mathbf{n} = \left[\bar{\mathbf{T}}^p.\mathbf{u}^p+\rho^p(\mathbf{u}^p-\mathbf{w})(Q^p+\frac{\mathbf{u}^p.\mathbf{u}^p}{2})\right].\mathbf{n}; \tag{5.23}$$

where the superscript p denotes the solid phase properties and Q^p is the solid propellant energy of combustion.

Again, these are almost identical to those given in Gough's paper where now there are two energies of combustion, the energy released due to the gas-phase combustion and the chemical energy inherently contained in solid propellant prior to burning. The old form of the energy transfer at the boundary can be recovered by setting c equal to zero in (5.23). In this case the energy equation implies that the chemical and kinetic energy in the solid-phase are transferred to gas-phase thermal and kinetic energy. In the new formulation, with non-zero mass-fraction, the solid-phase energy is now transferred to thermal energy, kinetic energy and chemical energy is carried by the reactant species where it may be released at a later time. The implication being that the energy of combustion of the solid propellant Q^p is not equal to the gas-phase energy of combustion Q. The boundary condition given for the mass-fraction states that at the interface half of the propellant decomposes into reactant O and the other half into F.

5.1.3 The Mass Equation

In order to gain some understanding of how the averaging process works, the conservation of mass will be derived in an identical manner as by Gough.

The conservation of mass is given microscopically as (5.16):

$$\frac{\partial}{\partial t}\rho+\nabla.\rho\mathbf{u}=0.$$

Multiplication by the weighting function g and use of equations (5.6) and (5.7) gives:

$$\frac{\partial}{\partial t}\epsilon\langle\rho\rangle+\nabla.\epsilon\langle\rho\mathbf{u}\rangle=-\int_\Sigma g\rho(\mathbf{u}-\mathbf{w}).\mathbf{n}dA. \tag{5.24}$$

Expand $\langle \rho \mathbf{u} \rangle$ according to (5.12) and neglect the correlations $\langle \rho'' \mathbf{u}'' \rangle$. Use the jump condition (5.20), the identity (5.8) and (5.9) to give finally:

$$\frac{\partial}{\partial t} \epsilon \langle \rho \rangle + \nabla . \epsilon \langle \rho \rangle \langle \mathbf{u} \rangle = (1 - \epsilon) \frac{S^p \rho^p}{V^p} \langle \dot{r} \rangle^i. \tag{5.25}$$

The term on the right-hand-side is the exposed surface area of propellant multiplied by the rate of mass transfer from the surface that is the expression is equivalent to the term $\dot{m}$.

5.1.4 The Mass-Fraction Equation

This is derived in an analogous fashion.

The mass-fraction equation is given as (5.17)

$$\frac{\partial}{\partial t} \rho c + \nabla . \rho c \mathbf{u} = K.$$

Multiply the mass-fraction equation by the weighting function g and then integrate over the region occupied by the gas. Using (5.6) & (5.7) produces the result:

$$\frac{\partial}{\partial t} \epsilon \langle \rho c \rangle + \nabla . \epsilon \langle \rho c \mathbf{u} \rangle = -\epsilon \langle K \rangle - \int_\Sigma g \rho c (\mathbf{u} - \mathbf{w}) . \mathbf{n} dA. \tag{5.26}$$

Expand $\langle \rho c \rangle$ and $\langle \rho c \mathbf{u} \rangle$ according to (5.12) and neglect the correlations $\langle \rho'' c'' \rangle$ and $\langle \rho'' c'' \mathbf{u}'' \rangle$. Finally use the jump condition (5.21) , the identity (5.8) and (5.9) to give

$$\frac{\partial}{\partial t} \epsilon \langle \rho \rangle \langle c \rangle + \nabla . \epsilon \langle \rho \rangle \langle c \rangle \langle \mathbf{u} \rangle = \epsilon \langle K \rangle + (1 - \epsilon) \frac{S^p \rho^p}{2 V^p} \langle \dot{r} \rangle^i. \tag{5.27}$$

5.1.5 Further Equations

The derivation of the momentum and energy equations are analogous to the derivation of Gough apart from a slightly different definition of the total energy of the gas:

$$E = \rho(\kappa + e + 2cQ), \tag{5.28}$$

where $\kappa = \frac{1}{2} \mathbf{u} . \mathbf{u}$ is the kinetic energy. The solid-phase mass and momentum equation are unchanged.

5.2 The One-dimensional Non-equilibrium Equations

The set of two-phase, chemical, one-dimensional equations will be stated here. Note that the notation $\langle . \rangle$ is dropped here for the sake of brevity, however, it must be remembered that all flow variables are averages.

$$\frac{\partial}{\partial t}(\rho\epsilon) + \frac{\partial}{\partial x}(\rho\epsilon u) = \dot{m} + \dot{m}_{ig}; \tag{5.29}$$

$$\frac{\partial}{\partial t}(\epsilon\rho c) + \frac{\partial}{\partial x}(\epsilon\rho c u) = \frac{\dot{m}}{2} - \epsilon\rho\Omega c^2; \tag{5.30}$$

$$\frac{\partial}{\partial t}(\rho\epsilon u) + \frac{\partial}{\partial x}\Big(\rho\epsilon(u^2 + p)\Big) = p\frac{\partial \epsilon}{\partial x} + \dot{m}u^p - D; \tag{5.31}$$

$$\begin{aligned} \frac{\partial}{\partial t}(\epsilon E) + \frac{\partial}{\partial x}(\epsilon u(E + p)) &= \dot{m}(Q^p + \kappa^p) + \dot{m}_{ig}e_{ig} \\ -p\frac{\partial(1-\epsilon)(u^p)}{dx} &- u^p D - W_l - q; \end{aligned} \tag{5.32}$$

$$\frac{\partial}{\partial t}(\rho^p(1-\epsilon)) + \frac{\partial}{\partial x}(\rho^p(1-\epsilon)u^p) = -\dot{m}; \tag{5.33}$$

$$\begin{aligned} \frac{\partial}{\partial t}(\rho^p(1-\epsilon)u^p) + \frac{\partial}{\partial x}\Big((1-\epsilon)(\rho^p u^{p2} + R)\Big) &= -(1-\epsilon)\frac{\partial p}{\partial x} - \dot{m}u^p \\ &+D; \end{aligned} \tag{5.34}$$

$$\frac{\partial}{\partial t}(N) + \frac{\partial}{\partial x}(Nu^p) = 0; \tag{5.35}$$

where the new variable N is the number of solid particles. Fragmentation or coalescence of the particles is assumed not to occur.

5.3 Numerical Solution

The basic strategy to computing two-phase flow using Godunov type methods was set out by Toro in [81]. These ideas, as outlined in some detail in [82], and the method applied to the single-phase ignition model of chapter 4 are used to solve the system of equations with a reactive species. Specifically, this involves time-operator splitting which produces a homogeneous hyperbolic problem for the gas and solid phases followed by a system of ordinary-differential-equations.

5.3.1 Time-Operator Splitting

The system of partial differential equations can be written in the form:

$$\mathbf{U}_t + \mathbf{F}(\mathbf{U})_x = \mathbf{S}(\mathbf{U}) \tag{5.36}$$

where $\mathbf{U}$, the vector of conserved variables, is given by.

$$\begin{aligned} \mathbf{U} &= (\mathbf{U}^g, \mathbf{U}^p)^T; \\ \mathbf{U}^g &= (\epsilon\rho, \epsilon\rho c, \epsilon\rho u, \epsilon E)^T, \\ \mathbf{U}^p &= ((1-\epsilon)\rho^p, (1-\epsilon)\rho^p u^p, N)^T \end{aligned} \tag{5.37}$$

and the flux and source terms, $\mathbf{F}(\mathbf{U})$ and $\mathbf{S}(\mathbf{U})$, are functions of $\mathbf{U}$.

The method of fractional steps is used to split the problem into subproblems so that the flow equations and source terms may be handled separately. The flow equations are then further split to handle the gas and solid phases individually. The solution procedure then involves two hyperbolic problems for the gas-phase and solid-phase,

$$\mathbf{U}^g_t + \mathbf{F}^g_x(\mathbf{U}^g) = 0; \tag{5.38}$$

$$\mathbf{U}^p_t + \mathbf{F}^p_x(\mathbf{U}^p) = 0; \tag{5.39}$$

followed by the solution of a system of ordinary differential equations that takes into account the source terms

$$\mathbf{U}_t = \mathbf{S}(\mathbf{U}). \tag{5.40}$$

5.3.2 The Homogeneous Hyperbolic Problems

In this section a lengthy discussion will be included to address some of the mathematical difficulties associated with the flow equations of Gough, and more generally, flow equations for two-phase incompressible flow.

According to Drew [83], early work on the problem of a particle immersed in a fluid dates back to as early as the late eighteenth century. However, in this work more recent studies will be considered. Some very influential books on the theory of two-phase flow began to emerge which brought together the ideas developed over previous years for a variety of diverse applications. For example the books by Soo [10] and Boothroyd [84] concentrated on mixtures

of particle-fluid motion. The work of these authors was based on the original work by Truesdell & Toupin [85] which provides the idea that each single phase can be treated as a continuum which occupy the same region in space. From this equations of mass, momentum and energy for each phase can be deduced along with jump conditions at the interface between the two-phases. The model derived by Gough [58] adopts a more intuitive averaging approach that allows the two phases to occupy distinct regions of space, described as the separated flow theory. The method derives macroscopic quantities from the microscopic equations for each individual phase. The paper by Drew similarly averages the equations but it is particularly relevant to some of the problems associated with the momentum equation. Drew applies the averaging process to two incompressible phases without phase changes. This produces just two mass and momentum equations which are of the same form as those derived by Gough but with fewer source terms, since Drew does not allow phase change and is just concerned with forces transmitted between the two-phases. The paper has an in depth look at the interrelation of the two phases and how forces are transmitted. He notes that for the intergranular stress model suggested by Gough [11] -where the intergranular stress becomes zero above a certain porosity- that in this case the particle momentum equation becomes meaningless. More importantly, he states that generally the one-dimensional, incompressible, inviscid-flow equations without virtual mass effects is ill-posed. By studying the equations he illustrates how the system is fundamentally unstable so that small scale phenomena grow rapidly distorting the true solution. This situation does not improve by extending to two or three dimensions and the system is still ill-posed. He concludes that the equations do not treat small-scale phenomena correctly:

> 'This seems to imply that an inviscid model is nowhere valid for two-phase flows, that is, viscous or eddy stresses are important everywhere.'

Although the addition of virtual mass can make the system well-posed [86], Drew does not feel that this is the total answer. However, if viscous and Reynolds stresses are included the equations are parabolic and well-posed. Finally, he notes some other contributions to this particular difficulty; Prosperretti & van Wijngaarden [87] produce a well-posed system using certain compressibility assumptions and Stuhmiller [88] shows that if the form drag is taken in the form $\xi\rho_2|u_2 - u_1|^2$ then the system is well-posed for sufficiently large ξ. The above discussion by Drew provides a good understanding of some of the detailed modelling that is required to produce a well-posed system.

However, although this addresses the difficulty with the inviscid two-phase flow model, Gough's system of equations has added complexity due to the fact that there are not two incompressible phases, but one compressible and one incompressible phase. In the work by Gough *et al.*, the mix of high speed gas dynamics and incompressible solid particles in the flow is avoided by insisting that supersonic flow can only occur in gas regions only. If this is not assumed to be the case, then the buoyancy force $\epsilon\frac{\partial p}{\partial x}$ can be extremely high causing propulsion of solid propellants and high solid density regions. In the model that assumes an incompressible solid, there is a theoretical minimum in porosity that can be violated if the buoyancy force is too high. In fact Harlow & Amsden [89] commented that

> 'the effect of the factors ϵ and $1-\epsilon$ modifying the pressure, gradients, amplify the tendency for particles to clump together'

so it is not surprising that in the presence of shock waves difficulties arise.

Experimentally [90], when a strong end-pad igniter[1] is adopted to ignite a granular propellant bed, this will force the movement of propellant away from the breech producing a region of ullage and the moving solid particles coagulate into a dense plug. This is the sort of scenario that can be produced using the governing equations in their present form. The most obvious suggestion would be to simply go the whole way and choose a mathematical model that performs well beyond the limit of the model proposed by Gough. This is to assume compressibility of both phases and to adopt the well-posed and robust model that was developed by Baer & Nunziato [21]. In their work- which is developed to predict DDT in granular explosives- equations of mass, momentum and energy conservation are taken for both phases, equations of state for both and finally a compaction equation that controls the change in porosity. However, it could also be argued that such a model is not necessary for the bulk of the burning cycle and perhaps special consideration could be made to allow for the more extreme circumstances that arise (usually) during the early times. Further, the work by Stewart *et al.* [91] addresses the issue, that this approach may be unnecessarily complicated, and constructs a much simplified system of equations that may be used to model the compaction process.

However, the real issue is, does the neglect of important terms (such as virtual mass) exaggerate compressibility effects or is the neglect of compressibility

[1] An end-pad igniter heats the propellant bed by venting igniter from the breech only producing a highly one-dimensional problem with strong pressure waves.

effects producing unphysical solutions?

Dimitrenko & Smirnov [92] simply neglect the pressure gradient at the interface using the argument that this is small compared to viscous drag effects. Soo [93] provides an argument to suggest that the virtual mass effect is of the same order as the buoyancy term so can be used to cancel this out altogether. Although the proposition that these exactly cancel is unlikely - a stationary fluid subject to a pressure gradient will start to move without the effect of drag- the virtual mass may substantially reduce the net contribution of the buoyancy term and viscous drag will be the dominant force on the particles. If the buoyancy force is zero in the solid-phase momentum equation the system is well-posed [94] and it will be shown in this work that a shock wave can form in the two-phase region without instability emerging in the solid phase velocity profiles.

Finally, many of the modern works on two-phase flow problems solve the Navier-Stokes equations rather than the inviscid equations. For example, the work of Gibeling *et al.*[22] is an extension of Gough's work. They use an existing Navier-Stokes code based on the internal ballistics code of Gough. In this work they note that artificial dissipation was employed to avoid numerical overshoots in the porosity. So the inclusion of the viscous terms does not remedy all of the difficulties described above.

To summarise, the inviscid, incompressible two-phase flow equations are ill-posed. The problem can be alleviated by inclusion of virtual mass and a well-behaved system is obtained if the buoyancy term is neglected altogether and viscous drag included. Although the inclusion of viscous effects also produces a well-posed solution difficulties can still arise when the porosity dips below the theoretical minimum which is necessary due to neglect of compressible effects.

5.3.3 The Solid-Phase Problem

In this work, the pressure gradient term in the solid-phase equations is to be neglected which necessitates the inclusion of drag forces and intergranular stress to produce a physical and well-posed model. In this case, the homogeneous part of the solid equations completely decouple from the gas-phase. It is in this respect that the work differs from the two-phase flow problem described in [82].

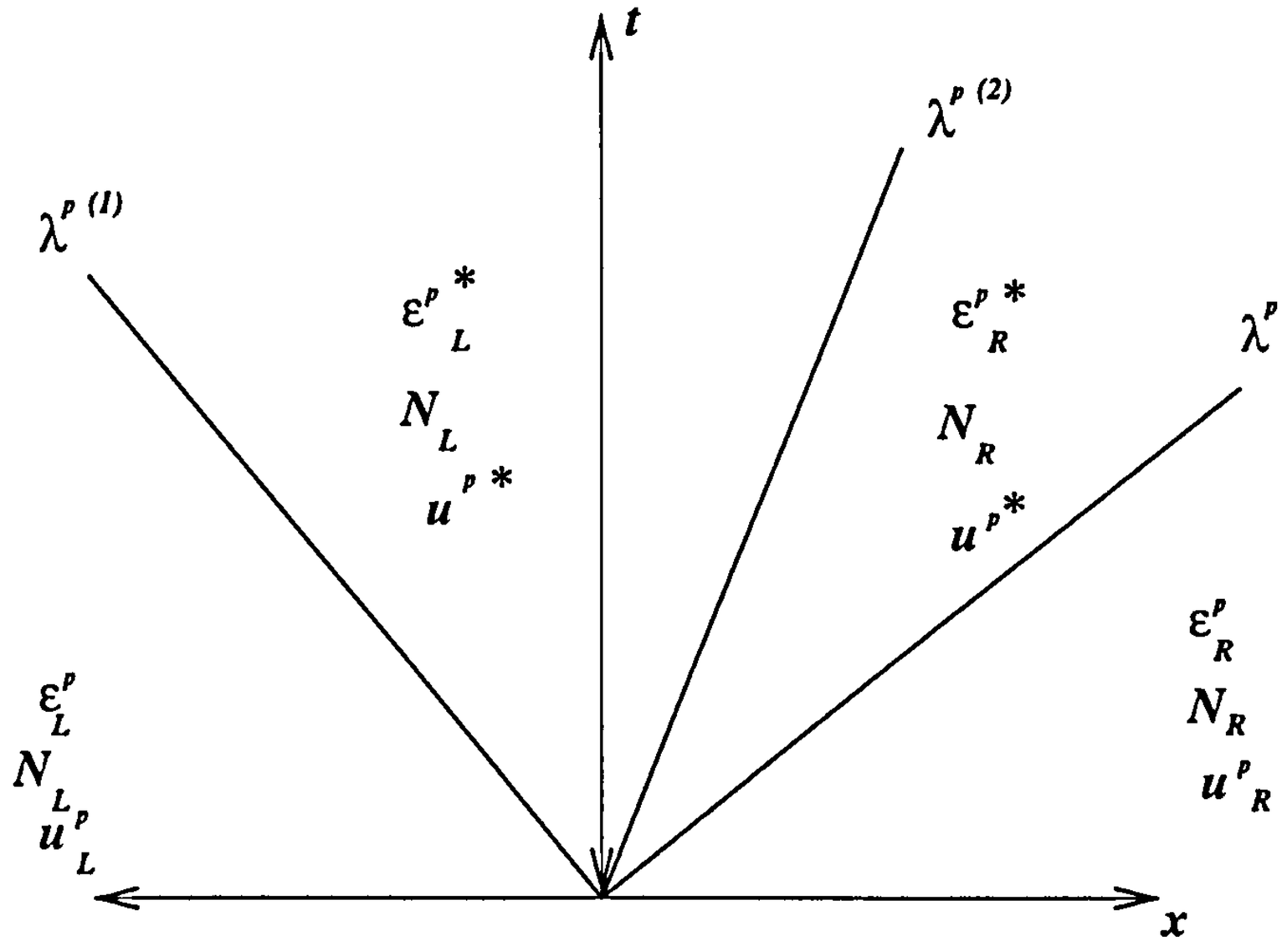

Figure 5.2: Riemann problem for the solid-phase.

For the solid-phase this defines the system:

$$\mathbf{U}^p_t + \mathbf{F}^p_x(\mathbf{U}^p) = 0 \tag{5.41}$$

where $\mathbf{U}^p = ((1-\epsilon)\rho^p, (1-\epsilon)\rho^p u^p, N)^T$ and $\mathbf{F}^p = ((1-\epsilon)\rho^p u^p, (1-\epsilon)(\rho^p u^{p2} + R), N)^T$. R is the intergranular stress that is a measure of how particle-particle forces are included in the momentum balance. An eigenvalue analysis produces three wave speeds $\lambda^{p(i)}$ that are given as u^p, $u^p + a^p$ and $u^p - a^p$ where a^p is a sort of 'sound-speed' associated with the granular fluid that is given by:

$$a^p = \sqrt{\frac{1}{\rho^p}\frac{d}{d\epsilon}(1-\epsilon)R(\epsilon)} \tag{5.42}$$

which, as will be shown below, is given empirically. Thus the equations are totally hyperbolic and well-posed.

Define $\epsilon^p = 1 - \epsilon$, then the solution structure of the solid-phase Riemann problem is given in figure (5.3.3).

The intergranular sound-speed is given empirically in the form

$$a^p = \begin{cases} \frac{a_L \epsilon_0}{\epsilon_1} & \text{if } \epsilon_1 < \epsilon_0 \\ a_L e^{-k(\epsilon_1 - \epsilon_0)} & \text{if } \epsilon_1 < \epsilon_0 < \epsilon^* \\ 0 & \text{if } \epsilon_1 > \epsilon^* \end{cases}, \tag{5.43}$$

where ϵ_0 is the settling porosity and a_L, ϵ^* and k are experimental constants.

The hyperbolic problem is solved using the weighted-average-flux scheme (WAF) [64] as described in section 4.1.15. This requires the solution to the Riemann problem in the solid phase.

5.3.4 The Solid-Phase Riemann Problem

The HLLC method that was described in section (4.1.12) will be used to approximate the solution to the Riemann problem in the solid phase where further details can be found in [81]. To recap, consider the Riemann problem:

$$\mathbf{U}_t + \mathbf{F}(\mathbf{U})_x = 0$$

with initial left and right conditions $\mathbf{U}_l$ and $\mathbf{U}_r$. The solution of the Riemann problem is determined by finding the star-state variables and corresponding left and right fluxes, $\mathbf{F^*}_L$ and $\mathbf{F^*}_R$. The HLLC method produces closed expressions for the left and right star fluxes in terms of the initial data and wavespeeds. The wave-speeds are estimated from the initial data and substituted into the derived formulations for the flux functions given in equations (4.95), (4.94) that is:

$$\mathbf{F^*}_L = \mathbf{F}_L + S_L(\mathbf{U}^*_L - \mathbf{U}_L). \tag{5.44}$$

$$\mathbf{F^*}_R = \mathbf{F}_R + S_R(\mathbf{U}^*_R - \mathbf{U}_R). \tag{5.45}$$

These expressions can be rewritten as:

$$S_L\mathbf{U}^*_L - \mathbf{F^*}_L = S_L\mathbf{U}_L - \mathbf{F}_L = \mathbf{Q}$$

$$S_R\mathbf{U}^*_R - \mathbf{F^*}_R = S_R\mathbf{U}_R - \mathbf{F}_R = \mathbf{R}$$

where $\mathbf{Q}$ is the vector $(q_1, q_2, q_3)^T$ and $\mathbf{R}$ is the vector $(r_1, r_2, r_3)^T$. In the formulae, wave-speeds S_L, S_R and S_M are assumed to be known so by manipulating vector $\mathbf{Q}$ and $\mathbf{R}$, and exploiting the fact that the star state velocity u^* is equal to S_M, explicit formulae for $\mathbf{U}^*_L$ and $\mathbf{U}^*_R$ can be obtained to substitute into equations (5.44) and (5.45). These left and right star fluxes are then used in the WAF method.

The wave-speed estimates will be constructed from the shock/rarefaction relations in an analogous manner to the solution to the gas-phase Riemann problem. These formulations will be summarized here:

$$S_L = u_l^p - q_l a_l^p; \quad S_M = u^{p*}; \quad S_R = u_r^p + q_r a_r^p; \tag{5.46}$$

where

$$q_\alpha = \begin{cases} 1; & \epsilon^{p*}/\epsilon_\alpha^p < 1; \\ \sqrt{\epsilon^{p*}/\epsilon_\alpha^p}; & \epsilon^{p*}/\epsilon_\alpha^p > 1. \end{cases} \tag{5.47}$$

These expressions are the exact shock or rarefaction waves relations for the solid-phase equations. To calculate the value of S_L, S_R and S_M estimates are only required for ϵ^{p*} and u^{p*}. These are chosen according to the local flow conditions:

Linear estimates for the star states are given from:

$$\epsilon^{p*} = \frac{\bar{\epsilon^p}}{2\bar{a}}(u_l - u_r) + \frac{(\epsilon_l^p + \epsilon_r^p)}{2} \tag{5.48}$$

$$u^* = \frac{(u_l + u_r)}{2} + \frac{\bar{a}^p}{2\bar{\epsilon^p}}(\epsilon_l^p - \epsilon_r^p) \tag{5.49}$$

where $\bar{\epsilon^p} = \sqrt{\epsilon_l^p \epsilon_r^p}$ and $\bar{a}^p = (a_l^p + a_r^p)/2$.

Let:

$$\epsilon_{min}^p = min(\epsilon_l^p, \epsilon_r^p), \quad \epsilon_{max}^p = max(\epsilon_l^p, \epsilon_r^p). \tag{5.50}$$

If:

$$\epsilon_{min}^p < \epsilon^{p*} < \epsilon_{max}^p. \tag{5.51}$$

then linear estimates are used in formulae (5.47) and (5.46).

Alternatively, if:

$$\epsilon^{p*} < \epsilon_{min}^p < \epsilon_{max}^p; \tag{5.52}$$

(5.53)

then the two-rarefaction approximation is given for ϵ^{p*} and u^{p*}:

$$\epsilon^{p*} = \bar{\epsilon^p} \exp \frac{u_l^p - u_r^p}{2\bar{a^p}}; \tag{5.54}$$

$$u^* = \frac{1}{2}(u_l + u_r + \bar{a^p} ln \frac{\epsilon_l^p}{\epsilon_r^p}) \tag{5.55}$$

Finally, a two-shock approximation will be adopted if:

$$\epsilon^{p*} > \epsilon^p_{max} > \epsilon^p min \quad ; \tag{5.56}$$

$$\epsilon^{p*} = 1/4(-b + \sqrt{b^2 - 4c})^2; \tag{5.57}$$

$$u^* = u_\alpha \pm a_\alpha(\epsilon^{p*} - \epsilon^p_\alpha)/\sqrt{\epsilon^p_\alpha \epsilon^{p*}}; \tag{5.58}$$

$$b = \frac{(u_r - u_l)\sqrt{\rho_2}\bar{\epsilon^p}}{\bar{a^p}(\sqrt{\epsilon^p_l} + \sqrt{\epsilon^p_r})}; \tag{5.59}$$

$$c = -\frac{\sqrt{\epsilon^p_l}\epsilon^p_r + \sqrt{\epsilon^p_r}\epsilon^p_l}{\sqrt{\epsilon^p_l} + \sqrt{\epsilon^p_r}}. \tag{5.60}$$

This is sufficient information to calculate the solution to the Riemann problems which are inserted into the construction of the WAF formulation as described in section 4.9.

5.3.5 The Gas-Phase Problem

Following the solution to the solid-phase equations, the solution of the gas-phase equations can be found. Any variables updated in the previous calculation which are involved in the gas equations, such as porosity, remain constant. The hyperbolic problem for the gas-phase is defined as:

$$\mathbf{U}^g_t + \mathbf{F}(\mathbf{U}^g)_x = 0. \tag{5.61}$$

Writing

$$\rho^g = \epsilon\rho; \quad u^g = u; \quad p^g = \epsilon p \tag{5.62}$$

will transform the homogeneous equation into the identical form considered in chapter 4. From this position the equivalent numerical methods can be used.

5.3.6 The System of O.D.E.'s

This is defined as:

$$\frac{\partial}{\partial t}(\rho\epsilon) = \dot{m} + \dot{m}_{ig} \tag{5.63}$$

$$\frac{\partial}{\partial t}(\epsilon\rho c) = \frac{\dot{m}}{2} - \epsilon\rho\Omega c^2 \tag{5.64}$$

$$\frac{\partial}{\partial t}(\rho\epsilon u) = p\frac{\partial\epsilon}{\partial x} + \dot{m}u^p - D \tag{5.65}$$

$$\frac{\partial}{\partial t}(\epsilon\rho E) = \dot{m}(Q + \kappa^p) + \dot{m}_{ig}e_{ig}$$

$$- p\frac{\partial(1-\epsilon)(u^p)}{dx} - u^p D - W_l - q \tag{5.66}$$

$$\frac{\partial}{\partial t}(\rho^p(1-\epsilon)) = -\dot{m} \tag{5.67}$$

$$\frac{\partial}{\partial t}(\rho^p(1-\epsilon)u^p) = -\dot{m}u^p + D \tag{5.68}$$

$$\frac{\partial}{\partial t}(N) = 0 \tag{5.69}$$

More simply this can be expressed as:

$$\mathbf{U}_t = \mathbf{S}(\mathbf{U}) \tag{5.70}$$

This system of equations needs to be solved over the whole spatial domain and the solver used previously [95] in the single-phase ignition model, is adopted. However, there are some fundamental differences between the single-phase problem and the new posed two-phase problem.

In the single-phase model there were four equations of mass, species concentration, momentum and energy. For each cell i the stiff solver was called to solve a system of four equations and in this manner the new solution could be obtained over the entire domain at the new time-level.

The immediate impression is that this method can be extended for the two-phase problem so that we have now mass and momentum equations for both phases, a species and energy equation for the gas-phase and finally a particle number equation for the solid phase. In total for each cell i a system of seven equations must be solved. Unfortunately, the two-phase flow equations involves a number of porosity derivative terms in the momentum and energy equations. These have been calculated in the past by using a second order central difference relation that is given in terms of the two-adjacent cells to any cell i e.g. for a uniform grid:

$$\frac{\partial\epsilon(i)}{\partial x} = \frac{\epsilon(i+1) - \epsilon(i-1)}{2\Delta x} \tag{5.71}$$

This means that the ordinary differential equation in cell i is **dependent** on the conditions in the two-adjacent cells, that is, the equations across the entire

domain are fully coupled meaning that we have a system of o.d.e.'s with $m \times 7$ equations where m is the number of cells in the domain. This entire system must be solved by the stiff solver.

As can be seen from the above system, the right-hand-side of equations (5.63) to (5.69) involve a number of source terms. The accurate determination of these is fundamental in the modelling of propellant combustion.

5.4 Source terms

5.4.1 Rate of Mass Addition

Mass addition to the system is controlled by the factors $\dot{m}_{ig}$ and $\dot{m}$.

The rate of addition of igniter gas $\dot{m}_{ig}$ is a prescribed constant flux calculated simply by dividing the total mass of igniter by the length of the primer tube and the duration over which the igniter-gas is vented. This factor will dominate the events at early times. Once combustion is sustained the high ratio between energy release due to propellant burning and any energy contribution from igniter gas will be so high that this term will be much less significant.

The function $\dot{m}$ is perhaps the most important factor in the combustion problem since this controls the rate of energy release throughout the bulk of the burning cycle. Much of the early work concentrated on detailed calculation of this function. The rate of mass addition from gasification of solid propellant is a function of exposed surface area $S^p(t)$ of the propellant granules and the rate of regression of the propellant surface $\dot{r}(t)$:

$$\dot{m} = \rho^p S^p \dot{r} \tag{5.72}$$

where ρ^p is the density of the propellant. Both the surface area and the rate of regression vary in time depending on the external influences on the solid such as rapid temperature changes. The methods that are used to calculate the change in surface area in time is well-founded. However, modelling the rate of regression of the propellant remains an unresolved problem. Empirical

methods have been used in the past that have been reliable and quite successful in normal burning regimes. However, unexplained deviations from these empirical laws under unconventional conditions have necessitated a more physical understanding of what is really happening at the gas/solid interface and detailed modelling. Also, if the burning is assumed to occur in the gas-phase as described previously then distinctions between the rate of solid gasification and gaseous combustion must be made.

5.4.2 The Form Function

Research on how the exposed surface area of a burning propellant grain changes in time dates back to the 1950's. A more detailed discussion of the theory described can be found in [2]. One of the most important observations that is used as a basis for the prediction of propellant burning is the idea of 'parallel burning'. This is the phrase used to describe how a propellant grain will burn in parallel layers so preserving the original grain geometry prior to burnout. By using this rule, functions can be derived that link the exposed grain surface area to the fraction of propellant that has been burnt at any time.

Define the size of the propellant grain, D, as the least thickness required for complete combustion. [2] Let f be the fraction of D remaining at time t, z be the fraction of weight burnt at time t and S be the surface area at that instant. The *form function* relates z to f (standard British method) or alternatively, S to z (some other continental countries) which depends on the initial geometry of the propellant grain. This function can be written in the form:

$$z = (1 - f)(1 + \theta f), \tag{5.73}$$

where θ is a function of f.

The shape of the propellant determines the form of θ. The sign of θ determines how the surface area changes in time; if θ is positive the surface area of the propellant decreases in time and the burning is said to be *degressive*. Conversely, if θ is negative then the surface increases in time and the burning is *progressive*.

The form function will now be used to calculate the rate of mass loss $\dot{m}$.

[2] For a multitubular propellant this is redefined as the least thickness before grain fragmentation and the distance is called the 'web'.

Consider the burning of a single propellant grain:

$$\dot{m}_{gr} = m_I \frac{dz}{dt} = m_I \frac{\partial z}{\partial f} \frac{\partial f}{\partial t}, \tag{5.74}$$

where $\dot{m}_{gr}$ is the mass-loss of the grain which varies in time, m_I is the initial mass of a propellant grain in kg and $z = 1 - m_{gr}/m_I$. Using equation (5.73) it is easy to show that:

$$\frac{\partial z}{\partial f} = -\sqrt{(1+\theta)^2 - 4\theta z}. \tag{5.75}$$

Now consider how the expression $\frac{\partial f}{\partial t}$, which is actually the rate of regression of the solid propellant surface, can be calculated.

5.4.3 Surface Regression

Most models of propellant burning rely on what is known as 'Piobert's law of burning' to calculate the rate of surface regression $\dot{r}$. This states that the rate of solid regression is a function of gas pressure:

$$\dot{r} = B_{cf} p^n \tag{5.76}$$

where B_{cf}[3] is the burn-rate coefficient and n is the pressure index, both empirical constants. For many propellants, the burn-rate coefficient and pressure index may change between different pressure ranges. The solid gasification is assumed to be controlled by this law once the gas temperature increases above some temperature T_d. Recall from section (3.2.1), gas-phase chemical kinetics dominate events in the chamber until the chemical time of the gas-phase reaction becomes negligible. It is at this point that the gas is said to be in chemical equilibrium and the combustion will then be determined by the rate of solid-phase gasification $\dot{m}$. The method that is used to calculate the empirical coefficients required in Piobert's burning law assume that chemical equilibrium has been established and so is actually a measure of both gasification and combustion. For arguments sake, it will be taken as a measure of solid-phase gasification alone here. However, in the next chapter, the whole

[3]Care must be taken when extracting the burn-rate coefficient from available data; in many countries the above theory is formulated in terms of surface area which gives a 'double-sided' burn-rate. This differs from the above description of burn-rate coefficient by a factor of two.

question of what physical processes occurr between the gas and solid material opens a challenging modelling problem. Use of equation (5.76) implies

$$\dot{r} = \frac{\partial(-fD)}{\partial t} = B_{cf}p^n. \tag{5.77}$$

In the two-phase flow work that follows, the number of grains per unit length at time t is given from the particle number $N(x,t)$ and in this case the total rate of addition of mass $\dot{m}$ per unit length is given as $N(x,t)\dot{m}_{gr}$. Substituting expressions (5.75), (5.77) and multiplication by N gives on substitution into equation (5.74):

$$\dot{m} = Nm_I.\sqrt{(1+\theta)^2 - 4\theta z}.\frac{B_{cf}p^n}{D}. \tag{5.78}$$

There are a number of possibilities that can be chosen to calculate the value of $z(t)$ that is still required to calculate $\dot{m}$ explicitly from equation (5.78). The mass of propellant present at any time can be calculated using the porosity $\epsilon(x,t)$. The porosity is the volume fraction that is occupied by gas at (x,t), whilst $(1-\epsilon(x,t))$ is the fraction occupied by propellant. This means that at any position and time the mass of propellant in the chamber is given as: $\rho^p(1-\epsilon)V$ where V is the volume of the vessel and so the fraction of mass burnt is

$$z = 1 - \frac{\rho^p(1-\epsilon)V}{Nm_I}$$

Thus, equation (5.78) provides a way to calculate the rate of change of solid into gas for any form function θ. θ depends on the propellant grain geometry and some possible grain geometries will be briefly described. The numerical code that has been written will accept any of the three geometries listed below.

Tubular

This is a cylindrical length of propellant with one hole through the center of the grain. Let the wall-thickness of the tube be D, the mean radius be R and the length be kD. It is easy to show that the form function can be given as:

$$z = (1-f)(1+f/k), \tag{5.79}$$

and the form function as defined in equation (5.73) can be given as $\theta = 1/k$.

Multitubular Propellant

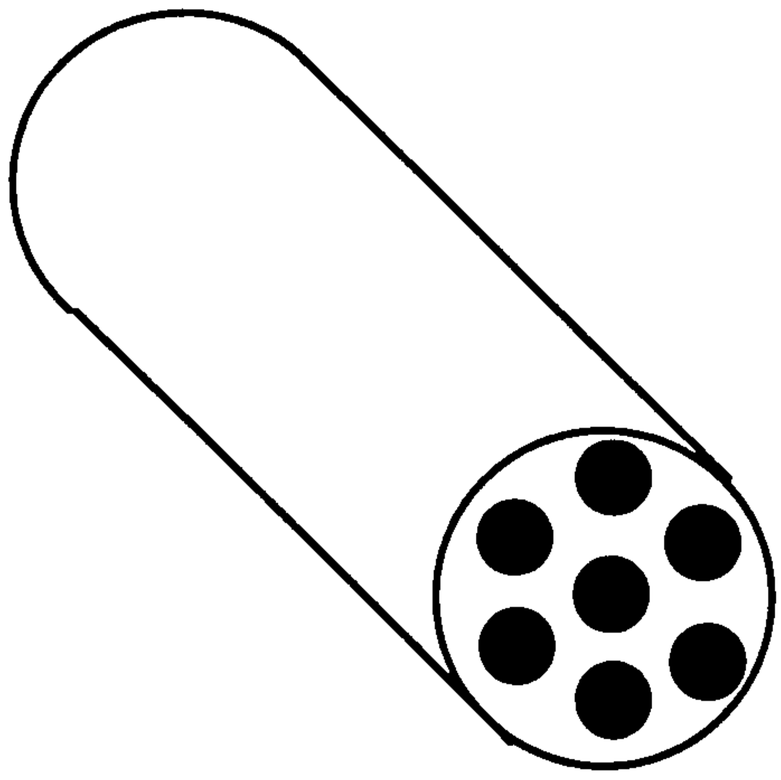

Figure 5.3: A typical seven perforation multi-tubular propellant grain.

Slotted Tube

These consist of tubes, as described above, which are slotted together. The geometry for this propellant is a little more difficult to deal with and an approximation can been used to give a value for the form function [2]. The result is only stated here: The tube parameters are defined as above but now a slot is also defined that is assumed to be formed of two radii inclined at an angle 2ω. The form function for the slotted tube can be given approximately as:

$$z = (1 - f)(1 + fD^2/\Omega), \tag{5.80}$$

where $\Omega = 2RD(\pi - \omega)$.

Multitubular

The propellant grains are short tubes with seven evenly spaced perforations running along the length as shown in figure (5.3). The web D is the distance required to burn before the tube will fragment into twelve curvilinear triangular prisms. About 85% of the burning occurs before fragmentation and the exact calculation of the burning surface needs to consider two completely different configurations before and after fragmentation. Pike[96] wrote a piece of code that does this and it is included in the full code as a subroutine. However, for simplicity there is a good approximation that holds well during the first 85% of burning. By redefining the web, D' by equating $D' = 1.15D$, then the form function is:

$$z = (1 - f)(1 - 0.172f) \tag{5.81}$$

where $\theta = -0.172$.

5.4.4 Drag

Since the buoyancy term has been neglected, the particle-phase will only move if drag is included. The units of drag $f_s = \frac{force}{m^3}$ describes the force on the solid particles due to the movement of gas which explains why this quantity is heavily dependent on the relative velocity of the two phases. This is taken directly from the work of Gough [11] which is in turn from the original ideas set down by Ergun [97].

$$f_s = \frac{(1-\epsilon)\rho^p k_D (u - u^p)|u - u^p|}{D_p} \frac{\sqrt{(1 - z\theta)}}{(1 - z)} \tag{5.82}$$

where θ is the form function; z is the fraction of propellant burnt and $D_p = 6\frac{V_0}{S_0}$ the effective diameter of the propellant grains given in terms of the initial volume V_0 and the initial surface area S_0 of the propellant grains. k_D is empirical given as

$$k_D = \begin{cases} 1.75 & \text{if } \epsilon < \epsilon_0 \\ 1.75\left[(\frac{1-\epsilon}{\epsilon})(\frac{\epsilon_0}{1-\epsilon_0})\right]^{0.45} & \text{if } \epsilon_0 < \epsilon < \epsilon_1 \\ 0.3 & \text{if } \epsilon > \epsilon_1 \end{cases} \tag{5.83}$$

$$\epsilon_1 = \frac{1}{1 + 0.02\frac{(1-\epsilon_0)}{\epsilon_0}} \tag{5.84}$$

and ϵ_0 is the settling porosity.

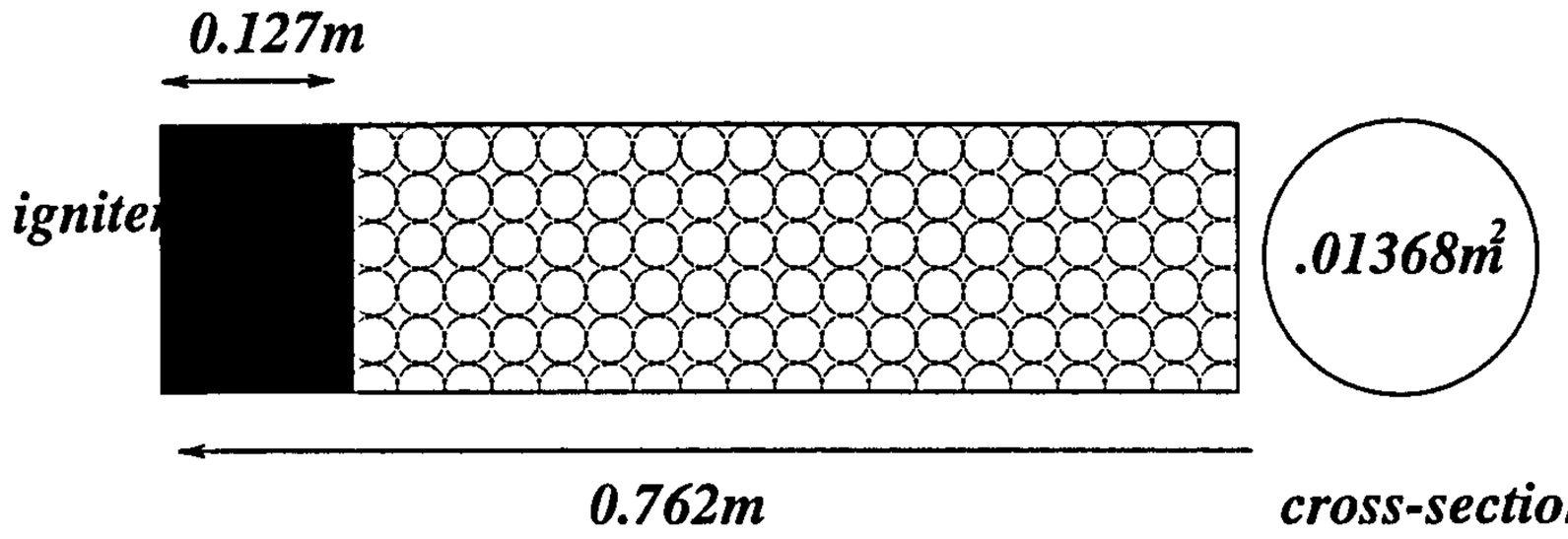

Figure 5.4: Two-phase flow test problem.

5.4.5 Further Sources

In the model the contribution of interphase heat-transfer q and heat loss to the walls W_l will be assumed to be negligible. However, in the following chapter the importance of q will be emphasized for if in reality there is no heat-transfer there will be no solid gasification to initiate combustion. The assumption made is that the energy of combustion is the net heat created, taking into account interphase heat transfer.

5.5 Two-Phase Flow Test Problem

The test problem described in chapter 4 is now extended where the chamber contains mass m of seven-perforation granular propellant as illustrated figure (5.4). The propellant has form function θ, outer diameter d_o, inner perforation diameter d_i and length d_l. The chamber length is l and the cross-sectional area of the chamber is A_s. The initial conditions are pressure p_0 and gas temperature T_0. Again, burning is initiated by the primer tube that runs along a sixth of the axial length and vents inert produce gas into the chamber. The total mass of igniter is given as m_{ig} which is vented at a constant rate for time t_{ig}. In this testcase, the igniter will introduce chemical energy e_{ig} immediately on introduction into the combustion chamber. The data set for this problem is given in the table below:

l	0.762m	A_s	$0.0136848m^2$
$ncell$	300	c_{fl}	0.75
γ	1.27	T_0	294.4K
p_0	$101400Pa$	b	$.0010838m/kg$
m_{ig}	$.2268kg$	t_{ig}	10ms
e_{ig}	$1.57\ \frac{MJ}{kg}$	ρ^p	$1.57\frac{kg}{m^3}$
Q^p	$3.7363\frac{MJ}{kg}$	B_{cf}	$6.241 \times 10^{-9} m/sec(pa)^n$
n	0.9	m	$9.5255kg$
d_o	$.0143m$	d_i	$.001143m$
d_l	$.0254cm$	W	21.13
R	$8313.3J/Kkgmole$	T_d	$420K$
ϵ_0	0.4	ϵ_1	1
a_L	$24.8m/sec$	k	3
E_A/R	5000K		

l is the length of domain, $ncell$ is the number of cells taken.

Flow variable histories for this two-phase problem were obtained over the first $2ms$ and the pressure, mass-fraction and two reaction rate plots are given in figure 5.2a-d. Flow profiles are given at times $0.5ms$, $0.75ms$ and $1ms$ in figures 5.3a-d and over times $1.25ms$, $1.5ms$ and $2ms$ in figures 5.4a-d.

Before the solutions are discussed, there are several major differences between the previous gas-phase ignition model experiment and the two-phase flow model that must be emphasized. The inclusion of the two-phase flow equations enables modelling of the movement of particles in the chamber which has a direct effect on the variable $\dot{m}$ as given by equation (5.78). Whilst in the single-phase flow model the rate of addition of igniter gas $\dot{m}_{ig}$ was much greater than the rate of addition of reactant gas $\dot{m}$ and both remained constant, in this full combustion problem this is not the case. Although $\dot{m}_{ig}$ will continue to be constant and at very early times will be greater that $\dot{m}$, the rate of gasification will now be calculated using Piobert's law so that it will be assumed that gasification increases with pressure. Finally, Pike's [96] formulation of the form function is employed which will mean a change in exposed surface area. As a consequence there will be a rather complicated interrelation of flow variables.

Figure (5.5) shows the pressure history during early times. A compression wave forms at the end of the primer length and travels towards the projectile-base. The wave reflects on the base just after $0.7ms$ and starts to travel towards the breech. Now consider the mass-fraction plot (5.6); the solution

looks quite different from the single-phase solution for now non-zero mass-fraction appears coincident with the compression. If the temperature profiles are consulted in figure (5.11), the gas temperatures behind the compression are now much higher than the gasification temperature $420K$ and so gasification is switched on immediately behind the compression.

Figure (5.10) illustrates a high pressure region at the primer and an almost linear decrease in pressure from the primer to the shock wave that is traveling towards the opposite end. This decrease is due to the switch on of gaseous mass addition behind the shock wave.

However, the higher temperatures in the primer region will still cause higher rates of gasification of propellant and the reactant wave feature introduced in chapter 4 can be seen once more between($x = 0.127m, t = 0.2ms$) and ($x = 0.7m, t = 1ms$). This illustrates the movement of reactant species into cooler regions of the chamber. The density profiles in figure (5.9) clearly displays a dense region of gas that stretches between $0.35m < x < 0.5m$ at $t = 0.5ms$ which causes a peak in temperature. This is the the presence of the reactant wave which produces a denser region of gas as can be confirmed from the mass-fraction profiles in figure (5.10).

Profiles of the solid velocity and particle number can be seen in figure (5.12) and the porosity is given in figure (5.11). Throughout these times the solid is moving at a relatively low speed away from the primer region producing higher porosity in the primer region. Comparison with the gas-velocity history confirms that the solid particles are being dragged by the gas movement. However, at later times, the gas velocity has clearly changed direction figure (5.13) but the drag forces are only sufficient to decelerate the particles as seen in figure (5.16) by the decline in the peak of the curve over time. Although the effect of this particle movement does not have any dramatic effect on the pressure history of the gas, the resulting change in porosity, particle number and $\dot{m}$ will have some influence.

The reaction rate in figure (5.7) is now plotted so that the effect of chemistry in the two-phase flow model can be fully appreciated. The absence of curves at early times indicates how the reaction rates are much higher after $0.75ms$ between $0.7m < x < 0.762m$. To capture the detail at earlier times, the plot (5.8) limits the range of reaction rate. This indicates that although the mass-fraction is switched on by the compression wave, the reaction rate behind this wave is relatively low. This is due to quite low quantities of reactant and modest temperature levels. The reaction rate is higher behind the reactant wave due to the much higher concentration of reactant. The reaction

rate increases along this wave as the increasing temperatures mean further gasification and enhanced combustion. This is illustrated by the temperature peak seen in figure (5.11). Ultimately the reflected shock meets the reactant wave producing even higher levels of reaction. After this, the reaction rate close to the projectile base remains higher than in any other location in the chamber which causes sustained high temperature in this region as seen in figure (5.15).

The effect of including the second-phase into the calculations is not dramatic and some of the features could have been reproduced in the gas-phase ignition model by just increasing the size of the constant mass source $\dot{m}$. This emphasizes the value of studying a simplified model in order to recognize some of the important features before the detail is obscured by solving the more complex model.

However, again this describes how the time and location of ignition can occur away from the primer. The reaction rate plots then indicate how location of ignition can have a dramatic effect on the release of chemical energy throughout the rest of the combustion cycle.

A deficiency of the above model is the use of empirical information that was originally derived for equilibrium chemistry models. Specifically, Piobert's law was designed to measure the rate of change of energy due to propellant gasification and combustion. In the above test, the law has been used as a measure of surface gasification alone. The use of this is only truly valid once gas-phase chemical times become negligible and equilibrium chemistry is approached. Furthermore, the model assumes that it is primarily the rate of change in gas-phase temperature that controls the rate of gasification, any influence of solid-phase thermochemistry is ignored. In the following chapter these issues will be addressed by concentrating on heat-transfer processes at the gas-solid interface- the site of solid gasification.

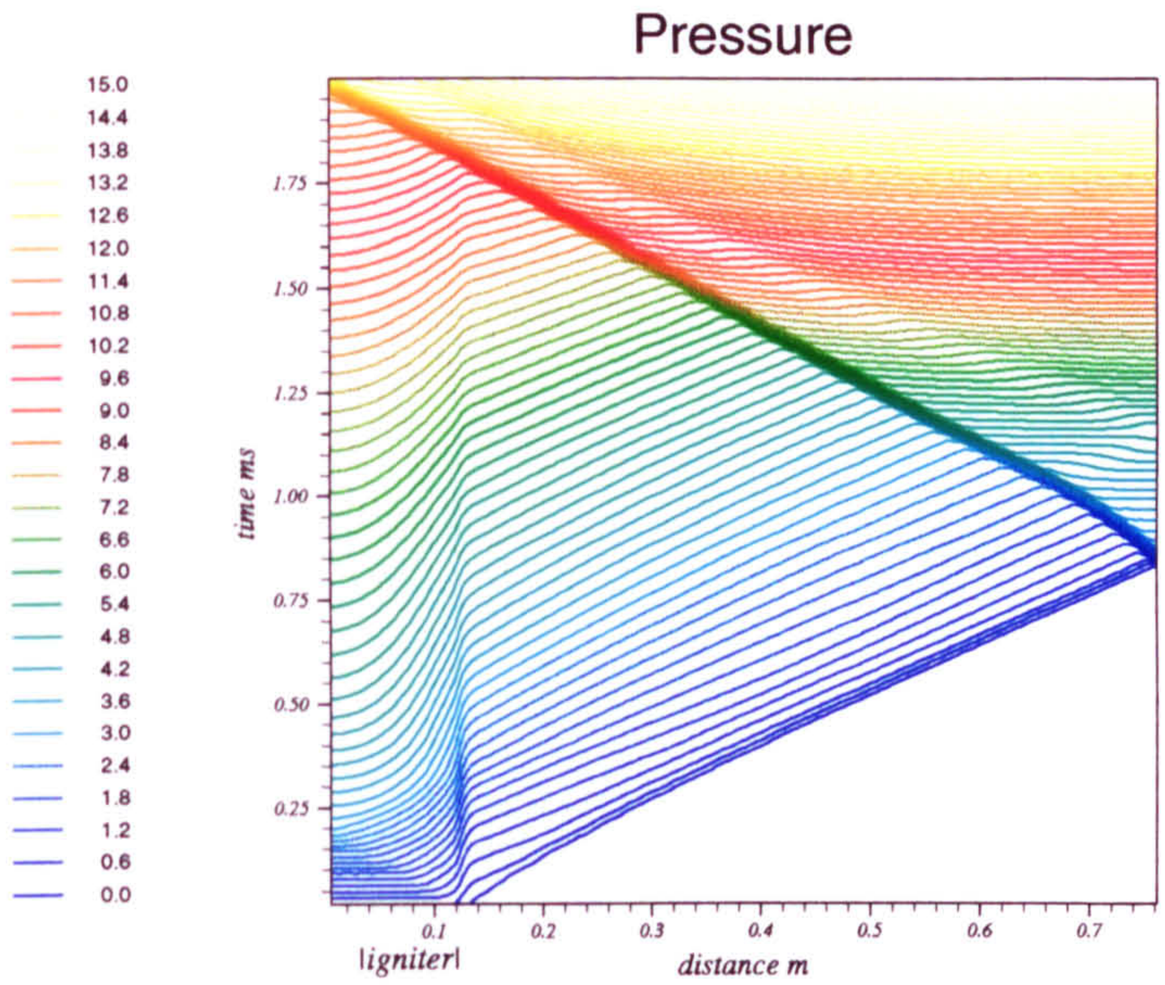

Figure 5.5: Pressure history over the first $2ms$

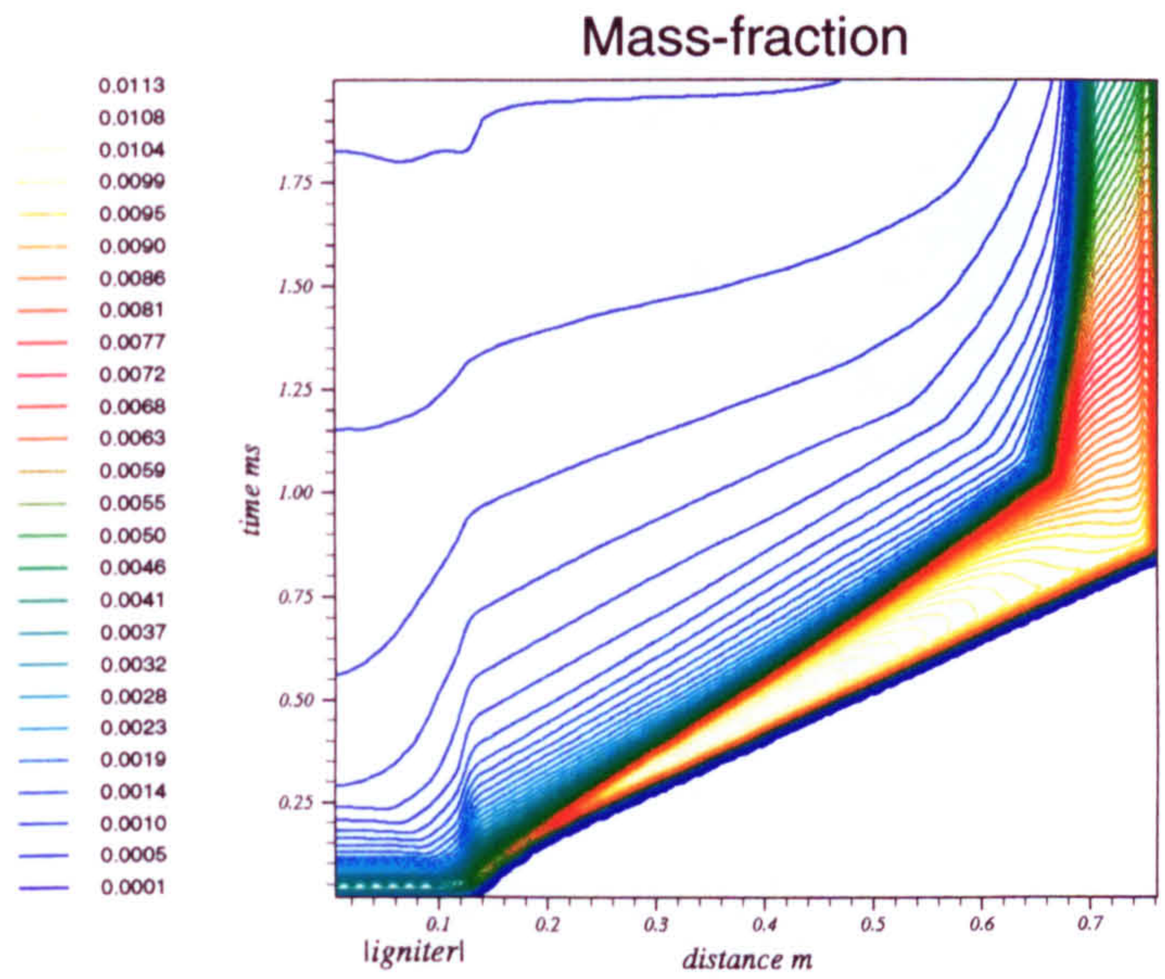

Figure 5.6: Mass-fraction history over the first $2ms$

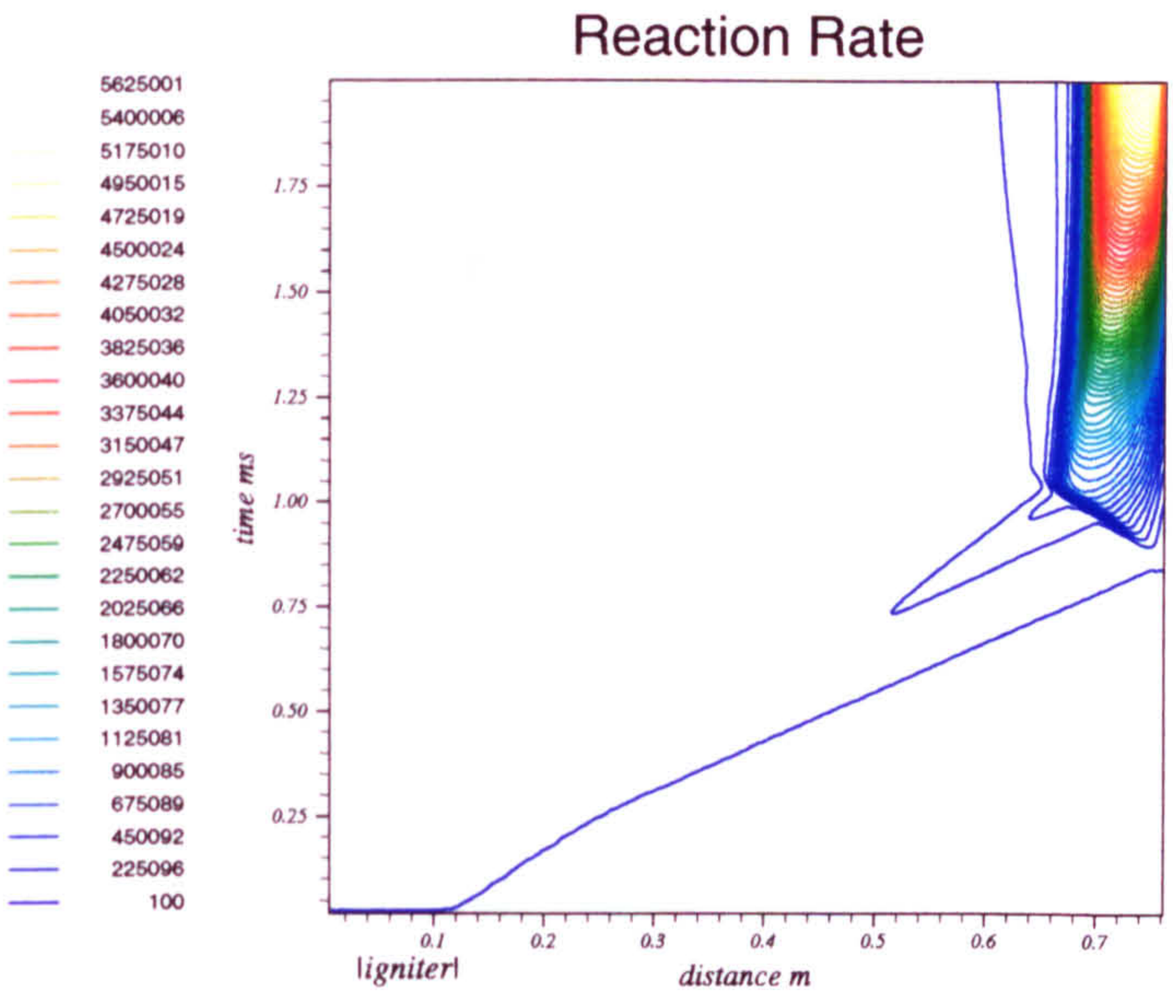

Figure 5.7: Reaction rate history over the first $2ms$

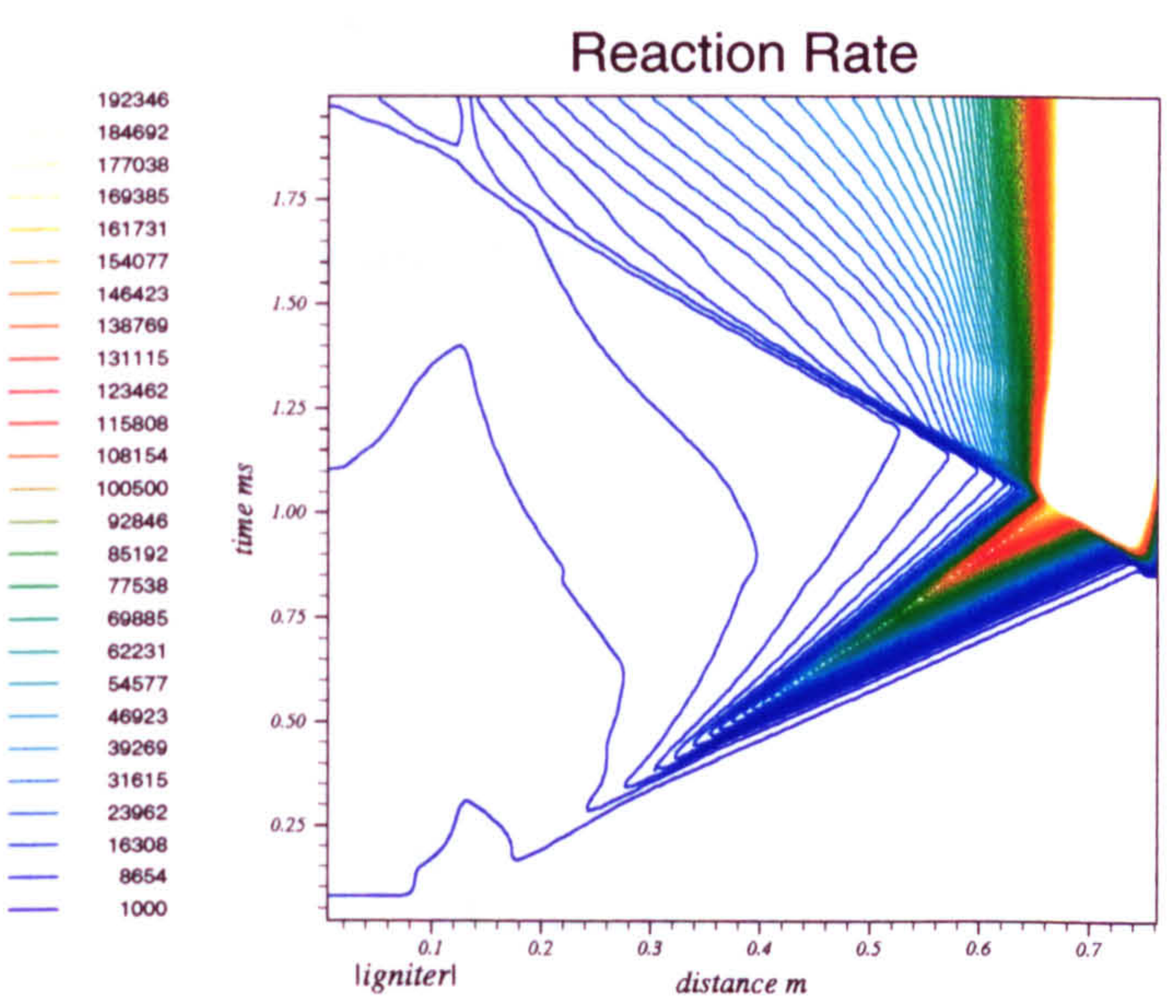

Figure 5.8: Reaction rate history over the first $2ms$

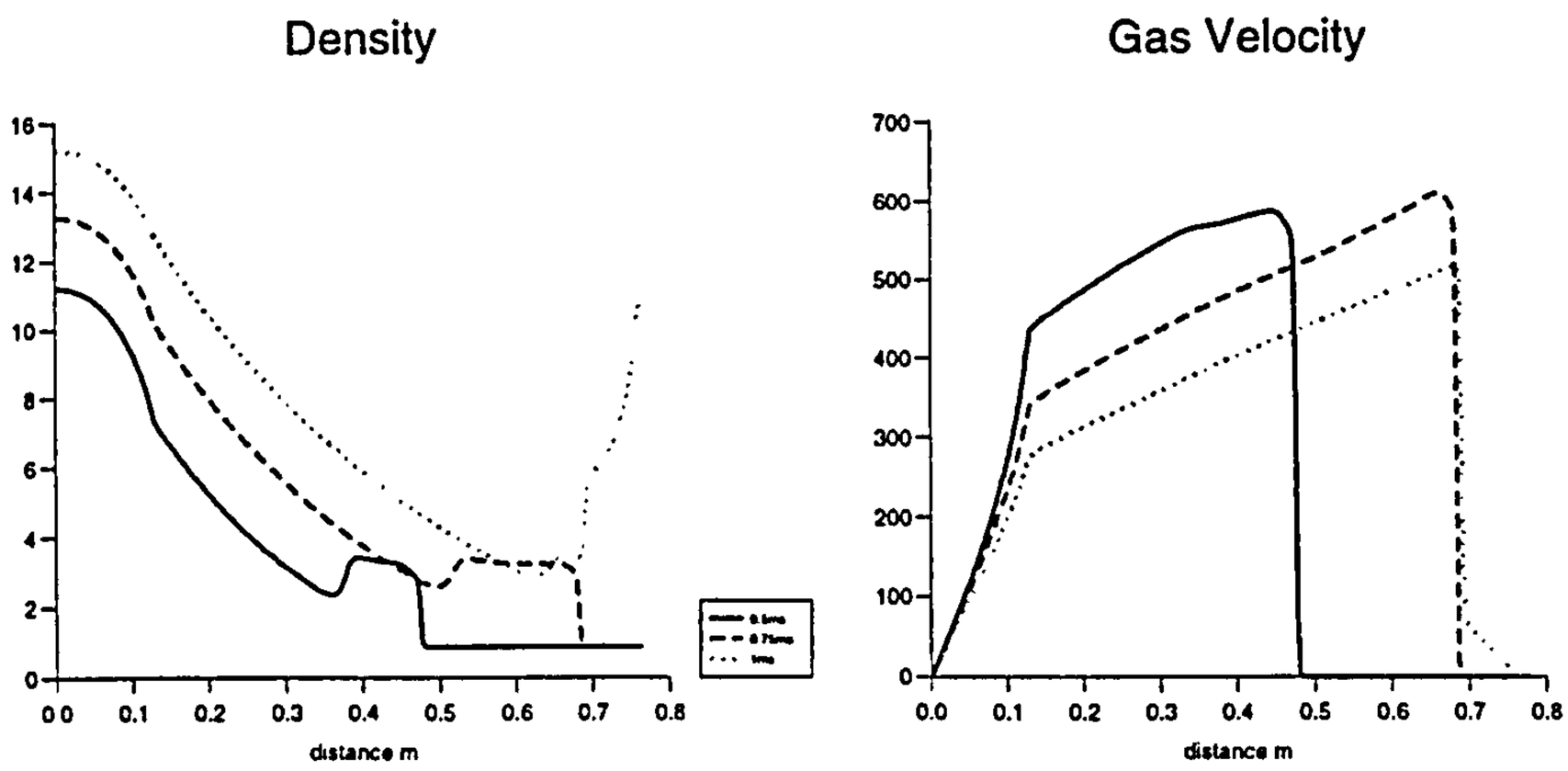

Figure 5.9: Density and gas-velocity profiles at $t = 0.5ms$ (full line), $t = 0.75ms$ (dashed line) and $t = 1ms$ (dotted line).

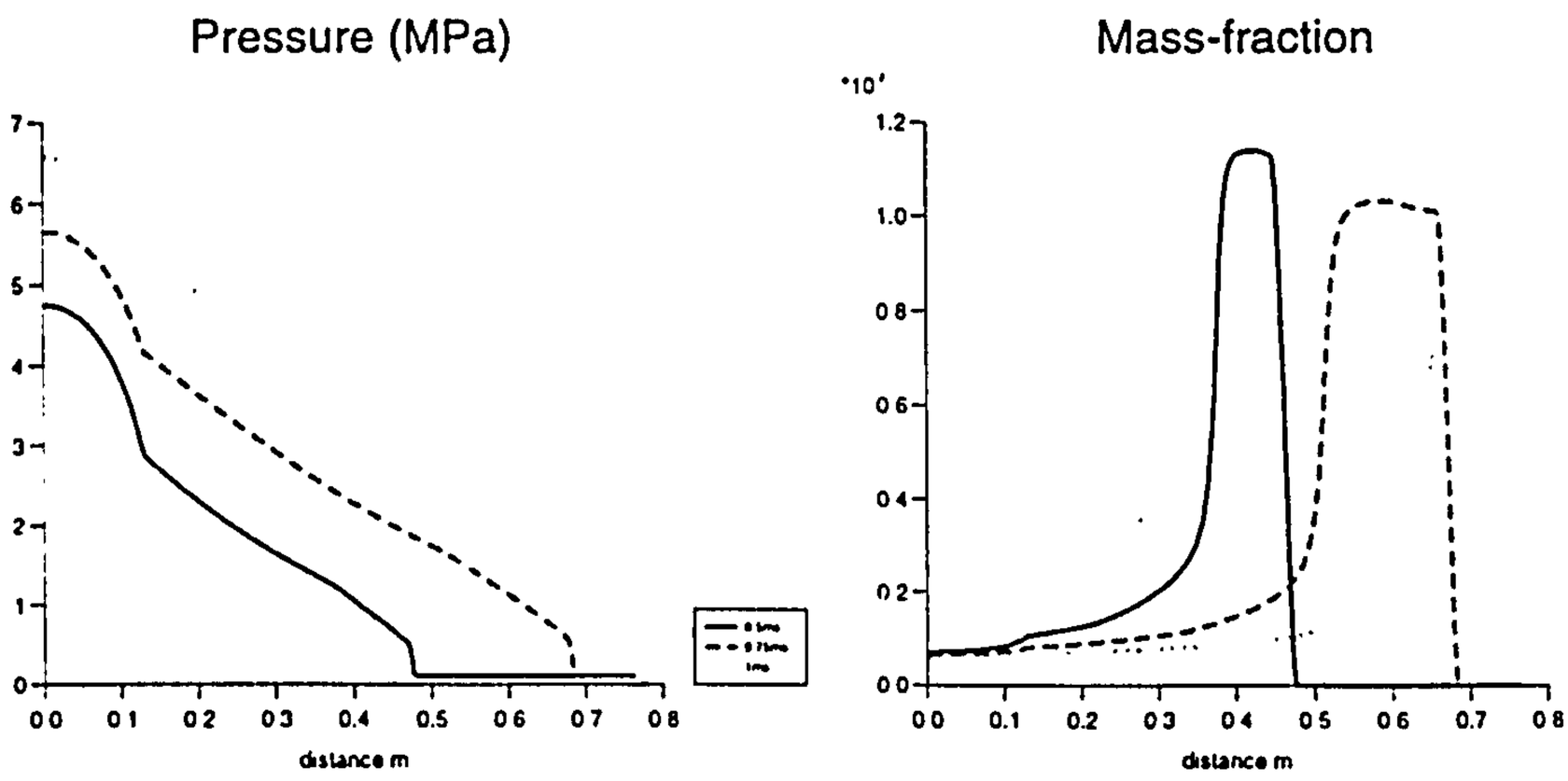

Figure 5.10: Pressure and mass-fraction profiles at $t = 0.5ms$ (full line), $t = 0.75ms$ (dashed line) and $t = 1ms$ (dotted line).

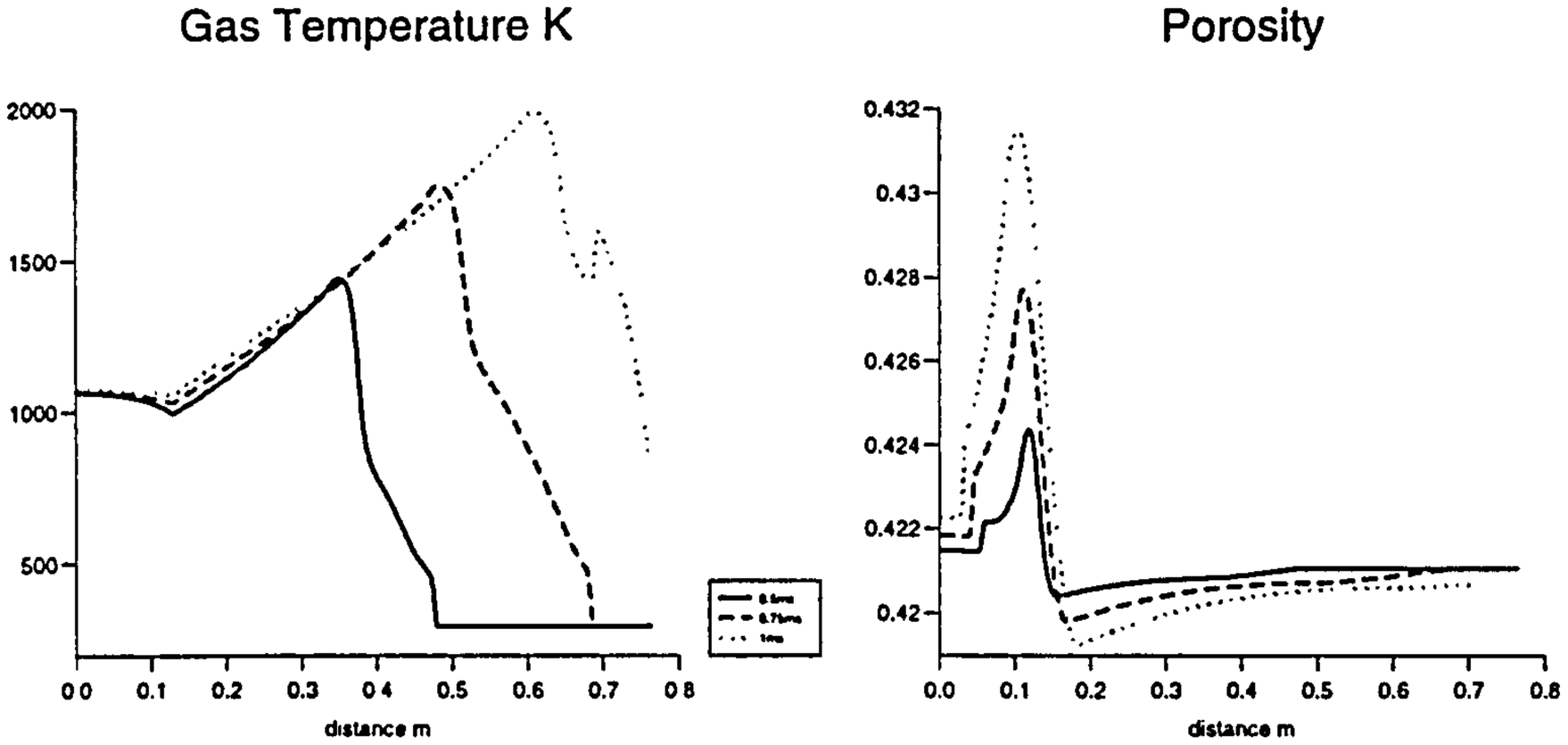

Figure 5.11: Temperature and porosity profiles at $t = 0.5ms$ (full line), $t = 0.75ms$ (dashed line) and $t = 1ms$ (dotted line).

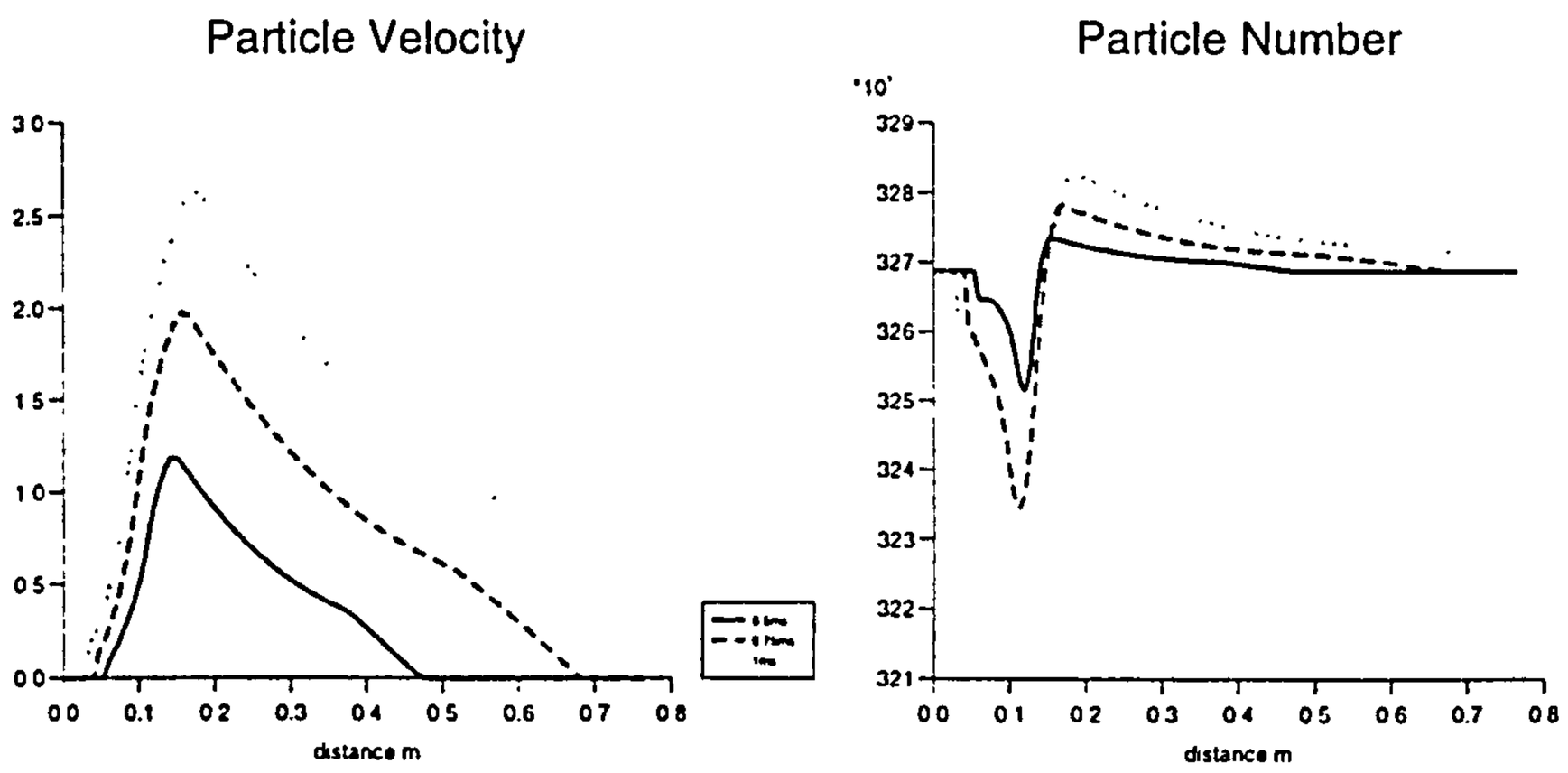

Figure 5.12: Particle velocity and number profiles at $t = 0.5ms$ (full line), $t = 0.75ms$ (dashed line) and $t = 1ms$ (dotted line).

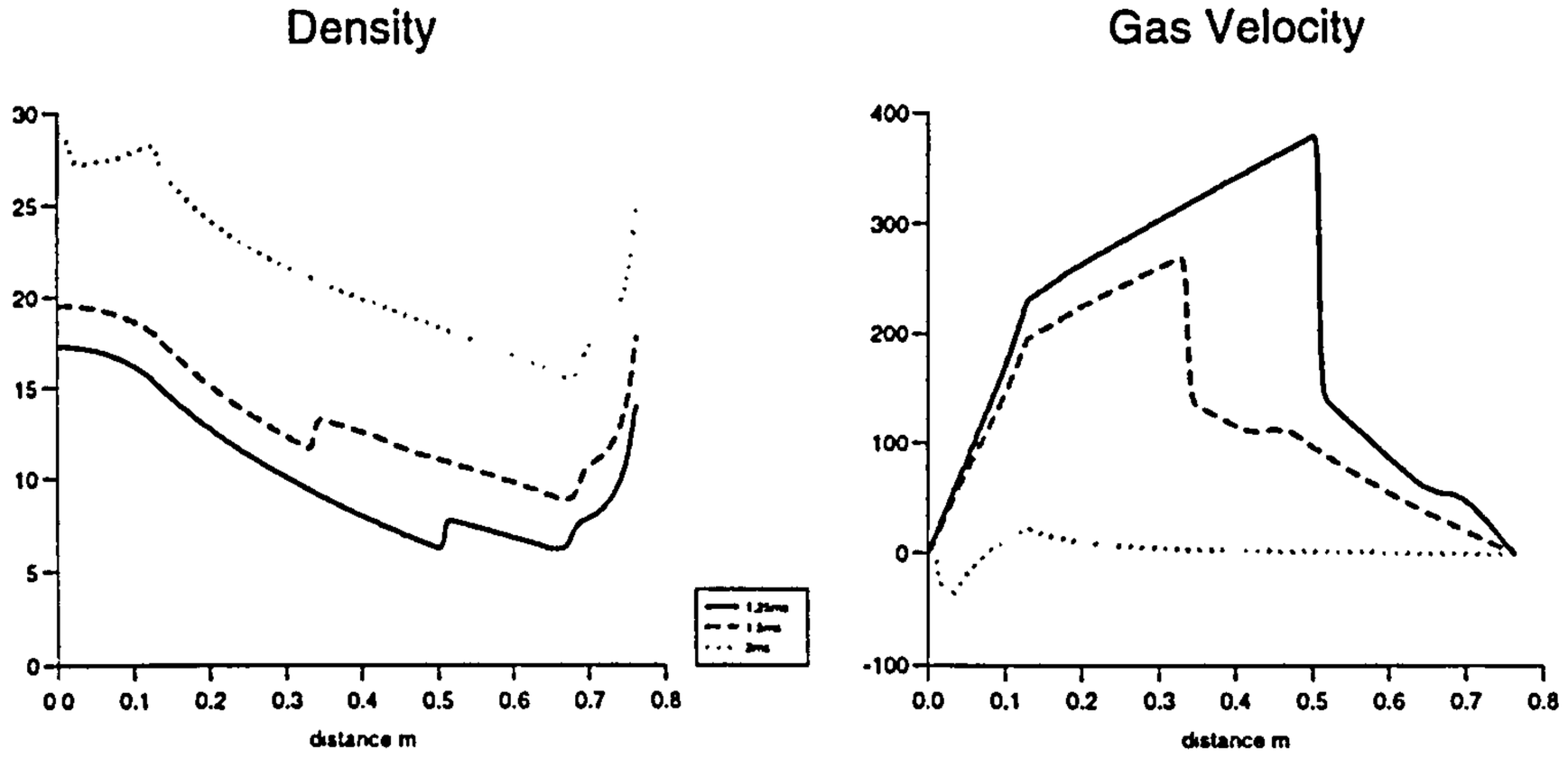

Figure 5.13: Density and gas-velocity profiles at $t = 1.25ms$ (full line), $t = 1.5ms$ (dashed line) and $t = 2ms$ (dotted line).

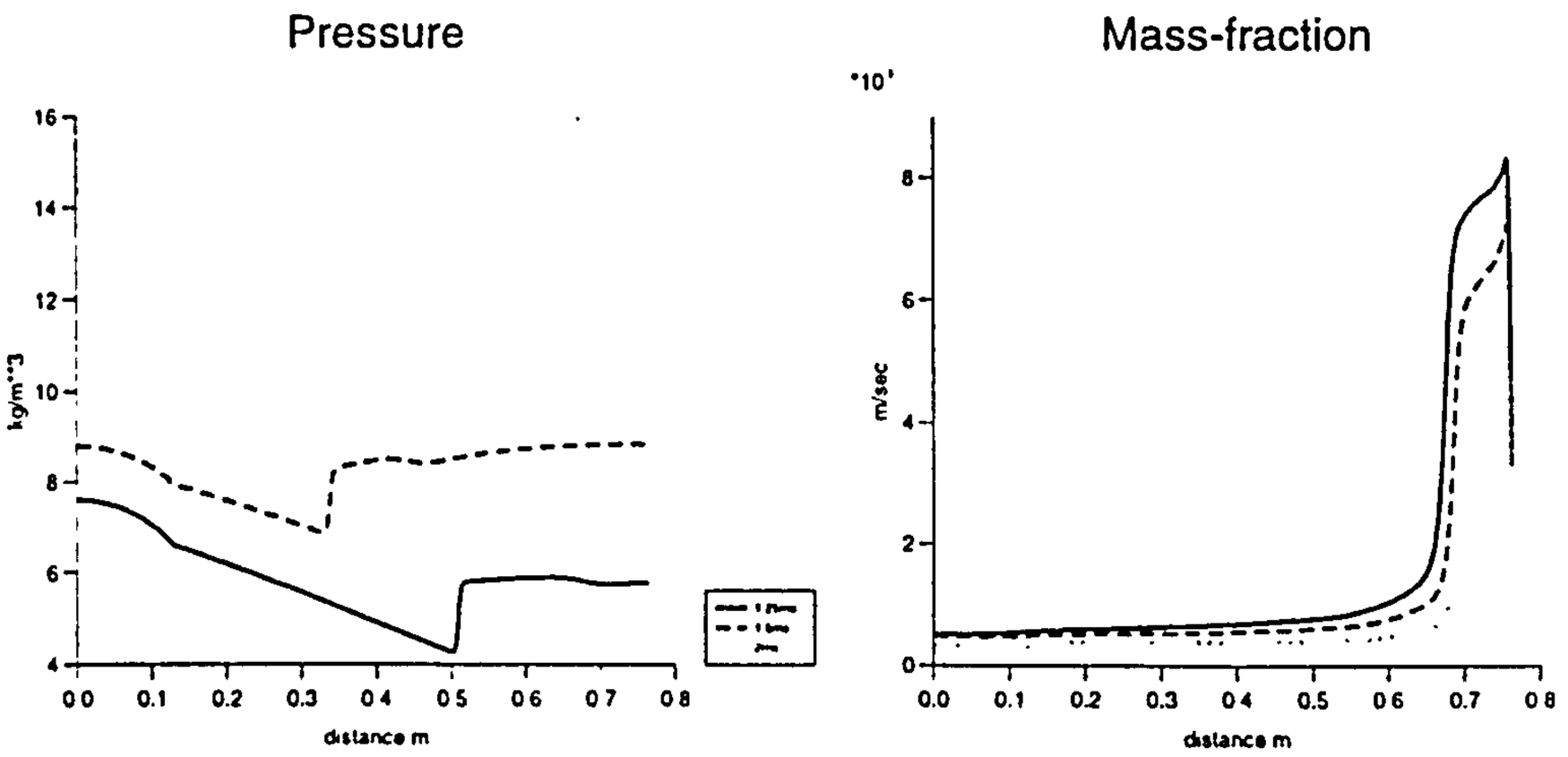

Figure 5.14: Pressure and mass-fraction profiles at $t = 1.25ms$ (full line), $t = 1.5ms$ (dashed line) and $t = 2ms$ (dotted line).

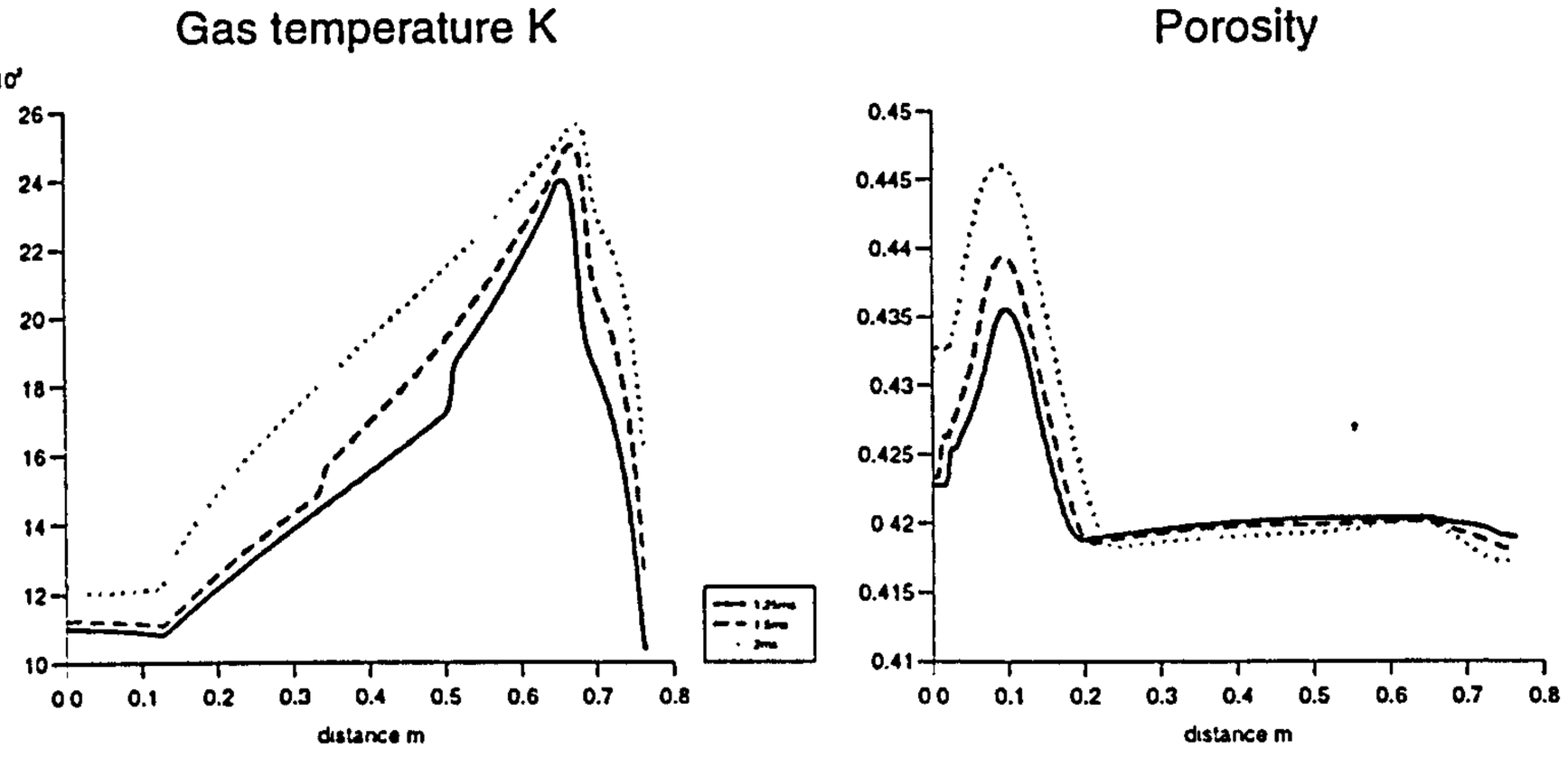

Figure 5.15: Temperature and porosity profiles at $t = 1.25ms$ (full line), $t = 1.5ms$ (dashed line) and $t = 2ms$ (dotted line).

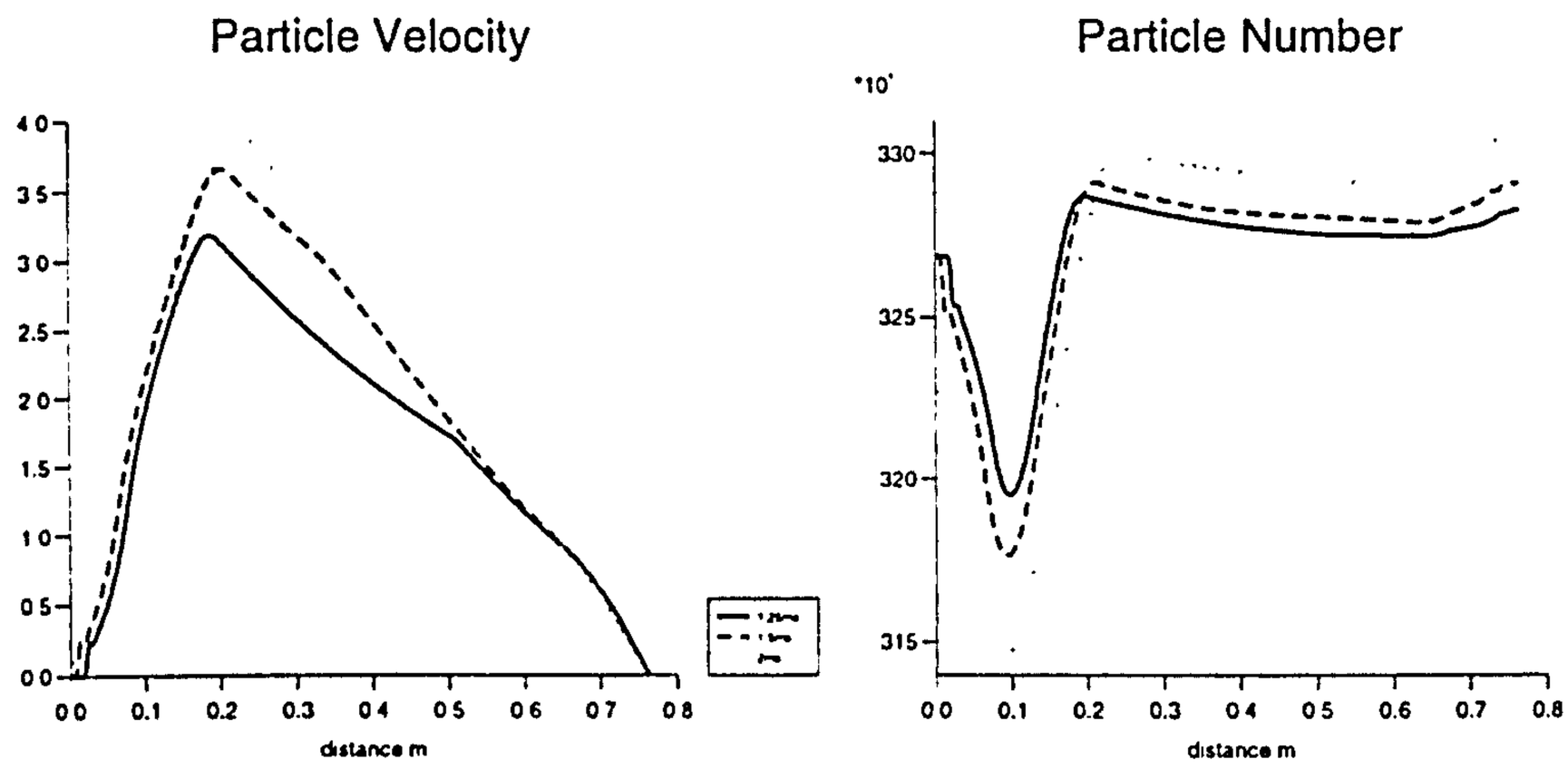

Figure 5.16: Particle velocity and number profiles at $t = 1.25ms$ (full line), $t = 1.5ms$ (dashed line) and $t = 2ms$ (dotted line).

Chapter 6

Interface Processes

This chapter will describe a simple model for the interface processes that occur between the gas and solid. A physical mechanism that defines a role for solid thermochemistry is developed. The evolution of the solid-phase thermal profile up to first solid decomposition is explored.

6.1 Transient Burning

Transient burning is the term used to describe the burn-rate when a material is exposed to severe pressure excursions. For example, a candle burns under constant ambient pressure conditions whilst propellant burning within an internal ballistic combustion chamber or a rocket motor is severely transient. Interest on the subject goes back to the 1930's; however, even today there seems to be no conclusive or uniform approach to providing the solution. However, most studies seems to stem from considering the mass and energy transfer between solid propellant and an external hot gas.

Consider figure (6.1) that illustrates this interface which is regressing at a rate $\dot{r}$ due to the decomposition of propellant. Observation of burning propellants reveal a decomposition process from solid into a thin liquid layer followed by decomposition of liquid into gas. However, for simplicity the liquid-phase will be omitted and the solid will be assumed to change directly into gas on decomposition. The burning process is initiated when the gas is heated to a temperature above the ambient temperature by some external stimulus. Heat-transfer from the hot gas to the cold solid is initiated producing a boundary

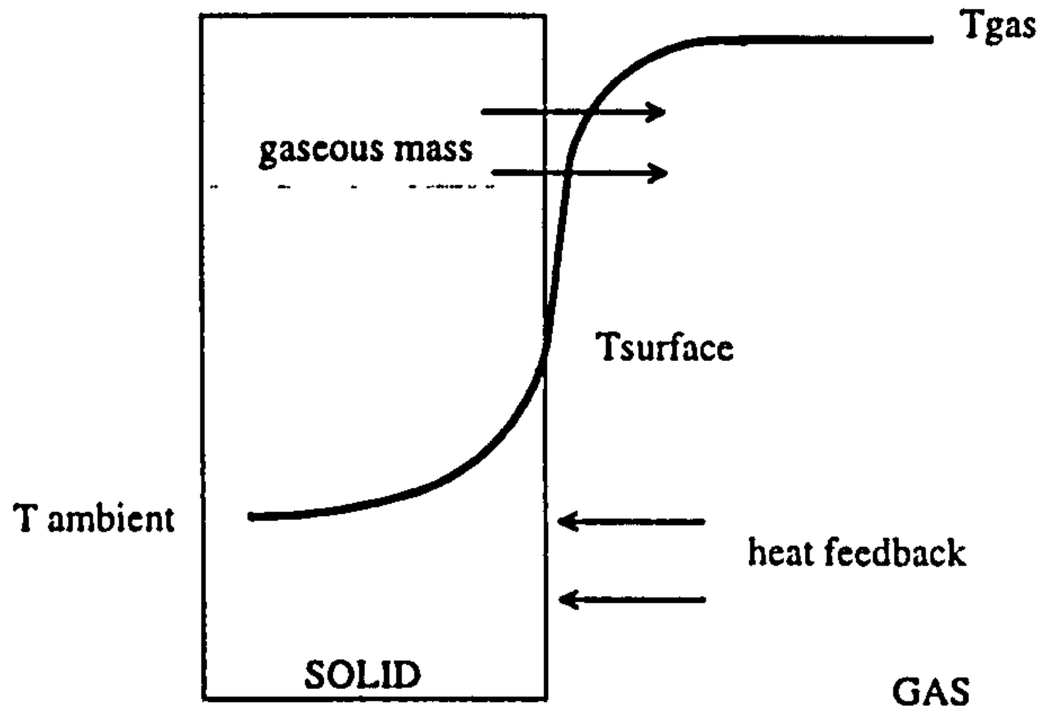

Figure 6.1: Surface of a typical propellant grain.

layer in the gas and a temperature gradient in the solid. The surface decomposition of the solid propellant is assumed to be an Arrhenius reaction dependent on temperature. It is assumed that the reaction layer is confined to a very thin surface region. In this case it is reasonable to approximate the rate of chemical reaction as a function of propellant surface temperature [26]. The chemical reaction can be be either exothermic or endothermic. The process of decomposition increases the gas energy due to adiabatic addition of mass and either produces energy in or removes energy from the gas due to the chemical reaction. The burning procedure continues with heat-transfer between gas and solid plus decomposition of the solid into gas. The modelling of the phenomena is basically a heat conduction problem. However, the different approaches generally concern the boundary condition at the interface that governs the heat feedback from the gas into the solid.

6.2 Mathematical Model

The one-dimensional heat conduction equation for a moving solid is given as:

$$\frac{\partial T^p}{\partial t} + \dot{r}\frac{\partial T^p}{\partial y} = \alpha^p \frac{\partial^2 T^p}{\partial y^2}, \tag{6.1}$$

where $T^p(y,t)$ is the temperature in the solid, and $\alpha^p = \frac{\lambda^p}{\rho^p C^p}$. Here λ^p is solid conductivity ; C^p is specific heat capacity and ρ^p is the solid density.

An expression will now be proposed to define the rate of surface gasification. The following burn-rate model will be used to tie up the old theory on interior ballistics with this more detailed formulation of the processes which are occurring at the surface.

6.2.1 Surface Regression

The burning rate $\dot{r}$ is given by the pyrolysis law:

$$\dot{r} \propto B_{cf}(p) e^{\frac{-E_A^p}{\mathcal{R}T_s}}, \tag{6.2}$$

where $B_{cf}(p)$ is a function of pressure that is identical to Piobert's law; $T_s(t)$ is the surface temperature and E_A^p is the activation energy of the surface reaction. This has been inspired by the work on ignition and transient burning [26], [24] that defines pyrolysis at the surface as an Arhennius exponential dependent on the solid surface temperature T_s

$$\dot{r} \propto \exp -E_A^p/\mathcal{R}T_s,$$

and Piobert's law used in internal ballistics that describes the solid gasification as a function of gas pressure only. Internal ballistics modelling often assumes that the solid decomposes once it reaches a decomposition temperature (assumed to correspond to some empirically measured gas-phase temperature) and from then on the regression is based on Piobert's law $\dot{r} = B_{cf}p^n$. Since for many applications this burning law has been quite successful it will be retained after the decomposition temperature has been reached. The intention of this model is to predict the propellant behavior prior to this temperature. Let the regression of the surface be such that:

$$\dot{r} = \begin{cases} B_{cf}p^n \exp\left(-E_A^p/\mathcal{R}(\frac{1}{T_d} - \frac{1}{T_s}\right) & T_s < T_d \\ B_{cf}p^n & T_s = T_d \end{cases} \tag{6.3}$$

where T_d is some 'decomposition' temperature. In effect this is just a switch that produces the standard burning law after some critical temperature T_d is achieved at the surface. Before this point the rate of surface reaction is controlled by the Arrhenius exponential term which produces a negligible burnrate at low temperatures but increases exponentially at higher temperatures. Physically this means that at early times the solid propellant starts to increase

in temperature but gasification is almost zero. As T_s approaches T_d, the exponential dramatically increases effectively switching on solid gasification. Once $T_s = T_d$ it remains at this temperature burning rapidly.

6.2.2 Boundary Conditions

The solid is initially at ambient temperature T_0. The boundary conditions to this problem are:

$$T^p(-\infty, 0) = T_0; \tag{6.4}$$

$$\lambda^p \frac{\partial T^p}{\partial y}|_s = \lambda \frac{\partial T}{\partial y}|_g + \rho^p \dot{r}(Q^p - L); \tag{6.5}$$

$$\Rightarrow q_s = q_g + \dot{r}\Delta Q_{chem} \tag{6.6}$$

where λ is the thermal conductivity of the gas; $Q^p(J/kg)$ is the heat generated due to the chemical decomposition; $L(J/kg)$ is the latent heat required for gasification q_s is the heat flux into the solid; q_g is the heat flux into the gas; and ΔQ_{chem} is the net heat created by the surface reactions. The heat flux from the gas will be given as an empirical heat-transfer relation such that:

$$q_s = F(T, T_s) \tag{6.7}$$

When the solid-surface temperature arrives at the decomposition temperature, the solution to the heat conduction equation could continue to be solved with the new boundary condition $T_s = T_d$. However, under the circumstances it is unnecessary since the rate of regression is assumed to be a function of the gas-phase pressure history alone and solid properties are no longer required to calculate the burn-rate. To some extent, a physical appreciation of what governs the gasification process after this critical temperature can be gathered by studying the interface relation at the solid surface. From equation (6.5) simple manipulation shows that:

$$\dot{r} = \frac{\Delta q}{\rho^p(L - Q^p)} \tag{6.8}$$

where $\Delta q = q_g - q_s = f(T, T_s, \lambda, \lambda^p)$, is the difference between the heat flux from the gas and the heat flux into the solid. Consider the case in which the heat produced by gasification Q^p is zero . The rate of regression can only be greater or equal to zero. If the regression rate is negligible, then this implies that $\Delta q \approx 0$ and the heat transfer from the gas is completely absorbed by the

propellant material causing increases in solid temperature. The work in this chapter concentrates on this part of the gasification process where latent heat and exothermic reaction contributions are small as $\dot{r}$ is negligible.

If the regression rate is non-zero, $T_s > T_d$, then Δq must be positive implying that heat-transfer occurs from the gas and into the solid. If the gas produced by gasification reacts exothermically, then this will increase the heat flux Δq into the solid surface. For constant solid density and latent heat this will mean increasing regression rate $\dot{r}$.

Conversely, if the gasification process is such that $L - Q^p < 0$, that is, the energy released on gasification is non-zero and greater than latent heat requirements, then Δq is negative implying heat-transfer from the solid into the gas and a self-sustaining gasification process.

Assume both latent heat and energy produced by the reaction are constant, if Piobert's law is substituted into equation (6.8) this implies that the energy flux is such that $\Delta q \propto p^n$.

6.3 Viscous Flows

The heat-conduction equation is a convection-diffusion problem that can be solved as by Toro & Brown [98] using time-operator splitting. This involves splitting the whole problem into two subproblems namely: a pure convection hyperbolic problem and a pure diffusion parabolic problem in a similar way as seen previously in the solution of the gas-phase ignition model.

6.3.1 Convection-Diffusion Splitting

Let equation (6.1) and the initial conditions be re-written as the following initial-value problem:

$$\frac{\partial T^p}{\partial t} + \dot{r}\frac{\partial T^p}{\partial y} = \alpha^p \frac{\partial^2 T^p}{\partial y^2}, \tag{6.9}$$

$$T^p(y,0) = T_0(y). \tag{6.10}$$

Let $L(t)$ be the exact solution operator of equation (6.9) so the solution in conjunction with initial conditions in equation (6.10) is given as:

$$T^p(y,t) = L(t)T_0. \tag{6.11}$$

Define $L_1(t)$ and $L_2(t)$ as the solution operators of the convection equation

$$\frac{\partial T^p}{\partial t} + \dot{r}\frac{\partial T^p}{\partial y} = 0, \tag{6.12}$$

and the diffusion equation

$$\frac{\partial T^p}{\partial t} = \alpha^p \frac{\partial^2 T^p}{\partial y^2}, \tag{6.13}$$

respectively. As seen previously, the first order fractional step is based on the approximation

$$L(t_n)T_0 \approx (L_2(\Delta t)L_1(\Delta t))^n T_0. \tag{6.14}$$

or equivalently with L_1 or L_2 reversed where Δt is the splitting step and L_1 and L_2 are at least first-order accurate.

To solve the full problem over time Δt, the convective step produces an intermediate solution for $T(y,t)$ which is used as the initial condition for the diffusion step which is then solved for timestep Δt. This results in an approximation to the full problem given in equation (6.9). Strang's second order split is

$$L(t_n)T_0 = (L_2(\frac{\Delta t}{2})L_1(\Delta t)L_2(\frac{\Delta t}{2}))^n T_0. \tag{6.15}$$

Brown [99] has shown that the solution is exact for the model convection-diffusion equation and second-order otherwise provided that L_1 and L_2 are at least second-order accurate.

6.3.2 Convective Step

This involves the solution to the partial-differential equation:

$$T_t^p + \dot{r}T_y^p = 0. \tag{6.16}$$

The WAF method, as described in chapter (4.1.15), is adopted. What is important in the present discussion is the selection of the timestep to guarantee stable solutions. As seen previously this can be given as a function of the maximum wave speed $\dot{r}$

$$\Delta t_C = \frac{c_{fl} \times \dot{r}}{\Delta y}, \tag{6.17}$$

where Δt_C is the convective time-step, Δy is the dimension of the spatial mesh and c_{fl} is the Courant number such that $c_{fl} \in [0,1]$.

6.3.3 Diffusion Step

This involves the solution to:

$$T_t^p = \alpha^p T_{yy}^p. \tag{6.18}$$

There are a numerous ways to solve this equation. The simplest would be to transform the partial-differential-equation to an ordinary-differential-equation by replacing the right-hand-side of equation (6.18) by a second-order central-difference approximation. Replace the continuous function $T^p(x,t)$ by the piecewise constant function $\mathbf{T} = (T_1, T_2, ..., T_m)^T$ where T_i^n is the value of temperature in cell i at time n:

$$(T_i)_{yy} \approx \left(\frac{T_{i+1}^n - 2T_i^n + T_{i-1}^n}{\Delta y^2} \right) \tag{6.19}$$

Using this substitution in equation (6.18) produces

$$\frac{d\mathbf{T}}{dt} = \mathbf{f}(\mathbf{T}), \tag{6.20}$$

where $\mathbf{f} = (f_1, f_2, ..., f_m)$. Usual discretization techniques mean that this is a system of ordinary-differential-equations that can be solved using the first-order Euler:

$$\mathbf{T}^{n+1} \approx \mathbf{T}^n + \Delta t.\mathbf{f}(\mathbf{T}^n). \tag{6.21}$$

However, if extra accuracy is required, as will be seen later, the modified Euler is second order accurate and the scheme given by:

$$\mathbf{T}^{n+1} \approx \mathbf{T}^n + \Delta t.\mathbf{f}\left(\mathbf{T}^n + \frac{\Delta t}{2}\mathbf{f}(\mathbf{T}^n)\right). \tag{6.22}$$

Note how the temperature at the new level $\mathbf{T}^{n+1}$ can be written as an explicit function of the temperature at the previous time level $\mathbf{T}^n$.

It has been shown [98] that stability restrictions require that the diffusive step Δt is such that:

$$\Delta t_D = \frac{\Delta y^2}{2\alpha^p} c_D \tag{6.23}$$

where c_D is the diffusion number such that $c_D \in [0, 1]$.

However, although the above method is very simple, the stability restrictions that are typical of all explicit methods can cause severe difficulties when rapidly changing boundary conditions are encountered. This means that if

the timescales associated with the change in external boundary conditions are small compared with the change in other flow variables then problems, similar to that of stiffness, will arise. To deal with such problems a semi-implicit method that is well documented- the Crank-Nicolson method- will be used through most of the following computations.

6.3.4 The Crank-Nicolson Method

The Crank-Nicolson method is second-order accurate and discretises using the following scheme:

$$(T_i)_t = \frac{T_i^{n+1} - T_i^n}{\Delta t} \tag{6.24}$$

$$(T_i)_{yy} = \left(\frac{T_{i+1}^{n+1} - 2T_i^{n+1} + T_{i-1}^{n+1}}{2\Delta x^2}\right) + \left(\frac{T_{i+1}^{n} - 2T_i^{n} + T_{i-1}^{n}}{2\Delta x^2}\right) \tag{6.25}$$

Substituting into equation (6.18) and manipulation gives:

$$-cT_{i+1}^{n+1} + T_i^{n+1}(1+2c) - cT_{i-1}^{n+1} = cT_{i+1}^{n} + T_i^{n}(1-2c) + cT_{i-1}^{n} \tag{6.26}$$

where $c = \frac{\alpha^p}{2\Delta x^2}$.

As can be seen, the solution at the new time-level T_i^{n+1} cannot be found explicitly. Instead a system of linear algebraic equations must be solved of the form:

$$\mathrm{A.T} = \mathrm{b}, \tag{6.27}$$

where:

$$\mathbf{A} = \begin{pmatrix} 1+2c+a_1 & -c & 0 & 0 & \dots & 0 \\ -c & 1+2c & -c & \ddots & \ddots & \vdots \\ 0 & -c & 1+2c & -c & 0 & \vdots \\ \vdots & 0 & \ddots & \ddots & \ddots & 0 \\ \vdots & \vdots & \ddots & -c & 1+2c & -c \\ 0 & 0 & \dots & 0 & -c & 1+2c+a_2 \end{pmatrix}, \tag{6.28}$$

and a_1 & a_2 are determined from the boundary conditions.

$$\mathbf{T} = \begin{pmatrix} T(1) \\ T(2) \\ \vdots \\ T(i) \\ \vdots \\ T(m-1) \\ T(m) \end{pmatrix}^{n+1} ; \quad \mathbf{b} = \mathbf{F} \begin{pmatrix} T(1) \\ T(2) \\ \vdots \\ T(i) \\ \vdots \\ T(m-1) \\ T(m) \end{pmatrix}^{n} . \tag{6.29}$$

A is a tridiagonal matrix, **T** is the unknown, **b** is a function of the initial conditions and $\mathbf{F} = (F_1, F_2, ..., F_m)^T$.

This is a system of linear equations which can be solved using **LU** decomposition and partial pivoting is employed to preserve accuracy. Partial pivoting transforms the tridiagonal form **A** into a matrix **A′**. The process introduces non-zero terms into the diagonal immediately above the upper-diagonal i.e.:

$$\mathbf{A}' = \begin{pmatrix} d_1 & u_1 & s_1 & 0 & \dots & 0 \\ l_1 & d_2 & u_2 & s_2 & \ddots & \vdots \\ 0 & l_2 & d_3 & u_3 & \ddots & \vdots \\ \vdots & 0 & \ddots & \ddots & \ddots & s_{n-2} \\ \vdots & \vdots & \ddots & l_{n-2} & d_{n-1} & u_{n-1} \\ 0 & 0 & \dots & 0 & l_{n-1} & d_n \end{pmatrix} \tag{6.30}$$

An appropriate algorithm [100] is then utilised to factorise **A′** into its **LU** decomposition where **L** is a lower diagonal and **U** is an upper diagonal matrix. The solution is then found using forward and back substitution:

$$\mathbf{L}.\mathbf{y} = \mathbf{b}; \quad \mathbf{U}.\mathbf{T} = \mathbf{y}. \tag{6.31}$$

The forward substitution firstly solves for **y** which is then used in the second equation to solve for **T**.

Details of the above may be found in reference [100].

6.3.5 Boundary Conditions

Boundary conditions provide the temperature at the cold-end of the spatial domain and the hot surface interface. As described in equation (6.4), the

cold-end is not permitted to rise above ambient temperature T_0 so that:

$$T(-\infty, t) = T_0. \tag{6.32}$$

At the regressing surface a gradient boundary condition is provided in equation (6.5). Simple finite-differences are used to approximate the temperature in this surface region. A second-order central difference approximation is given by:

$$\begin{aligned} \left[\frac{\partial T^p}{\partial y}\right]_s &\approx \frac{T^p_{s-} - T^p_{s+}}{\Delta y} = F(T, T_s); \\ &\Rightarrow \quad T^p_{s-} = T^p_{s+} + \Delta y F(T, T_s), \end{aligned} \tag{6.33}$$

where $s-$ and $s+$ denote small perturbations around the propellant interface. For the explicit method described above the inclusion of these boundary conditions are trivial source terms, function of $\mathbf{T}^n$, in the system of ordinary-differential-equations given in equations (6.21) and (6.22). However, the Crank-Nicolson method needs the definition of the boundary conditions at the unknown time-level $\mathbf{T}^{n+1}$ to calculate a_1 and a_2 that are inserted into matrix $\mathbf{A}$ of equation (6.28). Since these are still unknown, substitution of the boundary will produce a set of *non-linear* equations, as opposed to a set of linear equations. if the function $F(T_g, T_s)$ is a non-linear function of T_s. In the problem that will be considered radiation heat-transfer is a function of T_s^4. Newton's method will be used to solve the system of non-linear equations

$$\mathbf{A.T} = \mathbf{b} \Rightarrow \mathbf{A.T} - \mathbf{b} = 0 \tag{6.34}$$

.

6.3.6 Solution to a System of Non-linear Equations

The Newton method is used to solve the system of non-linear equations:

$$\mathbf{f(x)} - \mathbf{b} = \mathbf{F(x)} = 0, \tag{6.35}$$

for $\mathbf{x}$ where

$$\begin{aligned} \mathbf{x} &= (\mathbf{x_1}, \mathbf{x_2}, \mathbf{x_3}, ..., \mathbf{x_m})^{\mathbf{T}} \quad \mathbf{f} = (\mathbf{f_1}, \mathbf{f_2}, \mathbf{f_3}, ..., \mathbf{f_m})^{\mathbf{T}}; \\ \mathbf{b} &= (\mathbf{b_1}, \mathbf{b_2}, \mathbf{b_3}, ..., \mathbf{b_m})^{\mathbf{T}} \quad \mathbf{F} = (\mathbf{F_1}, \mathbf{F_2}, \mathbf{F_3}, ..., \mathbf{F_m})^{\mathbf{T}} \end{aligned} . \tag{6.36}$$

This can be solved using the following iterative method:

$$\mathbf{x}^{n+1} = \mathbf{x}^n - \mathbf{J}(\mathbf{x}^n)^{-1}\mathbf{F}(\mathbf{x}^n) \tag{6.37}$$

where **J** is the Jacobian of the function **F**.

This is reminiscent of the Newton-Raphson method for a single equation and details can be found in [100].

Since the inverse of a matrix is expensive to compute, the following scheme is exploited. Let:

$$\mathbf{z}^{n+1} = \mathbf{x}^{n+1} - \mathbf{x}^{n}, \tag{6.38}$$

Then equation (6.37) can be rewritten as:

$$\mathbf{J}(\mathbf{x}^{n})\mathbf{z}^{n+1} = -\mathbf{F}(\mathbf{x}^{n}). \tag{6.39}$$

This has now been transformed to a system of linear equations in unknown $\mathbf{z}^{n+1}$ and the form is tridiagonal. It can be solved using LU decomposition together with forward and back substitution as was outlined in the previous report and $\mathbf{x}^{n+1}$ can then be calculated using (6.37). This is an iterative process and is sufficiently accurate once:

$$\|\mathbf{F}(\mathbf{x}^{n})\|_{\infty} < tol. \tag{6.40}$$

In order to assist convergence to the solution, a damping procedure was used:

$$\begin{aligned} \mathbf{z}^{n+1} &= -J^{-1}F \\ i &:= min\left(j : 0 \leq j, \|\mathbf{F}(\mathbf{x}^{n} + \frac{\mathbf{h}}{2^{j}})\| \leq \|\mathbf{F}(\mathbf{x}^{n})\|\right), \\ \mathbf{x}^{n+1} &= \mathbf{x}^{n} + \frac{\mathbf{h}}{2^{i}} \end{aligned} \tag{6.41}$$

Details can again be found in [100]. This helps to hasten the convergence, which is quadratic for Newton's method.

6.4 A Model Problem

In order to test the validity and accuracy of the numerical solution produced using the above method, it is necessary to be able to compare with known or exact solutions. Since there is no exact solution to the full heat-conduction equation as proposed above, a slightly simpler problem that has however the same form as the full problem is considered,

$$\frac{\partial T}{\partial t} + a\frac{\partial T}{\partial y} = \alpha\frac{\partial^{2} T}{\partial y^{2}}. \tag{6.42}$$

λ	$0.31\ \frac{J}{msecK}$	C	$1550.0\frac{J}{kgK}$
ρ	$1577.8\ \frac{kg}{m^3}$	a	$0.007/.07\frac{m}{sec}$
q_{ig}	$1000\frac{J}{m^2 secK}$	l	$1.5 \times 10^{-4} m$

Table 6.1: Model heat-conduction problem.

This differs from the full problem as $\dot{r}$ has been replaced with a constant a. The initial temperature throughout is ambient:

$$T(y,0) = T_0 = 298K, \tag{6.43}$$

and boundary conditions are slightly simpler:

$$T(-\infty,0) = T_0 \tag{6.44}$$

$$\lambda \left[\frac{\partial T}{\partial y}\right]_s = q_{ig} T_s, \tag{6.45}$$

where now the interface boundary condition is only a linear function of surface temperature and where q_{ig} is a constant. In the Crank-Nicolson method the final system of equations will be linear and Newtons method will not be necessary for this model problem. A plausible choice of parameter values is given in table 6.1 where l is the length of computational domain.

The derivation of the exact solution for this problem can be found in [101] and is given by:

$$\begin{aligned} T(y) &= T_I - \frac{T_I}{2}\left[erfc(\frac{y-at}{2\sqrt{\alpha t}}) + (\frac{\alpha q_{ig}}{\alpha q_{ig}-a})e^{\frac{ay}{\alpha}} erfc(\frac{y+at}{2\sqrt{\alpha t}})\right] \\ &+ \frac{T_I}{2}\left[\left(\frac{2\alpha q_{ig}-a}{\alpha q_{ig}-a}\right) e^{(q_{ig}y - q_{ig}t[a-\alpha q_{ig}])} erfc\left(\frac{y+(2\alpha q_{ig}-a)t}{2\sqrt{\alpha t}}\right)\right] \end{aligned} \tag{6.46}$$

Two choices of a are taken since the burn-rate $\dot{r}$ will vary in the real problem.

Figure (6.2) gives the solution to the problem using a first order explicit method on a one hundred cell mesh for the two examples over $1ms$. The solution for a equal to $.007m/sec$ corresponds to a lower rate of decomposition of solid propellant. The solution is good and is seen to depart from the true solution only when the temperature gradient is at its steepest. The second solution shows the equivalent for a equal to $.07m/sec$. The temperature gradient in the solid is almost constant near the interface and comparison with

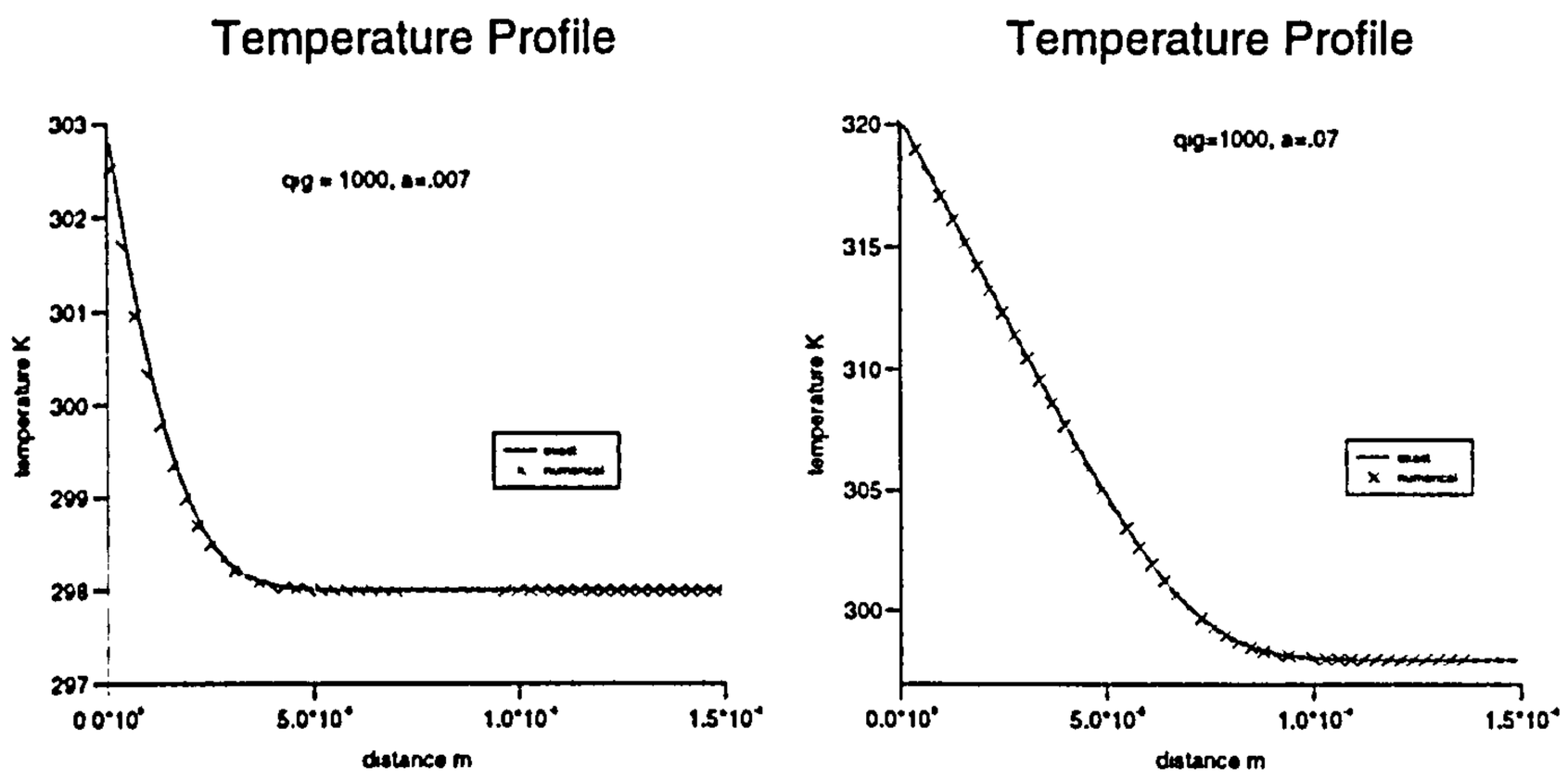

Figure 6.2: Exact (full line) and first-order implicit (X) temperature profiles at $1ms$.

the previous plot indicates how the the form of the diffusion-dominated and convection- dominated solutions will differ. In this case the first order solution is excellent.

Figure (6.3) compares the identical problems at time $2ms$ where the second order split is used with the implicit Crank-Nicolson method. For the first problem the agreement close to the gradient boundary condition is significantly improved.

Finally figure (6.4) compares the exact and numerical solutions where the second-order split, explicit method is used at $4ms$. The above examples go some way to validate the numerical techniques used but also illustrate a secondary difficulty. As the time increases to $4ms$ clearly the cold-end boundary condition will be invalid once the temperature at 1.5×10^{-4} increases above the ambient temperature. The difficult part when attempting to solve such a problem is selection of the initial size of the computational domain. For example the entire width of propellant could be selected as the size of the domain. However, not only would this necessitate the solution of at least a two-dimensional heat conduction problem, but also since the temperature variation is confined to a thin surface layer, if the domain is too large, too many cells are required

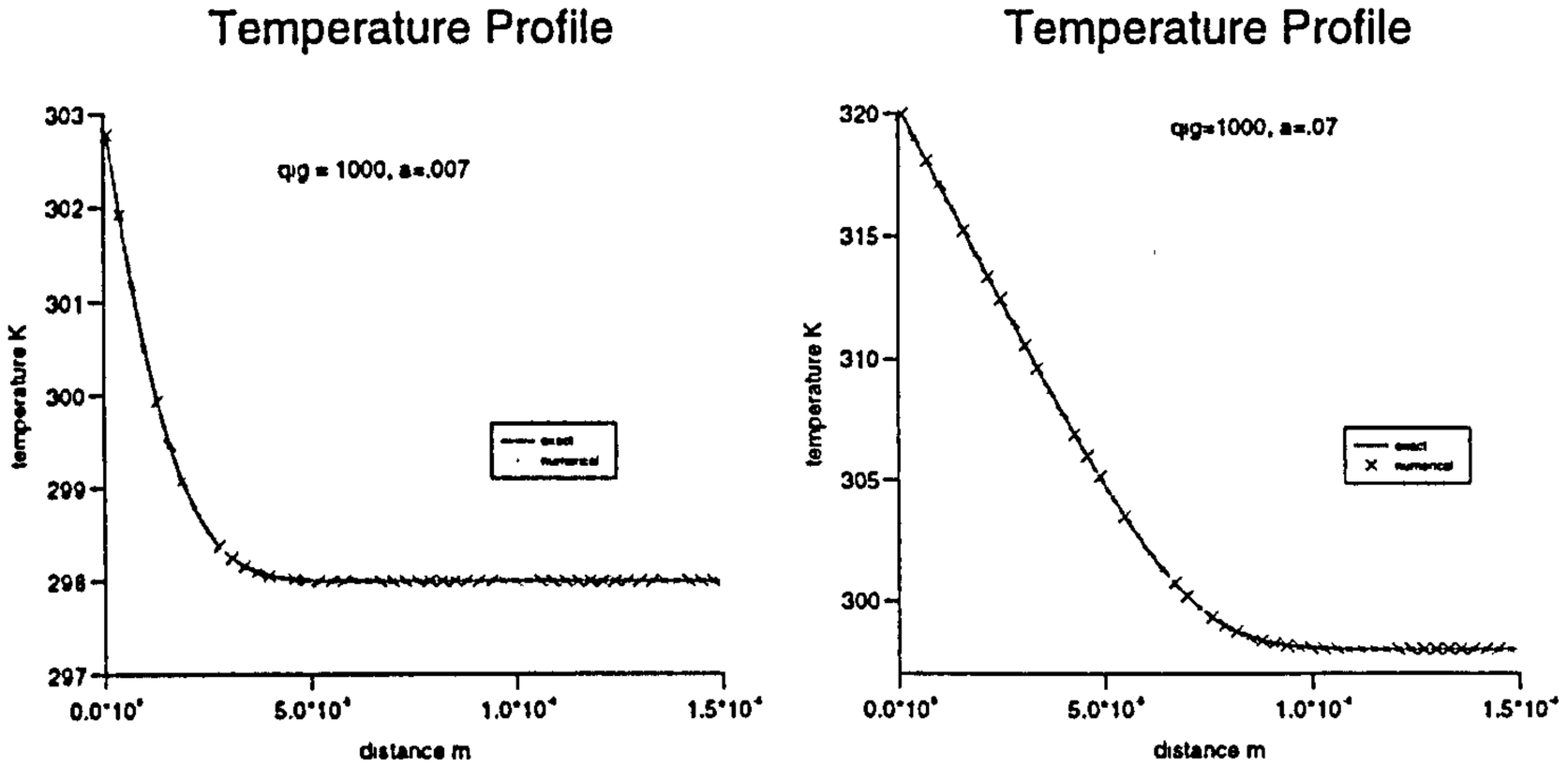

Figure 6.3: Exact (full line) and second-order implicit (X) temperature profiles at $2ms$.

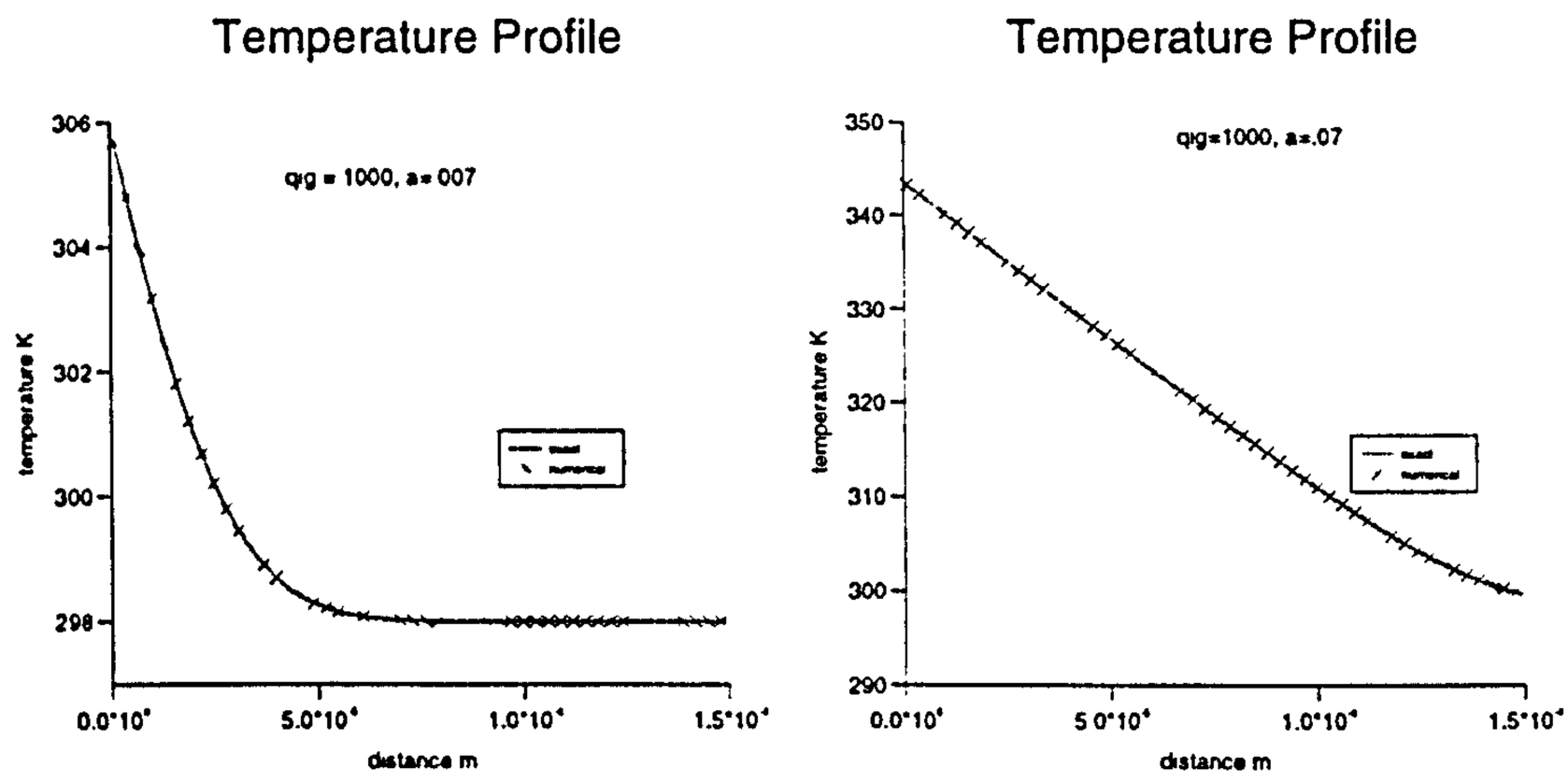

Figure 6.4: Exact (full line) and second-order explicit (X) temperature profiles at $4ms$.

to resolve the temperature variation in this fine layer. Similarly however, as time passes more and more of the spatial domain is affected by the external heat flux at the surface. If the domain is too small then the boundary condition at the cold-end which states that the temperature remains at ambient will be violated. It was purely a matter of trial and error that set the length of domain and restricted the time run so that no boundary conditions would be violated in the examples above. This is by no means a satisfactory answer to the difficulty and it has been necessary to track the variation of the 'thermal penetration depth' in a reliable and informed manner. Adding more cells to the domain is one possible solution. Unfortunately the thermal penetration depth can increase dramatically and ultimately this method could increase the number of mesh cells by an order of magnitude. In this case excessive computation would be needed at later times. The conventional diffusion problem has a characteristic length that can be obtained from studying:

$$T_t = \alpha^p T_{yy} \tag{6.47}$$

$$O\left(\frac{[T]}{[t]}\right) \approx O\left(\frac{\alpha^p [T]}{[y]^2}\right) \tag{6.48}$$

where t is the time. From this last relation a characteristic length $l_D = O(\sqrt{\alpha^p t})$ can be used as an estimate of the thermal penetration depth due to diffusion. A similar calculation for the convection problem gives $l_C = O(\dot{r}t)$. If the domain is taken as the maximum of the two $l = max(l_D, l_C)$ this proves to be quite a reliable estimate as demonstrated in figure (6.5). This compares the exact solution at times $1ms$, $2ms$ and $4ms$ where the domain length is varied according to the formula above. The size of domain varies according to the scheme described and captures the 'cold-end' of the propellant material.

However, whilst the exact solution does not require the solution at any other time to construct the solution at the time required, numerical methods build on the solution at previous times via timestepping. If this strategy is applied where the size of the domain varies in time then the temperature plots at different times will lie within two different domains. This problem is addressed by using interpolation between the two-time levels.

For example let the solution T_1 be the solution over time t_1 in the domain l_1. To calculate the solution at the new time t_2, the initial temperature conditions T_1 for the integration must be set up over the new domain l_2 that corresponds to the domain calculated for time t_2 which will be greater than l_1. Linear interpolation is used to map the temperature T_1 onto the temperature $T^0{}_2$ that provides values for the temperature over the larger domain l_2. However, normal interpolation will produce a temperature at the surface which is lower than the

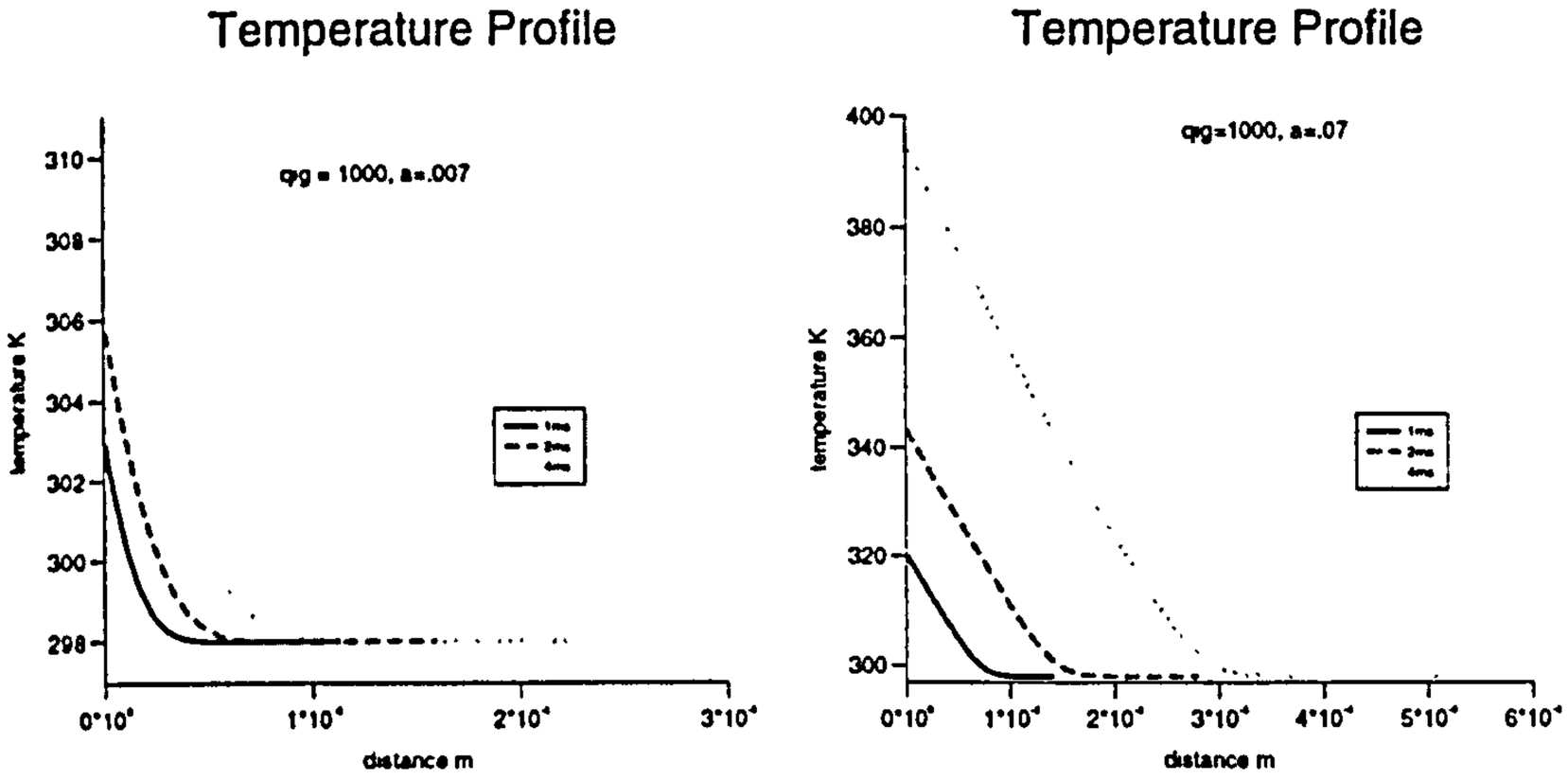

Figure 6.5: Exact solution to the heat-conduction equation over time that demonstrates the variable domain scheme.

pre-interpolated value. Under some conditions this can be a problem since the exponential $\left(\exp\left(E_A^p/R(\frac{1}{T_d}-\frac{1}{T_s}\right)\right)$ has the potential to change dramatically with T_s. Figure (6.6) illustrates how usual interpolation techniques would lower the temperature at the surface.

To prevent this problem the interpolation was constructed so that the value of the surface temperature remained constant through the interpolation procedure. Two examples of this interpolation scheme at different times from one domain to another is shown in figure (6.7).

The application of this will be illustrated in the following example. Before this, the empirical relations that are used to calculate the heat-transfer will be outlined here.

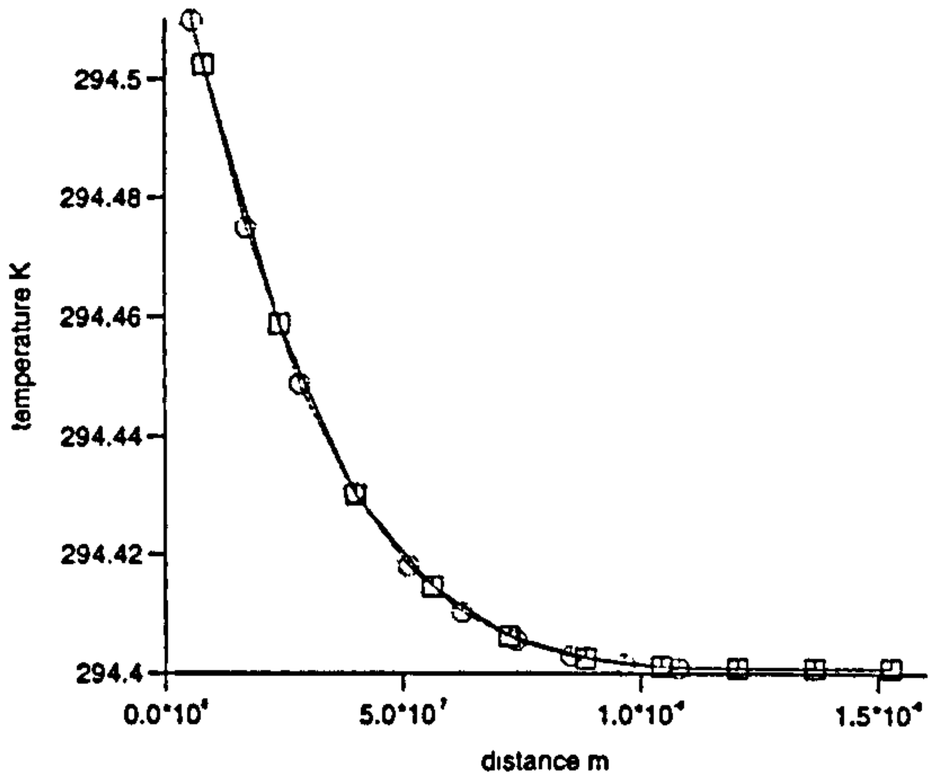

Figure 6.6: Typical interpolation procedure from domain l_1 (circle) to l_2 (square) where $l_1 < l_2$.

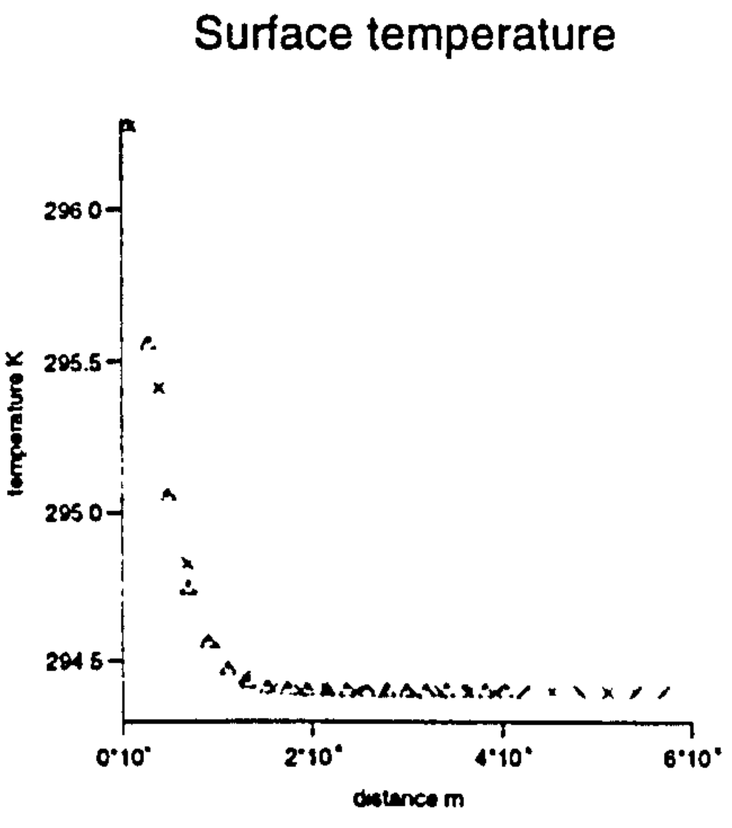

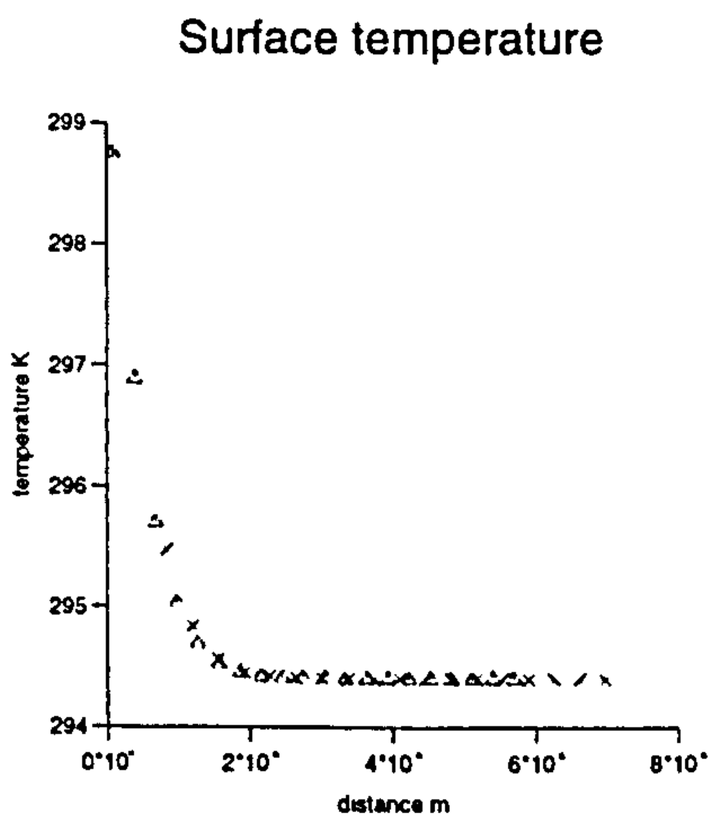

Figure 6.7: Examples of the modified interpolation procedure from domain l_1 (triangle) to l_2(cross) where $l_1 < l_2$.

6.5 Heat-Transfer

For investigative purposes, that will soon be apparent, the heat-transfer will be assumed to consist of radiation and conduction heat-transfer despite that fact that in reality convective heat-transfer is known to play a critical role. The net solid-phase heat-transfer will be given empirically as

$$q_s = q_r + q_c \tag{6.49}$$

where q_r is the heat flux due to radiation per unit time and q_c is the heat flux due to conduction per unit time. These can be given [1]:

$$q_r = c' E \left(T^4 - T_s^4 \right), \tag{6.50}$$

where c' is the radiation constant, E is the emissivity, T is the gas temperature and T_s is the surface temperature.

$$q_c = \lambda^p C^p T^{0.25} \frac{\dot{r}^{0.8}}{D_p^{0.2}} \left(T - T_s \right), \tag{6.51}$$

where C is the specific heat at constant pressure, $\dot{r}$ is the regression rate and D_p is the effective diameter. How realistic these expressions are, considering the neglect of convective heat-transfer, is uncertain and in the following experiments it was necessary to multiply these expressions by a factor ψ in order to produce realistic solid temperatures subject to the external conditions. On occasions this has been up to three orders of magnitude and for arguments sake attribute this to the substantial contribution of convection in the heat-transfer process. The formulae are devised to make the heat-transfer a function of the external gas temperature -as it is obvious that this must have a strong influence on the rate of surface temperature increase- and in particular include the radiation heat-transfer as a quartic function of gas temperature.

6.6 Closed Bomb Problems

The full two-phase flow equations with chemistry can be seen in the preceding chapter. However, to reduce the complexity of the problem and to concentrate only on transfer processes between the gas and solid interface, all spatial derivatives are neglected from equations (5.29), (5.30), (5.31), (5.32), (5.33), (5.34) and (5.35). This describes a 'closed-bomb' where it is the time rate of change

of gaseous pressure and temperature that is of interest rather than any particular aspects of the flow regime. By using these equations, the solid surface is exposed to a realistic transient gas-phase pressure and the heat-conduction equation can be solved in conjunction with the two-phase equations. This explains why convective heat-transfer has been neglected since the gas-phase velocity is assumed to be zero in such a simplification. This reduces the system to a set of ordinary-differential-equations that govern the rate of change of porosity, gas density, reactant mass-fraction and gas-phase energy in time:

$$\frac{d\epsilon}{dt} = \frac{\dot{m}}{\rho^p}; \tag{6.52}$$

$$\frac{d\epsilon\rho}{dt} = \dot{m} + \dot{m}_{ig}; \tag{6.53}$$

$$\frac{d\epsilon\rho c}{dt} = -\epsilon\rho\Omega c^2 + \frac{\dot{m}}{2}; \tag{6.54}$$

$$\frac{d\epsilon E}{dt} = \dot{m}Q^p + \dot{m}_{ig}e_{ig}; \tag{6.55}$$

$$\tag{6.56}$$

where $\dot{m} = \rho^p \dot{r} S^p$. The change in surface area is calculated accurately using the theory described in section (5.4.2) and the heat-up and rate of regression of the propellant surface will be calculated using the transient burning model.

Interface Solid Phase Equations

$$\frac{\partial T^p}{\partial t} + \dot{r}\frac{\partial T^p}{\partial y} = \alpha^p \frac{\partial^2 T^p}{\partial y^2} \tag{6.57}$$

$$\dot{r} = \begin{cases} Ap^n \exp\left(-E_A^p/\mathcal{R}(\frac{1}{T_d} - \frac{1}{T_s})\right), & T_s < T_d; \\ Ap^n, & T_s = T_d; \end{cases} \tag{6.58}$$

where

$$T^p(y,0) = T_0, \tag{6.59}$$

$$T^p(-\infty,0) = T_0, \tag{6.60}$$

$$\lambda^p \left[\frac{\partial T^p}{\partial y}\right]_s = F(T,T_s), \tag{6.61}$$

where T is the gas temperature.

These equations indicate how the solid and gas are coupled; the rate of mass addition $\dot{m}$ is dependent on the external gas temperature and pressure, and similarly the change in gas flow variables is dependent on $\dot{m}$.

$msol$	50	T_0	$294.4K$
p_0	$101400Pa$	c_0	0
γ	1.27	b	$0.0010838\ \frac{m}{kg}$
l	$0.762m$	A	$0.0136848m^2$
m_{ig}	$0.2268kg$	e_{ig}	$1.57MJ$
t_{ig}	$10ms$	ρ^p	$1577.8\frac{kg}{m^3}$
m	$9.5255kg$	Q^p	$3.7363MJ$
B_{cf}	$2.7131757^{-6}\frac{1}{sec(Pa)^n}$	n	0.9
E_A^p	$80\frac{MJ}{kgmole}$	θ	-0.17
d_o	$0.01143m$	d_i	$0.001143m$
d_l	$0.0254m$	W	21.13
R	$8313.3\frac{J}{Kkgmole}$	T_{ig}	$444.4K$
T_d	$420K$	λ^p	$0.00873\frac{J}{msecK}$
α^p	$8.68 \times 10^{-8}\frac{m^2}{sec}$	c'	$5.7 \times 10^{-8}\frac{J}{m^2 secK^4}$
E	0.8	A_g	$1000\frac{1}{secPa}$
$E_A/\mathcal{R}$	$5000K$	ψ	1000

Table 6.2: Spatially uniform test data.

The test configuration described in chapter (4.3) is modified here to provide the spatially uniform conditions that are required in this section of the modelling. The combustion chamber is of length L, constant cross-sectional area A_s and the volume remains constant. It is filled with seven perforation multi-tubular propellant grains. Combustion is initiated by an igniter which is vented uniformly along the entire axial length. The neglect of gravity and any heat losses from the chamber result in a so-called closed bomb problem. Recall that the idea of this reduction in complexity is so that, at this stage, emphasis can be placed on looking at the effect of gas-phase and interface chemistry alone without the complications of gas dynamic effects or solid phase movement that occur in the full combustion problem.

The input data can be seen in table 6.2:

Firstly, consider the case where equilibrium chemistry occurs in the gas phase only. This corresponds with standard ballistic-flow models in which all chemical energy is released from the propellant on gasification.

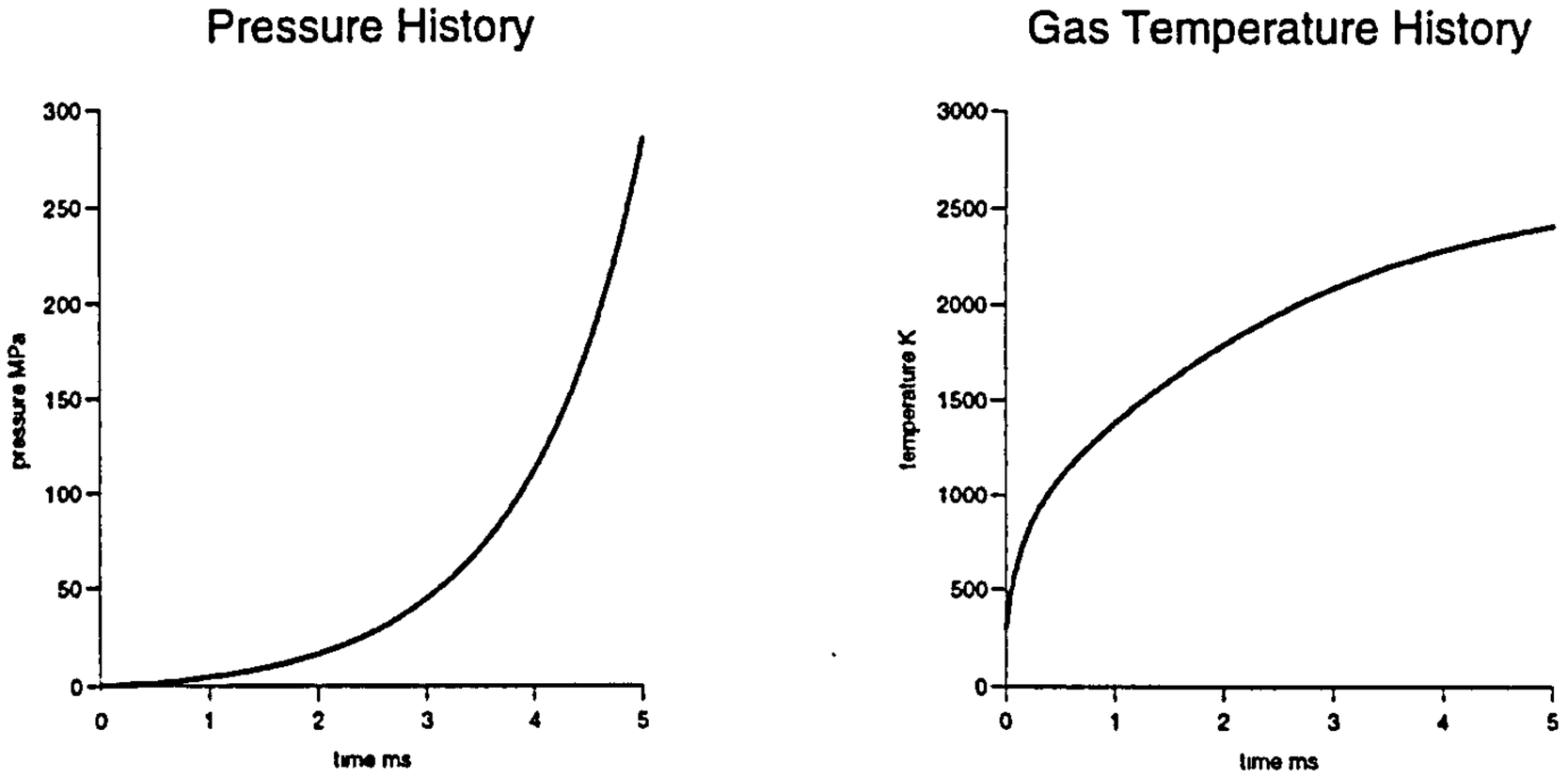

Figure 6.8: Closed bomb pressure and gas temperature history for $T_d = 420K$ over the first $5ms$.

6.7 Equilibrium Gas Phase Chemistry

Figure (6.8) shows the pressure and gas temperature variation in the chamber. The transient burn-rate modelling only plays a part at the very early instances and the effect on the bulk of the combustion cycle is negligible after decomposition is established. Figure (6.9) concentrates on very early times; the surface temperature rises to the decomposition temperature and remains there. The rate of increase of gas temperature is almost constant for $T_s < T_d$ due to the dominance of the constant supply of igniter gas at these times but the surface temperature clearly does not resemble this rate process. The non-linear heat-transfer terms and the role of the exponential factor mean that the rate of change in surface temperature is not linear but the rate increases in time. This implies that the increase in solid temperature cannot be calculated using some simple empiricism that assumes the solid temperature is directly proportional to the gas temperature. This means that there must be some error incurred by assuming the rate of change of solid temperature can be measured in terms of the gas-phase temperature alone as has been done in the past. The effect of the model is similar to the Heavyside function that is used in past models where the burn-rate is switched on at some critical point. However, whilst in

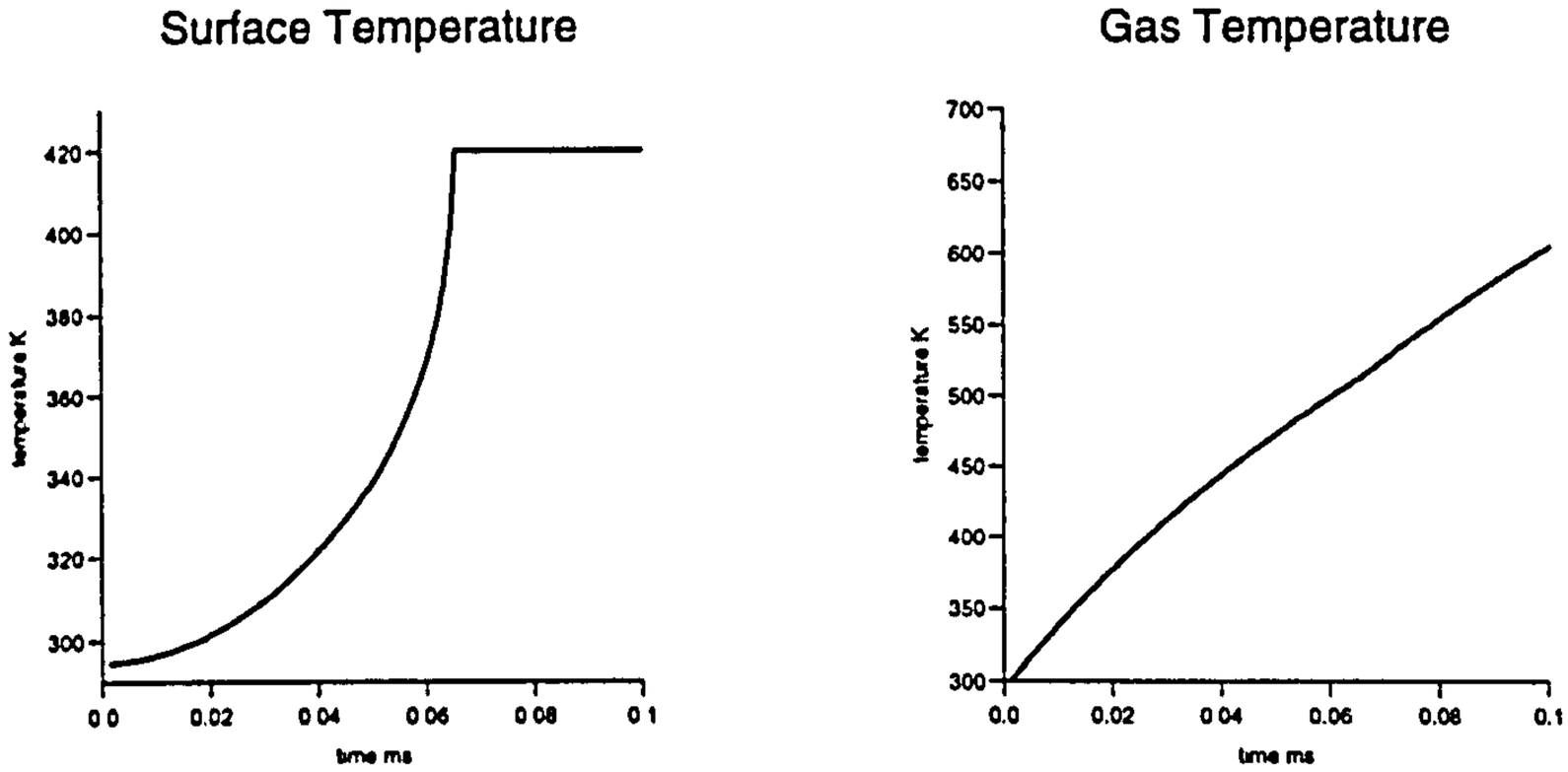

Figure 6.9: Early-time surface and gas temperature histories for $T_d = 420K$.

the past this has been when the gas temperature rises to some decomposition temperature, now decomposition is switched on when the *solid* surface rises to $420K$. In fact the gas temperature is approximately $510K$ at this time. The difference $T - T_s$ will be dependent on the rate of heat-transfer, diffusivity and exponential term.

Although the surface temperature remains constant after $420K$ this does not mean that there is no heat-transfer into the solid but that the rate of regression can now be modeled as a function independent of the surface temperature change using Piobert's pressure dependent law. The pressure and exponential factor can be seen in figure (6.10). The exponential is negligible at early times which means that the burn-rate will be close to zero. However, this rapidly tends to the maximum value of 1 and the conventional burnrate law $\dot{r} = B_{cf} p^n$ is retrieved once the surface reaches decomposition temperature at time $t_d = 0.07ms$. When the exponential rises to 1 the gasification is switched on and both the rate of pressure change and gas-temperature change slightly increase at $0.07ms$.

The temperature profiles at different times are illustrated in figure (6.11).

Clearly the thermal penetration depth increases with time and the plots

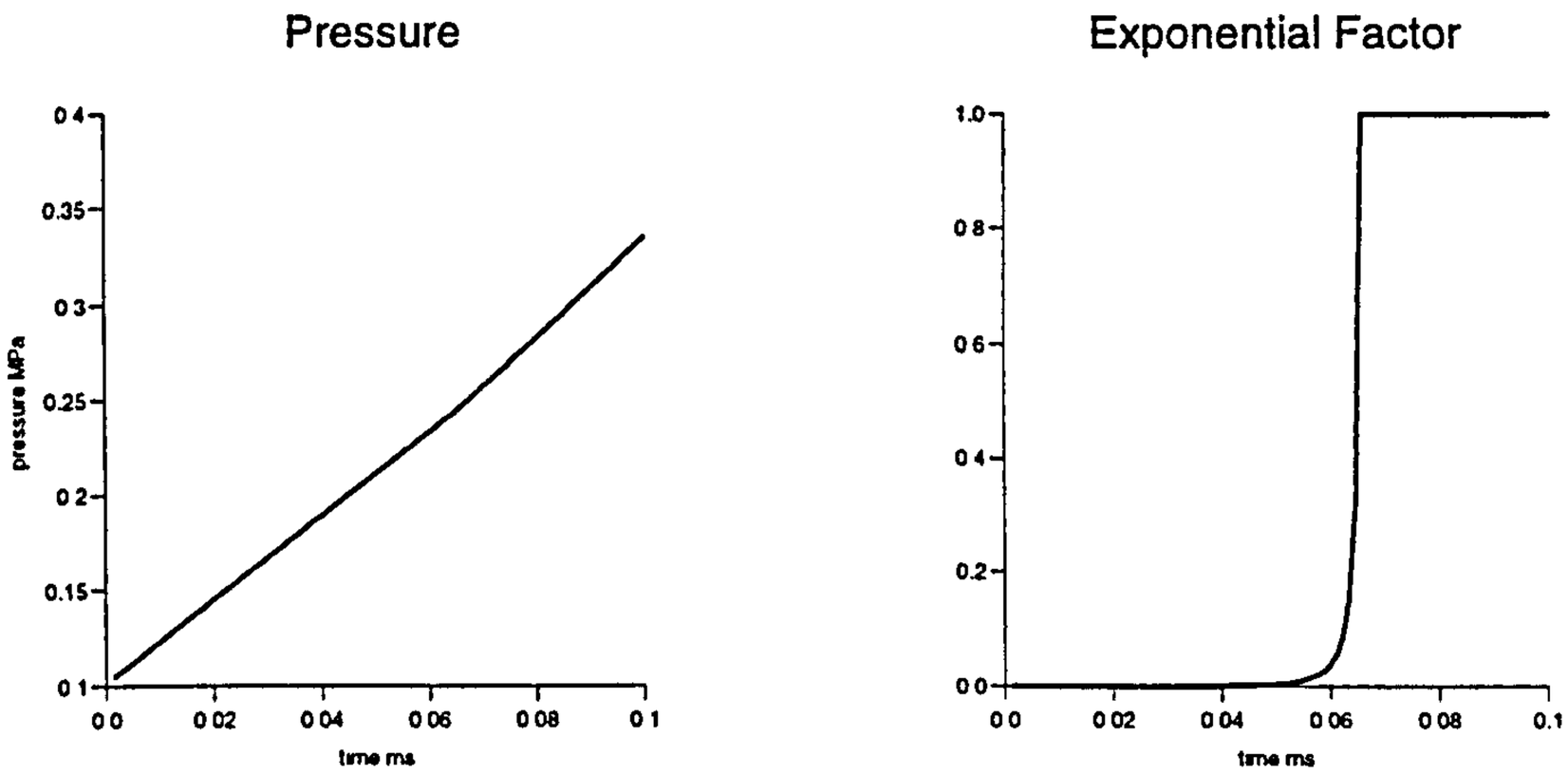

Figure 6.10: Early-time pressure and exponential factor history for $T_d = 420K$.

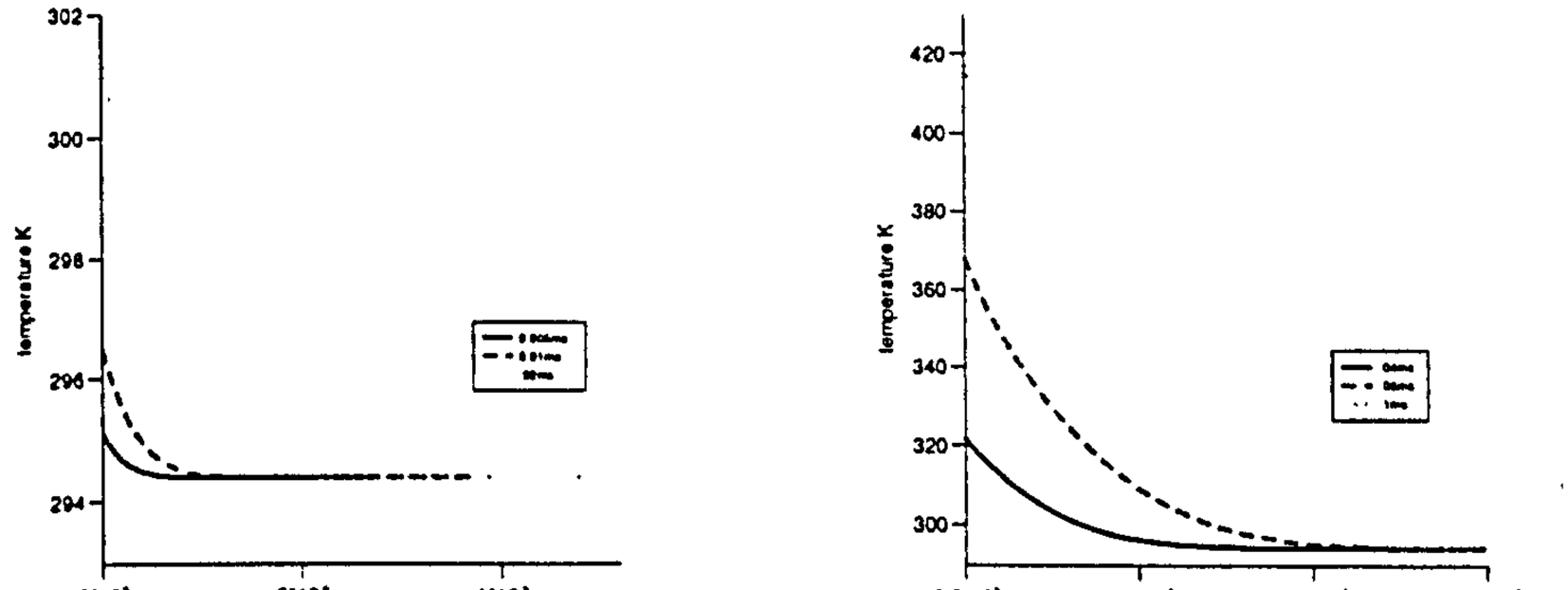

Figure 6.11: Early-time temperature profiles at various times for $T_d = 420K$.

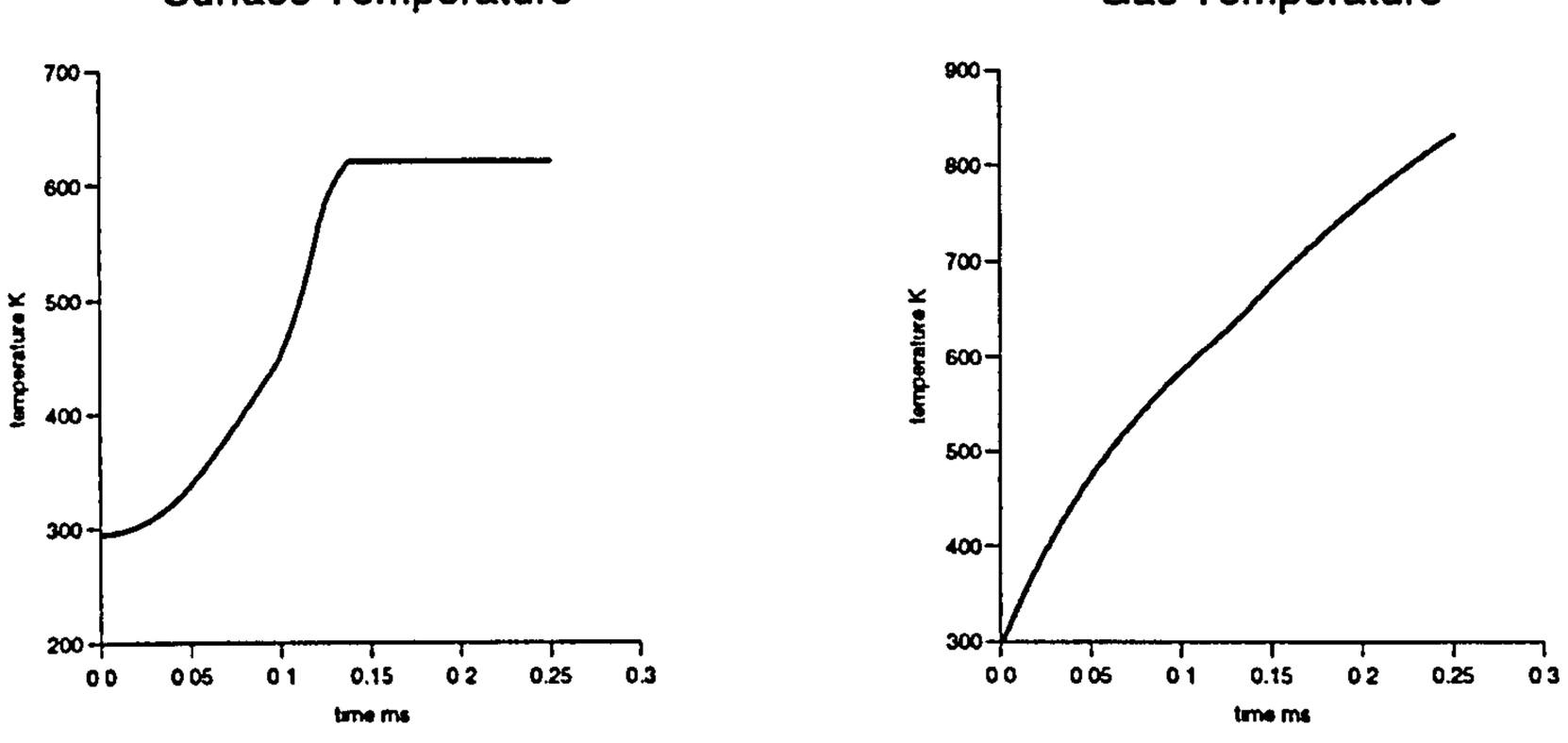

Figure 6.12: Early-time surface and gas temperature history for $T_d = 620K$.

illustrate how the numerical code successfully tracks this depth over time.

The dominating parameter in the above modelling is the choice of decomposition temperature which will dictate how the rate of change of surface temperature behaves. Under all circumstances the exponential factor must tend to 1 once the surface temperature attains the decomposition temperature.

Figures (6.12)-(6.14) illustrate the equivalent experiment where the decomposition is increased to $620K$ so that the effect of changing this important parameter can be investigated. The gas temperature and pressure histories look very similar to the experiment with $T_d = 420K$ for $T_s < 420K$. However, figure (6.13) shows that the change in exponential factor is delayed meaning that the rate of change in pressure and gas temperature does not occur until $0.14ms$ and t_d doubles for this higher choice of decomposition temperature. However, the gas temperature at this time is $\approx 650K$ which shows that the difference $T - T_s$ has decreased. This is an indication of how the non-linear heat-transfer terms cause the rate of increase in surface temperature to accelerate over longer time spans. The implication is that at much later times the difference between gas and surface temperature will be negligible. Under these circumstances, approximating the surface temperature by assuming that it is close to the gas temperature is more viable. From this it can be seen that

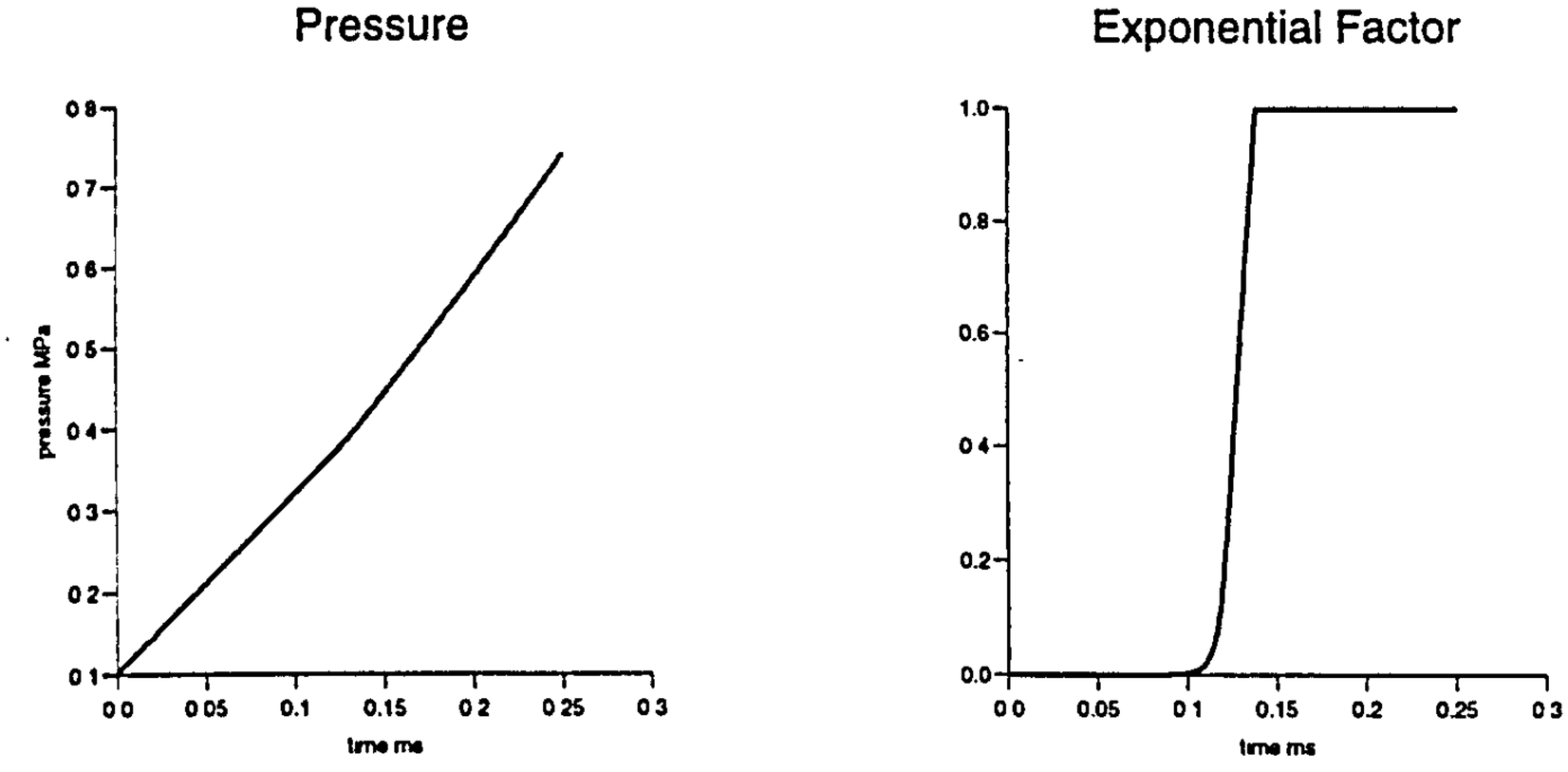

Figure 6.13: Early-time pressure and exponential factor for $T_d = 620K$.

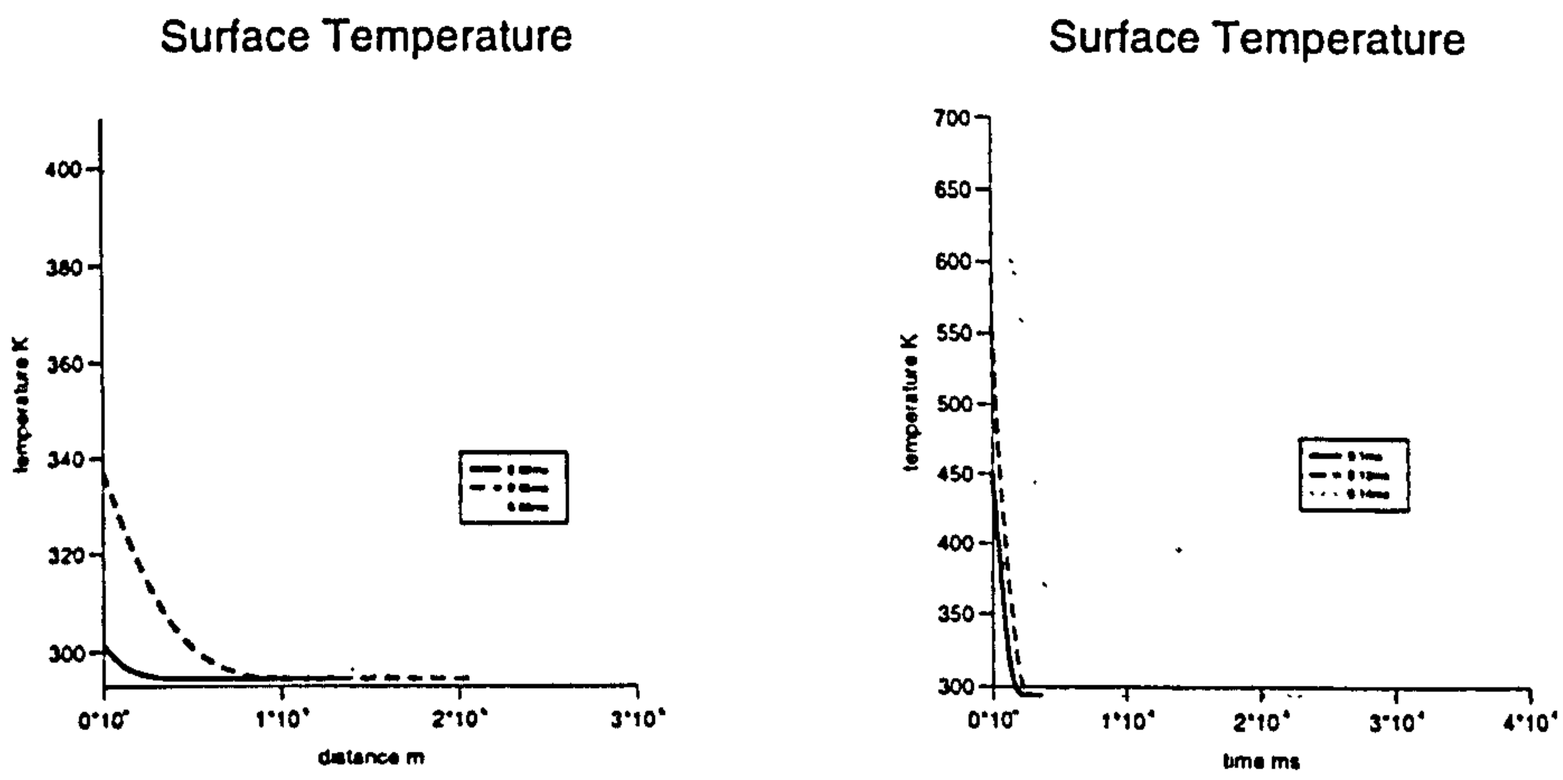

Figure 6.14: Early-time temperature profiles at various times for $T_d = 620K$.

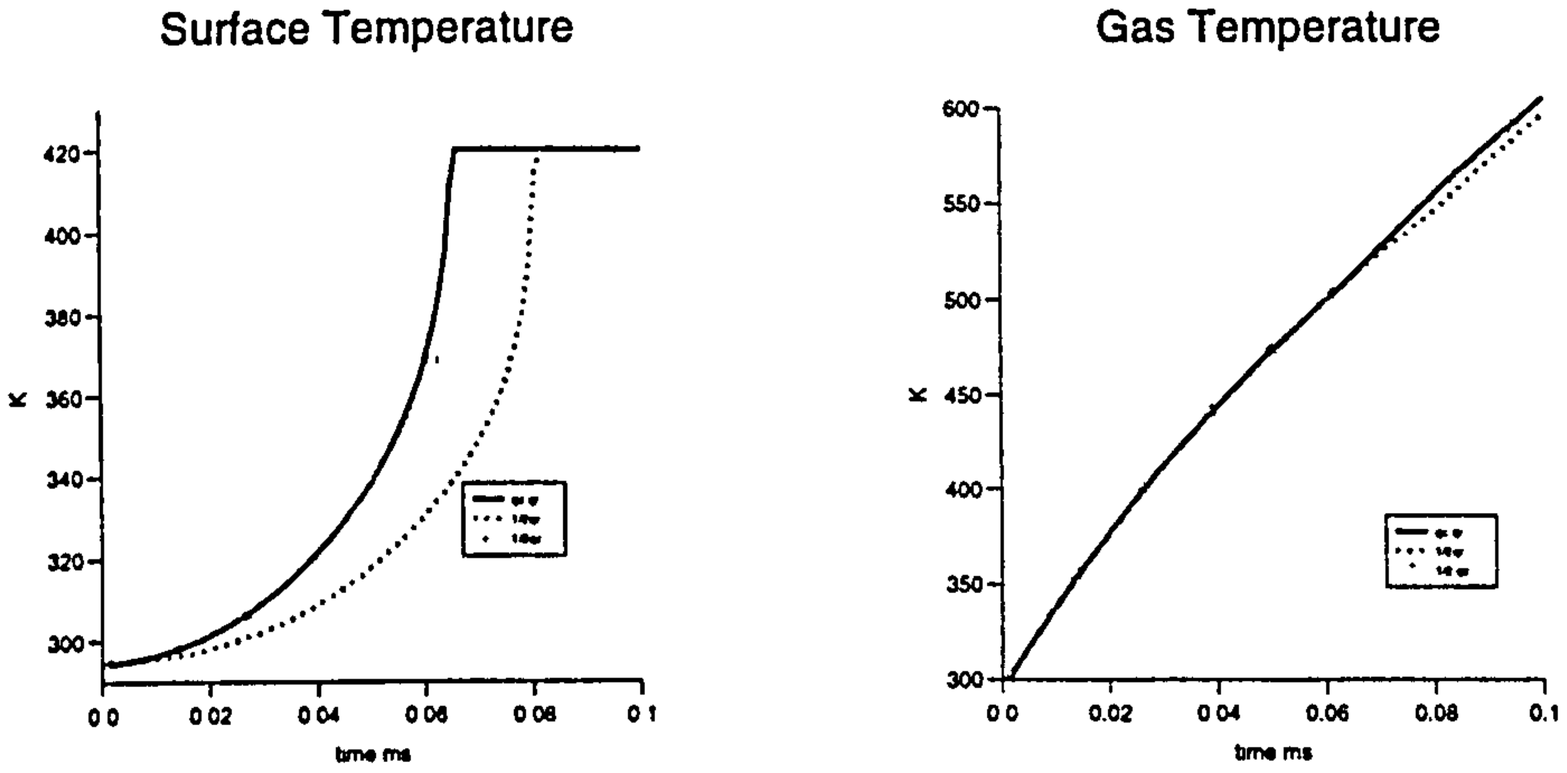

Figure 6.15: Temperature history for reduced heat-transfer.

calculating the interface gasification using Piobert's law, that solely refers to gaseous pressure, can be justified.

The temperature profiles demonstrate how the solid-surface temperature approaches the gas temperature since at later times after $0.08ms$ the temperature gradient at the surface is clearly decreasing in time implying that the heat-transfer into the solid is declining.

Now consider the effect of varying parameters that control the heat transfer due to radiation and conduction. Figure (6.15) compares the surface and gas temperature where the heat due to conduction and radiation are reduced by a factor of two independently. As expected the surface temperature arrives at decomposition slightly later than previously and although the effect on the gas temperature is small it is as would be expected. Is is also clear that the effect of heat-transfer due to radiation dominates since it is proportional to T^4 whilst heat conduction is only proportional to $T^{1.25}$.

The above indicates the role of the interface chemistry model without gas-phase chemistry effects. Early heat-up of the solid surface from ambient differs from the rate of change of gas temperature. However, as time proceeds non-linear radiation and conduction heat-transfer cause the solid surface to

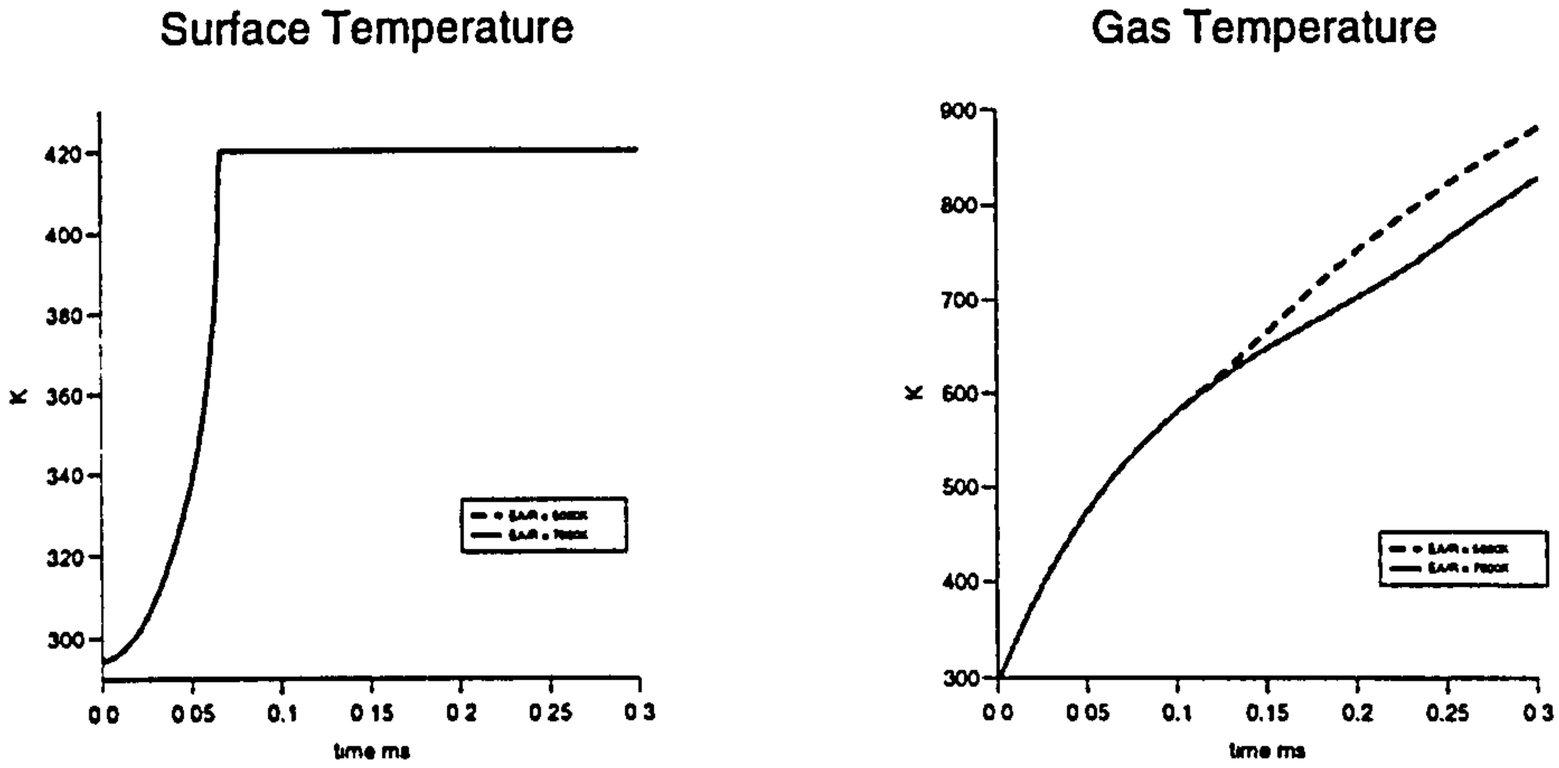

Figure 6.16: Early-time temperature histories for $E_A/\mathcal{R} = 5000K$ (—) and $E_A/\mathcal{R} = 7000K$ (full-line).

approach the rate of change in gas temperature until the surface starts to gasify.

The more complex coupling of the interface and gas chemistry will be investigated. This will also test the robustness of the methods that are used to solve the heat conduction equation when solved in conjunction with rapidly changing boundary conditions.

6.8 Non-equilibrium Gas-Phase Chemistry

Figure (6.16) illustrates the temperature profiles for two different gas-phase activation energies $E_A/\mathcal{R}$, $5000K$ and $7000K$. The rate of rise of surface temperature is not effected by the gas-phase chemistry and the two surface temperature plots are almost identical. Prior to $t = 0.05ms$, $\dot{r} \approx 0$ and this is reflected in the mass-fraction c which is negligible and the reaction rate in figure (6.17). The exponential quickly approaches 1 producing a rapid increase c and consequently in the reaction rate also. The values of E_A strongly influence the consumption of gaseous reactant mass.

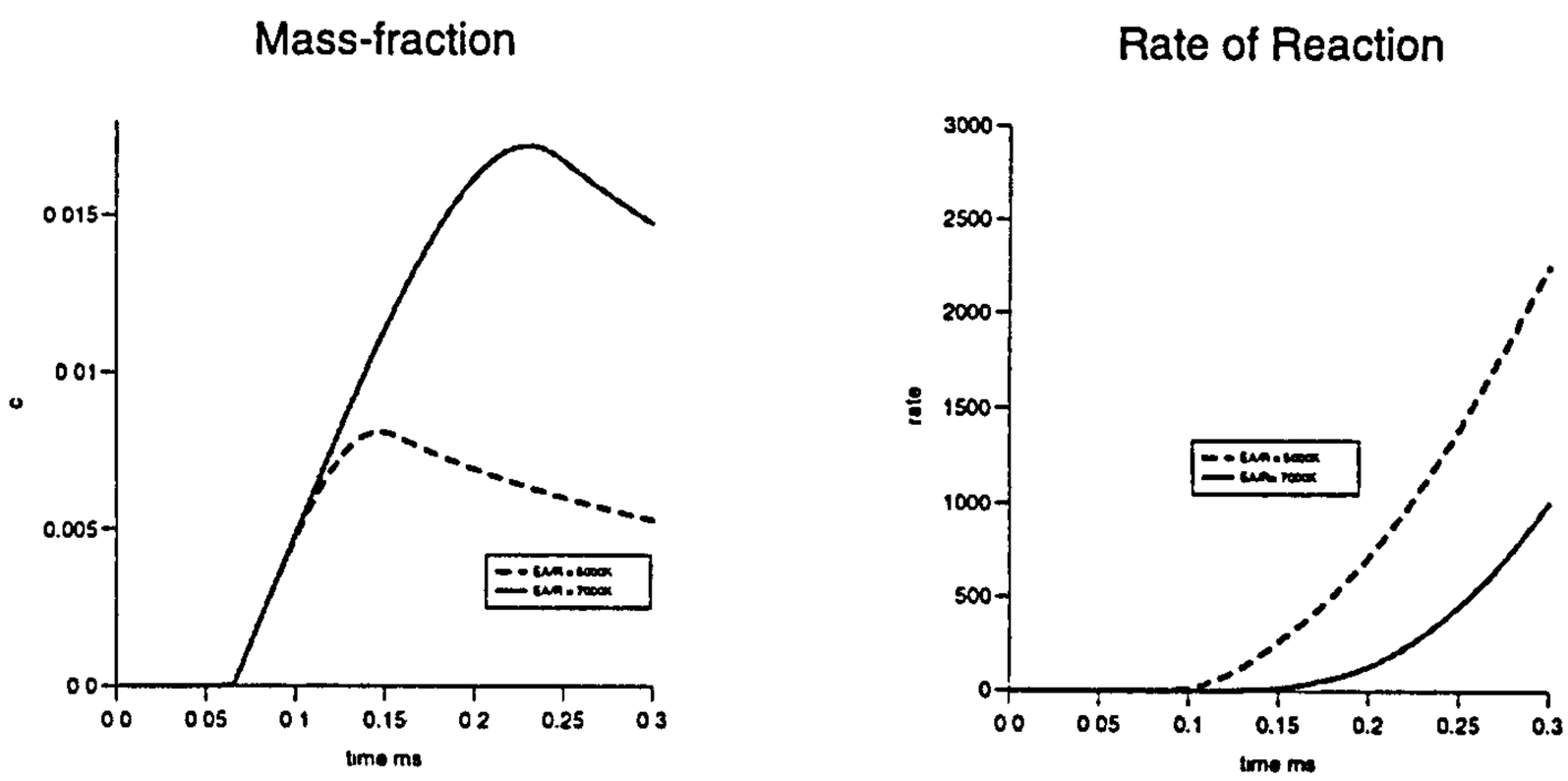

Figure 6.17: Early-time mass-fraction and reaction rate histories for $E_A/\mathcal{R} = 5000K$ (—) and $E_A/\mathcal{R} = 7000K$ (full-line).

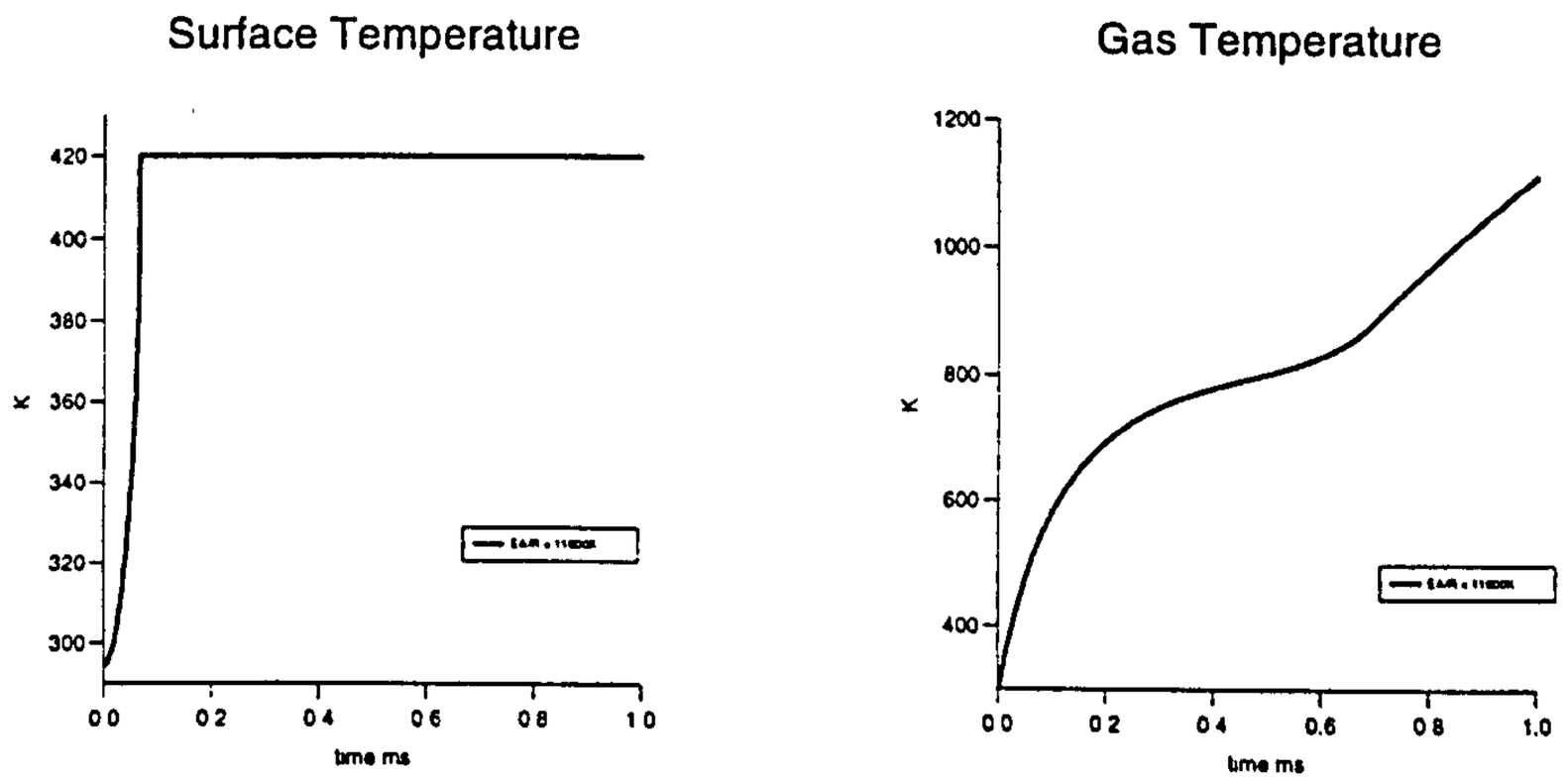

Figure 6.18: Early-time temperature histories for $E_A/\mathcal{R} = 11000K$ (full-line).

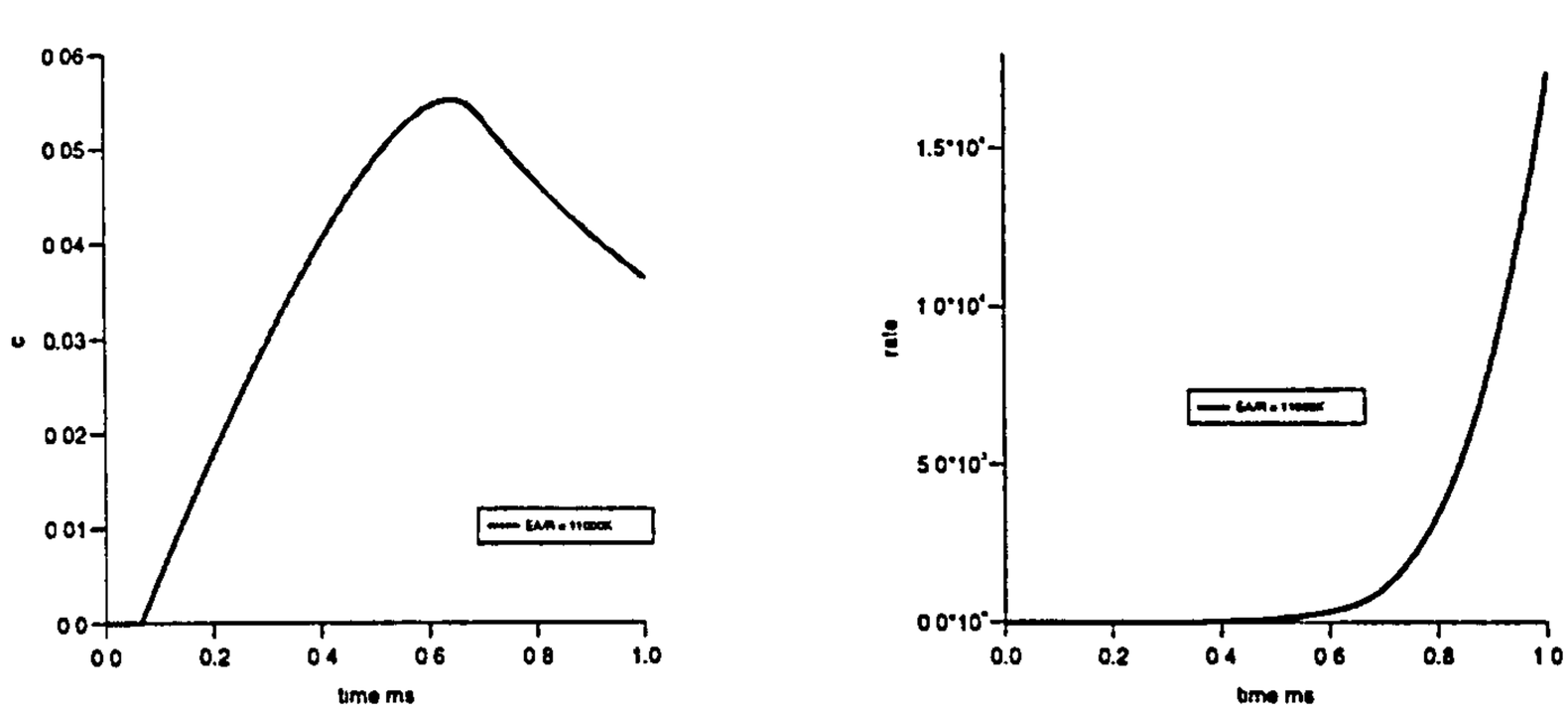

Figure 6.19: Early-time mass-fraction and reaction rate histories for $E_A/\mathcal{R} = 11000K$ (full-line).

The coupling of the rate of change in gasification $\dot{m}$ and rate of gas-phase reaction K introduces an important new dimension to the understanding of how the rate of mass addition effects the consumption of reactant gas. As the rate of addition of reactant mass increases, the rate of reaction rises with this. For E_A/R equal to $5000K$, thus an increase in c between times $0.07ms$ and $0.15ms$ implies that the rate of mass addition is greater than the rate of gaseous mass reaction in the vessel. After this the decline in mass-fraction implies that the rate of reaction is now greater than the mass addition. In chapter three it was predominately the gas temperature which drove the evolution of the gas-phase chemistry via the chemical frequency Ω and the ignition reaction was characterized by a steep decline in mass-fraction to near zero values. The present discussion illustrates how the more realistic scenario can differ from this now that $\dot{m}$ varies.

It is quite possible that if $\dot{m}$ continues increasing then comparison with the reaction rate would mean that the mass-fraction never falls to near zero values. In this case, when does ignition occur? Section (3.2.1) showed how the chemical process was such that over time when $K \rightarrow \dot{m}/2$ equilibrium chemistry was established. Ignition was assumed to have occurred when there was a steep increase in gas-phase temperature and reaction rate. In this study

this can be similarly accepted but now the added complication is that the rate $\dot{m}$ is not constant and now has a dependence on an activation energy E_A^p (at early times) and gas pressure. The rate of decomposition will continue to accelerate as the pressure increases so it is quite possible to imagine a scenario in which the rate of supply of gas-phase reactant *always* exceeds the rate of consumption. Non-equilibrium effects in the gas-phase will then prevail long after ignition.

Broadly speaking the coupling of the gas/interface chemistry will produce two possible scenarios prior to ignition:

- For $O(E_A^p) \approx O(E_A)$, decomposition and ignition will occur almost simultaneously as illustrated in figures (6.16) and (6.18).

- For $O(E_A^p) << O(E_A)$, decomposition will occur much earlier than ignition. This is illustrated in figure (6.17) and (6.19) which show identical plots for activation energy $E_A/\mathcal{R} = 11000K$. Decomposition occurs again before $0.1ms$ but high rates of reaction do not occur until $0.7ms$.

The transient burn-rate modelling dominates events until the exponential in the decomposition rate tends to one. After this, according to the present model, transient burning no longer plays a part and the gas-phase chemistry dominates. Once equilibrium chemistry is attained then the conventional burning models are retrieved that rely on Piobert's law alone. In reality this is not entirely true as the interface processes continue throughout burning. It is only for simplicity that all of this complicated interfacial chemistry is encompassed using Piobert's law.

For a more detailed and mathematically precise discussion of how the rate of solid gasification and the rate of gas-phase chemistry are related, the reader is directed to the recent analysis of Clarke [102]. In particular, a solution is analysed for the rather unusual case in which $E_A^p > E_A$. This will allow solutions categorized, in chapter two, as go/no-go solutions mathematically depicted as solutions that fall to either side of the separatrices around a saddle point in the T_c plane. However, it will also allow a new class of solutions mathematically corresponding to a focal node in the plane. Whilst the solutions around the saddle point have timescales measured in milli-seconds, the new solutions can span over hours. This might be interpretated as the 'hang-fire' phenomena whereby the the combustion products seem to 'cook' over a long period of time.

6.9 Conclusion

The above describes a possible mechanism for the interfacial chemistry that occurs between a hot gas and a reactive solid. This is a preliminary model and needs development for more complicated regimes such as extending the application of the model over the full combustion cycle, from initiation to burnout, and exploring the effect of latent heat and exothermic energy release in more detail. Heat-transfer relations also require improvement, in particular the model must be included in at least a one-dimensional context so that convective heat-transfer may be included. However, it provides insight on some of the controlling physical mechanisms and indicates a way forward.

Chapter 7

Conclusions and Further Work

The beginning of this study reviewed and discussed theory, and experiment, to describe the complex mechanisms that control the ignition of solid propellant. Most internal ballistics codes neglect a huge body of literature, that investigates detailed ignition processes, in favor of the very simplest ignition models. These simple models fail to provide adequate representation of some of the dominant factors known to influence ignition development. In particular, ignition models based solely on gas or solid-surface temperature attaining some empirical ignition temperature cannot predict the effect of gas-phase pressure and reactant species concentration on ignition delay. The participation of these elements motivates exploration of a gas-phase ignition model in a two-phase flow context. The goal has been to understand the ignition and consequent behavior of combusting propellant particles.

The first step of the investigation involved the development of a gas-phase reaction that controlled ignition and combustion. Detailed mathematical analysis of the governing equations that include simple chemical kinetics provides a precise criterion for ignition. Numerical methods have been described that solve the highly non-linear system of differential equations that is produced. These adopt modern shock-capturing methods, which provide high resolution of shocks, resulting in accurate, stable and, most importantly, physically meaningful solutions. Furthermore, application to realistic chamber configurations demonstrates the important coupling of the gaseous flow field and chemistry.

The gas-phase theory is still at a conceptual stage and needs to be extended to allow a much greater number of reactant species so that the true combustion cycle may be adequately represented. Investigation into the reactions that

occur during propellant combustion reveals hundreds of chemical reactions. For reasons of computational efficiency these must be severely reduced into a smaller number of the most important rate controlling reactions.

The second step has developed a model of solid propellant gasification that provides the source of gas-phase reactant species. This has exploited the vast amount of literature on ignition and transient burning that was specifically developed for rocket motor combustion. At present the model acts as the bridge to describe the events between first heating from ambient conditions to the establishment of gasification according to Piobert's law. However, the division of combustion into two constitutive reactions, gasification followed by gaseous combustion, throws question on the validity of Piobert's law in this context. Piobert's law is a measure of gasification rate and combustion simultaneously. It will only be valid in the above model once gas-phase reactions are in chemical equilibrium. When this is established, combustion is controlled by the rate of solid-phase gasification, since release of gas-phase exothermic energy occurs instantaneously on gasification. In essence this implies the obvious; accurate modelling of chemical processes requires accurate experimental information on the influential chemical rates. If the true nature of the propellant behavior is to be determined this will require unraveling some of the empiricism that has been adopted in the past.

Surface gasification can be either exothermic or endothermic depending on the choice of propellant. These reactions must be included into the heat-conduction equation to describe energy transfer particularly during the ignition transient. The present model implies that once the surface rises to some temperature then this is assumed to remain at this temperature regressing rapidly. However, throughout the burning cycle gaseous reaction will continue to provide heat feedback into the solid accelerating the rate of surface regression. If the gasification process is assumed to be endothermic, then these increasing quantities of thermal energy will be used for latent heat requirements. If gasification is exothermic then there may not be heat transfer into the solid since the solid may be very hot. To complement this, once again, chemical investigation into some of the actual reactions that are occurring must be investigated. The question of whether strong oxidiser actually attacks the solid propellant in a 'hypergolic' manner must be addressed.

To validate some of the work included, experimental data must be obtained. Closed bomb experiments that measure the time and temperature of first decomposition and ignition would provide an indication of the size of some of the chemical parameters involved. Following this the time and location of these processes must be measured in a one-dimensional context to validate the

concept of shock and reactant wave interaction as a controlling mechanism for ignition. It would also be interesting to examine the solution of the problem that contains a region of ullage. If the interface between the two-phase flow mixture and the ullage acts anything like the end of the primer tube, which is expected to be the case, then it is highly likely that reactant gas will fill the region of ullage producing high reactivity in this region. This has been frequently observed experimentally.

In the near future, the above model will be extended to include two-dimensional effects. It is anticipated that this will introduce a whole new area of difficulty due to the computational time required to solve the combination of two-dimensional transient two-phase flow and detailed gas and solid-surface chemistry.

Finally, perhaps the most fundamental question when it comes to interior ballistics in general, more detailed analysis of the governing equations has to be performed. If Gough's equations are correct upto the point of solid propellant incompressibility, then more precise criteria must be developed to calculate the exact point at which the limit is attained. Alternatively, if it is a question of ill-posedness, multi-phase flow theory should be exploited to resolve these issues for good.

It is highly likely that some of the complications are due to the numerical methods which have not been developed correctly to deal with some of the solid-phase behavior. For example, the numerical methods used in compressible high speed flow have taken years to be able to predict accurate propagation of shocks and contact discontinuities. The development of similar ideas may be required to model solid-phase features such as discontinuous changes in porosity. There seems little doubt that the action of gas-phase shocks on a wholly incompressible solid-phase is very likely to create difficulties physically and numerically. As the numerical methods have improved to provide excellent resolution of shocks these issues are becoming more important as the effect of the gas on the solid becomes more extreme. It seems that some of the older numerical methods based on high quantities of artificial viscosity, to provide stable solutions in the gas-phase, can attribute their success on the diffusion introduced in the system that smooths out discontinuous features. The equations may need some degree of compressibility to allow physical solutions to these problems. In fact it was not until the modelers of DDT, whom automatically assume solid-phase equations of state and compressibility, included thermodynamic considerations that physically meaningful solutions could be produced from the equations.

Some of these issues are urgently required for extending the generality of the model to allow a greater number of solid propellants with various different initial distributions. For example, if two different propellants occupy two distinct regions in the chamber, then there will be a jump in porosity between the propellant types. These issues are fundamental in the modelling of this two-phase flow problem and must be addressed before proceeding to multi-dimensional Navier Stokes calculations.

This discussion shows that despite the years of research into interior ballistics and solid propellant combustion in general, an accurate, all purpose model is still not within our capabilities in the immediate future.

Appendix A

Riemann Invariants

Riemann invariants are relations that can be constructed for a particularly simple class of homogeneous hyperbolic equations. Furthur details may be found in the text of Jeffrey [69].

Consider the set of equations written in conservative form:

$$\mathbf{U}_t + \mathbf{F}(\mathbf{U})_x = 0, \tag{A.1}$$

where $\mathbf{U} = [u_1, u_2, ..., u_n]$ and $\mathbf{F}$ are n dimensional vectors. Assume that this set of equations can be re-written in the form:

$$\mathbf{U}_t + \mathbf{A}(\mathbf{U})\mathbf{U}_x = 0, \tag{A.2}$$

where $\mathbf{A} = \mathbf{A}(\mathbf{U})$ is an explicit function of $\mathbf{U}$ and does not contain the independent variables x and t, that is, the system is 'reducible'. Since the system is hyperbolic it will have real eigenvalues $\lambda^{(i)}$ for $i = 1, n$ such that

$$|\mathbf{A} - \lambda\mathbf{I}| = 0, \tag{A.3}$$

with associated right eigenvectors $\mathbf{r}^{(i)} = [r_1^{(i)}, ..., r_n^{(i)}]$.

A generalised simple wave region is defined as any region $\mathcal{S}$ in the (x, t) plane in which the solution vector $\mathbf{U}$ can be written in the form $\mathbf{U}(u_j)$ where u_j is one particular element of $\mathbf{U}$. Generalized Riemann invariants apply in $\mathcal{S}$ space. This must be emphasized; the concept of a Riemann invariant is actually an exception to the rule and **only** applies in $\mathcal{S}$ space. Let $j = 1$ in the system, then since $\mathbf{U} = \mathbf{U}(u_1)$, substitution into equation (A.2) gives the result:

$$\left(\frac{\partial u_1}{\partial t}\mathbf{I} + \frac{\partial u_1}{\partial x}\mathbf{A}\right)\frac{d\mathbf{U}}{du_1} = 0. \tag{A.4}$$

If $\mathbf{U}$ is continuous and differentiable, it follows that:

$$d\mathbf{U} \equiv \frac{d\mathbf{U}}{du_1}, \tag{A.5}$$

A non-trivial solution to equation (A.4) can only exist provided that:

$$\left|\mathbf{A} - \lambda^{(i)}\mathbf{I}\right| = 0, \tag{A.6}$$

for $\lambda^{(i)} \equiv -\left(\frac{\partial u_1}{\partial t}/\frac{\partial u_1}{\partial x}\right)$. However, since the system of equation (A.2) are hyperbolic, then the system **has** n eigenvalues which by definition are identically equal to the $\lambda^{(i)}$ defined in (A.6). In fact when $\lambda = \lambda^{(i)}$, the associated right eigenvector $\mathbf{r}^{(i)}$ - by **definition** - must be such that it is proportional to $d\mathbf{U}$ to satisfy equation (A.4).

Define the set of characteristic curves $C^{(i)}$ by:

$$\frac{dx}{dt} = \lambda^{(i)} = -\left(\frac{\partial u_1}{\partial t}/\frac{\partial u_1}{\partial x}\right). \tag{A.7}$$

Then from the analysis:

$$\frac{\partial u_1}{\partial x}dx + \frac{\partial u_1}{\partial t}dt = 0, \quad \text{along each curve } C^{(i)}. \tag{A.8}$$

If $i = k$ then from this it is clear that $u_1(x,t)$ is constant along each of the curves $C^{(k)}$. The same result can be derived for all n families of characteristic curves; in particular concentrate on the k^{th} family. From this the system of generalized simple waves associated with this family will be determined. Since u_1 is constant along characteristics $C^{(k)}$, it follows that the solution $\mathbf{U}(u_1)$ must also be constant and by implication $\lambda^{(i)}$ is constant and the characteristics are in fact straight lines. This means that $d\mathbf{U} \propto \mathbf{r}^{(k)}$ along the straightline characteristics which results in a set of n differential equation:

$$\frac{du_1}{r_1^{(k)}} = \frac{du_2}{r_2^{(k)}} = ... = \frac{du_n}{r_n^{(k)}} = d\xi. \tag{A.9}$$

This set of equations provides a relationship across simple waves

$$\frac{du_j}{d\xi} = r_j^{(k)}, \tag{A.10}$$

and u_j can be found in terms of ξ by integrating the system. For example consider the case of one dimensional unsteady inviscid flow; for an ideal gas this can be written in the form given by equation (A.2) where:

$$\mathbf{U} = \begin{pmatrix} \rho \\ u \\ s \end{pmatrix}, \quad ,\mathbf{A} = \begin{pmatrix} u & \rho & 0 \\ a^2/\rho & u & 1/\rho\frac{\partial p}{\partial s} \\ 0 & 0 & u \end{pmatrix}, \tag{A.11}$$

where ρ is the gas density, u is the gas velocity, $p = p(\rho, s)$ is the gas pressure and the entropy $s = s(p, \rho)$. The eigenvalues are given by:

$$\lambda^{(1)} = u + a, \quad \lambda^{(2)} = u, \quad \lambda^{(3)} = u - a \tag{A.12}$$

where a is the gas-phase sound-speed and the right eigenvalues are:

$$\mathbf{r}^{(1)} = \begin{pmatrix} 1 \\ a/\rho \\ 0 \end{pmatrix}, \quad \mathbf{r}^{(2)} = \begin{pmatrix} -\frac{\partial p}{\partial s} \\ 0 \\ a^2 \end{pmatrix}, \quad \mathbf{r}^{(1)} = \begin{pmatrix} 1 \\ -a/\rho \\ 0 \end{pmatrix}. \tag{A.13}$$

Inserting these results into equation (A.10) gives the following:
Generalised Riemann invariants $\mathbf{J}^{(1)}$ for $\lambda^{(1)}$:

$$J_1^{(1)} \equiv u - \int \frac{a}{\rho} d\rho = \text{const, and} \qquad J_2^{(1)} \equiv S = \text{const.} \tag{A.14}$$

Generalised Riemann invariant for $\lambda^{(2)}$:

$$J_1^{(2)} \equiv p = \text{const, and} \qquad J_2^{(2)} \equiv u = \text{const.} \tag{A.15}$$

Generalised Riemann invariant for $\lambda^{(3)}$:

$$J_1^{(3)} \equiv u + \int \frac{a}{\rho} d\rho = \text{const, and} \qquad J_2^{(1)} \equiv S = \text{const.} \tag{A.16}$$

Entropy s is constant over the outer waves $\lambda^{(1)}$ and $\lambda^{(3)}$ and u and p are constant over $\lambda^{(2)}$.

Appendix B

Shock Speeds

This section is designed to describe to the reader how the formation of the Rankine Hugoniot jump conditions are manipulated to produce closed forms for the shock speeds and star velocity.

The one-dimensional Euler equations with a single species reactant equation are given as:

$$\mathbf{U}_t + \mathbf{F}(\mathbf{U})_x = 0, \tag{B.1}$$

where $\mathbf{U} = (\rho, \rho c, \rho u, E)^T$ and $\mathbf{F}(\mathbf{U}) = (\rho u, \rho u c, \rho u^2 + p, u(E + p))^T$.

Rankine-Hugoniot conditions are defined by:

$$S\Delta\mathbf{U} = \Delta\mathbf{F} \tag{B.2}$$

where S is the shock speed and Δ defines the jump in quantity across the shock where the conditions at either side are depicted in figure (4.3). For example figure (B.1) shows the change in variables across the left shock S_L.

It is easy to manipulate the equations to give a closed form for the shock speed S_L by transforming the equations to a frame of reference in which the shock is stationnary. This is described in figure (B.1) where a new variable is introduced, v, which replaces u in the equations:

$$v_l = u_l - S_L; \tag{B.3}$$

$$v^* = u^* - S_L. \tag{B.4}$$

Substituting equations (B.3) and (B.4) into equation (B.2) effectively gives

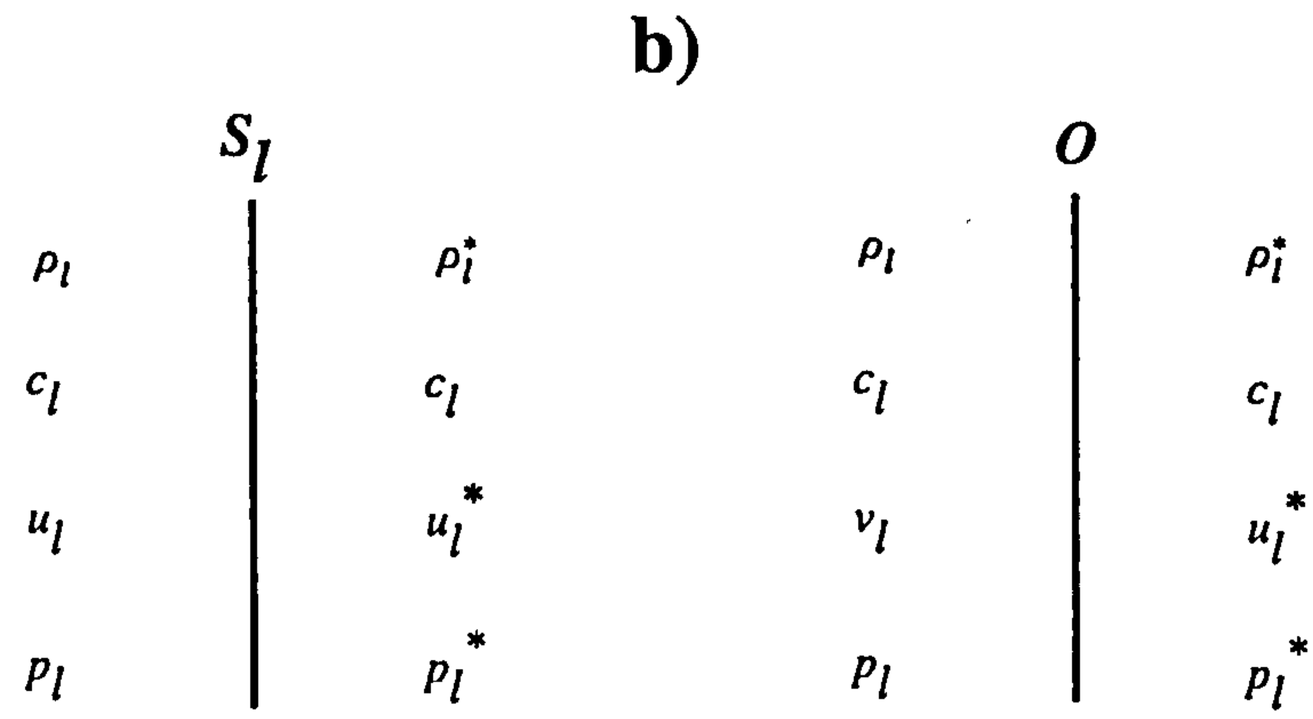

Figure B.1: Transformation of a shock wave from speed S_L to speed zero.

a zero shock speed and only the right-hand-side of the Rankine-Hugoniot conditions remain that is:

$$\Delta F \equiv 0 \tag{B.5}$$
$$\Rightarrow \rho_l v_l = \rho_l^* v^*; \tag{B.6}$$
$$\rho_l v_l c_l = \rho_l^* v^* c_l; \tag{B.7}$$
$$\rho_l v_l^2 + p_l = \rho_l^* v^{*2} + p^*; \tag{B.8}$$
$$v_l(E_l + p_l) = v^*(E_l^* + p^*). \tag{B.9}$$

Subtracting equation (B.3) from (B.4) implies $v_l - v^* = u_l - u^*$. Define the parameter

$$M_L \equiv \rho_l v_l = \rho_l^* v^*, \tag{B.10}$$

then substitution into (B.8) and simple manipulation gives:

$$M_L = -\frac{p_l - p^*}{v_l - v^*} = -\frac{p_l - p^*}{u_l - u^*}. \tag{B.11}$$

Recall from equation (B.10) that $v_l = M_L/\rho_l$ and $v_l = M_L/\rho_l^*$ then substition in equation (B.11) gives:

$$M_L^2 = \rho_l D_l \frac{p_l - p^*}{1 - D_l}, \tag{B.12}$$

where $D_l = \rho_l^*/\rho_l$. The third relation given in equation (B.9) can be manipulated to give:

$$e^* - e_l = \frac{1}{2}(\frac{p_l}{\rho_l})\left(\frac{(H_l+1)(D_l-1)}{D_l}\right), \tag{B.13}$$

where $H_l = p^*/p_l$.

The equation of state for a co-volume gas is:

$$\frac{e = p(1-\rho b)}{\rho(\gamma-1),}$$

where b is the covolume. Use of this in equation (B.13) gives a relationship between H_l and D_l across the shock that can be substituted into equation (B.12) to give:

$$M_l = \sqrt{\left(\frac{\gamma+1}{2}\frac{\rho_l p_l}{1-b\rho_l}\right)\left(H_l + \frac{\gamma-1}{\gamma+1}\right)}. \tag{B.14}$$

Recall that

$$S_L = u_l - v_l = u_l - M_l/\rho_l, \tag{B.15}$$

and the gas-phase sound speed can be defined as

$$a = \sqrt{\frac{\gamma p}{\rho(1-\rho b)}}$$

then this finally gives the the left shock speed as:

$$S_l = u_l - a_l\sqrt{1 + \frac{\gamma+1}{2\gamma}(\frac{p^*}{p_l} - 1)} \tag{B.16}$$

Use of equation (B.11) also gives the relation:

$$u^* = u_l - \frac{p^* - p_l}{M_l} = u_l - f_l(p^*, \mathbf{U}_l) \tag{B.17}$$

where $f_l(p^*, \mathbf{U}_l) = \frac{p^*-p_l}{M_l}$ which is used in the exact solution of the Riemann problem.

Identical manipulation of the right conditions gives the formula:

$$S_R = u_r + a_r\sqrt{1 + \frac{\gamma+1}{2\gamma}(\frac{p^*}{p_r} - 1)}. \tag{B.18}$$

Similarly it may be shown that:

$$u^* = u_r + \frac{p^* - p_r}{M_r} = u_r + f_r(p^*, \mathbf{U}_r) \tag{B.19}$$

where $f_r(p^*, \mathbf{U}_r) = \frac{p^* - p_r}{M_r}$.

These relations give closed forms for the left and right shock speeds and the star velocity in terms of the unknown star pressure p^* and all known initial data.

Bibliography

[1] Krier and Summerfield. *Interior Ballistics of guns*, volume 66 of *Progress in Astronautics and Aeronautics Series.* 1979.

[2] G.B. Ministry of Supply Scientific Advisory Council. *Internal Ballistics.* H.M. Stationnary Office, 1951.

[3] P.G. Baer and J.M. Frankle. The simulation of interior ballistic performance of guns by digital computer program. Technical Report BRL-1183, Ballistics Research Laboratory, Aberdeen Proving Ground, MD, 1963.

[4] May and Horst. *Gun Design and Pressure Waves*, volume 66 of *Progress in Astronautics and Aeronautics Series*, pages 177–196. 1979.

[5] K.K. Kuo and M. Summerfield. Theory of steady-state burning of gas-permeable propellants. *AIAA*, 12(1), 1974.

[6] H.Krier. Predictions of pressure wave propagation and flame fronts in reactive solid-gas mixtures. In *Proceedings on two-phase transport and reactor safety*, Fort Lauerdale, October 1976. Hemisphere Pub. Corp.

[7] F.E.C. Culick. Conservation equations for a reacting two-phase flow based on continuum theory. In *Proceedings of the 12th JANNAF Combustion Meeting*, 1975.

[8] P.S. Gough. *The flow of a compressible gas through an aggregate of mobile reacting particles.* McGill University, Dept. Mechanical Engineering, 1974.

[9] K.K. Kuo, J.H. Koo, T.R. Davis, and G.R. Coates. Transient combustion in mobile gas-permeable propellants. *Acta Astronautica*, 3:573–591, 1976.

[10] S.L. Soo. *Fluid dynamics of multiphase systems.* Waltham, 1967.

[11] P. Gough. The NOVA code-A users manual. Technical Report PGA-TR-79-5, Paul Gough Associates, Inc. Portsmouth, NH 03801, 1979.

[12] A.D. Fitt. Some aspects of internal ballistics theory. In *Proc. 5th Anglo-German Meeting on Ballistics*, Unterluss, W. Germany, June 1988.

[13] A.E. Wildegger-Gaissmaier and G.E. Keller. Investigation of axial and radial discharge of ignition products in a gun charge. In *The 14th International Symposium on Ballistics*, 1993.

[14] E.F. Toro. The WAFBC1 internal ballistic manual. Cranfield Institute of Technology report, Aerodynamics Dept., Cranfield Institute of Technology, Beds., U.K., 1989.

[15] B Porterie and J.C. Loraud. An investigation of interior ballistic ignition phase. *Shock Waves*, 4:81–93, 1994.

[16] R.W. MacCormack. The effect of viscosity in hypervelocity impact cratering. *AIAA*, 1969.

[17] K.K. Kuo, K.C. Hsieh, and M.M. Athavale. Modelling of combustion processes of stick propellants via combined Eulerian-Lagrangian approach. In *Proceedings of the 8th International Symposium on Ballistics*, pages 55–68, October 1984.

[18] J.M. Char and K.K. Kuo. Study of combustion processes of single-perforated stick propellants. In *AIAA/SAE/ASME/ASEE 23rd Joint Propulsion Conference*, 1976.

[19] A.W. Horst and G.E. Keller. A two-phase flow simulation of LOVA propellant interior ballistic behaviour using the XnOVAK code. Technical Report BRL-TR-2796, Ballistics Research Laboratory, Aberdeen Proving Ground, MD, 1987.

[20] G.E. Keller A.W. Horst and P.S. Gough. New directions in multiphase flow interior ballistic modeling. Technical Report BRL-TR-3102, Ballistics Research Laboratory, Aberdeen Proving Ground, MD, 1990.

[21] M.R. Baer and J.W. Nunziato. A two-phase mixture theory for the deflagation-to-detonation transition (DDT) in reactive granular materials. *Journal of Multiphase Flow*, 12(6):861–889, 1986.

[22] H.J. Gibeling and H. McDonald. Development of a two-dimensional interior ballistic code. Technical Report ARBRL-CR-00451, U.S. Army ARRADCOM/ Ballistic Research Laboratory,, 1981.

[23] S. Margolis and F. Williams. Effects of two-phase flow in a model for nitramine deflagation. *Combustion and Flame*, 80:329–349, 1990.

[24] K.K. Kuo and M. Summerfield. *Fundamentals of Solid Propellant Combustion.* Progress in Astronautics and Aeronautics Series. 1984.

[25] E.W. Price, H.H. Bradley, G.J. Dehority, and M.M. Ibiricu. Theory of ignition of solid propellants. *AIAA*, 7:1153–1181, 1966.

[26] A.G. Merzhanov and A.E. Averson. The present state of the thermal ignition theory: An invited review. *Combustion and Flame*, 16:89–124, 1971.

[27] A. Linan and F.A. Williams. Theory of ignition of a reactive solid by a constant energy flux. *Combustion Science and Technology*, 3:91–98, 1971.

[28] H.H. Bradley. Theory of ignition of a reactive solid by a constant energy flux. *Combustion Science and Technology*, 2:11–20, 1970.

[29] F.A. Williams. Theory of propellant ignition by heterogeous reaction. *AIAA*, 4(8):1354–1357, 1966.

[30] W.H. Andersen. Theory of surface ignition with application to cellulose, expolosives and propellants. *Combustion Science and Technology*, 2:213–221, 1970.

[31] D.A. Frank-Kamenetskii. *Diffusion and heat exchange in chemical kinetics.* Princeton University Press, 1955.

[32] W.H. Andersen. Model of transient burning to self-sustained burning. *Combustion Science and Technology*, 5:75–81, 1972.

[33] A. Linan and A. Crespo. An asymptotic analysis of radiant and hypergolic heterogeneous ignition of solid propellants. *Combustion Science and Technology*, 6(4):223–232, 1972.

[34] A. Linan and M. Kindelan. Gasification effects in the heterogenous ignition of condensed fuel by a hot gas. *Acta Astonautica*, 5:1199–1211, 1972.

[35] C.E. Hermance, R. Shinnar, and M. Summerfield. Ignition of an evaporating fuel in a hot oxidising gas, including effect of heat feedback. *Acta Astronautica*, 12(2):95–112, 1966.

[36] R.K. Kumar and C.E. Hermance. Gas phase ignition theory of a homogeneous solid propellant under shock conditions. *AIAA*, 8(9):1551–1558, 1970.

[37] R.K. Kumar and C.E. Hermance. Gas phase ignition theory of a heterogeneous solid propellant exposed to a hot oxidising gas. *Combustion Science and Technology*, 4:191–196, 1972.

[38] T. Kashiwagi and M. Summerfield. Ignition and flame spreading over a hot fuel: non-similar theory for a hot oxidising boundary layer. In *The 14th International Symposium on Combustion*, pages 1235–1247, 1973.

[39] R.K. Kumar and C.E. Hermance. Role of gas-phase reactions during radiant ignition of solid propellants. *Combustion Science and Technology*, 14(4-5-6):169–175, 1976.

[40] M. Kindelan and F.A. Williams. Theory for endothermic gasification of a solid by a constant energy flux. *Combustion Science and Technology*, 10:1–19, 1975.

[41] M. Kindelan and F.A. Williams. Radiant ignition of a combustible solid with gas-phase exothermicity. *Acta Astonautica*, 2:955–979, 1975.

[42] A. Peretz, K.K. Kuo, L.H. Caveny, and M. Summerfield. Starting transient of solid propellant rocket motors with high internal gas velocities. *AIAA*, 11(12):1719–1727, 1973.

[43] K.K.Kuo and Coates. General review of dynamic burning of solid propellants in gun and rocket propulsion systems. In *Proceedings of the 16th Symposium on Combustion*, pages 1177–1191, 1976.

[44] D.E. Kooker and C.W. Nelson. Numerical solution of three solid propellant combustion models during a gun pressure transient. Technical Report BRL no. 1953, Ballistics Research Laboratory, Aberdeen Proving Ground, MD, 1977.

[45] M. S. Miller. In search of an idealized model of homogeneous solid propellant combustion. *Combustion and Flame*, 46:51–73, 1982.

[46] M.S. Miller and T.P. Cofee. On the numerical accuracy of homogeneous solid propellant combustion models. *Combustion and Flame*, 50:75–88, 1983.

[47] R.A.Battista N. Kubota Yu.A.Gostinthev M. Summerfield, L.H.Caveny and H. Isoda. Theory of dynamic extinguishment of solid propellant with special reference to non-steady heat feedback law. *Journal of Spacecraft and Rockets*, 8(3):251–58, 1971.

[48] C.W. Nelson, F.W. Robbins, and P.S. Gough. Predicted effects of transient burning on gun flamespreading. Technical Report ARBRL-MR-02830, Ballistics Research Laboratory, Aberdeen Proving Ground, MD, 1978.

[49] S.S. Gokhale and H. Krier. Modeling of unsteady two-phase reactive flow in porous beds of propellant. *Progress in Energy and Combustion Science*, 8:1–39, 1982.

[50] C.W Gear. *Numerical initial value problems.* Prentice Hall, Englewood Cliffs, N.J., 1971.

[51] J.F. Clarke and McChesney. *Dynamics of reacting gases.* Butterworths, 2 edition, 1975.

[52] J.F. Clarke. Progress report August 1992 for DRA. Technical report, Cranfield University, Cranfield, Beds. U.K., 1992.

[53] J.F. Clarke and C.A. Lowe. Combustion with source flows. *Mathematical and Computer Modelling*, 1995.

[54] J.F. Clarke. Progress report March 1993 for DRA. Technical report, Cranfield University, Cranfield, Beds. U.K., 1993.

[55] D.W. Jordan and P. Smith. *Mathematical techniques: An introduction for the engineering, physical and mathematical sciences.* Research notes in mathematics. Oxford University Press, 1994.

[56] A.C. Hindmarsh. Linear multistep methods for ordinary differential equations: method formulations, stability, and the methods of nordsieck and Gear. Lawrence Livermore National Laboratory, UCRL-51186 Rev. 1, 1972.

[57] J.F. Clarke. Progress report June 1993 for DRA. Technical report, Cranfield University, Cranfield, Beds. U.K., 1993.

[58] P.S. Gough and F.J. Zwarts. Modeling heterogenous two-phase flow. *AIAA Journal*, 17(1):17–25, 1979.

[59] N. Yanenko. *The Method of Fractional Steps.* Springer Verlag, 1977.

[60] G. Strang. On the construction and comparison of difference schemes. *SIAM Journal of Numerical Analysis*, 5:506–517, 1968.

[61] M. Crandall and A. Majda. The method of fractional steps for conservation laws. *Numerical Mathematics*, 34:285–314, 1980.

[62] S.K. Godunov. A finite difference method for the numerical computation of discontinuous solutions of the equations of fluid dynamics. *Mat. U.S.S.R. Sb.*, 47:357–393, 1959.

[63] T. Tang and Z.H. Teng. Error bounds for fractional step methods for conservation laws with source terms. *SIAM Journal of Numerical Analysis*, 32(1):110–127, 1995.

[64] E.F. Toro. A weighted average flux method for hyperbolic conservation laws. In *Proceedings of the Royal Society London*, volume A 423, pages 401–18, 1989.

[65] E.F. Toro. A linearized solver for the time dependent Euler equations of gas dynamics. In *Proceedings of the Royal Society London*, volume A 434, pages 683–693, 1991.

[66] P.L. Roe. Approximate riemann solvers, parameter vectors and difference schemes. *Journal of Computational Physics*, 43:357–372, 1981.

[67] E.F. Toro. A fast Riemann solver with constant covolume applied to the randomn choice method. *International Journal for Numerical Methods in Fluids*, 1988.

[68] E.F. Toro, M. Spruce, and W. Speares. Restoration of the contact surface in the HLL solver. *Shock Waves*, 4:25–34, 1994.

[69] A. Jeffrey. *Quasilinear hyperbolic systems and waves.* Pitman, 1976.

[70] E.F. Toro. In *International Workshop on Wave Propagation*, Mathematics & Physics Department, Manchester Metropolitan University, Chester St., Manchester M15 GD, May 1995.

[71] S. Leppington. Progress on modelling of hybrid liquid-solid propellant propulsion systems. Technical report, Mathematics & Physics Department, Manchester Metropolitan University, Manchester M15 GD, December 1995.

[72] A. Harten, P.D. Lax, and B. Van-Leer. On upstream differencing and Godunov-type schemes for hyperbolic conservation laws. *SIAM Review*, 25:35–61, 1983.

[73] E.F.Toro. *Riemann solvers and numerical methods.* McGraw-Hill Series in Aeronautical and Aerospace Engineering. Springer-Verlang, 1 edition, to appear 1996.

[74] Randall J. LeVeque. *Numerical methods for conservation laws.* Lectures in Mathematics. Birkhauser Verlag, 2 edition, 1992.

[75] S.P.Spekreijse. *Multigrid solution of the steady Euler equations.*

[76] C.A.Lowe, E.F. Toro, and J.F. Clarke. Numerical methods for propellant systems. In *The First Asian Computational Fluid Dynamics Conference*, pages 541–549, Honk Kong University of Science and Technology, Clearwater Bay, Hong Kong, January 1995.

[77] C.A. Lowe & J.F. Clarke. Progress report October 1993 for DRA. Technical report, Cranfield University, Cranfield, Beds. U.K., 1993.

[78] J.D.Andersen. *Fundamentals of Aerodynamics.* McGraw-Hill Series in Aeronautical and Aerospace Engineering. New-York:Macgraw-Hill, 2 edition, 1991.

[79] S.L. Soo. Multiphase mechanics and distinctions from continuum mechanics. In *Two-phase flow and heat transfer symposium workshop*, Fort Lauerdale, 1976.

[80] P.S Gough. *Modelling of two-phase flows in guns*, volume 66 of *Progress in Astronautics and Aeronautics Series*, pages 177–196. 1979.

[81] E.F. Toro. Riemann-problem based techniques for computing reactive two-phase flows. In Dervieux and Larrouturou, editors, *Lecture Notes in Physics, Numerical combustion*, volume 351. Springer Verlag, 1989.

[82] C.A. Lowe. One-dimensional, two-phase flow for an internal ballistic model. Master's thesis, College of Aeronautics, Cranfield Institute of Technology, Cranfield, Beds.. U.K., 1992.

[83] D.A. Drew. Mathematical modelling of two-phase flow. *Annual Review of Fluid Mechanics*, 15:261–291, 1983.

[84] R.G. Boothroyd. *Flowing gas-solid suspensions.* Chapman and Hall, 1971.

[85] C. Truesdell and R. Toupin. *The classical field theories.* Springer, 1960.

[86] V.H. Ransom and D.L. Hicks. Hyperbolic two-pressure models for two-phase flow. *Journal of Computational Physics*, 53:124–151, 1984.

[87] L. Van Wijngaarden and A. Prosperetti. On the characteristics of the equations of motion for a bubbly flow and the related critical flow. *Journal of Engineering and Mathematics*, 10:153–62, 1976.

[88] J.H. Stuhmiller. The influence of interfacial pressure forces on the character of the two-phase flow model equations. *International journal of two-phase flows*, 3:551–560, 1977.

[89] F.H. Harlow and A.A. Amsden. Numerical calculation of multiphase fluid flow. *Journal of computational physics*, 17:19–52, 1975.

[90] V. Yang. Compaction of particles in granular propellant beds by mechanical and gas dynamic loadings. Master's thesis, Department of Mechanical Engineering, The Pennsylvania State University, U.S., 1980.

[91] Stewart, Powers, and H. Krier. Simplified model of transition to detonation in porous energetic material. Technical Report UILU-ENG 93-6002, Department of Theoretical and Applied Mechanics, University of Illinois at Urbana-Champaign, 1992.

[92] N.N. Smirnov and I.D. Dimitrenko. Convective combustion of porous compressible propellants. *Combustion and Flame*, 89:260–270, 1992.

[93] S.L. Soo. Equation of motion of a solid sphere suspended in a fluid. *Journal of multiphase flows*, 18:263–4, 1979.

[94] C.A. Lowe. Progress report June 1996 for DRA. Technical report, Cranfield University, Cranfield, Beds. U.K., 1996.

[95] A.C. Hindmarsh. Two new initial value ordinary differential equation solvers. *ACM SIGNUM Newsletter*, 15(4):10–11, 1980.

[96] J. Pike. Internal ballistics using two-different form functions. Technical report, Cranfield Institute of Technology, Aerodynamics Dept., Cranfield Institute of Technology, Beds U.K., 1990.

[97] S. Ergun. Fluid flow through packed beds. *Chemical Engineering Progress*, 48:89–96, 1952.

[98] R.E. Brown and E.F.Toro. The WAF method and splitting procedures for viscous shocks. In *Proceedings of the 18th International Symposium on Shock Waves*, Tohoku University, Sendai, Japan, July 1991.

[99] R.E. Brown. Numerical solution of the two-dimensional unsteady navier stokes equations using viscous-convective operator splitting. Master's thesis, College of Aeronautics, Cranfield Institute of Technology, Cranfield, Beds., U.K., 1990.

[100] S.D. Conte and C. de Boor. *Elementary Numerical Methods: An Algorithmic Approach.* International Series on Pure and Applied Mathematics. New York: McGraw-Hill, 1972.

[101] H.S. Carslaw and J.C. Jaegar. *Heat Conduction in Solids, 2nd Edition.* International Series on Pure and Applied Mathematics. Oxford University Press, 1959.

[102] J.F. Clarke. A reactor model for ignition and burning of a gasifying solid. *Journal of the Chemical Society: Faraday Transactions*, in the press, 1996.